Applications of Atomic Systems in Quantum Simulation, Quantum Computation and Topological Phases of Matter

by

Shengtao Wang

A dissertation submitted in partial fulfillment
of the requirements for the degree of
Doctor of Philosophy
(Physics)
in the University of Michigan
2017

Doctoral Committee:

Professor Luming Duan, Chair
Assistant Professor Emanuel Gull
Professor Georg A. Raithel
Professor Duncan G. Steel
Assistant Professor Kai Sun

Shengtao Wang

wangst@umich.edu

ORCID iD: 0000-0003-1403-5901

In loving memory of my grandma

ACKNOWLEDGMENTS

Whenever I come across a thesis, this part is always the first piece I read, and often the most fun and enjoyable part. It often steers one to follow the long journey of the author, through ups and downs, 'eureka' and 'damn', via an exceedingly vivid and personal sketch. This is also the part that one needn't worry about going through loads of revisions, for being too casual, lighthearted or utterly funny (or using contracted words). Here is my turn, to recollect, reflect, and say thank you to everyone who has been part of my journey.

During my undergrad senior year, when I was learning about the basics of quantum information science, I stumbled on a name, Luming Duan. Not many Chinese names popped up, so I asked my undergrad advisor who this person is. Not surprisingly, he told me Luming is a superb researcher and I should go and work with him—I applied. Six years later, I am finally at this stage to say: joining Luming's group has been one of the best choices I've made in life. More than a superb researcher, Luming has been a caring mentor, a patient advisor, and a humble colleague. Instead of treating his students as subordinates, Luming looks on us as respectable colleagues, challenging us to make our own decisions, after, of course, making sure we are well informed. Not once has my discussion with Luming been ineffective. For countless times, I would bring a thorny problem to his office—confident that he wouldn't be able to turn things around this time—but emerge feeling enlightened and

hopeful. Luming never fails to amaze me with his 'nonseparable' knowledge on all related fields, from theoretical technicalities to experimental nuts and bolts. And his magic to be able to see and distill the essence of a problem in a second is something I have been trying very hard to steal (but been failing). I am deeply indebted to Luming for everything he has imparted to me, either directly or indirectly. I am so proud to be his student.

I am also extremely lucky to be able to know and collaborate with Prof. Kai Sun. Much of my knowledge on topological matters comes from Kai, either from his class (one of my favorites) or from discussing with him. His deep knowledge on topological matters is only superseded by his terrific physical picture. Kai is like an 'unofficial' second advisor to me. I thank Kai for a myriad of things, from taking pains to answer my silly questions to encouraging me to apply for fellowship positions. I am glad I can call Kai a collaborator and a friend. I am also grateful to other members of my thesis committee, Prof. Duncan Steel, Prof. Georg Raithel and Prof. Emanuel Gull. I thank them for their service and help in making the last part of my journey a very smooth process.

I could not have completed this journey without the generous support from everyone in Luming's group. I am truly blessed to be able to know and work with Dong-Ling Deng. More than an awesome collaborator, to me, Dong-Ling is an altruistic brother and a best friend. From a 5am lesson on homotopy groups at Ke Yuan hotel (because we still had jet lag) to a 2am chat on academia and life during a DAMOP meeting, from forming a fearless team in the Ann Arbor badminton tournament to a drunken night of departure, Dong-Ling has packed my PhD years with a panoply of highlights. That is not to mention how immensely helpful Dong-Ling has been to my scientific development. I can only hope that this pure camaraderie will never rust. I am also very lucky to have Yang-Hao Chan taking me under his wing in my first two years. He never grew impatient with my simple questions

on numerical algorithms, cold atoms or basic condensed matter concepts. It's a pity that I didn't have a chance to write a paper together with Yang-Hao before he left (none of my naive ideas worked). In my last year, I have been fortunate to know Xun Gao, a student of Luming from the other side of the earth. Since then, we had countless (mostly remote) discussions. I thank Xun for teaching me loads of tensor network theory and complexity theory. Let's figure out a way for 'efficient' remote discussion. Zhe-Xuan Gong and Chao Shen were senior students when I joined the group. I had numerous fun discussions with them. I thank Zhe-Xuan for hosting me for my visit to Maryland and Chao for teaching me trapped ion physics. I wish them continued success in their career. Yong Xu joined our group in my last year. Our office Randall 4205 has been highly conducive in generating our daily impromptu discussions. I thank Yong for teaching me Weyl (point, ring, exceptional ring) physics. I look forward to visiting Yong in China in the future. I thank Xinxing Yuan for a fun collaboration on the Hopf experiment. I am grateful to a former group member, Zhen Zhang, and current members, Tanvi Gujarati, Zhengyu Zhang, Ceren Burcak Dag, Yukai Wu for delightful discussions. I hope I have been of slight help to the younger generation in the group (sorry for always pushing things back). I thank other group members and visitors at both Michigan and Tsinghua, Chong Zu, Weiran Huang, Mingxing Luo, Xiaolan Zong, Yue Jiang. I appreciate all your help, in one way or another.

Life outside of Michigan has been pivotal in my scientific and personal growth. I'd like to thank Institute for Interdisciplinary Information Sciences (IIIS) at Tsinghua University for hosting my visit every summer (and rob every single summer of mine from Ann Arbor. I didn't mean I can then randomly disappear and go home). At IIIS, I'd like to acknowledge Prof. Kihwan Kim for a number of lovely discussions (and for bringing me to lunch or dinner after that). I am incredibly fortunate to be able to know Prof. Misha Lukin and visit his group for a short period of time.

Every interaction with Misha has been enlightening. I admire his attitudes toward physics, work and life in general, which will undoubtedly be a source of inspiration for me in the next few years. I've also had the privilege to get to know many of Misha's former and current group members, who are all amazingly brilliant. I'd like to specially thank Prof. Norman Yao, whose vigor and buoyancy are infectious. A paragon of 'play hard, work harder', your work ethic and life style are something I can hardly emulate. I've met Prof. Liang Jiang a couple of times—your modesty and calm demeanor made a deep impression on me. I thank Liang for offering help with my postdoc application. I am indebted to Soonwon Choi for hosting me at Harvard and for a number of stimulating discussions.

At the opposite side of the earth, I am beholden to my undergrad advisors and friends. I had the chance to visit Singapore again during a conference in 2015. Prof. Leong Chuan Kwek hosted my talk at Center for Quantum Technologies. My interest in quantum information originates from working with Prof. Kwek (and thanks for recommending Luming to me). It was such a great pleasure to see you again and notice that your love for (teddy and otherwise) bears never wanes. And thank you for always taking me to feast on loads of sumptuous food. Mentorship from my undergrad advisors at NTU, Prof. Tieh-Yong Koh and Prof. Lock Yue Chew, was indispensable to my education and shaped my scientific stance. Tieh-Yong never grew tired of sharing his life and work experience with me, from his tangible passion for physics to the 'dark side' of academia. Lock Yue hosted my visit at NTU and he is forever as amiable and unassuming as I can possibly wish. And to my dear friends at NTU and Singapore: though I am notorious for bad memories, my time with you guys (and girls) has always been as vivid as it can be. You are the reasons for me to visit Singapore.

I've benefited enormously from collaborations and discussions with other professors and students outside of Michigan. I'd like to thank Prof. Chris Monroe and his group for illu-

minating discussions, especially from the experimental perspective. Discussion with Chris and attending a number of his seminar talks have always be a pleasure. I learnt a great deal from Chris' students and postdocs, Shantanu Debnath, Jake Smith, Phil Richerme, Norbert Matthias Linke, Caroline Figgatt, and Kevin Landsman. I'd also like to specially thank Prof. Joel Moore for introducing us the fascinating physics of Hopf insulators and for a fruitful collaboration on chiral topological insulators. Discussion and collaboration with Prof. Yingmei Liu and her student, Lichao Zhao, have been a truly rewarding experience.

Time at Les Houches was a highlight of my PhD (not just because of the scrumptious food). I regret not having enough fun with new friends (but instead focused on finishing some works, as unproductive and grudging as you can imagine). To David Wong-Campos, Alexander Keesling and Pablo Solano, I thank you guys for the fierce table tennis and foosball rivals. The day-long hike (actually just 12 hours) to Mont Lachat has set a record for me, thanks to Nikolett Nemet, Chris Parmee, Alessandro Fioretto ('you said yesterday!'), Chitram Banerjee, Mark Brown, Apichayaporn Ratkata ('you can do it!'), Tuvia Gefen and Yongguan Ke. Taking jump and posed photos with you guys were at the peak (pun intended) of the adventure.

Of course, a healthy PhD should be nothing short of fun. Without the fun time with and support from friends, old and new, my six years' journey will be downright unbearable. To my dear roommates, Tianpei Xie, Hao Sun, and Jiahua Gu, you are the reason for me to stay at 1351 for six years and never move. From countless hosting events at 1351 to fun excursions to sleeping bear dune and Boston, from midnight chats on life (and girls) to daily 'Dui time', I'm truly blessed to share the moments of growing-up and maturing with you. Remember to write 1351 into your autobiographies. I thank Lin Li for hosting scores of hot-pot sessions. Video games and 'three-kingdom' games with you, and others, are holiday activities that I have been consistently looking forward to. I thank Yunyi Zhang for confiding

in me and for having full trust in me despite my random advice. The Caribbean cruise with Li Chen and Yunyi (and of course my wife and others) was incredibly memorable. You helped to greatly improve my photo-shooting skills (for being charming models). To the badminton gangs, having fun with you has been the single event that I can hardly wait every single week. I'd like to specially thank Xiaoran Dong for rekindling the passion of an old man and for the thrilling time at the badminton tournament. You knew we couldn't afford to lose. To Yina Geng and Jiaxing Wu (plus Tianpei and Jiahua), the fun of playing badminton with you can be matched only by the random comments and teasings in our Wechat group (I am not trying to imply your badminton skills never improve). And to many other badminton buddies, Yang Liu, Zhenling Wang, Mengying Zhang, Bopeng Li, Yu Chen, Yong Xiao, Hui Li, Wenbo Sun, Ruijiao Miao, Zhen Xu, because of you, my badminton sessions may have a starting time but never an ending. To my undergrad buddies, You Quan Chong, Boon Chong Goh, Jeremy Hadidjojo and Sai Swaroop Sunku, the half-year Skype updates never fail to make me feel nostalgic. Our reunion at UIUC was nothing short of an absolute blast! To my friends at Randall, Zhaorong Wang, Deshpreet Bedi, Arash Arabiardehali, Uttam Paudel, Marta Luengo Kovac, Yue Ma, Wenbo Shen, Lu Ma, Xiao Zhang, Nithiwadee Thaicharoen, from cramming homework in our first year (convince yourself!) to regular Madras Masala buffet and yearly banquet, thank you all for bringing me around to try all kinds of food. I am also amazingly fortunate to have awesome friends at a place I can call a second home—Boston. I thank Yichen Shen for constantly encouraging me to be more explorative (man, I am old and lazy), Ruichao Ma for little discussions on cold atoms (you appeared on my paper acknowledgment part more often), and Xiaoqian Yu for her random(ly) 'high-pitch' comments on nearly everything and ultimately for taking care of my beloved girl.

Finally, time to mark an end. And, better, a new starting. Without everyone acknowledged

above, I could have barely finished this marathon. But without the unwavering and unconditional love from my family, I couldn't have started. Mom, thank you for being my biggest fan. Though you may never know what is 'quantum', or sometimes mistakenly relate my research to 'atomic bombs', your trust has been my strongest pillar, in life and in work. Dad, although your love is not as unconcealed, I feel it as deeply. It has been both sweet and saddening to see your changes over the years. Trust me, I shall spare no effort to spend more quality time with you, my dear parents. To my godparents, thank you for regarding me as your own child and I can only wish you will not spare me whenever you need me. Jie, you may not think it that way, but you are my ultimate tower of strength. Though the past fourteen years haven't been a chiral motion uphill, any obstacles (or backscattering) only served to bind us closer and make us stronger. And after such an unbearably long time of 2D communication, we can finally call it an end. To be blessed is to have you on my side, and to be able to laugh together, cry together, learn together, grow together, and never live in a different city, never again.

TABLE OF CONTENTS

LIST OF FIGURES

LIST OF TABLES

LIST OF APPENDICES

ABSTRACT

The ability to precisely and coherently control atomic systems has improved dramatically in the last two decades, driving remarkable advancements in quantum computation and simulation. In recent years, atomic and atom-like systems have also been served as a platform to study topological phases of matter and non-equilibrium many-body physics. Integrated with rapid theoretical progress, the employment of these systems is expanding the realm of our understanding on a range of physical phenomena. In this dissertation, I draw on state-of-the-art experimental technology to develop several new ideas for controlling and applying atomic systems.

In the first part of this dissertation, we propose several novel schemes to realize, detect, and probe topological phases in atomic and atom-like systems. We first theoretically study the intriguing properties of Hopf insulators, a peculiar type of topological insulators beyond the standard classification paradigm of topological phases. Using a solid-state quantum simulator, we report the first experimental observation of Hopf insulators. We demonstrate the Hopf fibration with fascinating topological links in the experiment, showing clear signals of topological phase transitions for the underlying Hamiltonian.

Next, we propose a feasible experimental scheme to realize the chiral topological insulator in three dimensions. They are a type of topological insulators protected by the chiral symmetry

and have thus far remained unobserved in experiment. We then introduce a method to directly measure topological invariants in cold-atom experiments. This detection scheme is general and applicable to probe of different topological insulators in any spatial dimension. In another study, we theoretically discover a new type of topological gapless rings, dubbed a Weyl exceptional ring, in three-dimensional dissipative cold atomic systems.

In the second part of this dissertation, we focus on the application of atomic systems in quantum computation and simulation. Trapped atomic ions are one of the leading platforms to build a scalable, universal quantum computer. The common one-dimensional setup, however, greatly limits the system's scalability. By solving the critical problem of micromotion, we propose a two-dimensional architecture for scalable trapped-ion quantum computation.

Hamiltonian tomography for many-body quantum systems is essential for benchmarking quantum computation and simulation. By employing dynamical decoupling, we propose a scalable scheme for full Hamiltonian tomography. The required number of measurements increases only polynomially with the system size, in contrast to an exponential scaling in common methods.

Finally, we work toward the goal of demonstrating quantum supremacy. A number of sampling tasks, such as the boson sampling problem, have been proposed to be classically intractable under mild assumptions. An intermediate quantum computer can efficiently solve the sampling problem, but the correct operation of the device is not known to be classically verifiable. Toward practical verification, we present an experimental friendly scheme to extract useful and robust information from the quantum boson samplers based on coarse-grained measurements. In a separate study, we introduce a new model built from translation-invariant Ising-interacting spins. This model possesses several advantageous properties, catalyzing the ultimate experimental demonstration of quantum supremacy.

CHAPTER I

Introduction

1.1 Background

1.1.1 Probe Topological Phases of Matter

Symmetry is arguably the most pervasive concept in modern physics. It plays a central role in the classification of phases of matter, as initially formulated by Landau and Ginzburg [1]. As matter experiences a continuous phase transition from one phase to another, Landau proposed that symmetry breaking is at the heart of the process. This paradigm has been successful in explaining a myriad of physical phenomena; but in recent decades, especially after the discovery of the integer and fractional quantum Hall effect [2, 3], physicists have realized that many other phenomena do not fit into Landau's framework. Another central theme begins to emerge in physics, i.e., the concept of topology. Phase transitions can occur without breaking any symmetry; instead the distinct phases can be distinguished by their 'topology', often characterized by some topological invariants.

This concept of topological phases and topological transitions has become ever clearer after the discovery of topological insulators [4, 5]. These materials typically insulate in the bulk,

but have protected conductivity on the surface. These discoveries have not only injected fresh insights into physics, but have also led to many potential applications. Since the breakthrough, a race between theory and experiment has begun, with both significantly pushing the field forward [4–14].

Initially, all experiments are performed on natural solid materials. In recent years, cold atomic experiments are joining the search for exotic topological phases. This is owing to atomic systems' distinctive advantages: precise controllability, novel detection possibility, and accessibility of extreme parameter regimes [15, 16]. In particular, it is possible to manipulate atomic behavior to realize textbook models and reach interesting physical regimes. Among numerous other breakthroughs, ultracold atoms have been applied to engineer spin-orbit coupling [17–19], realize the Hofstadter Hamiltonian [20,21] and the Haldane model [22], and directly measure quantized topological invariants [23–25].

1.1.2 Quantum Computation and Quantum Simulation

A quantum computer is believed to be able to solve certain tasks significantly faster than the current electronic computer [26,27]. Although a universal, scalable, and fault-tolerant quantum computer still seems far on the horizon, advances—especially experimental advances—in the past two decades have made great strides toward this long-term goal.

Various short-term goals have also been established, including quantum simulation [28,29], or the demonstration of simpler and nonuniversal quantum speedups. The former traces back to the vision of Richard Feynman in the 1980s [30]: the tasks of simulating one quantum system using another, more controllable one. This topic has since developed into a thriving field, one marked by a constant exchange of ideas between theorists and experimentalists [31–34].

Quantum supremacy [35]—a term coined for quantum computers that can solve a problem exceeding the capability of any classical computers (in a reasonable amount of time)—unfolds to be another short-term goal. Apart from via a full-fledged quantum computer, quantum supremacy may also be demonstrated with some intermediate, nonuniversal quantum machines. In the past few years, a growing amount of attention has been channeled toward this direction [36–40]. With concerted efforts from theorists and experimentalists, from both the academia and the industry, this important near-term milestone may be reached sooner than we have originally thought.

1.2 Outline of the Dissertation

In this dissertation, we focus on the application of atomic or atom-like systems in quantum simulation, quantum computation and topological phases of matter. The first half of the dissertation (Chapter II and III) centers on studies of topological phases, with a combination of theoretical works, experimental proposals and an experiment. In the second half, we present our studies in the direction of quantum simulation and quantum computation.

Chapter II is dedicated to our works on Hopf insulators. Hopf insulators [41] are intriguing three-dimensional (3D) topological insulators that elude the standard classification paradigm of topological phases for free fermions [9,10]. They originate from the mathematical theory of Hopf fibration and epitomize the deep connection between knot theory and topological phases of matter [42]. In the first section, we theoretically construct the Hopf Hamiltonians for arbitrary integer topological index [43,44]. These theoretical constructs help experimentalists realize those phases by engineering the specific Hamiltonian, which is suitable for atomic systems. In the second section, we present our experiment on the first observation of Hopf

insulators and topological links in a solid-state quantum simulator. We directly measure the integer-valued topological invariants and experimentally demonstrate the Hopf fibration with a remarkable topological linking structure.

Chapter III includes a number of our studies related to the simulation of topological phases with cold atoms. In considering all experimental capacities and limitations, we propose, in the first section, a feasible and detailed scheme to realize a special topological phase in cold-atom experiment [45] , the so-called chiral topological insulators in three dimensions. These phases possess unique properties, but they have so far eluded all experimental searches. In the second section, we theoretically study in more detail the intriguing properties of chiral topological insulators and propose possible ways to detect them [46]. More generally, since we know that all topological phases are characterized by some topological invariants, it is crucial to be able to measure these invariants in experiment. In the third section, we introduce a general method to directly measure topological invariants in cold-atom experiments based on standard time-of-flight imaging techniques [47]. The strength of our scheme lies in its generality and amenability to experiments. In the last section of this chapter, we consider dissipative cold atomic systems and find a new type of topological gapless rings, dubbed a Weyl exceptional ring, in three-dimensional dissipative systems [48]. They possess both a quantized Chern number and a quantized Berry phase. An experimental scheme based on dissipative cold atomic gases is proposed to realize and probe the Weyl exceptional ring.

In Chapter IV, we propose an architecture for scalable quantum computation with a 2D ion crystal in a Paul trap. Cold atomic ions confined in a well-designed trap are one of the most promising platforms to realize large-scale quantum computation [27]. The linear Paul trap with a 1D ion crystal was among the first to demonstrate the fundamental quantum logic gates [49]. However, this linear geometry has intrinsic limitations in terms of scalability:

difficulty in trapping too many ions in 1D and low error threshold for fault tolerance. We propose to use a 2D ion crystal for large-scale quantum computation [50]. The main obstacle that prevented earlier use of this 2D structure is a problem called micromotion, which unavoidably degrades the fidelity of a quantum gate. We show, in this chapter, that micromotion can be explicitly taken into account in the design of quantum gates. All effects of micromotion are considered, and our numerical simulation indeed demonstrate the feasibility of the 2D architecture.

As quantum computation and quantum simulation scale up, classical computers will be unable to solve the corresponding problem, and they may even have difficulties verifying the solution. Therefore, a critical issue is to assess whether the quantum machine performs as expected. The quantum processes are typically governed by some physical Hamiltonians. Characterization of all parameters in the Hamiltonian is therefore essential for benchmarking the quantum device. This task is called Hamiltonian tomography. In Chapter V [51], we tackle this problem with a new perspective by incorporating dynamical decoupling, another important idea in quantum control. This basic idea is to apply periodic laser pulses to decouple a pair of particles from the rest of the system and characterize their interactions internally. By repeating the decoupling procedure to all pairs, the required number of measurements grows at most polynomially with the system size for a full tomography, in contrast to the exponential cost with brute force.

Chapter VI continues on the topic and focuses on the goal of establishing quantum supremacy. A full-fledged universal quantum computer is believed to be able to solve certain tasks exponentially faster than current computers, but it imposes extremely stringent requirements on experiment. Recently, a number of sampling tasks, such as the boson sampling problem [36], have been proposed to be classically intractable. They are, at the same time,

particularly amenable to quantum experiment. Verification of the sampling outputs remains a major challenge. In the first section of Chapter VI, we present an experimental friendly scheme to extract useful and robust information from quantum boson samplers based on coarse-grained measurements [52]. The procedure can be applied to certify the equivalence of boson sampling devices while ruling out alternative fraudulent devices. In the second section, we introduce a new intermediate quantum computing model built from translation-invariant Ising-interacting spins [53]. For our model, a single fixed unitary evolution is sufficient to produce classically intractable results, compared to several other models that rely on implementation of an ensemble of different unitaries (instances). We propose an experimental scheme to implement our model Hamiltonian in optical lattices and put forward a certification protocol that only requires local measurements.

Most of the chapters in this dissertation have appeared in print elsewhere. Here is a list of previously published works by chapters: Chapter II in Ref. [43], Chapter III in Ref. [45–48], Chapter IV in Ref. [50], Chapter V in Ref. [51] and Chapter VI in Ref. [52, 53]. Below is a number of studies that I am also involved but they are not covered in this dissertation for space reasons: a theoretical study on the systematic construction of tight-binding Hamiltonians for topological insulators and superconductors [44], a proposal for observing non-abelian statistics of Majorana-Shockley fermions in an optical lattice [54], an experiment to observe first-order superfluid-to-Mott-insulator phase transitions in spinor condensates [55] and a theoretical study on probing knots and Hopf insulators with ultracold atoms [42].

CHAPTER II

Hopf Insulators: Theory and Experiment

The interplay of topology and symmetry plays a key role in the classification of quantum phases of matter [4, 5, 9–11]. It gives rise to a notable periodic table of topological phases for free fermions according to the system symmetry and dimensionality [9, 10]. The recently discovered $\mathbb{Z}_2$ topological insulators [12–14] protected by time-reversal symmetry fit into this classification paradigm. According to the classification, the class breaking time-reversal, particle-hole and chiral symmetry (Class A) should exhibit only trivial insulating phase in three dimensions. However, when the system Hamiltonian only has two bands, nontrivial Hopf insulators [41] exist. In this chapter, we first theoretically construct a class of tight-binding model Hamiltonians which realize all kinds of Hopf insulators with arbitrary integer Hopf index. We then proceed to present our experimental observation of Hopf insulators in a solid-state quantum simulator. The intriguing Hopf fibration with fascinating linking structures is demonstrated in the experiment.

2.1 Hopf Insulators with $\mathbb{Z}$ Topological Index

2.1.1 Introduction

Topological phases of matter may be divided into two classes: the intrinsic ones and the symmetry protected ones [11]. Symmetry protected topological (SPT) phases are gapped quantum phases that are protected by symmetries of the Hamiltonian and cannot be smoothly connected to the trivial phases under perturbations that respect the same kind of symmetries. Intrinsic topological (IT) phases, on the other hand, do not require symmetry protection and are topologically stable under arbitrary perturbations. Unlike SPT phases, IT phases may have exotic excitations bearing fractional or even non-abelian statistics in the bulk [56]. Fractional [3, 57] quantum Hall states and spin liquids [58–62] belong to these IT phases. Remarkable examples of the SPT phases include the well known 2D and 3D topological insulators and superconductors protected by time reversal symmetry [4,5,8,13,63,64], and the Haldane phase of the spin-1 chain protected by the $SO(3)$ spin rotational symmetry [65,66]. For interacting bosonic systems with on-site symmetry G, distinct SPT phases can be systematically classified by group cohomology of G [11], while for free fermions, the SPT phases can be systematically described by K-theory or homotopy group theory [67], which leads to the well known periodic table for topological insulators and superconductors [9, 10, 68].

Most 3D topological insulators have to be protected by some other symmetries [9, 10], such as time reversal, particle hole or chrial symmetry, and the $U(1)$ charge conservation symmetry [69]. A peculiar exception occurs when the Hamiltonian has just two effective bands. In this case, interesting topological phases, the so-called Hopf insulators [41], may exist. These Hopf insulator phases have no symmetry other than the prerequisite $U(1)$ charge conservation. To elucidate why this happens, let us consider a generic band Hamiltonian in 3D

with m filled bands and n empty bands. Without symmetry constraint, the space of such Hamiltonians is topologically equivalent to the Grassmannian manifold $\mathbb{G}_{m,m+n}$ and can be classified by the homotopy group of this Grassmannian [10]. Since the homotopy group $\pi_3(\mathbb{G}_{m,m+n}) = \{0\}$ for all $(m,n) \neq (1,1)$, there exists no nontrivial topological phase in general. However, when $m = n = 1$, $\mathbb{G}_{1,2}$ is topologically equivalent to $\mathbb{S}^2$ and the well-known Hopf map in mathematics shows that $\pi_3(\mathbb{G}_{1,2}) = \pi_3(\mathbb{S}^2) = \mathbb{Z}$ [67]. This explains why the Hopf insulators may exist only for Hamiltonians with two effective bands. The classification theory shows that the peculiar Hopf insulators may exist in 3D, but it does not tell us which Hamiltonian can realize such phases. It is even a valid question whether these phases can appear at all in physically relevant Hamiltonians. Moore, Ran, and Wen made a significant advance in this direction by constructing a Hamiltonian that realizes a special Hopf insulator with the Hopf index $\chi = 1$ [41].

In this section, we construct a class of tight-binding Hamiltonians that realize arbitrary Hopf insulator phases with any integer Hopf index χ. The Hamiltonians depend on two parameters and contain spin-dependent and spin-flip hopping terms. We map out the complete phase diagram and show that all the Hopf insulators can be realized with this type of Hamiltonians. We numerically calculate the surface states for these Hamiltonians and show that they have zero energy modes that are topologically protected and robust to arbitrary random perturbations with no other than the $U(1)$ symmetry constraint.

2.1.2 Model Hamiltonians for Hopf Insulators

To begin with, let us notice that any two-band Hamiltonian in 3D with one filled band can be expanded in the momentum space with three Pauli matrices $\boldsymbol{\sigma} = (\sigma^x, \sigma^y, \sigma^z)$ as

$$\mathcal{H}(\mathbf{k}) = \mathbf{u}(\mathbf{k}) \cdot \boldsymbol{\sigma}, \tag{2.1.1}$$

where we have ignored the trivial energy-shifting term $u_0(\mathbf{k})\mathbf{I}_2$ with $\mathbf{I}_2$ being the 2×2 identity matrix. By diagonalizing $\mathcal{H}(\mathbf{k})$, we have the energy dispersion $E(\mathbf{k}) = \pm|\mathbf{u}(\mathbf{k})|$, where $|\mathbf{u}(\mathbf{k})| = \sqrt{u_x^2(\mathbf{k}) + u_y^2(\mathbf{k}) + u_z^2(\mathbf{k})}$. The Hamiltonian is gapped if $|\mathbf{u}(\mathbf{k})| > 0$ for all $\mathbf{k}$. For the convenience of discussion of topological properties, we denote $\mathbf{u}(\mathbf{k}) = |\mathbf{u}(\mathbf{k})|(x(\mathbf{k}), y(\mathbf{k}), z(\mathbf{k}))$ with $x^2(\mathbf{k})+y^2(\mathbf{k})+z^2(\mathbf{k}) = 1$. Topologically, the Hamiltonian (1) can be considered as a map from the momentum space $\mathbf{k} = (k_x, k_y, k_z)$ characterized by the Brillouin zone $\mathbb{T}^3$ ($\mathbb{T}$ denotes a circle and $\mathbb{T}^3$ is the 3D torus) to the parameter space $\mathbf{u}(\mathbf{k}) \propto (x(\mathbf{k}), y(\mathbf{k}), z(\mathbf{k}))$ characterized by the Grassmannian $\mathbb{G}_{1,2} = \mathbb{S}^2$. Topologically distinct band insulators correspond to different classes of maps from $\mathbb{T}^3 \to \mathbb{S}^2$.

The classification of all the maps from $\mathbb{T}^3 \to \mathbb{S}^2$ is related to the *torus homotopy group* $\tau_3(\mathbb{S}^2)$ [70]. To construct non-trivial maps form $\mathbb{T}^3 \to \mathbb{S}^2$, we take two steps, first from $\mathbb{S}^3 \to \mathbb{S}^2$ and then from $\mathbb{T}^3 \to \mathbb{S}^3$. We make use of the following generalized Hopf map $f : \mathbb{S}^3 \to \mathbb{S}^2$ known in the mathematical literature [71]

$$x + iy = 2\lambda\eta_\uparrow^p \bar{\eta}_\downarrow^q, \; z = \lambda(|\eta_\uparrow|^{2p} - |\eta_\downarrow|^{2q}), \tag{2.1.2}$$

where p, q are integers prime to each other and $\eta_\uparrow$, $\eta_\downarrow$ are complex coordinates for $\mathbb{R}^4$ satisfying $|\eta_\uparrow|^2 + |\eta_\downarrow|^2 = 1$ with the normalization $\lambda = 1/(|\eta_\uparrow|^{2p} + |\eta_\downarrow|^{2q})$. Equation (2)

maps the coordinates $(\mathrm{Re}[\eta_\uparrow], \mathrm{Im}[\eta_\uparrow], \mathrm{Re}[\eta_\downarrow], \mathrm{Im}[\eta_\downarrow])$ of $\mathbb{S}^3$ to the coordinates (x, y, z) of $\mathbb{S}^2$ with $x^2 + y^2 + z^2 = 1$. The Hopf index for the map f is known to be $\pm pq$ with the sign determined by the orientation of $\mathbb{S}^3$ [71]. We then construct another map $g : \mathbb{T}^3 \to \mathbb{S}^3$ (up to a normalization), defined by the following equation

$$\begin{aligned} \eta_\uparrow(\mathbf{k}) &= \sin k_x + it \sin k_y, \\ \eta_\downarrow(\mathbf{k}) &= \sin k_z + i(\cos k_x + \cos k_y + \cos k_z + h), \end{aligned} \tag{2.1.3}$$

where t and h are constant parameters. The composite map $f \circ g$ from $\mathbb{T}^3 \to \mathbb{S}^2$ then defines the parameters $\mathbf{u}(\mathbf{k}) \propto (x(\mathbf{k}), y(\mathbf{k}), z(\mathbf{k}))$ in the Hamiltonian as a function of the momentum $\mathbf{k}$. From Eqs. (2) and (3), we have $\mathbf{u}(\mathbf{k}) = |\mathbf{u}(\mathbf{k})|(x(\mathbf{k}), y(\mathbf{k}), z(\mathbf{k})) = (\mathrm{Re}[2\eta_\uparrow^p \bar{\eta}_\downarrow^q], \mathrm{Im}[2\eta_\uparrow^p \bar{\eta}_\downarrow^q], [|\eta_\uparrow|^{2p} - |\eta_\downarrow|^{2q}])$, with $|\mathbf{u}(\mathbf{k})| = \frac{1}{\lambda(\mathbf{k})}$. The Hamiltonian $\mathcal{H}(\mathbf{k}) = \mathbf{u}(\mathbf{k}) \cdot \boldsymbol{\sigma}$ is $(p+q)$th order polynomials of $\sin(\mathbf{k})$ and $\cos(\mathbf{k})$, which corresponds to a tight-binding model when expressed in the real space. The Hamiltonian contains spin-orbital coupling with spin-dependent hopping terms. When we choose $p = q = 1$ and $(t, h) = (1, -3/2)$, the Hamiltonian (1) reduces to the special case studied in Ref. [41].

When the Hamiltonian is gapped with $|\mathbf{u}(\mathbf{k})| > 0$, one can define a direction on the unit sphere $\hat{\mathbf{u}}(\mathbf{k}) = (u_x(\mathbf{k}), u_y(\mathbf{k}), u_z(\mathbf{k}))/|\mathbf{u}(\mathbf{k})| = (x(\mathbf{k}), y(\mathbf{k}), z(\mathbf{k}))$. From $\hat{\mathbf{u}}(\mathbf{k})$, we define the Berry curvature $F_\mu = \frac{1}{8\pi}\epsilon_{\mu\nu\tau}\hat{\mathbf{u}} \cdot (\partial_\nu \hat{\mathbf{u}} \times \partial_\tau \hat{\mathbf{u}})$, where $\epsilon_{\mu\nu\tau}$ is the Levi-Civita symbol and a summation over the same indices is implied. A 3D torus $\mathbb{T}^3$ has three orthogonal cross sections perpendicular to the axis x, y, z, respectively. For each cross section of space $\mathbb{T}^2$, one can introduce a Chern number $C_\mu = \int_{-\pi}^{\pi}\int_{-\pi}^{\pi} dk_\rho dk_\lambda F_\mu$, where $\mu = x, y, z$ and ρ, λ denote directions orthogonal to μ. To classify the maps from $\mathbb{T}^3 \to \mathbb{S}^2$ represented by $\hat{\mathbf{u}}(\mathbf{k})$, a topological index, the so-called Hopf index, was introduced by Pontryagin, who showed

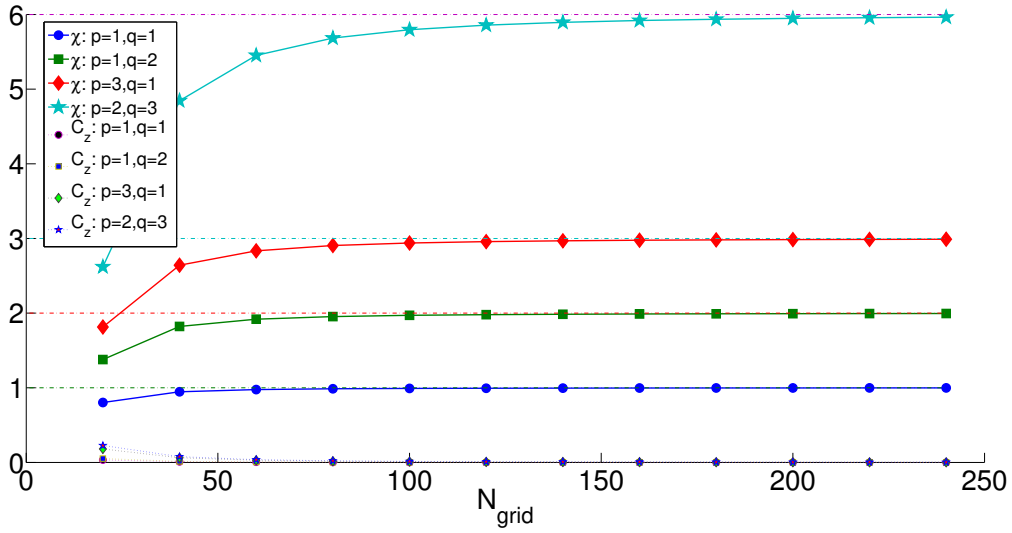

Figure 2.1.1: Plot of the Hopf index and the Chern number in z-direction for different (p, q). The Hopf index and the Chern number converge rapidly as the number of grids increases in discretization. The parameters t and h are chosen as $(t, h) = (1, 1.5)$.

that the Hopf index takes values in the finite group $\mathbb{Z}_{2\cdot\mathrm{GCD}(C_x,C_y,C_z)}$ when the Chern numbers C_μ are nonzero, where GCD denotes the greatest common divisor. If the Chern numbers $C_\mu = 0$ in all three directions, the Hopf index takes all integer values $\mathbb{Z}$ and has a simple integral expression [71, 72]

$$\chi\left(\hat{\mathbf{u}}\right) = -\int_{\mathrm{BZ}} \mathbf{F}\cdot\mathbf{A}\; d\mathbf{k}, \tag{2.1.4}$$

where $\mathbf{A}$ is the Berry connection (or called the gauge field) which satisfies $\nabla\times\mathbf{A} = \mathbf{F}$. The Hopf index $\chi\left(\hat{\mathbf{u}}\right)$ is gauge invariant although its expression depends on $\mathbf{A}$. As we will analytically prove in the appendix, the Chern numbers $C_\mu = 0$ for the map $\hat{\mathbf{u}}(\mathbf{k})$ defined above in the gapped phase, so we can use the integral expression of Eq. (4) to calculate the Hopf index $\chi\left(\hat{\mathbf{u}}\right)$. The index $\chi\left(\hat{\mathbf{u}}\right)$ can be calculated numerically through discretization of the torus $\mathbb{T}^3$ [41]. Using this method, we have numerically computed the Hopf index $\chi\left(\hat{\mathbf{u}}\right)$ for the Hamiltonian $\mathcal{H}(\mathbf{k})$ with various p and q, and the results are shown in Fig. 2.1.1. As

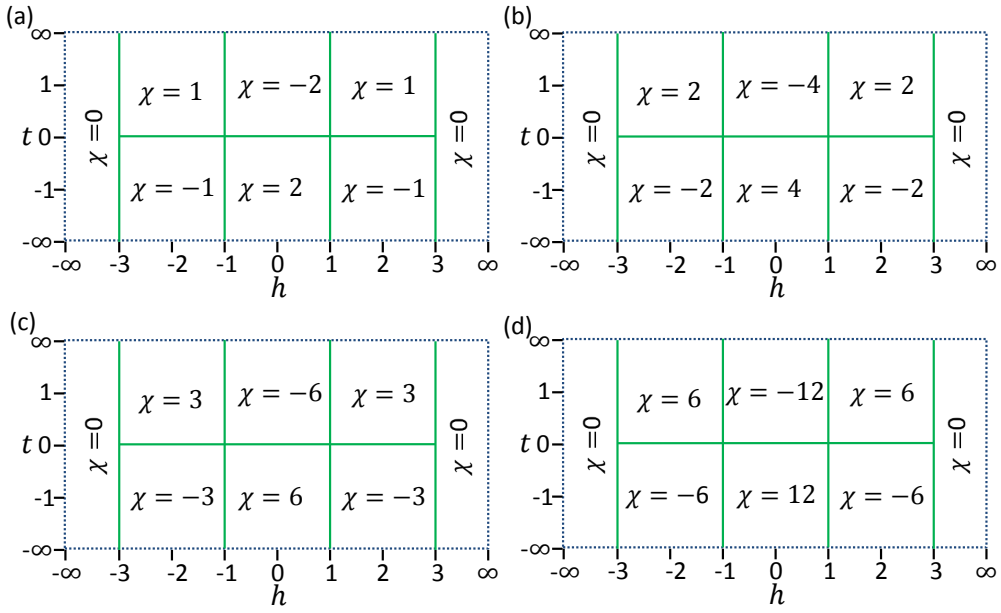

Figure 2.1.2: Phase diagrams of the Hamiltonian for different (p, q). The values of (p, q) in (a), (b), (c), and (d) are chosen to be $(1, 1)$, $(1, 2)$, $(3, 1)$, and $(2, 3)$, respectively.

the grid number increases in discretization, we see that the Chern numbers quickly drop to zero and the Hopf index approaches the integer values $\pm pq$ or $\pm 2pq$ depending on the parameters t, h. Based on the numerical results of $\chi(\hat{\mathbf{u}})$, we construct the phase diagrams of the Hamiltonian (1) for various p, q in Fig. 2.1.2. The phase boundaries are determined from the gapless condition. The phase diagrams exhibit regular patterns: they are mirror symmetric with respect to the axis $h = 0$ and anti-symmetric with respect to the axis $t = 0$. When $|h| > 3$, we only have a topologically trivial phase with $\chi(\hat{\mathbf{u}}) = 0$. From the result, we see that $\chi(\hat{\mathbf{u}})$ has an analytic expression with $\chi(\hat{\mathbf{u}}) = \pm pq$ when $1 < |h| < 3$ and $\chi(\hat{\mathbf{u}}) = \pm 2pq$ when $|h| < 1$.

To understand this result, we note that $\hat{\mathbf{u}}(\mathbf{k})$ is a composition of two maps $\hat{\mathbf{u}}(\mathbf{k}) = f \circ g(\mathbf{k})$. The generalized Hopf maps f from $\mathbb{S}^3 \to \mathbb{S}^2$ has a known Hopf index $\pm pq$ [71]. The maps g from $\mathbb{T}^3 \to \mathbb{S}^3$ can be classified by the torus homotopy group $\tau_3(\mathbb{S}^3)$ and a topological invariant

has been introduced to describe this classification [73], which has an integral expression

$$\Gamma(g) = \frac{1}{12\pi^2}\int_{\mathrm{BZ}} d\mathbf{k}\epsilon_{\alpha\beta\gamma\rho}\epsilon_{\mu\nu\tau}\frac{1}{|\boldsymbol{\eta}|^4}\boldsymbol{\eta}_\alpha\partial_\mu\boldsymbol{\eta}_\beta\partial_\nu\boldsymbol{\eta}_\gamma\partial_\tau\boldsymbol{\eta}_\rho,$$

where $\boldsymbol{\eta} = (\mathrm{Re}[\eta_\uparrow], \mathrm{Im}[\eta_\uparrow], \mathrm{Re}[\eta_\downarrow], \mathrm{Im}[\eta_\downarrow])$. Direct calculation of $\Gamma(g)$ leads to the following result:

$$\Gamma(g) = \begin{cases} 0, & |h| > 3 \\ 1, & 1 < |h| < 3 \text{ and } t > 0 \\ -2, & |h| < 1 \text{ and } t > 0. \end{cases}$$

Consequently, we have $\chi(\hat{\mathbf{u}}) = \Gamma(g)\chi(f) = \pm pq\Gamma(g)$, which is exactly the result shown in the phase diagrams in Fig. 2.1.2. A geometric interpretation is that $\Gamma(g)$ counts how many times $\mathbb{T}^3$ wraps around $\mathbb{S}^3$ under the map g, and $\chi(f)$ describes how many times $\mathbb{S}^3$ wraps around $\mathbb{S}^2$ under the generalized Hopf map f. Their composition gives the Hopf index $\chi(\hat{\mathbf{u}})$. A sign flip of t changes the orientation of the sphere $\mathbb{S}^3$, which induces a sign flip in $\chi(\hat{\mathbf{u}})$ and produces the anti-symmetric phase diagram with respect to the axis $t = 0$. As (p, q) are arbitrary coprime integers, $\chi(\hat{\mathbf{u}})$ apparently can take any integer value depending on the values of p, q and t, h. As a consequence, the Hamiltonian $\mathcal{H}(\mathbf{k})$ constructed here can realize arbitrary Hopf insulator phases.

2.1.3 Surface States of Hopf Insulators

The nontrivial topological invariant guarantees existence of gapless surface states at a smooth (i.e., adiabatic) boundary between a Hopf insulator and a trivial insulator (or vacuum). Numerically, we find that gapless surface states are still present even for sharp boundaries,

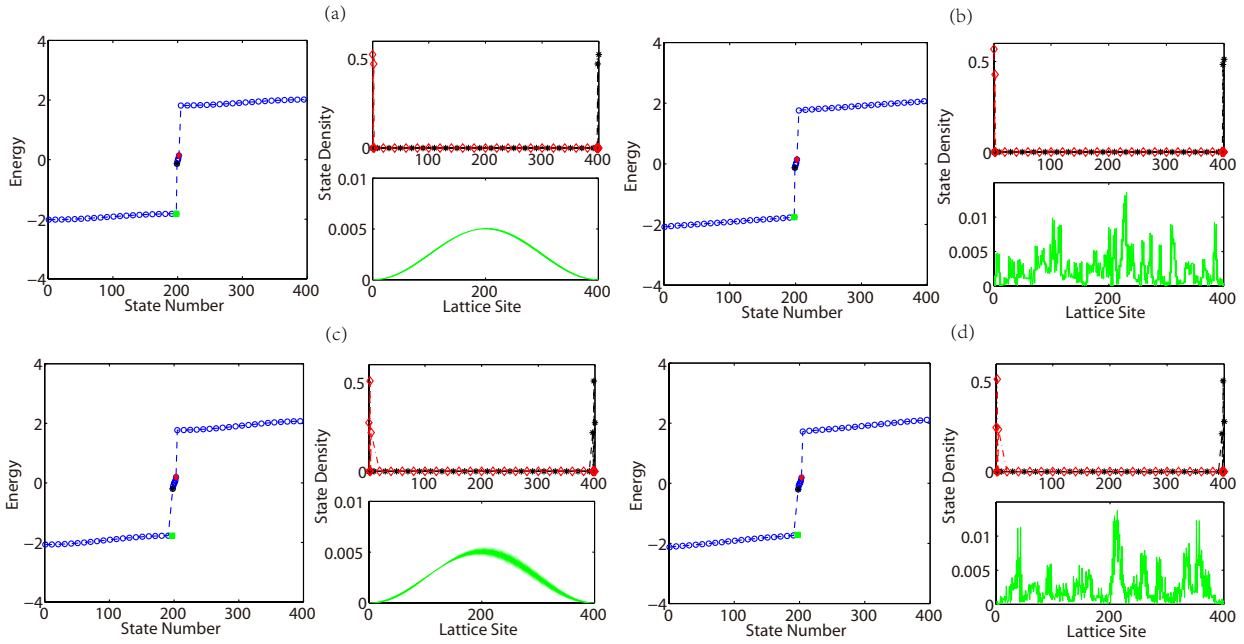

Figure 2.1.3: Surface states and zero-energy modes in the (001) direction for a 200-site-thick slab. The parameters t and h are chosen as $(t, h) = (1, 1.5)$ for all the figures. We have $(p, q) = (1, 2)$ for (a,b) and $(p, q) = (1, 3)$ for (c,d). In Fig. (b,d), we add random perturbations to the Hamiltonian, but otherwise keep the same parameters as (a,c). The left diagrams in (a,b,c,d) plot the energy spectrum of all 400 states at a fixed $(k_x, k_y) = (0.72, 0.72)$ for easy visualization. The points inside the gap represent the energies of the surface states. There are four (six) surface states in (a,b) ((c,d)), respectively. The right diagrams in in (a,b,c,d) show the wave functions of a surface state (upper one) and a bulk state (lower one).

although we do not have an intuitive explanation why this is necessarily so as the number of bands is not well-defined at a sharp boundary and the two-band condition required for existence of the Hopf insulator could be violated at the surface. Our results are summarized in Fig. 2.1.3. From the figure, surface states and localized zero-energy modes are prominent. These surface states are topologically protected and robust under arbitrary random perturbations that only respect the prerequisite $U(1)$ symmetry. This can be clearly seen from Fig. 2.1.3: while the wave functions of the bulk states change dramatically under random

perturbations, the wave functions of the surface states remain stable and are always sharply peaked at the boundary. This verifies that the Hopf insulators are indeed 3D topological phases. Besides the results shown in Fig. 2.1.3, we have calculated the surface states for a number of different choices of parameters (p, q) and (t, h), and the results consistently demonstrate that the surface states and zero energy modes are always present and robust even to substantial perturbations unless the bulk gap closes. Moreover, we roughly have more surfaces states when the absolute value of the Hopf index becomes larger. However, this is not always true. A direct correspondence between the Hopf index and the total winding number of surface states may exist and deserves to be further investigated [73]. It is also worthwhile to mention that these surface states are extended/metallic in a clean crystal, as discussed in Ref. [41], but how disorder will affect these states is an important topic that deserves further studies. The surface states might not be metallic with disorder since there is no obvious way to protect these surface state from localization without adding symmetries such as time-reversal.

2.1.4 Discussion

An important and intriguing question is how to realize these Hopf insulators in experiments. Laser assisted hopping of ultracold atoms in an optical lattice offers a powerful tool to engineer various kinds of spin-dependent tunneling terms [74–76], and thus provides a good candidate for their realizations although the details still need to be worked out. Dipole interaction between polar molecules in optical lattices also offers possibilities to realize effective spin-dependent hopping [77–79]. As argued in Ref. [41], frustrated magnetic compounds such as $X_2Mo_2O_7$ with X being a rare earth ion are other potential candidates. In addition, Hopf insulators may be realized in 3D quantum walks [80–83], where various hopping

terms are implemented by varying the walking distance and direction in each spin-dependent translation and the robust surface states can be observed with split-step schemes [82, 83].

In conclusion, we have introduced a class of tight-binding Hamiltonians that realize arbitrary Hopf insulators. The topologically protected surface states and zero-energy modes in these exotic phases are robust to random perturbations that only respect the $U(1)$ charge conservation symmetry. They are 3D topological phases and sit outside of the periodic table [9, 10] for topological insulators and superconductors.

2.2 Experimental Observation of Hopf Insulators and Topological Links

2.2.1 Introduction

In the previous section, we show that tight-binding models for arbitrary-index Hopf insulators exist. Implementation of Hopf insulators, however, poses a formidable experimental challenge [42, 43]. Recently, quantum simulation platforms have proven to be well suited for the experimental study of 1D and 2D topological insulators [34, 84, 85]. Here, we report the first observation of Hopf insulators in a solid-state quantum simulator and direct measurement of their integer-valued topological invariants by a 3D integration over parametric momentum space [47]. Through quantum state tomography, we experimentally demonstrate the Hopf fibration with fascinating topological links, showing clear signals of topological phase transitions for the underlying Hamiltonian. Our observation of Hopf insulators in a quantum simulator opens the door to probe their rich topological properties in experiment.

The quantum simulation and probing methods are also applicable to the study of other intricate 3D model Hamiltonians.

2.2.2 Model Hamiltonian for Observing Hopf Insulators

A general two-band Hamiltonian can be written in the form

$$H = \sum_{\mathbf{k}} \Psi_{\mathbf{k}}^{\dagger} H_{\mathbf{k}} \Psi_{\mathbf{k}} = \sum_{\mathbf{k}} \hbar\Omega \, \Psi_{\mathbf{k}}^{\dagger} \mathbf{u}(\mathbf{k}) \cdot \sigma \Psi_{\mathbf{k}}, \tag{2.2.1}$$

where $\hbar\Omega$ denotes the energy unit, the dimensionless coefficients $\mathbf{u}(\mathbf{k}) = (u_x, u_y, u_z)$ represent certain functions of 3D momenta $\mathbf{k} = (k_x, k_y, k_z)$, $\Psi_{\mathbf{k}} = (a_{\mathbf{k}\uparrow}, a_{\mathbf{k}\downarrow})^{\intercal}$ are fermionic annihilation operators with pseudo-spin states $|\uparrow\rangle$ and $|\downarrow\rangle$ at momentum point $\mathbf{k}$, and $\sigma = (\sigma_x, \sigma_y, \sigma_z)$ are Pauli matrices. The (composite) Hopf map is a projection from the momentum space (the Brillouin zone) described by the 3D torus $\mathbb{T}^3$ to the Bloch sphere $\mathbb{S}^2$ for the spin-1/2 state. For the Hopf map, the pre-image of each point on the sphere $\mathbb{S}^2$ corresponds to a closed loop in the torus $\mathbb{T}^3$—all these loops are topologically linked to each other, forming a fascinating topological structure called the Hopf fibration as shown in Fig. 2.2.1a. Armed with the Hopf map, Hopf insulators are characterized by an integer $\mathbb{Z}$ rather than a $\mathbb{Z}_2$ topological invariant [41, 43]. Several two-band model Hamiltonians supporting Hopf insulators have been constructed in Refs. [41, 43], and all of them involve complicated spin-

orbital interactions. We consider a primitive model with the coefficients $\mathbf{u}(\mathbf{k})$ given by

$$\begin{aligned} u_x &= 2\left[\sin k_x \sin k_z + C(\mathbf{k}) \sin k_y\right], \\ u_y &= 2\left[C(\mathbf{k}) \sin k_x - \sin k_y \sin k_z\right], \\ u_z &= \sin^2 k_x + \sin^2 k_y - \sin^2 k_z - \left[C(\mathbf{k})\right]^2, \end{aligned} \tag{2.2.2}$$

where $C(\mathbf{k}) \equiv \cos k_x + \cos k_y + \cos k_z + h$ with h being a dimensionless parameter. This Hamiltonian features two distinct topologically nontrivial phases with the parameter $|h| < 1$ and $1 < |h| < 3$, respectively [43]. Implementation of the Hamiltonian with cold atoms requires engineering of next-nearest-neighbor spin-orbital couplings [42], which is particularly challenging for experiments.

2.2.3 Nitrogen-Vacancy Center Based Quantum Simulator

Here, we experimentally realize this Hamiltonian and probe its topological properties with a solid-state quantum simulator represented by a single nitrogen-vacancy (NV) center in a diamond sample at room temperature shown in Fig. 2.2.1b. The diamond NV center has recently emerged as a promising experimental system for realization of quantum computing, simulation, and precision measurements [86–90]. The key observation here is that the Hamiltonian (1) for free fermions is diagonal in the momentum space, so there is no entanglement between different momentum components in its ground state. We can measure the quantum states for each momentum component separately in experiments [34, 47], and the properties of the whole system can then be determined by collating individual measurements. For each momentum component $\mathbf{k}$, the ground state of the Hamiltonian (1) can be probed through an adiabatic passage in a two-level system, which is realized through microwave manipulation

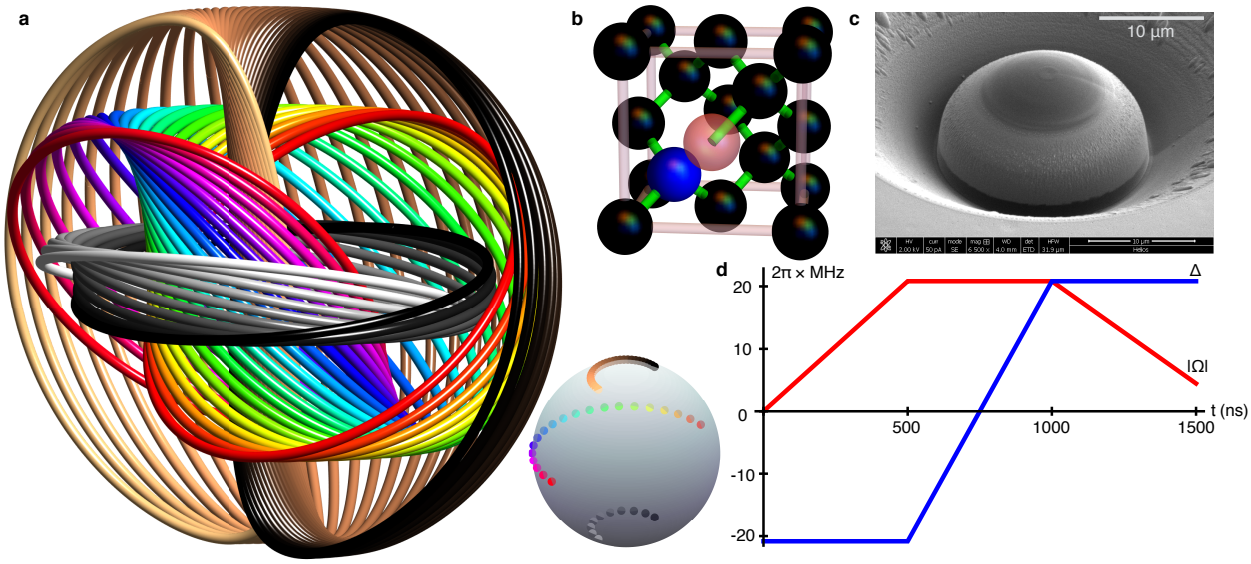

Figure 2.2.1: Illustration of Hopf fibration and the experimental system. **a**, Hopf fibration, where each point (distinguished by color) on the Bloch sphere in the right corner is mapped to a closed loop in the 3D space by the Hopf map and all loops are pairwise linked to each other (see Appendix for the explicit form of the Hopf map in our system). **b**, A diamond nitrogen-vacancy center with its defect spin used for the quantum simulation of the Hopf insulator. **c**, A solid-state immersion micro-lens is fabricated on top of the diamond nitrogen-vacancy center to increase its detection efficiency by optical readout. **d**, A typical path of adiabatic passage for the parameters in the Hamiltonian. The example shown here is for adiabatic preparation of the ground state of $H_{\mathbf{k}}$ with the momentum components $(k_x, k_y, k_z)/2\pi = (0.4, 0.3, 0.5)$ and the parameter $h = 2$.

of the spin levels $|0\rangle$ and $|-1\rangle$ of a single NV center. The viability of such an adiabatic procedure is guaranteed by the most salient feature of a topological phase, the topological gap—as long as the gap is maintained, topological properties are insensitive to perturbations or stretching of the energy bands.

We use a NV center under a micro-fabricated solid immersion lens (SIL) to implement the Hamiltonian (1) for each parametric momentum component $\mathbf{k}$. The SIL is used to enhance the data collection rate as we need to scan over many different momentum components to measure the topological properties of the Hamiltonian. By applying a microwave with phase

φ to the transition $|0\rangle \rightarrow |-1\rangle$, we realize the following Hamiltonian in the rotating frame

$$H_u = \hbar |\Omega| (\sigma_x \cos\varphi + \sigma_y \sin\varphi) + \hbar\Delta\sigma_z, \tag{2.2.3}$$

where $|\Omega|$ denotes the Rabi frequency of the microwave and Δ is the frequency detuning of the spin transition relative to the microwave frequency. Comparing with the Hamiltonian (1), we have $\Omega\mathbf{u}(\mathbf{k}) = (|\Omega|\cos\varphi, |\Omega|\sin\varphi, \Delta)$. At the initial time, we take $|\Omega| = 0$ and prepare the spin in state $|0\rangle$, which is the ground state of $H_u\,(t=0)$. We then adiabatically tune the microwave Rabi frequency $|\Omega|$ with phase $\tan\varphi = u_y(\mathbf{k})/u_x(\mathbf{k})$ and the detuning Δ so that for the final state we have $H_u(t) = H_{\mathbf{k}}$ in the Hamiltonian (1) for a certain momentum component $\mathbf{k}$. A typical adiabatic passage for the parameters is shown in Fig. 2.2.1d. By this adiabatic passage, we realize the ground state of $H_{\mathbf{k}}$, and through quantum state tomography (QST) measurements, we retrieve its full information. We scan all momentum components $\mathbf{k}$ via the above preparation and detection method to probe the properties of the full Hamiltonian (1).

2.2.4 Measuring Hopf Invariant

To measure the topological properties of the Hamiltonian (1), we use a topological invariant called the Hopf index [41, 43], which is defined as

$$\chi = -\int_{\mathrm{BZ}} \mathbf{F}\cdot\mathbf{A}\, d^3k, \tag{2.2.4}$$

where $\mathbf{F}$ is the Berry curvature with $F_\mu = (i/2\pi)\,\epsilon_{\mu\nu\tau}\,(\partial_{k_\nu}\langle\Psi_{\mathbf{k}}|)\,(\partial_{k_\tau}|\Psi_{\mathbf{k}}\rangle)$, $\epsilon_{\mu\nu\tau}$ is the Levi-Civita symbol with $\mu,\nu,\tau \in \{x,y,z\}$, $|\Psi_{\mathbf{k}}\rangle$ denotes the ground state of the Hamiltonian $H_{\mathbf{k}}$,

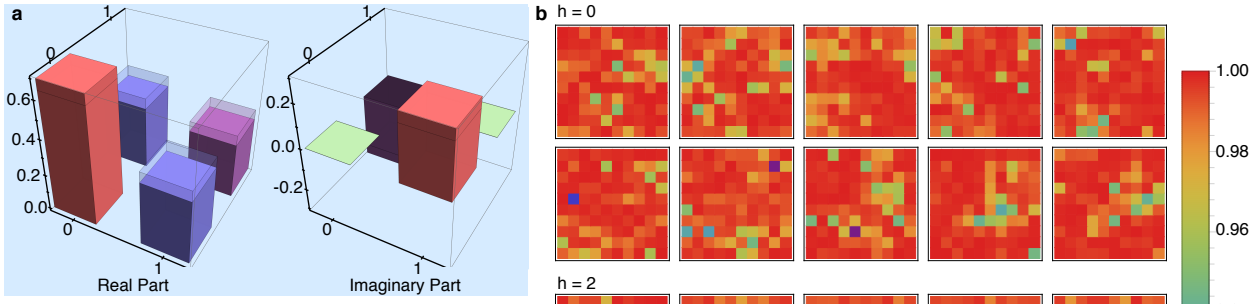

c

Hopf Index χ	h = 0	h = 2
Experiment (N = 10)	-2.066(3)	1.048(2)
Theory (N = 10)	-2.058	1.041
Theory (N = ∞)	-2	1

Figure 2.2.2: Measurement of the Hopf index using quantum state tomography. **a,** Real and imaginary parts of the experimentally reconstructed density matrix elements. This example shows the ground state density matrix $\rho_{\mathbf{k}}$ at one particular momentum $\mathbf{k}$ with $(k_x, k_y, k_z)/2\pi = (0.4, 0.2, 0.5)$. The hollow caps correspond to the ideal density matrix elements predicted by theory. **b,** State fidelities $F_{\mathbf{k}}$ measured through quantum state tomography are shown for different $\mathbf{k}$ with the values represented by the color map. The upper and the lower panels have the parameter $h = 0$ and $h = 2$, respectively. Each panel contains 10 sub-figures where the momentum $k_z/2\pi$ varies from 0 to 0.9 with an equal spacing of $\delta k_z/2\pi = 0.1$. The horizontal and vertical axes of each subfigure denote respectively $k_x/2\pi$ and $k_y/2\pi$, which vary from 0 to 0.9 with an equal spacing of 0.1. The average fidelity for the $10 \times 10 \times 10$ measured momentum points is 99.1% (99.2%) for the case of $h = 0$ ($h = 2$). **c,** The Hopf index from quantum state tomographic measurements with momentum $\mathbf{k}$ sampled over the $10 \times 10 \times 10$ mesh. The number in the bracket represents the standard deviation in the last digit. The measured Hopf index is close to its ideal integer values for the corresponding topological phases. The small differences are dominated by the discretization error of the 3D momentum integration in computing topological invariants. The scaling of the discretization error with the number of sampling points is shown in the Appendix.

$\mathbf{A}$ is the associated Berry connection satisfying $\nabla \times \mathbf{A} = \mathbf{F}$, and the integration of $\mathbf{k}$ is over the Brillouin zone (BZ). Depending on the parameter h, the Hopf index χ takes the following

values for the Hamiltonian (1):

$$\chi = \begin{cases} 1, & 1 < |h| < 3 \\ -2, & |h| < 1 \\ 0, & |h| > 3. \end{cases} \tag{2.2.5}$$

So the Hamiltonian H supports two topological Hopf insulator phases and one topologically trivial phase with the phase boundaries at $h = \pm 1, \pm 3$.

To measure the Hopf index χ, we use the discretization scheme in Ref. [47], which provides a general method to probe the topological invariants in any spatial dimension based on QST in the momentum space. As shown in the Appendix, the Hopf index χ quickly converges to its ideal value through mesh sampling over the momentum space. We sample (k_x, k_y, k_z) into a mesh of $10 \times 10 \times 10$ points with equal spacing and for each $H_{\mathbf{k}}$, we perform QST to measure its ground state density matrix. A typical reconstructed density matrix is shown in Fig. 2.2.2a. At each momentum $\mathbf{k}$, we compare the experimentally reconstructed density matrix $\rho_{\mathbf{k}}$ with the ideal ground state $|\Psi_{\mathbf{k}}\rangle$ and calculate the state fidelity $F_{\mathbf{k}} = \langle\Psi_{\mathbf{k}}| \rho_{\mathbf{k}} |\Psi_{\mathbf{k}}\rangle$. The measured fidelities for different momenta $\mathbf{k}$ are shown in Fig. 2.2.2b. We have achieved a high average fidelity of 99.2% in our experiment. From the measured data, we find the Hopf index shown in Fig. 2.2.2c for two different phases with $h = 0, 2$. The measured non-zero values of the Hopf index, close to the ideal integer numbers, provide an unambiguous experimental signature for the underlying topological structure of the Hopf insulator phase.

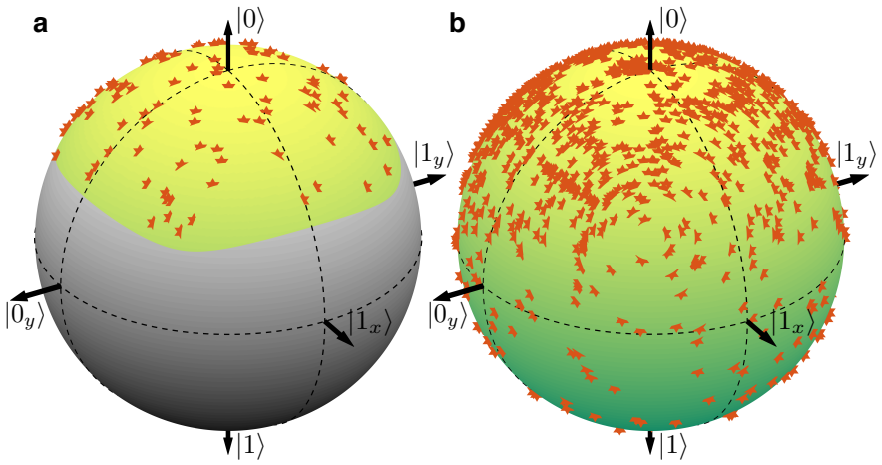

Figure 2.2.3: An intuitive indicator of intrinsic 3D topological insulator. **a,** The ground-state spin configurations of the Hamiltonian $H_{\mathbf{k}}$ for $h = 2$ are mapped onto the Bloch sphere, where $\mathbf{k}$ is scanned over a 2D cross section with $k_z = 0$. The stars show the experimental data and the yellow cover identifies the theoretical region from all the momentum points in this cross section. The partial covering of the Bloch sphere indicates that the Chern number for this layer is zero. We have verified with our experimental data that Chern numbers vanish for all 2D cross sections along different directions, so layered 2D topological (quantum Hall) insulators are not present in our system. **b,** The ground-state spin configurations with $\mathbf{k}$ scanned over all 3D momentum points are mapped onto the Bloch sphere. The Bloch sphere is fully covered, which is consistent with the characteristic of an intrinsic 3D topological insulator.

2.2.5 Nontrivial Topological Links and Phase Transition

Different from stacking layers of 2D quantum Hall insulators, the Hopf insulator is an intrinsic 3D topological insulator, where the Chern numbers characterizing 2D topological insulators are zero for all 2D momentum layers [41, 43]. To demonstrate this intuitively, in Fig. 2.2.3a we take a layer in the momentum space (e.g., with $k_z = 0$) and map all the measured spin states at different k_x and k_y to the Bloch sphere. The Chern number will be zero if these states cannot fully cover the Bloch sphere, which is the case in Fig. 2.2.3a. We have also computed the Chern numbers explicitly using our measured data along different 2D momentum layers [47] and checked they are all identically zero. On the other hand, if we

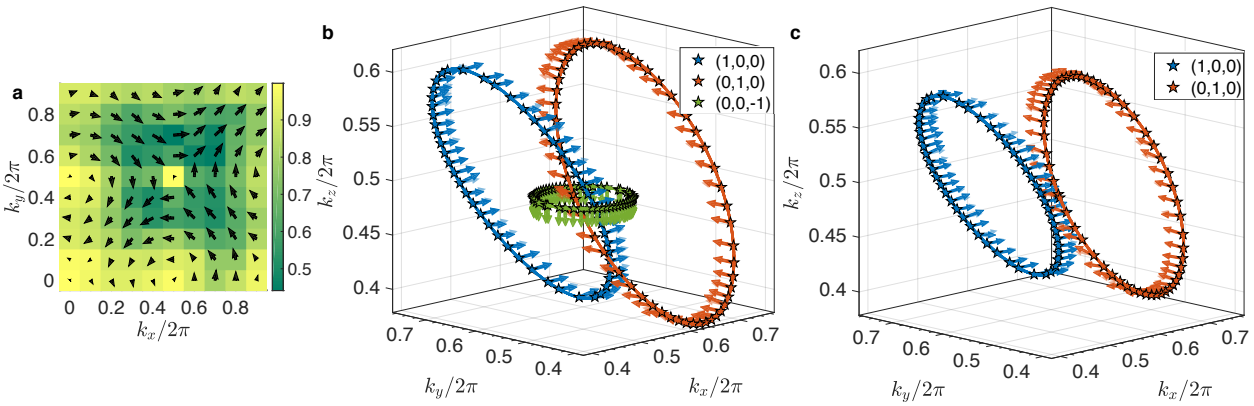

Figure 2.2.4: The Hopfion spin texture and topological links characterizing the Hopf insulator. **a,** A 2D cross section of the Hopfion is shown for the $k_z = 0$ layer and $h = 2$. The Hopfion represents the knotted 3D spin texture of the Hopf insulator. The arrows in the plane depict the x-y direction of the Bloch vectors and the color labels the magnitude of its z component. **b,** Topological links between the pre-images in the momentum space from three spin states on the Bloch sphere, $\mathbf{S} = (1, 0, 0)$, $(0, 1, 0)$, and $(0, 0, -1)$. The parameter $h = 2.9$, which determines the topological phase with the Hopf index $\chi = 1$. The linking number between any pair of pre-image loops is equal to the Hopf index for this phase. The Solid arrows show experimentally measured spin orientations $\mathbf{S}_{\rm exp}$, which are in close proximity to the transparent arrows corresponding to the ideal theoretical directions $\mathbf{S}_{\rm th}$. Solid lines are preimage curves from theoretical calculations. We find the average deviation $\overline{|\mathbf{S}_{\rm exp} - \mathbf{S}_{\rm th}|} \approx 0.082, 0.076, 0.063$ for the blue, red and green curves. **c,** When we cross the topological phase transition point at $h = 3$ and move to $h = 3.1$, the pre-image loops become unlinked, which implies that our system is in the trivial phase at $h = 3.1$. We have $\overline{|\mathbf{S}_{\rm exp} - \mathbf{S}_{\rm th}|} \approx 0.082, 0.071$ for the blue and red curves. The preimage loop for the spin state $(0, 0, -1)$ shrinks and vanishes at $h = 3.1$ because none of the ground state of $H_{\mathbf{k}}$ could reach the Bloch vector $(0, 0, -1)$. This is another indication that the system is in the trivial phase at $h = 3.1$, since the ground-state spin orientations do not fully cover the Bloch sphere.

map the spin states at all 3D momentum points to the Bloch sphere, they fully cover the sphere as shown in Fig. 2.2.3b. This provides an intuitive indicator that the Hopf insulator is an intrinsic 3D topological insulator.

In the Hopf insulator, the momentum-space spin texture forms a representation of the sought-after knotted structure known as the Hopfion [91]. Distinct from 2D Skyrmion spin configura-

tions where swirling orientations are a salient feature [92], a 3D Hopfion exhibits a nontrivial twisting. In Fig. 2.2.4a, we show a cross-section of the measured spin texture along the $k_z = 0$ layer, which provides a glimpse of the 3D twisting of the Hopfion (see Appendix for the full 3D spin texture). If we fix a spin orientation on the Bloch sphere and trace its pre-image in the momentum space $\mathbb{T}^3$, a closed loop will be formed. For the Hopf insulator phase, the loops corresponding to different points (spin states) on the Bloch sphere are always topologically linked to each other (see Hopf fibration in Fig. 2.2.1a). In order to measure these topological links, we experimentally fix three spin states on the Bloch sphere and scan the momentum $\mathbf{k}$ so that the ground state of $H_{\mathbf{k}}$ is along these spin directions. In Fig. 2.2.4b, we show the pre-images in the momentum space for the spin states $\mathbf{S} = (1, 0, 0)$, $(0, 1, 0)$, and $(0, 0, -1)$ on the Bloch sphere with the parameter $h = 2.9$. Clearly, these pre-images each form a closed loop and they are pairwise linked with a linking number exactly equal to the Hopf index χ. When we cross the topological phase transition point (at $h = 3$) and enter the topologically trivial phase (with $h = 3.1$), the corresponding pre-images are shown in Fig. 2.2.4c—they are no longer linked. Hence the Hopf links observed here provide a direct and intuitive characterization of topological properties of the Hopf insulator.

2.2.6 Discussion

Our experimental probe of Hopf insulators in a solid state quantum simulator represents the first experimental observation of 3D topological insulators with integer-valued topological invariants and it paves the way for study of complicated topological models using the powerful quantum simulation toolbox [29, 31, 32, 34]. The framework directly carries over to other types of topological models that are predicted to exist in the periodic table [9, 10, 44] but have not yet been observed in any experiments. The observation of Hopf links in our experiment

reveals the fascinating topological structure of the Hopf fibration, and similar techniques can be employed to study higher index Hopf insulators [43] that can host a range of complex knots and links [42]. This raises the possibility for experimental exploration of the intimate connection between topological insulators and mathematical knot theory. Based on measurement of momentum space correlations, our first detection of an integer-valued topological invariant in 3D complements well with other methods for measuring topological invariants in 1D [85, 93] and 2D [23, 34, 84, 94, 95] systems. The demonstrated detection scheme is general and applicable to probe of different topological insulators in any spatial dimension predicted by the periodic table.

CHAPTER III

Simulating Topological Phases with Cold Atoms

In the last two decades, the exquisite control and novel detection methods of cold atoms have enabled physicists to discover countless new phenomena [15, 16, 76], many of which are not possible otherwise. From the exploration of the Bose-Hubbard and Hubbard physics in the lab [96–98] to the engineering of spin-orbit coupling [18] and simulation of exotic topological phases such as the Hofstadter model [20, 21] and the Haldane model [22], the application of cold atoms has been deepening and broadening at the same time. In this chapter, we focus on a few of our studies on using cold atom systems to simulate topological phases of matter.

In the first two sections, we study the properties of chiral topological insulators and present a feasible experimental scheme to realize and probe the phase in three dimensions. In the third section, we introduce a general scheme to measure topological invariants in cold atoms. The method is applicable to any spatial dimension. In the last section of this chapter, we consider dissipative systems and find a new type of topological gapless rings, the Weyl exceptional rings.

3.1 Probe Chiral Topological Insulators in Optical Lattices

3.1.1 Introduction

In this section, we propose a feasible experimental scheme to realize a three-dimensional chiral topological insulator with cold fermionic atoms in an optical lattice, which is characterized by an integer topological invariant distinct from the conventional $\mathbb{Z}_2$ topological insulators and has a remarkable macroscopic zero-energy flat band. To probe its property, we show that its characteristic surface states—the Dirac cones—can be probed through time-of-flight imaging or Bragg spectroscopy and the flat band can be detected via measurement of the atomic density profile in a weak global trap. The realization of this novel topological phase with a flat band in an optical lattice will provide a unique experimental platform to study the interplay between interaction and topology and open new avenues for application of topological states.

The exploration of topological phases of matter has become a major theme at the frontiers of condensed matter physics since the discovery of topological insulators (TIs) [4–6]. The TIs are band insulators with peculiar topological properties that are protected by time reversal symmetry. A recent remarkable theoretical advance is the finding that there are various other kinds of topological phases of free fermions apart from the conventional TIs, which can be classified by a periodic table according to system symmetry and dimensionality [9, 10]. An important question then is whether the new topological phases predicted by the periodic table can be physically realized. Several model Hamiltonians have been proposed to have the predicted topological phases as their ground states [41, 43, 68, 73, 99, 100]. However, these

model Hamiltonians typically require complicated spin-orbital couplings that are hard to be realized in real materials. Implementations of these model Hamiltonians still remain very challenging for experiments.

In this section, we propose an experimental scheme to realize a three-dimensional (3D) chiral TI with cold fermionic atoms in an optical lattice. The chiral TI is protected by the chiral symmetry, also known as the sublattice symmetry [68, 101, 102]. Unlike the conventional TIs protected by the time reversal symmetry, which is characterized by a $\mathbb{Z}_2$ topological invariant, the chiral TI is characterized by a topological invariant taking arbitrary integer values [9, 10]. By controlling the spin-orbital coupling of cold fermionic atoms in a tilted optical lattice based on the Raman-assisted hopping [20, 21, 103], we realize a tight-binding model Hamiltonian first proposed in Ref. [73], which supports a chiral TI with a zero-energy flat band. In such a flat band, the kinetic energy is suppressed and the atomic interaction, which can be tuned by the Feshbach resonance technique [104], will lead to a novel nonperturbative effect. In a cold atom experiment, flat bands have been studied in a 2D frustrated Kagome lattice [105]. Inspired by the discovery of the fractional quantum Hall effect in a topologically nontrivial flat-band Landau level, one expects that the atomic interaction in a flat-band TI may lead to exciting new physics [106–108]. To probe the properties of the chiral TI in our proposed realization, we show that topological phase transition and the characteristic surface states of the TIs, the Dirac cones, can both be detected by mapping out the Fermi surface structure through time-of-flight imaging [109–111] or Bragg spectroscopy [112]. Furthermore, we show that the flat band can be verified by measurement of the atomic density profile under a weak global harmonic trap [98, 113].

3.1.2 Model Hamiltonian and Experimental Scheme

We consider realization of the following tight-binding model Hamiltonian in the momentum space [73]

$$\mathcal{H}(\mathbf{k}) = \begin{pmatrix} 0 & 0 & q_1 - iq_2 \\ 0 & 0 & q_3 - iq_0 \\ q_1 + iq_2 & q_3 + iq_0 & 0 \end{pmatrix}, \tag{3.1.1}$$

with $q_0 = 2t\,(h + \cos k_x a + \cos k_y a + \cos k_z a)$, $q_1 = 2t \sin k_x a$, $q_2 = 2t \sin k_y a$, $q_3 = 2t \sin k_z a$, where $\mathbf{k} = (k_x, k_y, k_z)$ denotes the momentum, a is the lattice constant, t is the hopping energy, and h is a dimensionless control parameter. This model Hamiltonian has a chiral symmetry represented by $S\mathcal{H}(\mathbf{k})S^{-1} = -\mathcal{H}(\mathbf{k})$ with the unitary matrix $S \equiv \mathrm{diag}(1, 1, -1)$. It has three bands, with a flat middle band exactly at zero energy protected by the chiral symmetry. The other two bands have energies $E_{\pm}(\mathbf{k}) = \pm 2t[\sin^2(k_x a) + \sin^2(k_y a) + \sin^2(k_z a) + (\cos k_x a + \cos k_y a + \cos k_z a + h)^2]^{1/2}$. The topological index for this model can be characterized by the integral [44, 73]

$$\Gamma = \frac{1}{12\pi^2} \int_{\mathrm{BZ}} d\mathbf{k}\, \epsilon^{\alpha\beta\gamma\rho} \epsilon^{\mu\nu\tau} \frac{1}{E_+^4} q_\alpha \partial_\mu q_\beta \partial_\nu q_\gamma \partial_\tau q_\rho, \tag{3.1.2}$$

where ϵ is the Levi-Civita symbol with $(\alpha, \beta, \gamma, \rho)$ and (μ, ν, τ) taking values respectively from $\{0, 1, 2, 3\}$ and $\{k_x, k_y, k_z\}$.

To realize the model Hamiltonian (3.1.1), we consider interaction-free fermionic atoms in an optical lattice and choose three internal atomic states in the ground state manifold to carry three spin states $|1\rangle, |2\rangle, |3\rangle$. The other levels in the ground state manifold are irrelevant as they are initially depopulated by the optical pumping and transitions to these levels are forbidden during Raman-assisted atomic hopping because of a large energy detuning. The

Hamiltonian (3.1.1), expressed in real space, has the following form

$$
\begin{aligned}
H &= t\sum_{\mathbf{r}}\left[\left(2ihc^{\dagger}_{3,\mathbf{r}}c_{2,\mathbf{r}}+\text{H.c.}\right)+H_{\mathbf{rx}}+H_{\mathbf{ry}}+H_{\mathbf{rz}}\right],\\
H_{\mathbf{rx}} &= ic^{\dagger}_{3,\mathbf{r}-\mathbf{x}}(c_{1,\mathbf{r}}+c_{2,\mathbf{r}})-ic^{\dagger}_{3,\mathbf{r}+\mathbf{x}}(c_{1,\mathbf{r}}-c_{2,\mathbf{r}})+\text{H.c.},\\
H_{\mathbf{ry}} &= -c^{\dagger}_{3,\mathbf{r}-\mathbf{y}}(c_{1,\mathbf{r}}-ic_{2,\mathbf{r}})+c^{\dagger}_{3,\mathbf{r}+\mathbf{y}}(c_{1,\mathbf{r}}+ic_{2,\mathbf{r}})+\text{H.c.},\\
H_{\mathbf{rz}} &= 2ic^{\dagger}_{3,\mathbf{r}-\mathbf{z}}c_{2,\mathbf{r}}+\text{H.c.},
\end{aligned}
\tag{3.1.3}
$$

where $(\mathbf{x},\mathbf{y},\mathbf{z})$ represents a unit vector along the (x,y,z)-direction of a cubic lattice, and $c_{j,\mathbf{r}}$ $(j=1,2,3)$ denotes the annihilation operator of the fermionic mode at the lattice site $\mathbf{r}$ with the spin state $|j\rangle$. To implement this Hamiltonian, the major difficulty is to realize the spin-transferring hopping terms $H_{\mathbf{rx}}, H_{\mathbf{ry}}, H_{\mathbf{rz}}$ along each direction [114]. The hopping terms and the associated spin transformation can be visualized diagrammatically as

$$
\begin{aligned}
&x\text{-direction: } |3\rangle \overset{i\sqrt{2}}{\curvearrowleft} |1_x\rangle \overset{\times}{\curvearrowright} \;+\; \overset{\times}{\curvearrowleft} |2_x\rangle \overset{-i\sqrt{2}}{\curvearrowright} |3\rangle \;+\; \text{H.c.}\\
&y\text{-direction: } |3\rangle \overset{-\sqrt{2}}{\curvearrowleft} |1_y\rangle \overset{\times}{\curvearrowright} \;+\; \overset{\times}{\curvearrowleft} |2_y\rangle \overset{\sqrt{2}}{\curvearrowright} |3\rangle \;+\; \text{H.c.}\\
&z\text{-direction: } |3\rangle \overset{2i}{\curvearrowleft} |2\rangle \overset{\times}{\curvearrowright} \;+\text{H.c.}
\end{aligned}
\tag{3.1.4}
$$

where $\overset{\times}{\curvearrowright}$ indicates that hopping is forbidden along that direction, and $|1_x\rangle = (|1\rangle+|2\rangle)/\sqrt{2}, |2_x\rangle = (|1\rangle-|2\rangle)/\sqrt{2}, |1_y\rangle = (|1\rangle-i|2\rangle)/\sqrt{2}, |2_y\rangle = (|1\rangle+i|2\rangle)/\sqrt{2}$ are superpositions of the original spin-basis vectors $|1\rangle, |2\rangle, |3\rangle$.

We use Raman-assisted tunneling to achieve the spin-transferring hopping terms depicted in Eq. (3.1.4). Note that the parity (left-right) symmetry is explicitly broken by these hopping terms. To break the parity symmetry, we assume the optical lattice is tilted with a homogeneous energy gradient along the x-,y-,z-directions. This can be achieved, for instance,

through the natural gravitational field, the magnetic field gradient, or the gradient of a dc- or ac-Stark shift [20, 21, 103]. Raman-assisted hopping in a tilted optical lattice has been demonstrated in recent experiments [20, 21]. In our scheme, we require a different linear energy shift per site $\Delta_{x,y,z}$ along the x-,y-,z-directions. In particular, we take $\Delta_z \approx 1.5\Delta_y \approx 3\Delta_x$ with the energy difference lower bounded by Δ_x, and assume the natural tunneling rate $t_0 \ll \Delta_x$ so that the hopping probability $(t_0/\Delta_x)^2$ induced by the natural tunneling is negligible in this tilted lattice.

To realize the hopping terms in Eq. (3.1.4), we apply two-photon Raman transitions with the configuration (polarization and propagating direction) of the laser beams depicted in Fig. 3.1.1 [114]. The internal states $|1\rangle, |3\rangle, |2\rangle$ differ in the magnetic quantum number m by one successively so that the atomic addressing can be achieved using polarization selection. The π-polarized lights consist of two laser beams $\Omega_1^\pi = \Omega_0 e^{ikx}$ and $\Omega_2^\pi = \Omega_0 e^{iky}$, propagating along the x and y directions respectively, where k is the magnitude of the laser wave vector. The other five beams $\Omega_{1,2}^{x,y,z}$ are all propagating along the z direction and the polarizations are shown in Fig. 3.1.1. The Rabi frequencies $\Omega_{1,2}^{x,y,z}$, expressed in terms of the unit Ω_0, are given in the caption of Fig. 3.1.1 to produce the required phase and amplitude relations of the hopping terms in Eq. (3.1.4). Between the sites $\mathbf{r}$ and $\mathbf{r}+\mathbf{m}$, the Raman-assisted hopping rate is given by

$$t_{\mathbf{r},\mathbf{m}} = \frac{\Omega^*_{\beta\mathbf{m}}\Omega_{\alpha\mathbf{m}}}{\delta}\int d^3\mathbf{r}' w^*(\mathbf{r}'-\mathbf{r}-\mathbf{m})e^{i\delta\mathbf{k}\cdot\mathbf{r}'}w(\mathbf{r}'-\mathbf{r}),$$

where δ is a large single-photon detuning to the excited state, $w(\mathbf{r}'-\mathbf{r})$ is the Wannier-(Stark) function at the site $\mathbf{r}$ [115], and $\delta\mathbf{k} = \mathbf{k}_\alpha - \mathbf{k}_\beta$ is the momentum difference between the relevant Raman beams with the corresponding single-photon Rabi frequencies $\Omega_{\alpha\mathbf{m}}$ and

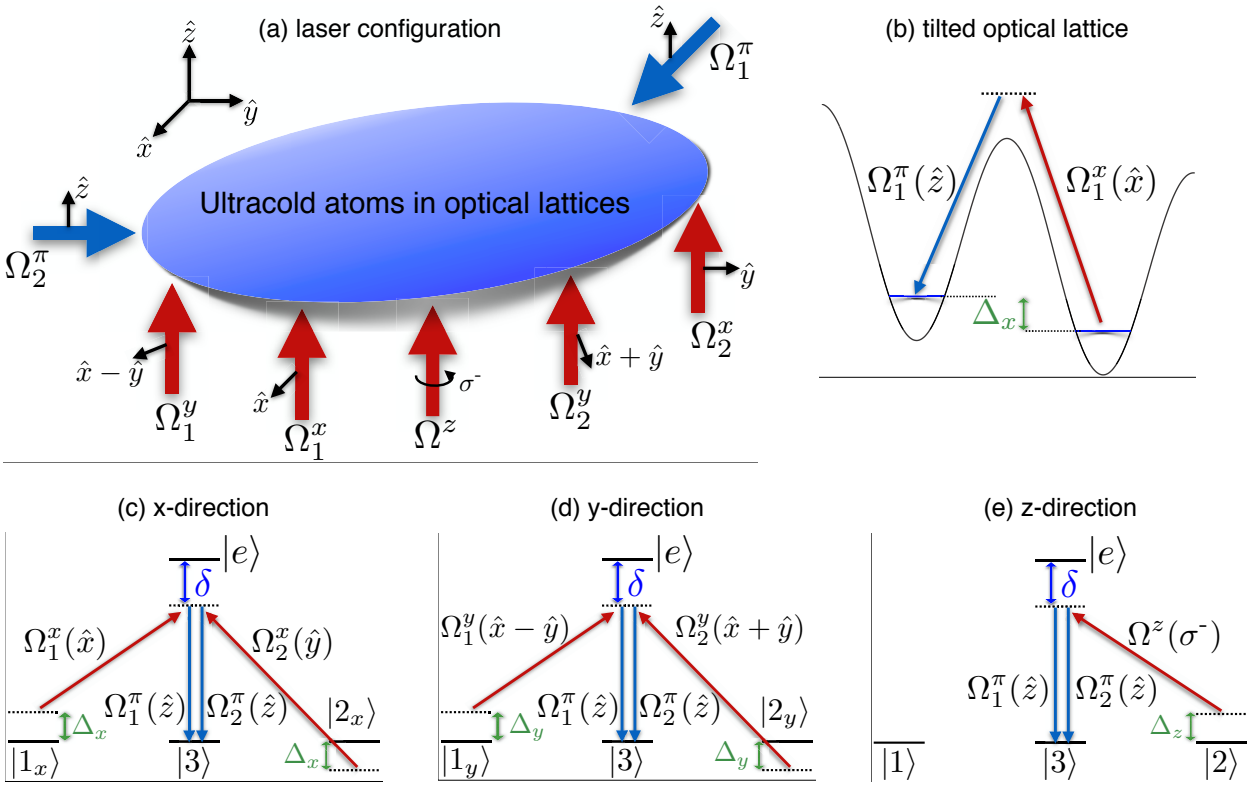

Figure 3.1.1: Schematics of the laser configuration to realize the Hamiltonian in Eq. (3.1.3). Panel (a) shows the propagation direction (big arrows) and the polarization (small arrows) of each laser beam. (b) A linear tilt $\Delta_{x,y,z}$ per site in the lattice along each direction. The detuning in each direction matches the frequency offset of the corresponding Raman beams, which are shown in panels (c), (d), and (e). Polarizations of each beam are shown in brackets. Rabi frequencies for each beam are: $\Omega_1^\pi = \Omega_0 e^{ikx}, \Omega_2^\pi = \Omega_0 e^{iky}, \Omega_1^x = i\sqrt{2}\Omega_0 e^{ikz}, \Omega_2^x = -i\sqrt{2}\Omega_0 e^{ikz}, \Omega_1^y = -\sqrt{2}\Omega_0 e^{ikz}, \Omega_2^y = \sqrt{2}\Omega_0 e^{ikz}, \Omega^z = 2i\Omega_0 e^{ikz}$. [114]

$\Omega_{\beta\mathbf{m}}$. Because of the fast decay of the Wannier function, we consider only the nearest-neighbor Raman-assisted hopping with $\mathbf{m} = \pm\,\mathbf{x}, \pm\mathbf{y}, \pm\mathbf{z}$. When $\delta\mathbf{k} = \mathbf{0}$, we have $t_{\mathbf{r},\mathbf{m}} = 0$ for any $\mathbf{m} \neq \mathbf{0}$ terms because of the orthogonality of Wannier functions. Let us take one of the tunneling terms along the x direction $|3\rangle \overset{i\sqrt{2}}{\curvearrowleft} |1_x\rangle$ as an example to explain the Raman-assisted hopping rate. The relevant Raman pair is $\Omega_1^x = i\sqrt{2}\Omega_0 e^{ikz}$ and $\Omega_1^\pi = \Omega_0 e^{ikx}$ in Fig. 3.1.1, so $\Omega_{\alpha\mathbf{m}} = i\sqrt{2}\Omega_0$ and $\Omega_{\beta\mathbf{m}} = \Omega_0$. The laser beam Ω_1^x has two frequency components,

generated, e.g., by an electric optical modulator (EOM), which are resonant with the levels $|1\rangle, |2\rangle$ respectively so that in the rotating frame the levels $|1\rangle$ and $|2\rangle$ are degenerate in energy. The beam Ω_1^x is polarized along the x direction, so, together with Ω_1^π, it couples the state $|1_x\rangle$ to the state $|3\rangle$ through the two-photon transition. The two-photon detuning Δ_x is in resonance with the potential gradient along the x direction so that the beams only induce the nearest-neighbor hopping from $\mathbf{r}$ to $\mathbf{r}-\mathbf{x}$. Using factorization of the Wannier function $w(\mathbf{r}') = w(x')w(y')w(z')$ in a cubic lattice, we find the hopping rate $t_{\mathbf{r},-\mathbf{x}} = i\sqrt{2}\beta\Omega_{\mathbf{R}}e^{i\delta\mathbf{k}\cdot\mathbf{r}}$, where $\Omega_{\mathbf{R}} \equiv |\Omega_0|^2/\delta$ and $\beta \equiv \int dx w^*(x+a)e^{-ikx}w(x)\int dy w^*(y)w(y)\int dz w^*(z)e^{ikz}w(z)$. For this hopping term, $\delta\mathbf{k} = (-k, 0, k)$. Actually, for the beams shown in Fig. 3.1.1, any nonzero $\delta\mathbf{k}$ has the form $(\pm k, 0, \mp k)$ or $(0, \pm k, \mp k)$, so the site dependent phase term can always be reduced to $e^{i\delta\mathbf{k}\cdot\mathbf{r}} = 1$ if we take the lattice constant a to satisfy the condition $ka = 2\pi$ by adjusting the interfering angle of the lattice beams. Under this condition, all the hopping terms in Eq. (3.1.4) are obtained through the laser beams shown in Fig. 3.1.1 with the hopping rate $t = \beta\Omega_{\mathbf{R}}$ [114]. The on-site spin transferring term $hc_{3,\mathbf{r}}^\dagger c_{2,\mathbf{r}}$ can be achieved through application of a simple radio-frequency (rf) field (or another copropagating Raman beam). The Raman beams $\Omega_{1,2}^{x,y,z}$ and $\Omega_{1,2}^\pi$ may also induce some on-site spin transferring terms, which can be similarly compensated (canceled) with additional rf fields.

Although the laser configuration illustrated in Fig. 3.1.1 involves several beams, all of them can be drawn from the same laser, with the small relative frequency shift induced by an acoustic optical modulator (AOM) or EOM. The absolute frequencies of these beams and their fluctuations are not important as long as we can lock the relative frequency differences, which can be well controlled with the driving rf fields of the AOMs and EOMs. To show that the proposed scheme is feasible with current technology, we give a parameter estimation for typical experiments. For instance, with ^{40}K atoms of mass m in an optical lattice with the

lattice constant $a = 2\pi/k = 764$ nm [116,117], gravity induces a potential gradient (per site) $\Delta = mga/\hbar \approx 2\pi \times 0.75\,\mathrm{kHz}$. Gravity provides the gradients for free along three directions with an appropriate choice of the relative axes of the frame to satisfy $\Delta_x : \Delta_y : \Delta_z = 1 : 2 : 3$ and $\Delta = \sqrt{\Delta_x^2 + \Delta_y^2 + \Delta_z^2}$. We then have $\Delta_x \approx 2\pi \times 200\,\mathrm{Hz}$. For a lattice with depth $V_0 \approx 2.3E_r$, where $E_r = \hbar^2 k^2/2m$ is the recoil energy, the overlap ratio $\beta \approx 0.34$ and the natural tunneling rate $t_0/\hbar \approx 2\pi \times 50\,\mathrm{Hz}$ [114]. For Raman beams with $\Omega_0/2\pi \approx 15\,\mathrm{MHz}$ and the single-photon detuning $\delta/2\pi \approx 1.7\,\mathrm{THz}$ [116], we have $\Omega_{\mathbf{R}} = |\Omega_0|^2/\delta \approx 2\pi \times 120\,\mathrm{Hz}$ and the Raman-assisted hopping rate $t/\hbar \approx 2\pi \times 40\,\mathrm{Hz}$. Apparently, the undesired off-resonant hopping probabilities, upper bounded by t^2/Δ_x^2 or t_0^2/Δ_x^2, are less than 6% and the effective spontaneous emission rate, estimated by $|\Omega_0/\delta|^2\Gamma_s$ ($\Gamma_s \approx 2\pi \times 6\,\mathrm{MHz}$ is the decay rate of the excited state), is negligible during the experimental time of the order of $10/t$.

3.1.3 Detection Methods

We now proceed to discuss detection methods to probe the exotic phases of the realized Hamiltonian. The topological index Γ defined in Eq. 3.1.2 is shown in Fig. 3.1.2(a) under different values of h. The system is topologically nontrivial for $|h| < 3$, and Γ changes at $|h| = 1, 3$, indicating a topological quantum phase transition. We calculate the band structure numerically for a homogeneous system by keeping x and y directions in momentum space and z direction in real space with open boundaries. Figure 3.1.2(b) shows the result, revealing the macroscopic flat band as well as the surface states with Dirac cones. Experimentally, the band structure can be probed by mapping out the crystal quasimomentum distribution $\rho_{\mathrm{cry}}(\mathbf{k})$. By abruptly turning off the lattice potential, one could measure the momentum distribution $\rho(\mathbf{k})$, and the quasimomentum can then be extracted as $\rho_{\mathrm{cry}}(\mathbf{k}) = \rho(\mathbf{k})/|w(\mathbf{k})|^2$, where $w(\mathbf{k})$ is the Fourier transform of the Wannier function $w(\mathbf{r})$ [109, 110]. Here, we

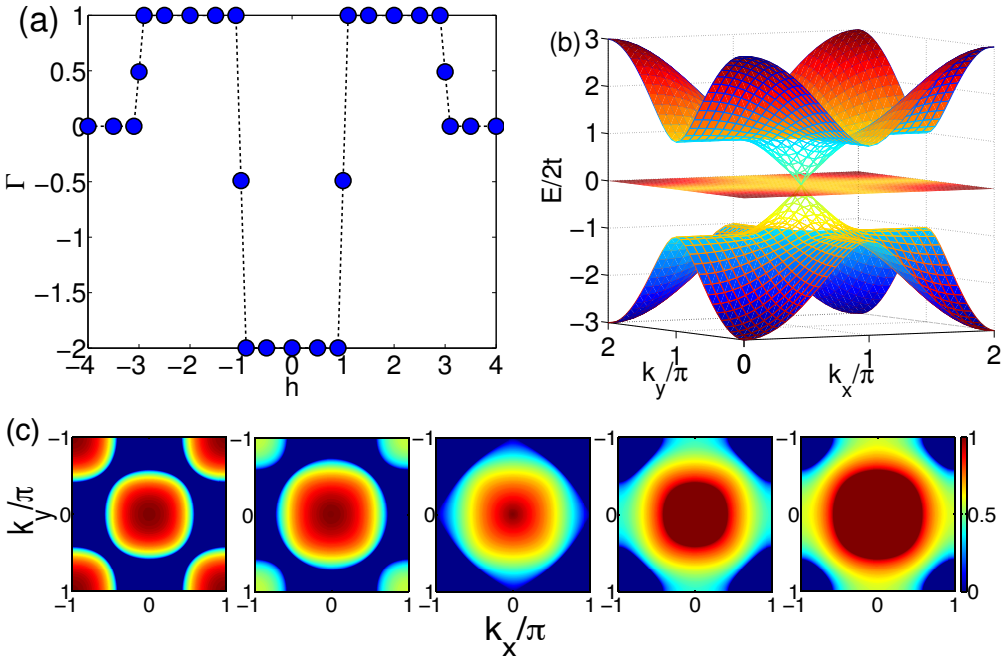

Figure 3.1.2: Topological index and band structure of the chiral topological insulator. (a) The topological index Γ as a function of the parameter h. (b) Energy dispersion for three bulk bands (surface plot) and surface states (mesh plot) at the boundary along the z direction for $h = 2$. (c) Quasimomentum distribution $\rho_{\rm cry}(\mathbf{k})$ for various $h = 0, 0.5, 1, 1.5, 2$ at a fixed chemical potential $\mu/2t = -2$ [114]. One hundreds layers are taken along the z direction with open boundaries in (b) and (c).

numerically calculate the crystal quasimomentum distribution, which can be used to track the topological phase transition [Fig. 3.1.2(c)]. At a fixed chemical potential, as one varies h from 0 to 2, the quasimomentum distribution reshapes accordingly when the bulk gap closes and reopens and the number of surface Dirac cones changes from 2 to 1, indicated by a change of topology of the Fermi surface [114].

Bragg spectroscopy is a complementary detection method to reveal the Dirac cone structure [112, 113]. One could shine two laser beams at a certain angle to induce a Raman transition from an occupied spin state to another hyperfine level and focus them near the surface of the 3D atomic gas. The atomic transition rate can be measured, which is peaked when

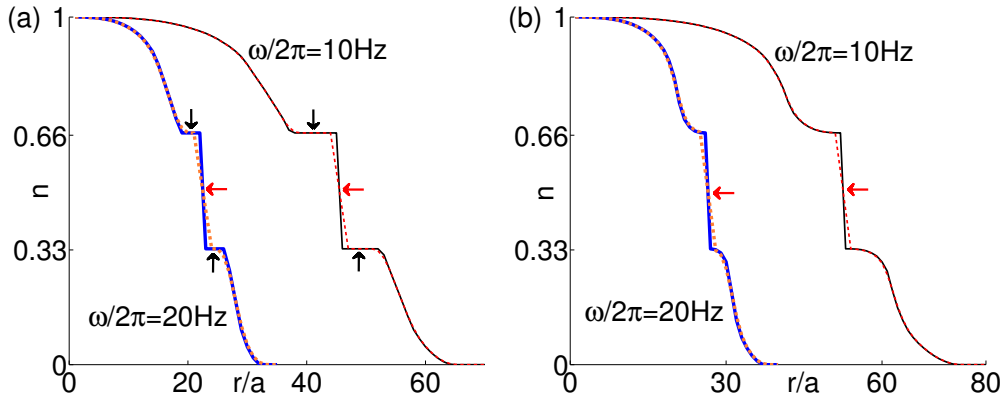

Figure 3.1.3: The atomic density profile n as a function of the radial distance r under the LDA. (a) $h = 0, \mu_0/2t = 3$. (b) $h = 1, \mu_0/2t = 4$. ^{40}K is used and $t/\hbar$ is taken to be $2\pi \times 40\,\text{Hz}$.

the momentum and energy conservation conditions are satisfied. By scanning the Raman frequency difference, one can map out the surface energy-momentum dispersion relation [113]. The surface Dirac cones, with their characteristic linear dispersion, can therefore be probed through Bragg spectroscopy.

So far, we considered a homogeneous system under a box-type trap at zero temperature. In a realistic experiment, finite temperature and a weak confining harmonic trap may introduce noise. To include these effects, an important element to consider is the size of the bulk gap. In our parameter regime, the minimum band gap from the top or bottom bulk band to the middle flat band is $2t = (2\pi\hbar) \times 80\,\text{Hz}$ at $h = 2$ [Fig. 3.1.2(b)], which corresponds to a temperature around 4 nK. Direct cooling to subnanokelvin temperature is challenging but has been attained experimentally [118, 119]. Parametric cooling based on adiabatic preparation can be used to further reduce the effective temperature of the system. With a band gap considerably larger than the probing Raman Rabi frequency, bulk contribution to the Bragg spectroscopy is negligible. In the following, we include the effect of a weak harmonic trap via the local density approximation (LDA) and consider the finite temperature effects to be

minimal.

The characteristic flat band can be detected through measurement of the atomic density profile under the global harmonic trap [98,120]. Under the LDA, the local chemical potential of the system is $\mu(r) = \mu_0 - m\omega^2 r^2/2$, where μ_0 denotes the chemical potential at the center of a spherically harmonic trap with the potential $V(r) = m\omega^2 r^2/2$. The local atomic density $n(r)$ is uniquely determined by $\mu(r)$, and μ_0 is specified by the total atom number N through $\int n(r) 4\pi r^2 \, dr = N$. The atomic density profile $n(r)$, which can be measured *in situ* in experiments [98], is calculated and shown in Fig. 3.1.3. A steep fall or rise in $n(r)$ is a clear signature of a macroscopic flat band (horizontal arrows in Fig. 3.1.3). The plateaus at 1/3 and 2/3 fillings [vertical arrows in Fig. 3.1.3(a)] reveal the corresponding band gap. At $h = 1$, the plateaus vanish [Fig. 3.1.3(b)]. The disappearance of the plateaus at this point indicates the phase transition where the band gap closes. In experiments, due to the finite spatial resolution, the detected signal may correspond to a locally averaged $n(r)$. The dashed lines show the local average density $\bar{n}_i = \sum_{j=-1}^{1} n_{i+j}/3$, averaged over a spherical shell of 3 lattice sites. One can see that major features associated with the band gap and the flat band remain clearly visible even when the signal is blurred by the local spatial averaging.

In summary, we have proposed an experimental scheme to realize and probe a 3D chiral TI with a zero-energy flat band. The experimental realization of this model will mark an important advance in the ultracold atom simulation of topological phases.

3.2 Physical Response of Chiral Topological Insulators

3.2.1 Introduction

Protected by the chiral symmetry, three dimensional chiral topological insulators are characterized by an integer-valued topological invariant. How this invariant could emerge in physical observables is an important question. In this section, we show that the magneto-electric polarization can identify the integer-valued invariant if we gap the system without coating a quantum Hall layer on the surface. The quantized response is demonstrated to be robust against weak perturbations. We also study the topological properties by adiabatically coupling two nontrivial phases, and find that gapless states appear and are localized at the boundary region. Finally, an experimental scheme is proposed to realize the Hamiltonian and measure the quantized response with ultracold atoms in optical lattices.

The periodic table of topological insulators (TIs) and superconductors classifies topological phases of free fermions according to the system symmetry and spatial dimensions [9, 10]. Notable examples include integer quantum Hall insulators breaking all those classification symmetries and the time-reversal-invariant TIs protected by the time-reversal symmetry [4–8, 121]. Mathematically, these exotic states can be characterized by various topological invariants. An interesting question is how to relate these invariants to physical observables. For integer quantum Hall insulators, the Chern number ($\mathbb{Z}$ invariant) corresponds to the quantized Hall conductance [122], while for the time-reversal-invariant TIs, the $\mathbb{Z}_2$ invariant is associated with a quantized magneto-electric effect in three dimensions (3D) [123, 124].

The 3D chiral TIs protected by the chiral symmetry [68,101] are of particular interest as they are 3D TIs characterized by a $\mathbb{Z}$ (instead of $\mathbb{Z}_2$) invariant and may be realized in ultracold

atomic gases with engineered spin-orbital coupling [15, 17, 74]. An experimental scheme was recently proposed to implement a three-band chiral TI in an optical lattice [45]. For such 3D chiral TIs, it is known that the topological magneto-electric effect should also arise, but in theory it captures only the $\mathbb{Z}_2$ part of the $\mathbb{Z}$ invariant due to the gauge dependence of the polarization in translationally invariant systems [101]. It is thus an important question to find out how the $\mathbb{Z}$ character could manifest itself in experiments. It was proposed in Ref. [125] that the $\mathbb{Z}$ effect may become visible in certain carefully engineered heterostructures, but the implementation of such a heterostructure is experimentally challenging.

In this section, we study the nontrivial $\mathbb{Z}$ character of the chiral TI by exploring the adiabatic transition between two nontrivial phases and by numerically simulating the magneto-electric effect in a single phase. We show that not only the $\mathbb{Z}_2$ response but the $\mathbb{Z}$ character can be observed by gapping the system without adding a quantum Hall layer on the surface, i.e., the ambiguity resulting from different terminations appears to be avoidable in practice. Also, the quantized polarization is demonstrated to be robust against small perturbations even in the absence of a perfect chiral symmetry. This observation is important for experimental realization, because in a real system the chiral symmetry is typically an approximate instead of exact symmetry. Lastly, we propose an experimental scheme to realize the Hamiltonian and probe the integrally quantized response with cold atomic systems.

3.2.2 Model and Topological Characterization

We first introduce a minimal lattice tight-binding model for chiral topological insulators with the Hamiltonian in the momentum space given by $H_1 = \sum_{\mathbf{k}} \Psi_{\mathbf{k}}^\dagger \mathcal{H}_1(\mathbf{k}) \Psi_{\mathbf{k}}$, where $\Psi_{\mathbf{k}} = (a_{\mathbf{k}\uparrow}, a_{\mathbf{k}\downarrow}, b_{\mathbf{k}\uparrow}, b_{\mathbf{k}\downarrow})^T$ denotes fermionic annihilation operators with spins $\uparrow, \downarrow$ on sublattices

or orbitals a, b. In cold atom systems, the pseudospins and orbitals can be represented by different atomic internal states. The 4×4 Hamiltonian is

$$\mathcal{H}_1(\mathbf{k}) = \begin{pmatrix} 0 & 0 & -iq_0 + q_3 & q_1 - iq_2 \\ 0 & 0 & q_1 + iq_2 & -iq_0 - q_3 \\ iq_0 + q_3 & q_1 - iq_2 & 0 & 0 \\ q_1 + iq_2 & iq_0 - q_3 & 0 & 0 \end{pmatrix} \tag{3.2.1}$$

where $q_0 = h + \cos k_x + \cos k_y + \cos k_z, q_1 = \sin k_x + \delta, q_2 = \sin k_y, q_3 = \sin k_z$, with h, δ being control parameters. The lattice constant and tunneling energy are set to unity. In real space, this Hamiltonian represents on-site and nearest neighbor hoppings and spin-flip hoppings between two orbitals in a simple cubic lattice. These hoppings can be realized by two-photon Raman transitions in cold atoms [20, 21, 45, 103]. The energy spectrum for this Hamiltonian is $E_{\pm}(\mathbf{k}) = \pm[(\sin k_x + \delta)^2 + \sin^2 k_y + \sin^2 k_z + (\cos k_x + \cos k_y + \cos k_z + h)^2]^{1/2}$, with two-fold degeneracy at each $\mathbf{k}$. For $\delta = 0$, the system acquires time-reversal symmetry T, particle-hole symmetry C, and chiral symmetry $S = TC$, which can be explicitly seen as [68]:

$$T: \quad (\sigma_x \otimes \sigma_y)[\mathcal{H}_1(\mathbf{k})]^*(\sigma_x \otimes \sigma_y) = \mathcal{H}_1(-\mathbf{k}) \tag{3.2.2}$$

$$C: \quad (\sigma_y \otimes \sigma_y)[\mathcal{H}_1(\mathbf{k})]^*(\sigma_y \otimes \sigma_y) = -\mathcal{H}_1(-\mathbf{k}) \tag{3.2.3}$$

$$S: \quad (\sigma_z \otimes I_2)[\mathcal{H}_1(\mathbf{k})](\sigma_z \otimes I_2) = -\mathcal{H}_1(\mathbf{k}) \tag{3.2.4}$$

with σ_i as Pauli matrices, and I_2 as the 2×2 identity matrix. When $\delta \neq 0$, time-reversal and particle-hole symmetries are explicitly broken, but the chiral symmetry survives.

The topological property of the Hamiltonian $\mathcal{H}_1(\mathbf{k})$ can be characterized by the winding

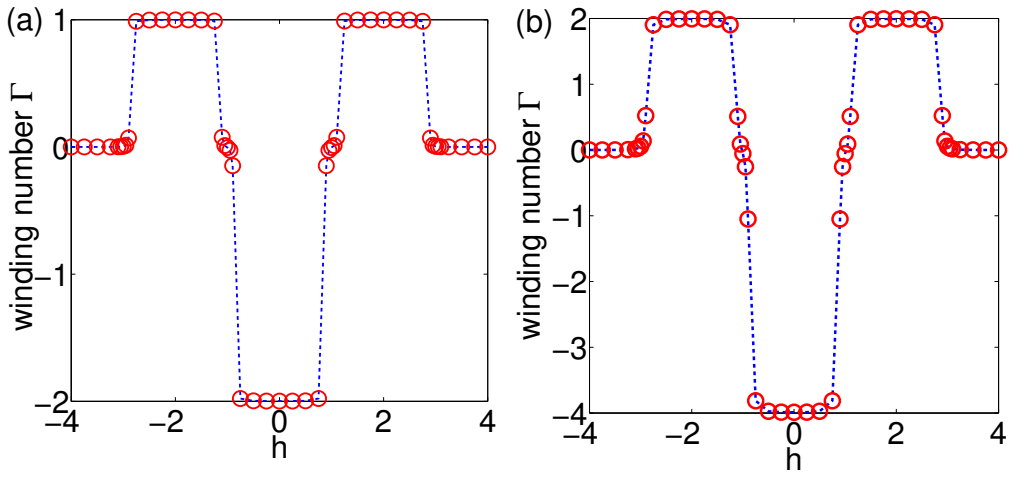

Figure 3.2.1: The winding number Γ as a function of the parameter h. The Hamiltonians are $\mathcal{H}_1(k)$ in (a) and $\mathcal{H}_2(k)$ in (b) respectively. $\delta = 0.5$ for both panels.

number Γ [10, 68]. To define the winding number, let us introduce the Q matrix, $Q(\mathbf{k}) = 1 - 2P(\mathbf{k})$, where $P(\mathbf{k}) = \sum_f |u_f(\mathbf{k})\rangle\langle u_f(\mathbf{k})|$ is the projector onto the filled Bloch bands with wave-vectors $|u_f(\mathbf{k})\rangle$. The Q matrix can be brought into the block off-diagonal form $Q(\mathbf{k}) = \begin{pmatrix} 0 & b(\mathbf{k}) \\ b^\dagger(\mathbf{k}) & 0 \end{pmatrix}$ with the chiral symmetry. With the matrix $b(\mathbf{k})$, one can write [10, 68]

$$\Gamma = \frac{1}{24\pi^2} \int_{\mathrm{BZ}} d\mathbf{k}\, \epsilon^{\mu\rho\lambda} \mathrm{Tr}[(b^{-1}\partial_\mu b)(b^{-1}\partial_\rho b)(b^{-1}\partial_\lambda b)], \tag{3.2.5}$$

where $\epsilon^{\mu\rho\lambda}$ is the antisymmetric Levi-Civita symbol and $\partial_\mu b \equiv \partial_{k_\mu} b(\mathbf{k})$. The Hamiltonian $\mathcal{H}_1(\mathbf{k})$ supports topological phases with $\Gamma = 1, -2$. To obtain chiral TIs with arbitrary integer topological invariants, one can use the quaternion construction proposed in Ref. [44]. By considering $q = q_0 + q_1\boldsymbol{i} + q_2\boldsymbol{j} + q_3\boldsymbol{k}$ as a quaternion and raising to a power, all $\mathbb{Z}$ topological phases can be realized by the family of tight-binding Hamiltonians. By taking the quaternion square, for example, one obtains $q^2 = q_0^2 - q_1^2 - q_2^2 - q_3^2 + 2q_0q_1\boldsymbol{i} + 2q_0q_2\boldsymbol{j} + 2q_0q_3\boldsymbol{k}$, and we can therefore acquire another tight-binding Hamiltonian $H_2 = \sum_{\mathbf{k}} \Psi_{\mathbf{k}}^\dagger \mathcal{H}_2(\mathbf{k}) \Psi_{\mathbf{k}}$ with each

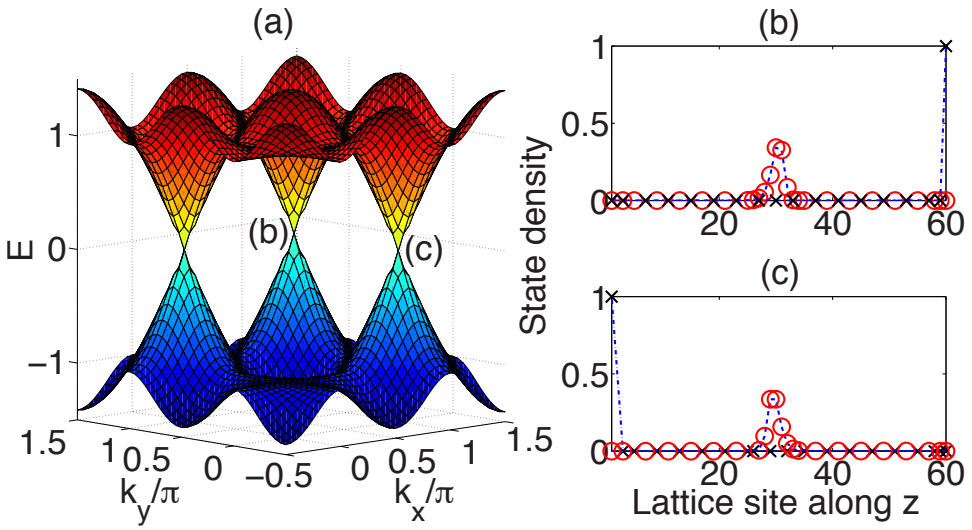

Figure 3.2.2: Coupling two topologically nontrivial phases by varying the parameter h adiabatically from 0 to 2 along the z direction. x and y directions are periodic. Sixty slabs are taken for the z direction. (a) The energy dispersion for the lowest conduction band and highest valence band. (b) and (c) show the surface states near the respective Dirac points. The Γ point is displaced from the center for a better display of the Dirac cones.

component of q^2 replacing the respective components q_0, q_1, q_2, q_3 in $\mathcal{H}_1(\mathbf{k})$. This second Hamiltonian $\mathcal{H}_2(\mathbf{k})$ contains next-nearest-neighbor hopping terms. The winding number Γ can be calculated numerically by discretizing the Brillouin zone and replacing the integral by a discrete sum [44]. The results are shown in Fig. 3.2.1 for both $\mathcal{H}_1(\mathbf{k})$ and $\mathcal{H}_2(\mathbf{k})$.

3.2.3 Surface States and Heterostructure of Nontrivial Topological Phases

By imposing an open boundary condition along the z direction, and keeping the x and y directions in momentum space, surface Dirac cones are formed for nontrivial topological phases. We find that the winding number coincides with the total number of Dirac cones counted for all inequivalent surface states (i.e. not counting the twofold degeneracy for each

band), which confirms explicitly the bulk-edge correspondence (See Appendix B.2.1). A distinctive difference from the time-reversal invariant TI is that any number of Dirac cones on the surface is protected by the chiral symmetry [101].

With an integer number of nontrivial phases, it is intriguing to study the topological phase transition between two different phases. A simple way to explore this is to adiabatically vary h from one end to the other end of the sample. The parameter h concerns the onsite tunneling strength between opposite orbitals ($a_\uparrow^\dagger b_\uparrow$ and $a_\downarrow^\dagger b_\downarrow$ terms). This hopping can be realized by a two-photon Raman process, and the strength h can be controlled by the laser intensity [45]. Numerically, we vary h in the form of $h = 1 + \tanh(z - L_z/2)$, where z denotes the zth layer and L_z the total number of slabs along the z direction. This form ensures that h changes adiabatically from 0 on one end to 2 on the other end of the sample, so that it effectively couples two nontrivial phases. For the Hamiltonian $\mathcal{H}_1$, it couples two topological phases with winding numbers $\Gamma = -2$ and $\Gamma = 1$. Similar to the interface between a topological insulator and the trivial vacuum, a surface state should appear at the interface. As shown in Fig. 3.2.2, three Dirac cones are formed inside the band gap. In addition to the surface states observed on both ends of the sample, a localized state is formed at the interface between two topologically distinct regions. These interface states are always present regardless of the detailed structure of the interface. Even for sharp boundaries, the interface states remain. The Dirac cone structure may be probed through Bragg spectroscopy in cold atom experiments [112, 113].

The above heterostructure could be used to probe the topological properties of the chiral TI, but it is experimentally difficult to engineer such a heterostructure, especially in cold atom systems. In Ref. [125], it was shown that the $\mathbb{Z}$ character of the topological invariant could be seen in some carefully engineered heterostructures. In the following, we show that

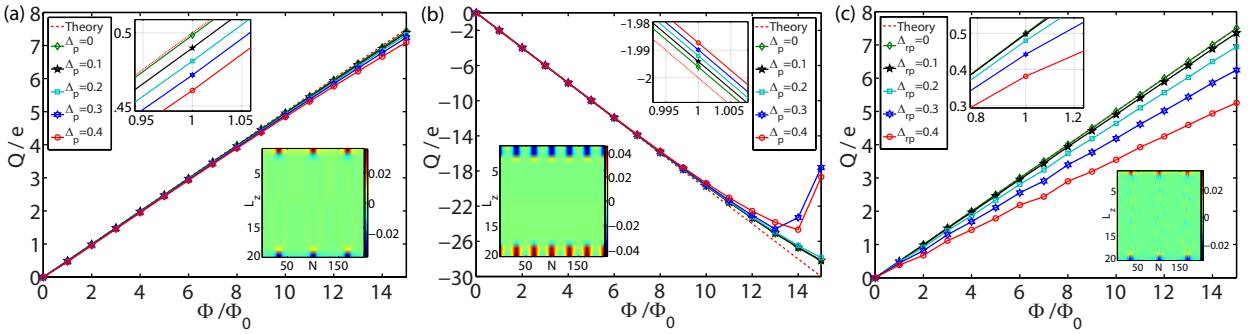

Figure 3.2.3: Charge Q accumulated on the surface in the z direction due to a uniform magnetic field with total flux Φ at $k_x = k_y = 0$. $N = 199, L_z = 20$ for all three panels. (a) and (b) consider the perturbative effect of an intra-site nearest neighbor hopping. (c) adds a random onsite potential characterized by Δ_{rp}. The insets show the charge density at $\Phi = 3\Phi_0$ without perturbations, and a closeup for the slope. The parameters in each panel are: (a) Hamiltonian $\mathcal{H}_1(\mathbf{k})$ with $h = 2, \delta = 0.5, \Delta_S = 1, \Gamma = 1$; (b) Hamiltonian $\mathcal{H}_2(\mathbf{k})$ with $h = 0, \delta = 0, \Delta_S = 1, \Gamma = -4$; (c) Hamiltonian $\mathcal{H}_1(\mathbf{k})$ with $h = 2, \delta = 0, \Delta_S = 1, \Gamma = 1$. In all panels, the accumulated charge Q is relative to the case when $\Phi = 0$ and is summed over all particle species for the upper half of the sample at half fillings.

the $\mathbb{Z}$ topological invariant can be observed via the magneto-electric polarization in a single nontrivial phase with a gapped surface. We further show that the detection will be robust to realistic experimental perturbations and present a feasible experimental scheme to observe the quantized response.

3.2.4 Magneto-electric Effect

The magneto-electric effect is a remarkable manifestation of the bulk non-trivial topology. The linear response of a TI to an electromagnetic field can be described by the magneto-electric polarizability tensor as [124]

$$\alpha_{ij} = \frac{\partial P_i}{\partial B_j}\bigg|_{E=0} = \frac{\partial M_j}{\partial E_i}\bigg|_{B=0}, \tag{3.2.6}$$

where E and B are the electric and magnetic field, P and M are the polarization and magnetization. Unique to topological insulators is a diagonal contribution to the tensor with $\alpha_{ij} = \theta \frac{e^2}{2\pi h} \delta_{ij}$. This is a peculiar phenomenon as an electric polarization is induced when a magnetic field is applied along the same direction [123]. This effect can be described by a low-energy effective field theory in the Lagrangian as ($c = 1$)

$$\Delta \mathcal{L} = \theta \frac{e^2}{2\pi h} \mathbf{B} \cdot \mathbf{E} \tag{3.2.7}$$

known as the "axion electrodynamics" term [124]. For time-reversal-invariant TIs, an equivalent understanding will be a surface Hall conductivity induced by the bulk magneto-electric coupling. When the time-reversal symmetry is broken on the surface generating an insulator, a quantized surface Hall conductance will be produced:

$$\sigma_H = \theta \frac{e^2}{2\pi h} \tag{3.2.8}$$

where θ is quantized to be 0 or π to preserve the time-reversal invariance [123]. $\theta = \pi$ corresponds to the non-trivial time-reversal-invariant TI with a fractional quantum Hall conductivity. The electric polarization can be understood with Laughlin's flux insertion argument [126]. A changing magnetic field through the insulator induces an electric field (by Faraday's law), which together with the quantized Hall conductivity will produce a transverse current and accumulate charge around the magnetic flux tube at a rate proportional to σ_H as $Q = \sigma_H \Phi$ [127].

Numerical Results

Theoretically, chiral TIs are also predicted to have this topological magneto-electric effect [68, 101]. The field theory only captures the $\mathbb{Z}_2$ part of the integer winding number due to the 2π periodicity of θ associated with a gauge freedom in transitionally invariant systems. However, we numerically show that the $\mathbb{Z}$ character can actually be observed by gapping the system without adding a strong surface orbital magnetic field. Apparently, this corresponds to a particular gauge such that the $\mathbb{Z}$ character can be distilled from the polarization. More concretely, we consider the chiral TI represented by both Hamiltonians $\mathcal{H}_1(\mathbf{k})$ and $\mathcal{H}_2(\mathbf{k})$. A uniform magnetic field is inserted through the chiral TI sample via the Landau gauge $\mathbf{A} = Bx\hat{y}$ with a minimal coupling by replacing k_y with $k_y - \frac{e}{\hbar}Bx$. We keep x and y directions in momentum space, and the z direction in real space with open boundaries and L_z slabs. By taking a magnetic unit cell with N sites along the x direction, the Hamiltonian can be partially Fourier transformed to be a $4L_z \times N$ matrix for each k_x and k_y, with 4 taking into account of spins $\uparrow, \downarrow$ and orbitals a, b. For a unit magnetic cell with N lattice cells, the total magnetic flux through the unit cell is quantized to be integer multiples of a full flux quantum $\Phi = n\Phi_0 = n\frac{h}{e}$ due to the periodic boundary condition along the x direction, so the flux through a single lattice plaquette is quantized to be Φ/N. In the weak magnetic field limit, one needs to take a large N. Besides the bulk Hamiltonian $\mathcal{H}_1(\mathbf{k})$ or $\mathcal{H}_2(\mathbf{k})$, we also add a surface term to break the chiral symmetry and open a gap on the surface,

$$H_S = \Delta_S \sum_{k_x,k_y} \sum_{j\in\text{surf}} \hat{\mathbf{S}} \cdot \hat{z} \left(\Psi^\dagger_{j,k_x,k_y} \left(I_2 \otimes \sigma_z \right) \Psi_{j,k_x,k_y} \right), \tag{3.2.9}$$

where $\hat{\mathbf{S}}$ represents the unit vector perpendicular to the surface along z direction, so $\hat{\mathbf{S}} \cdot \hat{z} = 1$ for the upper surface, and $\hat{\mathbf{S}} \cdot \hat{z} = -1$ for the lower surface. This term represents a surface

magnetization with a Zeeman coupling, creating a different chemical potential for spins $\uparrow$ and $\downarrow$. It can be directly verified that this surface term breaks the chiral symmetry S in Eq. (3.2.4).

As the surface becomes gapped, at half filling, an increasing uniform magnetic field accumulates charges on the surface via the magneto-electric coupling. In the weak magnetic field limit, the charge accumulated on the surface is proportional to σ_H as

$$Q = \sigma_H \Phi = \frac{\theta}{2\pi} ne. \tag{3.2.10}$$

A priori, θ needs not be quantized. However, analogous to the role played by time-reversal symmetry, chiral symmetry pins down θ to be $m\pi$ with an integer value m [68]. The fractional Hall conductivity, which cannot be removed by surface manipulations, emerges when m is odd [101, 123, 128]. The integer part of σ_H, however, depends on the details of the surface [123, 124, 129]. An intuitive picture is that the 2π ambiguity in θ results from the freedom to coat an integer quantum Hall layer on the surface, or equivalently to change the chemical potential and hence the Landau level occupancy of the surface in an orbital magnetic field. However, once a fixed surface Hamiltonian is defined, the adiabatic change in polarization associated with the increase in magnetic flux does have a physical meaning. This ambiguity can be avoided in cold atom systems, where the precise Hamiltonian can be engineered, allowing a direct link between the winding number Γ and the charge accumulation rate $\theta/2\pi$.

Numerical results in Fig. 3.2.3 show that $\Gamma = \theta/\pi$, which reveals that the magneto-electric polarization is a direct indication of the non-trivial bulk topological phase characterized by the integer winding number. To gain some intuition for why in our Hamiltonian the value

$\Gamma = \theta/\pi$ is observed, consider how a Zeeman term and an orbital magnetic term produce different quantum Hall effects for a Dirac fermion: the latter leads to Landau levels with many intervening gaps and a chemical-potential dependence of the Hall effect, while the former leads to a single gap and only one value of the Hall effect. The surface term (3.2.9) apparently acts more like a Zeeman field in leading to a single gap and a unique value of the magneto-electric effect. We have confirmed this intuition by adding a strong orbital magnetic field in a single-layer Hamiltonian $\mathcal{H}_1(\mathbf{k})$ (see Appendix B.2.2). Landau-level like bands are formed, and the charge accumulation rate is changed by an integer value by varying the chemical potential.

Robustness to Perturbations

In real physical systems, the chiral symmetry may not be strictly observed. We therefore consider the effect of weak perturbations to the charge quantization. A natural term to add is an intra-site nearest neighbor hopping term:

$$\mathcal{H}_p(\mathbf{k}) = \Delta_p(\cos k_x + \cos k_y + \cos k_z) I_4. \tag{3.2.11}$$

This term breaks the chiral symmetry and permits nearest-neighbor hoppings within the same sublattice. Figures 3.2.3(a) and 3.2.3(b) show the charge accumulation on the surface with increasing magnetic field for various strengths of perturbations. The quantized slope is indeed robust to small perturbations in the limit of weak magnetic field. Fig. 3.2.3(c) takes into account of random onsite potential with various perturbing strengths, and it again shows the robustness of the topological effect. This includes the effect of a weak harmonic trap typically present in cold atom systems. Note that strong perturbations destroy the topological

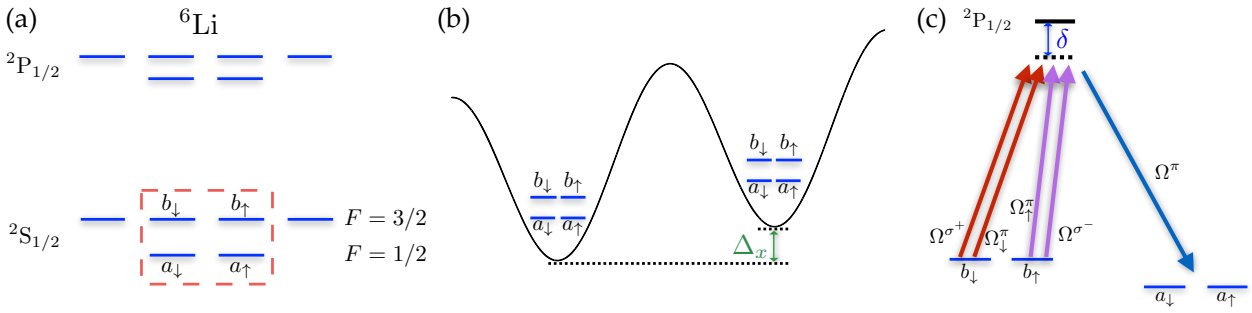

Figure 3.2.4: Schematics to realize the Hamiltonian H_1 with cold atoms. (a) Atomic level structure of ^{6}Li and the four internal states used to represent the spin and orbital degrees of freedom. (b) The optical lattice is tilted with a homogeneous energy gradient along each direction. (c) Laser configurations to create the first term in $H_{\mathbf{rx}}$. The superscript on each Rabi frequency denotes the polarization of the beam.

phase. We also performed similar calculations by squeezing the entire uniform magnetic field into a single flux tube with open boundaries. It shows the same linear relationship between the surface charge accumulation and the magnetic flux. This indicates the uniformity of magnetic field is not crucial to observe the topological magneto-electric polarization, which may be an advantage to experimental realization.

3.2.5 Experimental Implementation and Detection

In this section, we present more details on the implementation scheme with ultracold atoms. In Ref. [45], an experimental proposal for a three-band chiral TI was put forward. The realization scheme for the four-band Hamiltonian studied here will be similar, with the atomic internal states representing the spin and orbital degrees of freedom. In the previous sections, we studied two Hamiltonians $\mathcal{H}_1(\mathbf{k})$ and $\mathcal{H}_2(\mathbf{k})$. The latter involves next-nearest-neighbor hopping terms, which will be very challenging for experiment to engineer. In the following, we demonstrate, however, that the implementation of $\mathcal{H}_1(\mathbf{k})$ is possible with

current technologies. $\mathcal{H}_1(\mathbf{k})$ supports topological phases with index $\Gamma = 0, 1, -2$. It would be very exciting if experiment could simulate $\mathcal{H}_1(\mathbf{k})$ and probe its nontrivial topological properties via magneto-electric polarization.

The Hamiltonian $\mathcal{H}_1(\mathbf{k})$ was written in momentum space in Sec. 3.2.2. The real space equivalent can be expressed as (for simplicity, we take $h = 0$, $\delta = 0$.)

$$
\begin{aligned}
H_1 &= \sum_{\mathbf{r}} H_{\mathbf{rx}} + H_{\mathbf{ry}} + H_{\mathbf{rz}}, \qquad (3.2.12)\\
H_{\mathbf{rx}} &= -i/2 \left(a^\dagger_{\uparrow,\mathbf{r}+\mathbf{x}} + a^\dagger_{\downarrow,\mathbf{r}+\mathbf{x}} \right) (b_{\uparrow,\mathbf{r}} + b_{\downarrow,\mathbf{r}}) \\
&\quad - i/2 \left(a^\dagger_{\uparrow,\mathbf{r}-\mathbf{x}} - a^\dagger_{\downarrow,\mathbf{r}-\mathbf{x}} \right) (b_{\uparrow,\mathbf{r}} - b_{\downarrow,\mathbf{r}}) + \text{H.c.}, \\
H_{\mathbf{ry}} &= -i/2 \left(a^\dagger_{\uparrow,\mathbf{r}+\mathbf{y}} + i a^\dagger_{\downarrow,\mathbf{r}+\mathbf{y}} \right) (b_{\uparrow,\mathbf{r}} - i b_{\downarrow,\mathbf{r}}) \\
&\quad - i/2 \left(a^\dagger_{\uparrow,\mathbf{r}-\mathbf{y}} - i a^\dagger_{\downarrow,\mathbf{r}-\mathbf{y}} \right) (b_{\uparrow,\mathbf{r}} + i b_{\downarrow,\mathbf{r}}) + \text{H.c.}, \\
H_{\mathbf{rz}} &= -i a^\dagger_{\uparrow,\mathbf{r}+\mathbf{z}} b_{\uparrow,\mathbf{r}} - i a^\dagger_{\downarrow,\mathbf{r}-\mathbf{z}} b_{\downarrow,\mathbf{r}} + \text{H.c.}
\end{aligned}
$$

where $\mathbf{x}, \mathbf{y}, \mathbf{z}$ represents a unit vector along the x, y, z-direction of the cubic lattice, and $a_{\sigma,\mathbf{r}}$ ($b_{\sigma,\mathbf{r}}$) denotes the annihilation operator of the fermionic mode at the a (b) orbital and site $\mathbf{r}$ with the spin state σ. Basically, all terms in the Hamiltonian are some spin superpositions from one orbital hopping to another orbital. In the following, we take the fermionic species ^{6}Li, for instance, to illustrate the implementation scheme. Other fermionic atoms can also be used with suitable atomic levels. We make use of four internal states of the hyperfine ground state manifold to carry two pseudospins and two orbitals as depicted in Fig. 3.2.4(a). On top of the cubic optical lattice, a linear tilt is assumed along each direction to break the left-right symmetry as does the Hamiltonian [Fig. 3.2.4(b)]. This linear tilt can be accomplished with the natural gravitational field, the magnetic field gradient, or the gradient of a dc- or

ac-Stark shift [20,21,45,103]. The hopping between orbitals can be activated by two-photon Raman transitions. Here, we show how to get the first term in the Hamiltonian $H_{\mathbf{rx}}$, which is $-i/2(a^{\dagger}_{\uparrow,\mathbf{r}+\mathbf{x}}+a^{\dagger}_{\downarrow,\mathbf{r}+\mathbf{x}})\,(b_{\uparrow,\mathbf{r}}+b_{\downarrow,\mathbf{r}})$. Every other terms are of similar forms and can be likewise laser-induced. We may decompose it to four separate hoppings from b states at site $\mathbf{r}$ to a states at site $\mathbf{r}+\mathbf{x}$. As shown in Fig. 3.2.4(c), each of the hopping terms can be induced by a Raman pair:

$$(\Omega^{\pi}_{\uparrow},\Omega^{\pi})\rightarrow -\tfrac{i}{2}\,a^{\dagger}_{\uparrow,\mathbf{r}+\mathbf{x}}b_{\uparrow,\mathbf{r}},\ (\Omega^{\sigma^-},\Omega^{\pi})\rightarrow -\tfrac{i}{2}\,a^{\dagger}_{\downarrow,\mathbf{r}+\mathbf{x}}b_{\uparrow,\mathbf{r}}$$
$$(\Omega^{\sigma^+},\Omega^{\pi})\rightarrow -\tfrac{i}{2}\,a^{\dagger}_{\uparrow,\mathbf{r}+\mathbf{x}}b_{\downarrow,\mathbf{r}},\ (\Omega^{\pi}_{\downarrow},\Omega^{\pi})\ \rightarrow -\tfrac{i}{2}\,a^{\dagger}_{\downarrow,\mathbf{r}+\mathbf{x}}b_{\downarrow,\mathbf{r}}$$

The superscript on each Rabi frequency denotes the polarization of the respective beam. The relative phase and amplitude of the hoppings can be controlled by the laser beams. We have four free parameters here, $\Omega^{\pi}_{\uparrow},\Omega^{\sigma^-},\Omega^{\sigma^+},\Omega^{\pi}_{\downarrow}$, each of which can be adjusted individually to yield the required configuration. These degrees of freedom ensure all other terms in the Hamiltonian can be produced in a similar way. One important aspect we need to be careful is that no spurious terms will be generated with undesired laser coupling. This is guaranteed by energy matching and polarization selection rules. In the undressed atomic basis, all four internal states are at different energies (split by a magnetic field for example), so the four beams coupling b states to the excited states will not interfere with each other. In addition, the different detunings along each direction, $\Delta_{x,y,z}$, preempt the interference of beams that induce hoppings along different directions. There will be, however, some onsite spin-flipping terms induced by the laser beams, but those can be explicitly compensated by some r.f. fields.

The above scheme is hence able to engineer the Hamiltonian H_1 and is feasible with current

technologies. The actual experiment will be challenging since many laser beams are involved with careful detunings. Nonetheless, all these beams can be drawn from the same laser with small frequency shifts produced by an acoustic or electric optical modulator. The uniform orbital magnetic field required to observe the topological polarization can be imprinted from the phase of the laser beams as an artificial gauge field [20, 21, 45, 103]. Lastly, the gap opening term in Eq. (3.2.9) can be created by extra laser beams focused on the surfaces, producing an effective Zeeman splitting. Other gap opening mechanisms on the surface should also work since the magneto-electric polarization is a bulk effect. The accumulated charge will be detectable from atomic density measurements [47, 130–132]. Note that the density measurements do not need to be restricted to the surfaces, as a measurement for half of the sample produces good results, as shown in Fig. 3.2.3. One half of the sample can be removed to another state by shining a laser beam. The density on the other half of the sample can in turn be measured by time-of-flight imaging [47]. As we have demonstrated in the previous section, the charge quantization is very robust to perturbations, so any weak perturbations introduced to the Hamiltonian, even those breaking the chiral symmetry in the bulk, should not alter detection results.

3.2.6 Conclusions

In summary, we study the $\mathbb{Z}$ character of chiral topological insulators by simulating the quantized magneto-electric effect of a nontrivial phase. We show that the $\mathbb{Z}$ character, not only the $\mathbb{Z}_2$ part, can be observed through magneto-electric polarization by properly gapping the system. An experimental scheme is also proposed for implementation and detection with cold atoms. This demonstrates explicitly how the topological invariant appears in physical observables for chiral TIs and will be important for experimental characterization.

3.3 Direct Measurement of Topological Invariants in Cold Atoms

3.3.1 Introduction

Cold-atom experiments in optical lattices offer a versatile platform to realize various topological quantum phases. A key challenge in those experiments is to unambiguously probe the topological order. In this section, we propose a method to directly measure the characteristic topological invariants (order) based on the time-of-flight imaging of cold atoms. The method is generally applicable to detection of topological band insulators in one, two, or three dimensions characterized by integer topological invariants. Using detection of the Chern number for the 2D anomalous quantum Hall states and the Chern-Simons term for the 3D chiral topological insulators as examples, we show that the proposed detection method is practical, robust to typical experimental imperfections such as limited imaging resolution, inhomogeneous trapping potential, and disorder in the system.

The study of topological phases of matter, such as topological band insulators and superconductors, has attracted a lot of interest in recent years [4–6]. Various topological phases have been found associated with the free-fermion band theory and classified into a periodic table according to the system symmetry and dimensionality [9, 10, 68]. The topology of the band structure is characterized by a topological invariant taking only integer values, which gives the most direct and unambiguous signal of the corresponding topological order. To experimentally probe the topological order, it is desirable to have a way to measure the underlying topological invariant. For some phase, the topological invariant may manifest itself through certain quantized transport property or characteristic edge state behavior [122]. For

instance, the quantized Hall conductivity is proportional to the underlying topological Chern number that characterizes the integer quantum Hall states [122, 133, 134]. For many other topological phases in the periodic table, it is not clear yet how to experimentally extract information of the underlying topological invariants.

Cold atoms in optical lattices provide a powerful experimental platform to simulate various quantum states of matter. In particular, recent experimental advance in engineering of spin-orbit coupling and artificial gauge field for cold atoms [74, 117, 135–138] has pushed this system to the forefront for realization of various topological quantum phases [15, 20, 21, 76, 139–141]. The detection method for cold-atom experiments is usually quite different from those for conventional solid-state materials. A number of intriguing proposals have been made for detection of certain topological order in cold-atom experiments, such as those based on the dynamic response [142–145], the Bragg spectroscopy [146, 147], imaging of the edge states [148], counting peaks in the momentum distribution [149] or detection of the Berry phase or curvature [93, 144, 150–155]. Most of these proposals are targeted to detection of the quantum Hall phase. Similar to solid-state systems, it is not clear yet how to probe the topological invariants for various other topological phases in the periodic table.

In this section, we propose a general method to directly measure the topological invariants in cold-atom experiments based on the state-of-the-art time-of-flight (TOF) imaging. The TOF imaging, combined with the quench dynamics from the Hamiltonian, has been exploited in recent schemes for detection of the Chern numbers associated with two-band topological models in one or two dimensional optical lattices [144]. Compared with the previous work, our method has the following distinctive features: 1) it is applicable to detection of any topological band insulators with spin degrees of freedom in one, two, or three dimensions that are characterized by integer topological invariants in the periodic table. 2) The method

is not limited by the requirement of a two-band structure for the Hamiltonian [144, 150] or occupation of only the lowest band [152]. Instead, it detects the topological invariants associated with each band for any multi-band Hamiltonians. 3) Our proposed detection method is very robust to practical experimental imperfections. As examples, we numerically simulate two experimental detections: one for the Chern number of the 2D anomalous quantum Hall phase and the other for the Chern-Simons term of the 3D chiral topological insulator. Both simulations show that accurate values of the topological invariants can be obtained experimentally under imaging resolution of a few to a dozen pixels along each spatial dimension, even with inhomogeneous traps and random potentials or interactions. The robustness is also found in Ref. [144] for detection of the Chern number in a different 2D model using the tomography method.

3.3.2 Measurement Scheme

The topological band insulators are described by effective free-fermion Hamiltonians, typically with complicated spin-orbit couplings. We consider a real-space Hamiltonian with N spin (pseudo-spin) degrees of freedom, referred as $|m\rangle$ with $m = 1, 2, ..., N$. In the momentum $\mathbf{k}$ space, the Hamiltonian has N bands and is described by an N-by-N Hermitian matrix $H(\mathbf{k})$. The energy spectrum is obtained by solving the Schröinger equation in the momentum space

$$H(\mathbf{k})|u_b(\mathbf{k})\rangle = E_b(\mathbf{k})|u_b(\mathbf{k})\rangle, \tag{3.3.1}$$

where $b = 1, 2, \cdots, N$ is the band index and $|u_b(\mathbf{k})\rangle$ denotes the corresponding Bloch state with eigen-energy $E_b(\mathbf{k})$. For simplicity, we assume the bands are non-degenerate. Expressed

in the original spin basis $|m\rangle$, the Bloch state has the form

$$|u_b(\mathbf{k})\rangle = \sum_{m=1}^{N} c_{bm}(\mathbf{k})|m\rangle, \tag{3.3.2}$$

where $c_{bm}(\mathbf{k})$ is the Bloch wavefunction with normalization $\sum_m |c_{bm}(\mathbf{k})|^2 = 1$.

An topological invariant can be defined for each band, which usually takes the form of the Chern numbers for even spatial dimensions and the Chern-Simons terms (or the winding numbers in certain cases) for odd spatial dimensions. The Chern numbers (or Chern-Simons terms) can be expressed as momentum-space integrals of the Berry curvature and connection associated with the Bloch state $|u_b(\mathbf{k})\rangle$. For instance, in 2D (x, y-plane), the Chern number C_b for the band b is defined by

$$C_b = -\frac{1}{2\pi}\int_{\mathrm{BZ}} dk_x dk_y F_{xy}^{(b)}(\mathbf{k}), \tag{3.3.3}$$

where the Berry curvature $F_{xy}^{(b)}(\mathbf{k}) \equiv \partial_{k_x} A_y^{(b)}(\mathbf{k}) - \partial_{k_y} A_x^{(b)}(\mathbf{k})$ and the Berry connection $A_\mu^{(b)}(\mathbf{k}) \equiv \langle u_b(\mathbf{k})|i\partial_{k_\mu}|u_b(\mathbf{k})\rangle$ ($\mu = x, y$), and the integration is over the whole Brillouin zone (BZ) which forms a compact manifold.

To probe the topological invariant such as the Chern number in Eq. (3), what we need to measure is the Bloch wave function $c_{bm}(\mathbf{k})$. The Berry connection and curvature can be obtained as derivatives of $c_{bm}(\mathbf{k})$ and the Chern number is just a two-fold integration of $F_{xy}^{(b)}(\mathbf{k})$. For cold atoms in an optical lattice, we can map out the momentum distribution with the conventional time-of-flight imaging and separate different spin components through a magnetic field gradient [156]. Through the band mapping technique employed in experiments [76], populations in different bands are mapped to atomic densities in different spatial

regions, so by this measurement we can get information about $n_{bm}(\mathbf{k}) = |c_{bm}(\mathbf{k})|^2$ for all occupied bands. To extract the wavefunction $c_{bm}(\mathbf{k})$, it is also crucial to measure the phase information. For this purpose, we apply an impulsive pulse right before the flight of atoms to induce a rotation between different spin components [157]. The rotation should keep the atomic momentum unchanged but mix their spins. For instance, a $\pi/2$-rotation between spin components m and m' induces the transition $c_{bm}(\mathbf{k}) \to [c_{bm}(\mathbf{k}) + c_{bm'}(\mathbf{k})]/\sqrt{2}$ and $c_{bm'}(\mathbf{k}) \to [-c_{bm}(\mathbf{k}) + c_{bm'}(\mathbf{k})]/\sqrt{2}$, which can be achieved by applying two co-propagating Raman beams or a radio frequency pulse that couples the spin components m, m' and preserves the momentum $\mathbf{k}$. The pulse is short so that expansion of the atomic cloud is negligible during the pulse. With this prior $\pi/2$-pulse, the time-of-flight (TOF) imaging then measures the densities $|c_{bm}(\mathbf{k}) \pm c_{bm'}(\mathbf{k})|^2/2$, whose difference gives the interference terms $\mathtt{Re}\,[c^*_{bm}(\mathbf{k})c_{bm'}(\mathbf{k})]$. By the same method but with a different phase of the $\pi/2$-pulse, one can similarly measure the imaginary part $\mathtt{Im}\,[c^*_{bm}(\mathbf{k})c_{bm'}(\mathbf{k})]$ between any two spin components m and m'. The measurement of the population and interference terms $c^*_{bm}(\mathbf{k})c_{bm'}(\mathbf{k})$ for all m, m' fully determines the Bloch wave function $c_{bm}(\mathbf{k})$ up to arbitrariness of an overall phase $c_{bm}(\mathbf{k}) \to c_{bm}(\mathbf{k})e^{i\varphi(\mathbf{k})}$, where $\varphi(\mathbf{k})$ in general is $\mathbf{k}$-dependent but independent of the spin index.

In experiments, one needs to discretize the TOF image and measure the density distribution at each pixel of the BZ. The wavefunction $c_{bm}(\mathbf{k})$ is fixed up to an overall phase $\varphi(\mathbf{k})$ at each pixel with the above method. This arbitrary $\mathbf{k}$-dependent phase poses an obstacle to measurement of the topological invariants. To overcome this difficulty, we use a different way to calculate the Berry curvature based on the so-called $U(1)$-link defined for each pixel $\mathbf{k_J}$ of the discrete BZ [158]. The $U(1)$-link is defined as $U^{(b)}_\nu(\mathbf{k_J}) \equiv \langle u_b(\mathbf{k_J})|u_b(\mathbf{k_{J+\hat{\nu}}})\rangle/|\langle u_b(\mathbf{k_J})|u_b(\mathbf{k_{J+\hat{\nu}}})\rangle|$, where $\hat{\nu} = \hat{x}, \hat{y}, \hat{z}$, a unit vector in the corresponding

direction. A gauge-independent field is obtained from the $U(1)$-link as [158]

$$\mathcal{F}_{\mu\nu}^{(b)}(\mathbf{k_J}) \equiv i \ln \frac{U_\mu^{(b)}(\mathbf{k_J}) U_\nu^{(b)}(\mathbf{k_{J+\hat{\mu}}})}{U_\mu^{(b)}(\mathbf{k_{J+\hat{\nu}}}) U_\nu^{(b)}(\mathbf{k_J})}, \tag{3.3.4}$$

where $\mathcal{F}_{\mu\nu}^{(b)}(\mathbf{k_J}) \in (-\pi, \pi]$ corresponds to a discrete version of the Berry curvature and it reduces to the latter in the large size limit. $\mathcal{F}_{\mu\nu}^{(b)}(\mathbf{k_J})$ can be obtained directly from the TOF images associated with the pixel $\mathbf{k_J}$ of the BZ, independent of the overall phase factor $\varphi(\mathbf{k})$. The topological invariant can be calculated from $\mathcal{F}_{\mu\nu}^{(b)}(\mathbf{k_J})$ by a direct summation over all the pixels of the BZ (instead of $\mathbf{k}$ integration in Eq. (3)). This gives a simple and robust way to experimentally extract the topological invariant from the TOF images.

The detection method described above is general and applicable to various topological phases in different spatial dimensions. To show that the method is robust to experimental imperfections, in the following we numerically simulate detection of two kinds of topological invariants: one is the Chern number associated with the 2D quantum anomalous Hall effect and the other is the Chern-Simons term associated with the 3D chiral topological insulator.

3.3.3 Example: 2D Quantum Anomalous Hall (QAH) Effect

The conventional quantum Hall effect requires application of a strong magnetic field. For the QAH effect, a combination of spontaneous magnetization and spin-orbit coupling gives rise to quantized Hall conductivity in the absence of an external magnetic field [159]. In solid-state systems, a recent experiment has observed this peculiar phenomenon in thin films of a magnetically doped topological insulator [128]. A simple square-lattice Hamiltonian

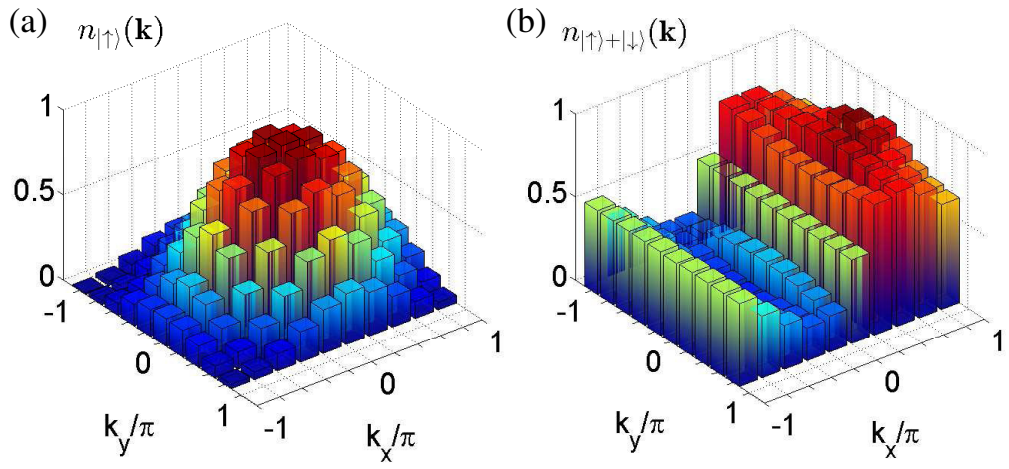

Figure 3.3.1: Density distributions in momentum space for the first band of $H_{\rm QAH}$ under two different spin bases with lattice size 10×10 and open boundary condition. The total density at each $\mathbf{k}$ is normalized to unity (e.g., $n_{|\uparrow\rangle}(\mathbf{k}) + n_{|\downarrow\rangle}(\mathbf{k}) = 1$) corresponding to the unit filling. The parameters are chosen to be $\lambda_{\rm SO}^{(x)} = \lambda_{\rm SO}^{(y)} = h = t$, $\gamma_T = 0.01t$, and $\gamma_P = 0.1t$.

which captures the essential physics of the QAH effect has the following form in real space:

$$
\begin{aligned}
H_{\rm QAH} = {} & \lambda_{\rm SO}^{(x)} \sum_{\mathbf{r}} [(a_{\mathbf{r}\uparrow}^\dagger a_{\mathbf{r}+\hat{x}\downarrow} - a_{\mathbf{r}\uparrow}^\dagger a_{\mathbf{r}-\hat{x}\downarrow}) + \text{H.c.}] \\
& + i\lambda_{\rm SO}^{(y)} \sum_{\mathbf{r}} [(a_{\mathbf{r}\uparrow}^\dagger a_{\mathbf{r}+\hat{y}\downarrow} - a_{\mathbf{r}\uparrow}^\dagger a_{\mathbf{r}-\hat{y}\downarrow}) + \text{H.c.}] \\
& - t \sum_{\langle \mathbf{r},\mathbf{s} \rangle} (a_{\mathbf{r}\uparrow}^\dagger a_{\mathbf{s}\uparrow} - a_{\mathbf{r}\downarrow}^\dagger a_{\mathbf{s}\downarrow}) + h \sum_{\mathbf{r}} (a_{\mathbf{r}\uparrow}^\dagger a_{\mathbf{r}\uparrow} - a_{\mathbf{r}\downarrow}^\dagger a_{\mathbf{r}\downarrow}),
\end{aligned}
\tag{3.3.5}
$$

where $a_{\mathbf{r}\sigma}^\dagger (a_{\mathbf{r}\sigma})$ is the creation (annihilation) operator of the fermionic atom with pseudospin $\sigma = (\uparrow, \downarrow)$ at site $\mathbf{r}$, and $\hat{x}, \hat{y}$ are unit lattice vectors along the x, y directions. The first term in the Hamiltonian describes the spin-orbit coupling. The second and the third terms denote respectively the spin-conserved nearest-neighbor hopping and the Zeeman interaction. It was proposed recently that $H_{\rm QAH}$ may be realized with cold fermionic atoms trapped in a blue-detuned optical lattice [160].

In momentum space, this Hamiltonian has two Bloch bands. The topological structure of this model is characterized by the Chern number defined in Eq. (3). Direct calculation shows that $C_2 = -C_1 = \text{sign}(h)$ when $0 < |h| < 4t$ and $C_2 = -C_1 = 0$ otherwise. Experimentally, one can measure $\mathcal{F}^{(b)}_{\mu\nu}(\mathbf{k_J})$ by our proposed method to extract the Chern number through $C_b \approx -\sum_{\mathbf{J}} \mathcal{F}^{(b)}_{xy}(\mathbf{k_J})/(2\pi)$, where the band index $b = 1, 2$.

To simulate experiments, we consider a finite-size lattice with open boundary condition. In addition, we add a global harmonic trap of the form $V_T = m_a\omega^2 r^2/2$ for atoms of mass m_a as in real experiments and use $\gamma_T = m_a\omega^2 a^2/2t$ to parameterize the relative strength of the trap, where a denotes the lattice constant. To account for possible experimental noise, we add a random perturbation Hamiltonian of the following general form

$$H_{\text{P}} = \gamma_{\text{P}} t \sum_{\langle \mathbf{r},\mathbf{s}\rangle,\alpha,\beta} a^{\dagger}_{\mathbf{r},\alpha} \mathcal{P}_{\mathbf{r}\alpha,\mathbf{s}\beta} a_{\mathbf{s},\beta}, \tag{3.3.6}$$

where γ_{P} is a dimensionless parameter characterizing the strength of random perturbation, $\langle \mathbf{r}, \mathbf{s}\rangle$ denotes the neighboring sites, and $\mathcal{P}$ is a random Hermitian matrix with its largest eigenvalue normalized to unity. We numerically diagonalize the real-space Hamiltonian on a finite lattice with different number of sites and calculate the corresponding momentum density distributions (see Appendix). An an example, in Fig. 3.3.1, we show the reconstructed density distribution in two complementary bases ($\{|\uparrow\rangle, |\downarrow\rangle\}$, $\{|\uparrow\rangle \pm |\downarrow\rangle\}$) under open boundary condition with a harmonic trap and random perturbations (more detailed calculation results are shown in the Appendix). The Chern numbers for each case are calculated and listed in Table 3.1 under choices of different parameters and system sizes. The extracted Chern numbers exactly equal the corresponding theoretical values, even under a small system size and significant disorder potentials. This is so as Chern numbers characterize the

	h(m)	Size	Periodic	Open	Trap	Pert.+Trap
QAH	1	4^2	-1	-1	-1	-1
	1	10^2	-1	-1	-1	-1
	5	10^2	0	0	0	0
CTI	2	10^3	1.041	1.056	1.055	1.080
	2	12^3	1.031	1.009	0.981	1.014
	4	10^3	0	$-2 * 10^{-4}$	$1.1 * 10^{-3}$	$1.2 * 10^{-3}$

Table 3.1: Simulated experimental results of the topological invariants for different lattice sizes under various realistic conditions. For QAH, the invariant is the Chern number for the first band (C_1), whereas for CTI, it is the Chern-Simons term for the middle flat band (CS_2/π). Results for both the nontrivial phase ($h = 1$ for QAH and $m = 2$ for CTI) and the trivial phase ($h = 5$ for QAH and $m = 4$ for CTI) are presented. All these invariants are extracted directly from the momentum density distribution images. The parameters are the same as in Fig. 3.3.1 and Fig. 3.3.2.

topological property, which does not change under perturbations. Furthermore, our detection method through measurement of $\mathcal{F}_{\mu\nu}^{(b)}(\mathbf{k_J})$ guarantees an integer value for the extracted Chern number [158], so it automatically corrects small errors due to experimental imperfections. Ref. [144] also points out the robustness of Fukui *et al.*'s method [158] in computing the Chern number.

3.3.4 Example: 3D Chiral Topological Insulator

Chiral topological insulators (CTIs) are protected by the chiral symmetry (also known as the sub-lattice symmetry) and belong to the AIII class in the periodic table for topological

phases [9, 10, 68]. A simple Hamiltonian that supports 3D CTIs has the form [73]:

$$\begin{aligned} H_{\mathrm{CTI}} &= \frac{t}{2}\sum_{\mathbf{r}}\sum_{j=1}^{3}[\psi_{\mathbf{r}}^{\dagger}(iG_{3+j}-G_7)\psi_{\mathbf{r}+\mathbf{e}_j}+\mathrm{H.c.}] \\ &\quad +h\sum_{\mathbf{r}}\psi_{\mathbf{r}}^{\dagger}G_7\psi_{\mathbf{r}}, \end{aligned} \tag{3.3.7}$$

where the operator $\psi_{\mathbf{r}}^{\dagger}=(a_{\mathbf{r},1}^{\dagger},a_{\mathbf{r},2}^{\dagger},a_{\mathbf{r},3}^{\dagger})$ with $a_{\mathbf{r},\alpha}^{\dagger}(\alpha=1,2,3)$ creating a fermion at site $\mathbf{r}$ with spin state α, $\mathbf{e}_1,\mathbf{e}_2,\mathbf{e}_3$ are unit vectors along the x,y,z directions, and G_ν ($\nu=4,5,6,7$) denotes the νth Gell-Mann matrix (see Appendix). In the momentum space, this model Hamiltonian has three gapped bands, with a zero-energy flat band in the middle protected by the chiral symmetry. An experimental scheme has been proposed to realize this model Hamiltonian with cold fermionic atoms in an optical lattice [45]. The topological property of this Hamiltonian can be described by the Chern-Simons term. For the b-th ($b=1,2,3$) Bloch band, the Chern-Simons term CS_b takes the form

$$CS_b=-\frac{1}{4\pi}\int_{\mathrm{BZ}}d\mathbf{k}\epsilon^{\mu\nu\tau}A_{\mu}^{(b)}(\mathbf{k})\partial_{k_\nu}A_{\tau}^{(b)}(\mathbf{k}), \tag{3.3.8}$$

where $A_{\mu}^{(b)}(\mathbf{k})=\langle u_b(\mathbf{k})|\partial_{k_\mu}|u_b(\mathbf{k})\rangle$ ($\mu=x,y,z$). Explicit calculations show that $CS_3=CS_1=CS_2/4=\pi\Gamma(h)/4$ with $\Gamma(h)=-2$ for $|h|<t$, $\Gamma(h)=1$ for $t<|h|<3t$, and $\Gamma(h)=0$ otherwise.

As an example application of our general detection method, here we show how to measure the topological invariant CS_b through the TOF imaging. As shown in Fig. 3.3.2(a), we first use the TOF imaging to reconstruct the 3D atomic momentum distribution. After expansion of the atomic cloud, we apply a pair of co-propagating Raman beams focused in the z-axis to transfer a layer of atoms with a fixed z-coordinate z_i to another hyperfine or Zeeman

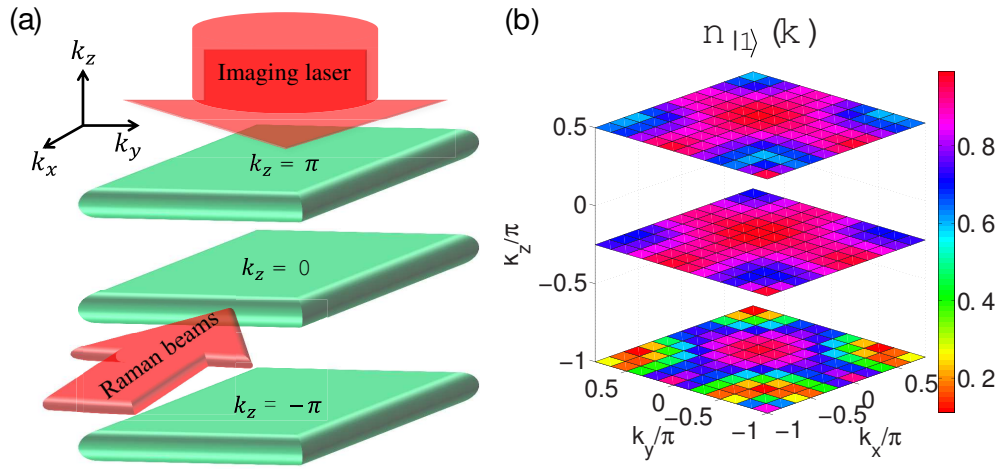

Figure 3.3.2: 3D atomic momentum distribution. (a) An illustration to show reconstruction of the 3D atomic momentum distribution by the TOF imaging. (b) Momentum distribution in one particular spin basis (other results are shown in the Appendix) for the middle flat band of H_{CTI} with open boundary condition under lattice size $12 \times 12 \times 12$. Layers corresponding to $k_z = -\pi, -\pi/4, \pi/2$ are displayed. The parameters are $h = 2t$, $\gamma_T = 0.001t$, $\gamma_P = 0.1t$.

level denoted as $|r\rangle$. We apply the imaging laser to couple the atoms only on the $|r\rangle$ level, so the imaging reads out the 2D momentum distribution $n(k_x, k_y, k_{z_i})$ with a fixed $k_{z_i} \propto z_i$. We repeat this measurement by scanning the coordinate z_i so that each image gives a 2D distribution $n(k_x, k_y, k_{z_i})$ with a different k_{z_i}. By this method, we reconstruct the 3D momentum distribution $n(k_x, k_y, k_z)$, where l images give l pixels of k_z.

To extract the Chern-Simons term CS_b, we measure the 3D momentum distribution $n_{bm}(k_x, k_y, k_z)$ in different spin bases to obtain the Bloch wave function $c_{bm}(\mathbf{k})$. We then use the measured $c_{bm}(\mathbf{k})$ to calculate the gauge independent field $\mathcal{F}^{(b)}_{\mu\nu}(\mathbf{k_J})$ defined in Eq. (4). By solving a discrete version of the equation $\nabla \times \mathbf{A} = \mathbf{F}$ in the momentum space with the Coulomb gauge $\nabla \cdot \mathbf{A} = 0$, we obtain the Berry connection $A^{(b)}_{\mu}(\mathbf{k_J})$ from $\mathcal{F}^{(b)}_{\mu\nu}(\mathbf{k_J})$. With $A^{(b)}_{\mu}$, we extract the Chern-Simons term CS_b using Eq. (8).

The Chern-Simons terms extracted from our numerically simulated experiments are shown

in Table 3.1 under various conditions. Different from the Chern number case, extraction of the Chern-Simons term using Eq. (8) does not guarantee the result to be an integer, so the calculated values are subject to influence of numerical inaccuracies and experimental noise. Nevertheless, from the results listed in Table 3.1, we see that the extracted values quickly approach the corresponding theoretical limits when we take a dozen of pixels along each spatial dimension in the time-of-flight imaging and the detection method remains robust to experimental imperfections (traps and random perturbation Hamiltonians change the result by less than 3%).

In summary, we have proposed a general method to experimentally measure the topological invariants for ultracold atoms. The method is shown to be robust to various experimental imperfections through numerically simulated experiments.

3.4 Weyl Exception Rings in Dissipative Cold Atomic Systems

3.4.1 Introduction

Three-dimensional topological Weyl semimetals can generally support a zero-dimensional Weyl point characterized by a quantized Chern number or a one-dimensional Weyl nodal ring (or line) characterized by a quantized Berry phase in the momentum space. Here, in a dissipative system with particle gain and loss, we discover a new type of Weyl ring, dubbed Weyl exceptional ring consisting of exceptional points at which two eigenstates coalesce. Such a Weyl exceptional ring is characterized by both a quantized Chern number and a quantized Berry phase, which are defined via the Riemann surface. We propose an experimental scheme

to realize and measure the Weyl exceptional ring in a dissipative cold atomic gas trapped in an optical lattice.

Recently, condensed matter systems have proven to be a powerful platform to study low energy gapless particles by using momentum space band structures to mimic the energy-momentum relation of relativistic particles [161, 162] and beyond [163–166]. One celebrated example in three dimensions is the zero-dimensional Weyl point [167–177] described by the Weyl Hamiltonian, which has been long sought-after in particle physics but only experimentally observed in condensed matter materials [178–180]. Such a Weyl point can be viewed as a magnetic monopole [181] in the momentum space and possesses a quantized Chern number on a surface enclosing the point. Another example is the one-dimensional Weyl nodal ring [163, 182–184], which has no counterpart in particle physics. It can be regarded as the generalization of zero-dimensional Dirac cones in two-dimensional systems, such as in graphene, to three-dimensional systems. Such a nodal ring has a quantized Berry phase over a closed path encircling it but does not possess a nonzero quantized Chern number. This leads to a natural question of whether there exists a ring exhibiting both a quantized Chern number and a quantized Berry phase in the momentum space.

So far, studies on those gapless states focus on closed and lossless systems. However, particle gain and loss are generally present in natural systems. Such systems can often be described by non-Hermitian Hamiltonians [185–188], which are widely applied to many different systems [175, 189–198]. Due to the non-Hermiticity, eigenvalues of the Hamiltonian are generically complex unless the $\mathcal{PT}$ symmetry [199] is conserved and the imaginary part of energy is associated with either decay or growth. Another intriguing feature of a non-Hermitian system is the existence of exceptional points (EPs) [185–188] at which two eigenstates coalesce and the Hamiltonian becomes defective, leading to many novel phenomena, such as

loss-induced transparency [189], single-mode lasers [196,197], and reversed pump dependence of lasers [195].

In this section, we investigate a system of Weyl points in the presence of a spin-dependent non-Hermitian term and find a Weyl exceptional ring composed of EPs. In stark contrast to a Weyl nodal ring [163,183,184], which does not have a nonzero Chern number, remarkably, this ring exhibits a nonzero quantized Chern number as long as the integral of the Berry curvature is evaluated over a surface (labeled by $\mathcal{S}$) that encloses the whole ring. Since energy is multi-valued in the complex parameter space due to its square root form, a state on the surface $\mathcal{S}$ may be defined over the Riemann surface, on which a function is single valued. On the other hand, the Chern number is zero when the surface $\mathcal{S}$ does not enclose any part of the ring even when it is located inside it. Besides the Chern number, such a Weyl exceptional ring has a quantized Berry phase over a trajectory encircling the ring twice, instead of once in the case of the Weyl nodal ring. Furthermore, we propose a feasible scheme to engineer and probe the Weyl exceptional ring in a dissipative ultracold atomic gas. In such a system, we find that the Fermi arc can still exist but is suppressed, even though the Weyl point transforms into a ring.

3.4.2 Toy Model of Weyl Exceptional Ring

Near a Weyl point in the momentum space, a system can be described by the Weyl Hamiltonian $H_W = \pm \sum_\nu v_\nu k_\nu \sigma_\nu$, where σ_ν represent Pauli matrices and $\pm$ the chirality. For clarity, we consider the positive chirality and choose $v_\nu = 1$ hereafter. In the presence of a non-Hermitian term $i\gamma\sigma_z$ ($\gamma > 0$) associated with particle gain for spin up atoms and loss

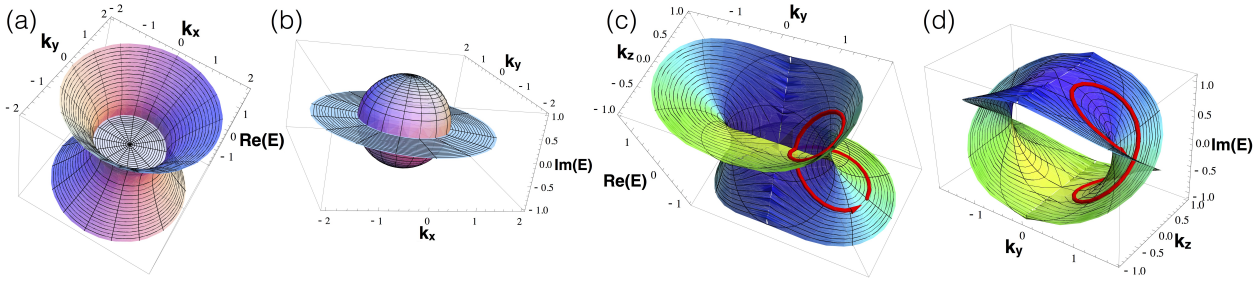

Figure 3.4.1: Energy spectra and the Riemann surface of the toy model in Eq. (3.4.1). Spectra with respect to k_x and k_y for $k_z = 0$ in (a) (real parts) and (b) (imaginary parts). Real (c) and imaginary parts (d) of the Riemann surface as a function of k_y and k_z for $k_x = 0$. In (c) and (d), the color represents the strength of θ mod 4π, and the red tube arrow shows a path from $\theta = 0$ to $\theta = 4\pi$.

for spin down ones, the Hamiltonian becomes

$$H(\mathbf{k}) = \sum_{\nu=x,y,z} k_\nu \sigma_\nu + i\gamma\sigma_z, \tag{3.4.1}$$

taking the energy unit to be 1. The eigenvalues are $E_\theta(\mathbf{k}) = \sqrt{k^2 - \gamma^2 + 2ik_z\gamma} = \sqrt{A(\mathbf{k})}e^{i\theta/2}$, where $A(\mathbf{k}) = \sqrt{(k^2-\gamma^2)^2 + 4k_z^2\gamma^2}$ with $k^2 = k_x^2 + k_y^2 + k_z^2$, and θ is defined via $\cos\theta = (k^2 - \gamma^2)/A(\mathbf{k})$ and $\sin\theta = 2k_z\gamma/A(\mathbf{k})$. Here, θ is used to label two branches, given that $e^{i\theta/2}$ gains a minus sign upon $\theta \to \theta + 2\pi$, corresponding to the other band. In the absence of γ, energy of both bands is real and two bands touch at $\mathbf{k} = 0$ with linear dispersion along all three momentum directions. In this case, θ takes only two nonequivalent discrete values: 0 and 2π (corresponding to two distinct and separate bands). When $\gamma > 0$, the eigenvalues become complex, and the single touching point morphs into a Weyl exceptional ring in the $k_z = 0$ plane characterized by $k_x^2 + k_y^2 = \gamma^2$. On this ring, both the real and imaginary parts of the eigenvalues vanish [shown in Fig. 3.4.1(a) and (b)] and two eigenstates coalesce into a single one (different from the case of degeneracy). Fig. 3.4.1(a) and (b) also illustrate that in the $k_z = 0$ plane energy is purely real outside the ring (with

conserved $\mathcal{PT}$ symmetry) and purely imaginary inside it for this simple model. Interestingly, θ takes continuous values from 0 to 4π (θ and $\theta + 4\pi$ are equivalent) and gains 2π when a state travels through the ring and returns, ending up at another state with opposite energy, arising from the role of branch points that the Weyl exceptional ring plays.

In complex analysis, besides using branch cuts, an alternative visual representation to depict a multi-valued function is the Riemann surface, a two-dimensional (2D) manifold that wraps around the complex plane infinite (noncompact) or finite (compact) number of times. Before we discuss the topology of the Weyl exceptional ring, let us first focus on the definition of a closed 2D surface $\mathcal{S}$ via the Riemann surface. In Fig. 3.4.1(c) and (d), we plot the Riemann surface of E_θ for $k_x = 0$ (the color represents the strength of θ mod 4π), showing that energy is single-valued on the surface, which connects the different bands. Given the single value property, we define each state on $\mathcal{S}$ to be living on the Riemann surface. For example, if we consider a state at $\mathbf{k}_0$ with θ_0, any other states on the surface $\mathcal{S}$ can be obtained by starting from this state and travelling on the momentum space surface $\mathcal{S}$ while keeping $E_\theta(\mathbf{k})$ on the Riemann surface.

With the proper definition of a closed 2D surface, we can characterize the topology of a Weyl exceptional ring by the Chern number on the surface based on two approaches: the integral of spin vector fields and the Berry curvature. For the former, the Chern number is given by [200]

$$N_3 = \frac{1}{4\pi} \oint_{\mathcal{S}} \mathbf{d}_\theta \cdot \left(\frac{\partial \mathbf{d}_\theta}{\partial u_1} \times \frac{\partial \mathbf{d}_\theta}{\partial u_2} \right) du_1 du_2, \tag{3.4.2}$$

which characterizes the number of times that the spin field $\mathbf{d}_\theta = \sum_{\nu=x,y,z} \langle \sigma_\nu \rangle \mathbf{e}_\nu$ wraps around a closed surface $\mathcal{S}$ parametrized by (u_1,u_2). Here, $\mathbf{e}_\nu$ denotes the unit vector along the ν direction and $\langle \sigma_\nu \rangle \equiv \langle u_\theta(\boldsymbol{k}) | \sigma_\nu | u_\theta(\boldsymbol{k}) \rangle$ with $|u_\theta(\boldsymbol{k})\rangle$ being the normalized right eigenstate of

$H(\mathbf{k})$ [i.e., $H(\mathbf{k})|u_\theta(\boldsymbol{k})\rangle = E_\theta(\mathbf{k})|u_\theta(\boldsymbol{k})\rangle$ and $\langle u_\theta(\boldsymbol{k})|u_\theta(\boldsymbol{k})\rangle = 1$]. Direct calculations show that $N_3 = \pm 1$ when the surface $\mathcal{S}$ encloses the whole ring as shown in Fig. 3.4.2(a), while $N_3 = 0$ when it does not enclose any part of the ring [shown in Fig. 3.4.2(b)].

Analogous to the scenario without decay [201], we may also define the first Chern number via the Berry curvature

$$C_2 = \frac{1}{2\pi} \oint_{\mathcal{S}} \boldsymbol{\Omega}_\theta(\boldsymbol{k}) \cdot d\boldsymbol{S}, \tag{3.4.3}$$

where $\boldsymbol{\Omega}_\theta(\boldsymbol{k}) = i\langle \nabla_{\boldsymbol{k}} u_\theta(\boldsymbol{k})| \times |\nabla_{\boldsymbol{k}} u_\theta(\boldsymbol{k})\rangle$ is the Berry curvature. Our calculations show that $C_2 = \pm 1$ when the surface $\mathcal{S}$ encloses the Weyl exceptional ring and $C_2 = 0$ otherwise, suggesting that the topological charge is entirely carried by the ring.

The physical meaning of the Berry curvature in this system can be understood from the following semiclassical equation under an external gradient force $\mathbf{F}$

$$\dot{\mathbf{r}}_c = \partial_{\mathbf{k}_c} \bar{E}(\mathbf{k}_c) - \dot{\mathbf{k}}_c \times \boldsymbol{\Omega}_\theta(\boldsymbol{k}_c), \tag{3.4.4}$$

$$\hbar \dot{\mathbf{k}}_c = \mathbf{F}, \tag{3.4.5}$$

where $\bar{E}(\mathbf{k}_c) = \mathrm{Re}[E_\theta(\mathbf{k}_c)] + \bar{\mathbf{A}}_\theta(\mathbf{k}_c) \cdot \dot{\mathbf{k}}_c$, $\bar{\mathbf{A}}_\theta(\mathbf{k}_c) \equiv \mathrm{Re}[\mathbf{A}_\theta(\mathbf{k}_c) - \tilde{\mathbf{A}}_\theta(\mathbf{k}_c)]$ with the Berry connection being $\mathbf{A}_\theta(\mathbf{k}) = i\langle u_\theta(\mathbf{k})|\partial_{\mathbf{k}} u_\theta(\mathbf{k})\rangle$ and $\tilde{\mathbf{A}}_\theta(\mathbf{k}) = i\langle \tilde{u}_\theta(\mathbf{k})|\partial_{\mathbf{k}} u_\theta(\mathbf{k})\rangle$, where $\langle \tilde{u}_\theta(\boldsymbol{k})|$ is the normalized left eigenstate of H [i.e., $\langle \tilde{u}_\theta(\boldsymbol{k})|H(\mathbf{k}) = \langle \tilde{u}_\theta(\boldsymbol{k})|E_\theta(\mathbf{k})$ and $\langle \tilde{u}_\theta(\mathbf{k})|u_\theta(\mathbf{k})\rangle = 1$]; $\mathbf{r}_c$ and $\mathbf{k}_c$ are the center coordinate of a wave packet in the real space and momentum space, respectively. Clearly, the Berry curvature plays the same role as in the traditional semiclassical equation in a closed system [202]. However, in this open system, the equation includes a term that effectively modifies the energy spectra, resulting from the difference between left and right eigenstates, a feature in a non-Hermitian Hamiltonian. Without $\mathbf{F}$, the group velocity is dictated by the real part of the spectra, which implies that inside the

Weyl exceptional ring in the $k_z = 0$ plane, the group velocity vanishes.

Other than the Chern number on the surface, there also exists a quantized Berry phase characterizing the Weyl exceptional ring, defined as

$$C_1 = \oint_{2\mathcal{L}} i\langle \tilde{u}_\theta(\mathbf{k})|\partial_{\mathbf{k}} u_\theta(\mathbf{k})\rangle \cdot d\boldsymbol{k}, \tag{3.4.6}$$

where the path $2\mathcal{L}$ travels across the ring twice along the Riemann surface so that the state returns to the original one after the entire trajectory as shown in Fig. 3.4.1(c) and (d). Direct calculations yield $C_1 = \pm\pi$, consistent with the result for a single EP [185]. This Berry phase is different from that of a Weyl nodal ring in which the quantized Berry phase is obtained when the trajectory encircles the ring once [163, 183, 184].

3.4.3 Realization in Dissipative Cold Atomic Gases

To realize the Weyl exceptional ring in cold atoms, we consider the following model

$$\begin{aligned} H = \quad & \sum_{k_z,\mathbf{x}} \Big[(\bar{h}_z + i\gamma)\hat{c}^\dagger_{k_z,\mathbf{x}}\sigma_z\hat{c}_{k_z,\mathbf{x}} + \sum_{\nu=x,y}(-J\hat{c}^\dagger_{k_z,\mathbf{x}}\hat{c}_{k_z,\mathbf{x}+a\mathbf{e}_\nu} \\ & +(-1)^{j_x+j_y}J_{SO\nu}\hat{c}^\dagger_{k_z,\mathbf{x}}\sigma_\nu\hat{c}_{k_z,\mathbf{x}+a\mathbf{e}_\nu} + H.c.) + h_0 \Big], \end{aligned} \tag{3.4.7}$$

where $\mathbf{x} = j_x a\mathbf{e}_x + j_y a\mathbf{e}_y$ (with a being the lattice constant) labels the location of sites, $\hat{c}^\dagger_{k_z,\mathbf{x}} = (\ \hat{c}^\dagger_{k_z,\mathbf{x},\uparrow}\ \ \hat{c}^\dagger_{k_z,\mathbf{x},\downarrow}\ )$ with $\hat{c}^\dagger_{k_z,\mathbf{x},\sigma}$ ($\hat{c}_{k_z,\mathbf{x},\sigma}$) being the creation (annihilation) operator, J and $J_{SO\nu}$ ($J_{SOx} = -J_{SOy} = J_{SO}$) stand for the tunneling and spin-orbit coupling strength, $h_0 = [-i\gamma + \hbar^2 k_z^2/(2m)]\hat{c}^\dagger_{k_z,\mathbf{x}}\hat{c}_{k_z,\mathbf{x}}$, with γ denoting the decay strength, and $\bar{h}_z = \alpha k_z + h_z$ is the effective Zeeman field with $\alpha = \hbar^2 k_{Lz}/(2m)$ where k_{Lz} depends on the wave vector of Raman laser beams along the z direction, m is the mass of atoms, and h_z the Zeeman field

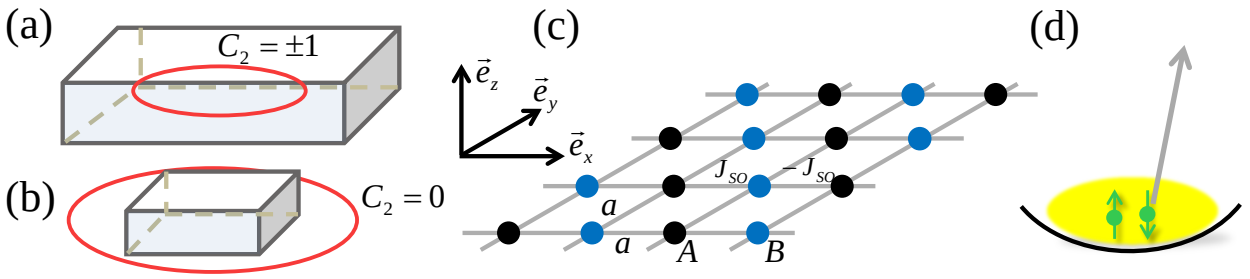

Figure 3.4.2: Schematics for the Weyl exceptional ring. (a) A surface enclosing a Weyl exceptional ring and (b) a surface located inside the ring. (c) Lattice structure in the (x, y) plane. (d) Schematic of trapped atoms being kicked out by a resonant optical beam (denoted by the grey arrow).

proportional to the two-photon detuning. Here, we consider the atoms to be trapped in an optical lattice in the x and y directions while there is no lattice along the z direction.

Without γ, this Hamiltonian, which has two Weyl points and a fourfold degenerate point, can be experimentally engineered by coupling two hyperfine states with two pairs of Raman laser beams in cold atom optical lattices [203]. To generate the decay term representing an atom loss $-2i\gamma$ for spin down atoms, one may consider using a resonant optical beam to kick the atoms in the $|\downarrow\rangle$ state out of a weak trap as shown in Fig. 3.4.2(d), which has been experimentally realized in ^{6}Li [194]. Alternatively, one may consider applying a radio frequency pulse to excite atoms in the $|\downarrow\rangle$ state to another irrelevant state $|3\rangle$, leading to an effective decay for spin down atoms when atoms in $|3\rangle$ experience a loss by applying an anti-trap.

To see the energy spectra, we write down the Hamiltonian in the momentum space,

$$H(\mathbf{k}) = (\bar{h}_z + i\gamma)\sigma_z - h_t\tau_x + \tau_y(-b_x\sigma_x + b_y\sigma_y), \tag{3.4.8}$$

in the basis $\Psi(\mathbf{k})^T$ with $\Psi(\mathbf{k}) = (\ e^{ik_x a}\hat{A}_{\mathbf{k}\uparrow}\ \ e^{ik_x a}\hat{A}_{\mathbf{k}\downarrow}\ \ \hat{B}_{\mathbf{k}\uparrow}\ \ \hat{B}_{\mathbf{k}\downarrow}\ )$, where $\hat{A}_{\mathbf{k}\sigma}$ ($\hat{B}_{\mathbf{k}\sigma}$) annihi-

lates a state with spin σ and momentum $\mathbf{k}$ located at A (B) site [A and B constitute a unit cell as shown in Fig. 3.4.2(c)]. Here, $h_t = 2J[\cos(k_x a)+\cos(k_y a)]$, $b_x = 2J_{SO}\sin(k_x a)$ and $b_y = -2J_{SO}\sin(k_y a)$; $\tau_{x,y}$ are Pauli matrices acting on A, B sublattices. This Hamiltonian can be transformed into a block diagonal matrix, i.e., $H \to H' = (\bar{h}_z+i\gamma)\sigma_z - h_t\sigma_z\tau_z+\tau_z(b_x\sigma_y+b_y\sigma_x)$, which commutes with τ_z. Note that we have neglected the spin-independent term h_0, which has no essential effects on the physics.

Similar to the toy model in Eq. (3.4.1), eigenvalues of this Hamiltonian are $E_{\theta_\pm}(\mathbf{k}) = \sqrt{b_\pm^2 - \gamma^2 + 2ib_{z\pm}\gamma} = \sqrt{A_\pm(\mathbf{k})}e^{i\theta_\pm/2}$, where $A_\pm(\mathbf{k}) = \sqrt{(b_\pm^2-\gamma^2)^2 + 4b_{z\pm}^2\gamma^2}$ with $b_\pm^2 = b_x^2 + b_y^2 + b_{z\pm}^2$ and $b_{z\pm} = \pm h_t + \bar{h}_z$ ($\pm$ label two particle or hole bands associated with the subspace $\tau_z = \mp$ for H'), and $\theta_\pm$ are defined by $\cos\theta_\pm = (b_\pm^2 - \gamma^2)/A_\pm(\mathbf{k})$ and $\sin\theta_\pm = 2b_{z\pm}\gamma/A_\pm(\mathbf{k})$. Without γ, energy is purely real, and Weyl points emerge at $\mathbf{k}_{W0} = (k_x a, k_y a, k_z a_z) = [\pi, 0, -2m\pi h_z/(\hbar^2 k_{Lz}^2)]$ or $\mathbf{k}_{W\pm} = [0, 0, -2m\pi(\pm 4J + h_z)/(\hbar^2 k_{Lz}^2)]$, where $a_z = \pi/k_{Lz}$. The touching point is fourfold (doubly) degenerate at $\mathbf{k}_{W0}$ ($\mathbf{k}_{W\pm}$). When $\gamma > 0$, the spectrum becomes complex and it is purely real only in the plane $b_{z\pm} = 0$. A touching point transforms into a closed line (i.e., Weyl exceptional ring) at which particle and hole bands coalesce when $b_{z\pm} = 0$ and $b_x^2 + b_y^2 = \gamma^2$, as shown in Fig. 3.4.3(a). Around $\mathbf{k}_{W0}$, the fourfold degeneracy of the touching point is broken, and there emerge two Weyl exceptional rings that are not degenerate except at four points with $|\sin k_x a_x| = \gamma/(2\sqrt{2}J_{SO})$, $k_x = \pm k_y - \pi$, and $k_z = -h_z/\alpha$ [as shown in Fig. 3.4.3(a)]. Around $\mathbf{k}_{W\pm}$, each Weyl point morphs into a single Weyl exceptional ring, which can be approximated by $k_x^2 + k_y^2 = \gamma^2/(4J_{SO}^2)$ and $k_z = [-h_z \pm J(4 - \gamma^2/(4J_{SO}^2))]/\alpha$ when $\gamma \ll 2J_{SO}$.

Analogous to the toy model, a Weyl exceptional ring in this realistic model can be characterized by the Chern number defined in Eq. (3.4.3), i.e., evaluated by an integral of the Berry curvature over a closed surface $\mathcal{S}$ via the Riemann surface. Around k_{W0}, there are two

Weyl exceptional rings associated with two branches $\theta_\pm$, and the Chern number is defined for each band with $C_{\theta_\pm} = 1$ ($C_{\theta_\pm+2\pi} = -1$) when $\mathcal{S}$ encloses one ring. Around $k_{W\pm}$, the corresponding band contributes $C_{\theta_\pm} = -1$ ($C_{\theta_\pm+2\pi} = 1$). Furthermore, apart from the Chern number, we can characterize the ring by a quantized Berry phase defined in Eq. (3.4.6), i.e., evaluated along a closed trajectory enclosing the Weyl exceptional ring twice for a considered band with a ring.

Another intriguing feature of Weyl semimetals is the existence of a Fermi arc, surface states that connect two Weyl points with opposite Chern numbers in a geometry with edges. When $\gamma > 0$, Weyl points develop into Weyl exceptional rings, and one may wonder on the existence of surface states with open boundaries. Here, we calculate the spectra of the open system under open boundaries along the x direction and plot the real, imaginary and absolute parts of the spectra in Fig. 3.4.3(b), (c), and (d), respectively. We neglected the spin-independent energy $\hbar^2 k_z^2/2m$ for clarity. Interestingly, zero energy states emerge for both real and imaginary parts of the spectra. Yet, the surface states (Fermi arc) are only associated with those of zero absolute energy, which connect the Weyl exceptional ring at the center ($\mathbf{k}_{W0}$) to those on two sides ($\mathbf{k}_{W\pm}$). These states are doubly degenerate eigenvectors (not generalized ones [204, 205]), one (the other) of which is localized on the left (right) surface. Compared to the surface states without γ, their range along k_z decreases with respect to γ because the size of the rings along the z direction grows with γ. Fig. 3.4.3(d) shows the shrinking surface states for $\gamma = 0$, $0.35J$, $0.7J$ and $0.86J$. As γ becomes sufficiently large, the rings around $(k_x a_x, k_y a_y) = (0, 0)$ overlap with those around $(\pi, 0)$ in the k_z direction and surface states completely disappear.

To measure the Weyl exceptional ring, a possible approach is to probe the dynamics of atom numbers of each spin component after a quench [194]. Initially, if we only keep the

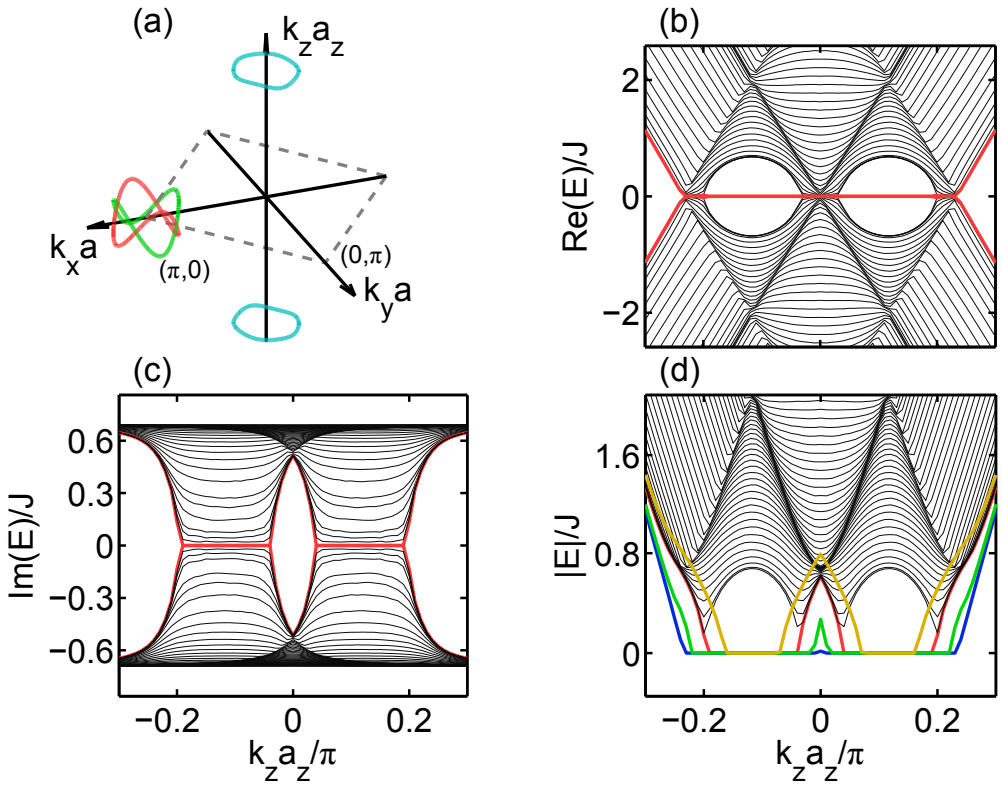

Figure 3.4.3: Surface states of Weyl exceptional rings. (a) Schematic of Weyl exceptional rings denoted by closed red, green and cyan lines for the system described by the Hamiltonian in Eq. (3.4.8). The dashed box depicts the first Brillouin zone. (b) Real (c) imaginary and (d) absolute values of the eigenenergy with respect to $k_z a_z$ for $k_y = 0$ and $\gamma = 0.7J$ when the open boundary condition is imposed along the x direction. The red lines are the surface states. In (d), additional surface states for $\gamma = 0, 0.35J, 0.86J$ are plotted as blue, green and yellow lines respectively. Note that only the parts with zero absolute energy are associated with surface states.

spin-independent optical lattices but switch off the spin-dependent ones (contributing to the spin-orbit coupling) and dissipation, we can load spin up atoms into the system and the ground state is $\Psi(\mathbf{k} = 0, t = 0) = (\ 1 \quad 0 \quad 1 \quad 0\ )/\sqrt{2}$ since the Hamiltonian reduces to $H = -h_t \tau_x$. This state can be driven to a state with $\mathbf{k} \neq 0$ by accelerating the optical lattices or by applying an external gradient force. After that, the spin-orbit coupling and dissipation can be suddenly turned on. So this state is no longer the eigenstate of the system

and the atom numbers will change with time. For example, if $\mathbf{k}$ lies in the $b_{z-}=0$ plane, the normalized atom number for spin down is given by

$$n_{\downarrow}=\frac{b_x^2+b_y^2}{4|E_\theta|^2}\Big[\sum_{\lambda=\pm}e^{\lambda 2\mathrm{Im}(E_\theta)t/\hbar}-2\cos\Big(\frac{2\mathrm{Re}(E_\theta)t}{\hbar}\Big)\Big], \tag{3.4.9}$$

where $n_{\downarrow}=N_{\downarrow}e^{\gamma t/\hbar}$ with $N_{\downarrow}$ being the atom number. Outside of the ring, $\mathrm{Im}(E_\theta)=0$ and $n_{\downarrow}=(b_x^2+b_y^2)\sin^2(E_\theta t/\hbar)/E_\theta^2$ with an oscillation period of $2\pi\hbar/E_\theta$ and inside the ring $\mathrm{Re}(E_\theta)=0$ and $n_{\downarrow}=(b_x^2+b_y^2)[\sum_{\lambda=\pm}e^{\lambda 2\mathrm{Im}(E_\theta)t/\hbar}-2]/(4|E_\theta|^2)$ with no oscillation. The existence of the Weyl exceptional ring will be manifested through the change in oscillation periods. In experiments, one may choose ^{87}Rb (bosons) atoms and apply blue-detuned laser beams at wavelength $\lambda=767\,\mathrm{nm}$ [19] to generate the optical lattices with Weyl points. With specific experimental settings, our model parameters are given by $J_{SO}=0.5J$ and $J=0.058E_R$, where the recoil energy is $E_R/\hbar=\hbar k_R^2/2m=2\pi\times 3.9\,\mathrm{kHz}$ with $k_R=2\pi/\lambda$ and λ being the wavelength of laser beams. The decay strength γ can be experimentally tuned by controlling the intensity of the resonant optical beam.

In summary, we have discovered a Weyl exceptional ring in a dissipative system of Weyl points with particle gain and loss. Such a ring is characterized by both a quantized Chern number and a quantized Berry phase, which are defined via the Riemann surface. We further propose an experimental scheme in cold atoms to realize the Weyl exceptional ring, which paves the way for future experimental investigation of such a ring and its unusual topological properties.

CHAPTER IV

Quantum Computation in a Planar Ion Crystal

4.1 Introduction

In this chapter, we propose a scheme to realize scalable quantum computation in a planar ion crystal confined by a Paul trap. We show that the inevitable in-plane micromotion affects the gate design via three separate effects: renormalization of the equilibrium positions, coupling to the transverse motional modes, and amplitude modulation in the addressing beam. We demonstrate that all of these effects can be taken into account and high-fidelity gates are possible in the presence of micromotion. This proposal opens the prospect to realize large-scale fault-tolerant quantum computation within a single Paul trap.

Scalable quantum computation constitutes one of the ultimate goals in modern physics [26, 27]. Towards that goal, trapped atomic ions are hailed as one of the most promising platforms for the eventual realization [206, 207]. The linear Paul trap with an one-dimensional (1D) ion crystal was among the first to perform quantum logic gates [49, 208, 209] and to generate entangled states [210–212], but in terms of scalability, the 1D geometry limits the number of ions that can be successfully trapped [213, 214]. Another shortcoming of the 1D architecture is that the error threshold for fault-tolerant quantum computation with short-range gates is

exceptionally low and very hard to be met experimentally [215–217].

Generic ion traps, on the other hand, could confine up to millions of ions with a 2D or 3D structure [218–220]. More crucially, large scale fault-tolerant quantum computation can be performed with a high error threshold, in the order of a percent level, with just nearest neighbor (NN) quantum gates [221–224]. This makes 2D or 3D ion crystals especially desirable for scalable quantum computation. Various 2D architectures have been proposed, including microtrap arrays [225], Penning traps [218, 226–228], and multizone trap arrays [229,230]. However, the ion separation distance in microtraps and penning traps is typically too large for fast quantum gates since the effective ion-qubit interaction scales down rapidly with the distance. In addition, fast rotation of the ion crystal in the Penning trap makes the individual addressing of qubits very demanding. Distinct from these challenges, Paul traps provide strong confinement; however, they are hampered by the micromotion problem: fast micromotion caused by the driving radio-frequency (rf) field cannot be laser cooled. It may thus create motion of large amplitudes well beyond the Lamb-Dicke regime [231,232], which becomes a serious impediment to high-fidelity quantum gates.

In this chapter, we propose a scheme for scalable quantum computation with a 2D ion crystal in a quadrupole Paul trap. We have shown recently that micromotion may not be an obstacle for design of high-fidelity gates for the two-ion case [233]. Here, we extend this idea and show that micromotion can be explicitly taken into account in the design of quantum gates in a large ion crystal. This hence clears the critical hurdle and put Paul traps as a viable architecture to realize scalable quantum computation. In such a trap, DC and AC electrode voltages can be adjusted so that a planar ion crystal is formed with a strong trapping potential in the axial direction. In-plane micromotion is significant, but essentially no transverse micromotion is excited due to negligible displacement from the axial

plane. We perform gates mediated by transverse motional modes and show that the in-plane micromotion influences the gate design through three separate ways: (1) It renormalizes the average positions of each ion compared to the static pseudopotential equilibrium positions. (2) It couples to and modifies the transverse motional modes. (3) It causes amplitude modulation in the addressing beam. In contrast to thermal motion, the fluctuation induced by micromotion is coherent and can be taken into account explicitly. Several other works also studied the effect of micromotion on equilibrium ion positions and motional modes [234–236], or used transverse modes in an oblate Paul trap to minimize the micromotion effect [237]. Here, by using multiple-segment laser pulses [238–240], we demonstrate that high-fidelity quantum gates can be achieved even in the presence of significant micromotion and even when many motional modes are excited. Our work therefore shows the feasibility of quadrupole Paul traps in performing large scale quantum computation, which may drive substantial experimental progress.

4.2 Quantum Computation under Micromotion in a Planar Ion Crystal

A generic quadrupole Paul trap can be formed by electrodes with a hyperbolic cross-section. The trap potential can be written as $\Phi(x,\, y,\, z) = \Phi_{\mathrm{DC}}(x,\, y,\, z) + \Phi_{\mathrm{AC}}(x,\, y,\, z)$, where

$$\Phi_{\mathrm{DC}}(x,\, y,\, z) = \frac{U_0}{d_0^2}\left[(1+\gamma)x^2 + (1-\gamma)y^2 - 2z^2\right], \tag{4.2.1}$$

$$\Phi_{\mathrm{AC}}(x,\, y,\, z) = \frac{V_0\cos(\Omega_T t)}{d_0^2}\left(x^2 + y^2 - 2z^2\right). \tag{4.2.2}$$

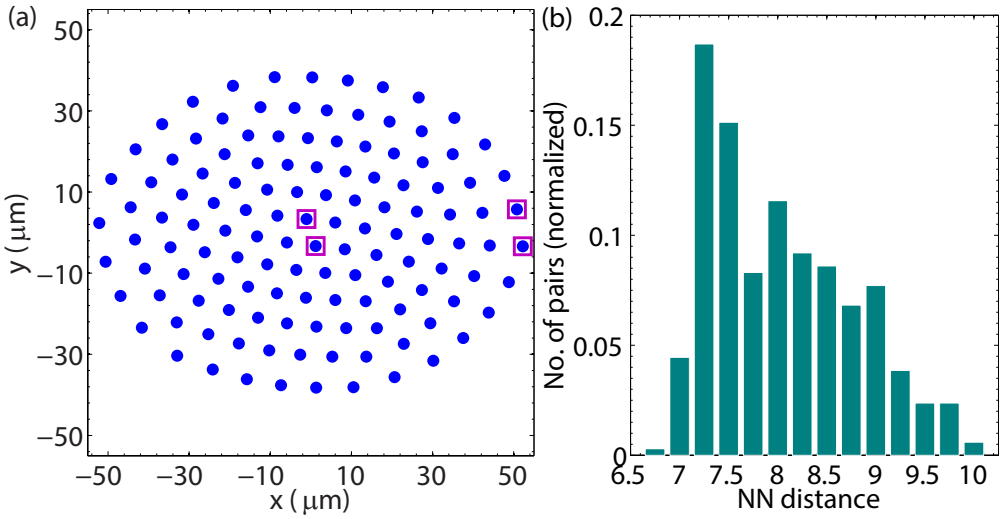

Figure 4.2.1: Crystal structure and distance distribution. (a) Average positions $\vec{r}^{(0)}$ of 127 ions in a planar crystal. Breathing oscillations about these average positions occur due to micromotion. Two pairs of ions (enclosed in squares), one pair in the center and one near the edge, are used for the demonstration of a quantum gate later. (b) The distribution of nearest neighbor (NN) distance. The minimum, maximum, and average NN distances are 6.9 μm, 10 μm and 8.0 μm respectively. Parameters used are: the number of ions $N = 127$; DC and AC potential $U_0 = -1.1\,\mathrm{V}$, $V_0 = 90\,\mathrm{V}$; AC rf frequency $\Omega_T/2\pi = 50\,\mathrm{MHz}$; the characteristic electrode size $d_0 = 200\,\mu\mathrm{m}$; ion mass $m = 171u$ (u is the atomic mass unit) corresponds to $^{171}\mathrm{Yb}^+$ ion; the anisotropy parameter $\gamma = 0.01$; corresponding Mathieu parameters are $a_x \approx -1.27 \times 10^{-3}, a_y \approx -1.25 \times 10^{-3}, a_z \approx 2.52 \times 10^{-3}, q \approx -0.051$, with respective secular trap frequencies $\omega_x/2\pi \approx 0.18\,\mathrm{MHz}$, $\omega_y/2\pi \approx 0.22\,\mathrm{MHz}$, $\omega_z/2\pi \approx 2.21\,\mathrm{MHz}$; $\omega_z/\omega_{x,y} > 10$ ensures a planar crystal is formed.

It contains both a DC and an AC part, with U_0 being the DC voltage, and V_0 being the AC voltage forming an electric field oscillating at the radiofrequency Ω_T. The parameter d_0 characterizes the size of the trap and γ controls the anisotropy of the potential in the x-y plane. We choose γ to deviate slightly from zero, so that the crystal cannot rotate freely in the plane, i.e. to remove the gapless rotational mode. The AC part, on the contrary, is chosen to be isotropic in the x-y plane. We let $U_0 < 0$ such that the trapping is enhanced along the z direction in order to form a 2D crystal in the x-y plane. Disregarding the Coulomb

potential first, the equations of motion of ions in such a trap can be written in the standard form of Mathieu equations along each direction:

$$\frac{d^2 r_\nu}{d\xi^2} + [a_\nu - 2q_\nu \cos(2\xi)]\, r_\nu = 0, \tag{4.2.3}$$

where $\nu \in \{x, y, z\}$, and the dimensionless parameters are $\xi = \Omega_T t/2$, $a_x = 8(1+\gamma)eU_0/md_0^2\Omega_T^2$, $a_y = 8(1-\gamma)eU_0/md_0^2\Omega_T^2$, $a_z = -16eU_0/md_0^2\Omega_T^2$, $q_x = q_y = q = -4eV_0/md_0^2\Omega_T^2$, $q_z = -2q$. Neglecting micromotion, one could approximate the potential as a time-independent harmonic pseudopotential with secular trapping frequencies $\omega_\nu = \beta_\nu \Omega_T/2$, with $\beta_\nu \approx \sqrt{a_\nu + q_\nu^2/2}$ being the characteristic exponents of the Mathieu equations [241, 242].

4.2.1 Dynamic Ion Positions

Adding Coulomb interactions back, the static equilibrium positions can be found by minimizing the total pseudopotential [227,243], or use molecular dynamics simulation with added dissipation, which imitates the cooling process in experiment [244,245]. In our numerical simulation, we start with $N = 127$ ions forming equilateral triangles in a 2D hexagonal structure. We then solve the equations of motion with a small frictional force to find the equilibrium positions $\vec{r}^{\,(0)} = \vec{r}(t \to \infty) = (x_1^{(0)}, y_1^{(0)}, \cdots, x_N^{(0)}, y_N^{(0)})$, which is the starting point for the expansion of the Coulomb potential. Micromotion is subsequently incorporated by solving the decoupled driven Mathieu equations (see Appendix). The average ion positions $\vec{r}^{\,(0)}$ are found self-consistently, which differ slightly from the pseudopotential equilibrium positions

(an average of $0.03\,\mu$m shift). Dynamic ion positions $\vec{r}(t)$ can be expanded successively as

$$\vec{r}(t) = \vec{r}^{(0)} + \vec{r}^{(1)}\cos(\Omega_T t) + \vec{r}^{(2)}\cos(2\Omega_T t) + \cdots . \tag{4.2.4}$$

Numerically, we found that $\vec{r}^{(1)} \approx -\frac{q}{2}\vec{r}^{(0)}$ and $\vec{r}^{(2)} \approx \frac{q^2}{32}\vec{r}^{(0)}$, where the expression for $\vec{r}^{(1)}$ is consistent with previous results [233, 234, 244]. Micromotion thus only results in breathing oscillations about the average positions.

Fig. 4.2.1(a) shows the average ion positions $\vec{r}^{(0)}$ in the planar crystal. The distribution of NN distance is plotted in figure 4.2.1(b). We choose the voltages U_0 and V_0 such that the ion distance is kept between $6.5\,\mu$m and $10\,\mu$m. This ensures that crosstalk errors due to the Gaussian profile of the addressing beam are negligible, at the same time maintaining strong interaction between the ions. As micromotion yields breathing oscillations, the further away the ion is from the trap center, the larger the amplitude of micromotion becomes. With the furthest ion around $52\,\mu$m from the trap center, the amplitude of micromotion is $-q/2 \times 52 \approx 1.4\,\mu$m, which is well below the separation distance between the ions but larger than the optical wavelength (see Appendix for the distribution of the amplitude of micromotion).

4.2.2 Normal Modes in the Transverse Direction

With the knowledge of ion motion in the x-y plane, we proceed to find the normal modes and quantize the motion along the transverse (z) direction. As ions are confined in the plane, micromotion along the transverse direction is negligible. The harmonic pseudopotential approximation is therefore legitimate. Expanding the Coulomb potential to second

order, we have $\frac{\partial^2}{\partial z_i \partial z_j}\left(\frac{1}{\tilde{r}_{ij}}\right)\Big|_{\vec{r}(t)} = \frac{1}{r_{ij}^3}$, where $\tilde{r}_{ij} = \sqrt{(x_i - x_j)^2 + (y_i - y_j)^2 + (z_i - z_j)^2}$ is the 3D distance and $r_{ij} = \sqrt{(x_i - x_j)^2 + (y_i - y_j)^2}$ is the planar distance between ions i and j. To the second order, transverse and in-plane normal modes are decoupled. Note that coupling between the in-plane micromotion and the transverse normal modes has been taken into account in this expansion as the Coulomb potential is expanded around the dynamic ion positions $\vec{r}(t)$. With significant in-plane micromotion, distances between ions are time-dependent, which in turn affects the transverse modes. We can expand the quadratic coefficients in series:

$$\frac{1}{r_{ij}^3} \approx \left\langle \frac{1}{r_{ij}^3} \right\rangle + M_{ij}\cos(\Omega_T t) + \cdots . \tag{4.2.5}$$

The time-averaged coefficients $\left\langle 1/r_{ij}^3 \right\rangle$ can be used to compute the transverse normal modes. The next order containing $\cos(\Omega_T t)$ terms can be considered as a time-dependent perturbation to the Hamiltonian. It contributes on the order of $O\left(q\omega_k^2/\Omega_T^2\right) \sim O(qq_z^2)$ in the rotating wave approximation, where ω_k is the transverse mode frequency. The term $\left\langle 1/r_{ij}^3 \right\rangle \approx \left(1/r_{ij}^{(0)}\right)^3(1 - 3q^2/4) + O(q^3)$, where $r_{ij}^{(0)}$ is the ion distance computed with $\vec{r}^{\,(0)}$ without considering micromotion (see Appendix). Here, the micromotion effect is an overall renormalization in the term $1/r_{ij}^3$, so it does not modify the normal mode structure. Instead, it slightly shifts down the transverse mode frequencies (in the order of $O(q^2)$). Numerically, we found an average reduction of around 0.4 kHz in each transverse mode frequency with our chosen parameters. Although mode structure is not altered by this overall renormalization, the discrepancy in equilibrium positions compared to the pseudopotential approximation will modify both the normal mode structure and mode frequencies.

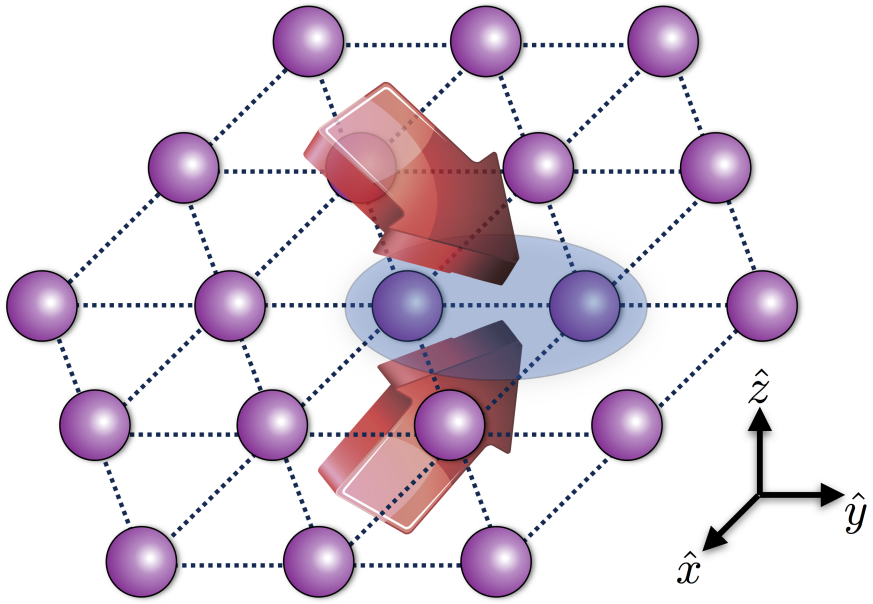

Figure 4.2.2: Nearest neighbor quantum gate in a 2D planar crystal. Two laser beams with a wave vector difference Δk aligned in the z direction exert a spin-dependent force on the neighboring ions. Parameters used are: The wave vector difference of addressing beams $\Delta k = 8\,\mu\text{m}^{-1}$; Laser beams are assumed to take a Gaussian profile with a beam waist $w = 3\,\mu$m centered at the average positions of the respective ion; The Lamb-Dicke parameter $\eta_z = \Delta k\sqrt{\hbar/2m\omega_z} \approx 0.029$. Other parameters are the same as in Fig. 4.2.1.

4.2.3 High-fidelity Quantum Gates

After obtaining the correct transverse normal modes, we now show how to design high-fidelity quantum gates with in-plane micromotion. Since NN gates are sufficient for fault-tolerant quantum computation in a planar crystal, we show as a demonstration that high-fidelity entangling gates can be achieved with a pair of NN ions in the trap center and near the trap edge. One may perform the gate along the transverse direction by shining two laser beams on the two NN ions with wave vector difference $\Delta k\hat{z}$ and frequency difference μ (see Fig. 4.2.2) [240,246]. The laser-ion interaction Hamiltonian is [239] $H = \sum_{j=1}^{2} \hbar\Omega_j \cos(\Delta k \cdot \delta z_j + \mu t)\sigma_j^z$, where Ω_j is the (real) Raman Rabi frequency for the jth ion, σ_j^z is the Pauli-Z matrix acting

on the pseudospin space of internal atomic states of the ion j, and δz_j is the ion displacement from the equilibrium position. Quantize the ion motion, $\delta z_j = \sum_k \sqrt{\hbar/2m\omega_k} b_j^k (a_k + a_k^\dagger)$, with b_j^k (ω_k) being the mode vector (frequency) for mode k and $a_k^\dagger$ creates the k-th phonon mode. Expanding the cosine term and ignoring the single-bit operation, the Hamiltonian can be written in the interaction picture as

$$H_{\rm I} = -\sum_{j=1}^{2} \sum_k \chi_j(t) g_j^k \left(a_k^\dagger e^{i\omega_k t} + a_k e^{-i\omega_k t}\right) \sigma_j^z, \tag{4.2.6}$$

where $\chi_j(t) = \hbar\Omega_j \sin(\mu t)$, $g_j^k = \eta_k b_j^k$, and the Lamb-Dicke parameter $\eta_k = \Delta k \sqrt{\hbar/2m\omega_k} \ll 1$. The evolution operator corresponding to the Hamiltonian $H_{\rm I}$ can be written as [239, 240, 247]

$$U(\tau) = \exp\left(i \sum_j \phi_j(\tau) \sigma_j^z + i \sum_{j<n} \phi_{jn}(\tau) \sigma_j^z \sigma_n^z\right), \tag{4.2.7}$$

where the qubit-motion coupling term $\phi_j(\tau) = -i \sum_k \alpha_j^k(\tau) a_k^\dagger - \alpha_j^{k*}(\tau) a_k$ with $\alpha_j^k(\tau) = \frac{i}{\hbar} g_j^k \int_0^\tau \chi_j(t) e^{i\omega_k t} dt$ and the two-qubit conditional phase $\phi_{jn}(\tau) = \frac{2}{\hbar^2} \sum_k g_j^k g_n^k \int_0^\tau \int_0^{t_2} \chi_j(t_2) \times \chi_n(t_1) \sin(\omega_k(t_2 - t_1)) dt_1 dt_2$. To realize a conditional phase flip (CPF) gate between ions j and n, we require $\alpha_j^k \approx 0$ so that the spin and phonons are almost disentangled at the end of the gate, and also $\phi_{jn}(\tau) = \pi/4$. It is worthwhile to note that in deriving Eq. (4.2.7), we dropped single-qubit operations as we are interested in the CPF gate. These fixed single-qubit operations can be explicitly compensated in experiment by subsequent rotations of single spins. (see Appendix for more detailed derivation and analysis).

As the number of ions increases, transverse phonon modes become very close to each other in frequencies. During typical gate time, many motional modes will be excited. We use multiple-segment pulses to achieve a high-fidelity gate [238, 239]. The total gate time is di-

vided into m equal-time segments, and the Rabi frequency takes the form $\Omega_j(t) = \Omega_j^{(i)}\Omega_j^{\mathrm{G}}(t)$, with $\Omega_j^{(i)}$ being the controllable and constant amplitude for the ith segment ($(i-1)\tau/m \leq t < i\tau/m$). Due to the in-plane micromotion, the laser profile $\Omega_j^{\mathrm{G}}(t)$ seen by the ion is time-dependent. In our calculation, we assume the Raman beam to take a Gaussian form, with $\Omega_j^{\mathrm{G}}(t) = \exp\left\{-\left[\left(x_j(t) - x_j^{(0)}\right)^2 + \left(y_j(t) - y_j^{(0)}\right)^2\right]/w^2\right\}$, where w is the beam waist and $\left(x_j^{(0)}, y_j^{(0)}\right)$ are the average positions for the jth ion. Any other beam profile can be similarly incorporated.

To gauge the quality of the gate, we use a typical initial state for the ion spin $|\Phi_0\rangle = (|0\rangle + |1\rangle) \otimes (|0\rangle + |1\rangle)/2$ and the thermal state ρ_m for the phonon modes at the Doppler temperature. The fidelity is defined as $F = \mathrm{tr}_m\left[\rho_m \left|\langle\Psi_0|U_{\mathrm{CPF}}^{\dagger}U(\tau)|\Psi_0\rangle\right|^2\right]$ tracing over the phonon modes, with the evolution operator $U(\tau)$ and the perfect CPF gate $U_{\mathrm{CPF}} \equiv e^{i\pi\sigma_1^z\sigma_2^z}$. For simplicity, we take $\Omega_j^{(i)} = \Omega_n^{(i)} = \Omega^{(i)}$ for the ions j and n. For any given detuning μ and gate time τ, we optimize the control parameters $\Omega^{(i)}$ to get the maximum fidelity F. Fig. 4.2.3 shows the gate infidelity $\delta F = 1 - F$ and the maximum Rabi frequency $|\Omega|_{\max} = \max_i \Omega^{(i)}$ for the center pair [(a) and (b)] and the edge pair [(c) and (d)] with 13 segments and a relatively fast gate $\tau \approx 23\,\mu$s. Detuning μ can be used as an adjusting parameter in experiment to find the optimal results. All transverse phonon modes are distributed between $0.85\omega_z$ and ω_z. We optimize the gate near either end of the spectrum since optimal results typically occur there. Blue solid lines indicate the optimal results with micromotion and red dashed lines show the results for a genuine static harmonic trap, which are almost identical in (a), (b) and (c). It implies that micromotion can almost be completely compensated, but with a stronger laser power for the edge pair. If we apply the optimal result for the static trap to the realistic case with micromotion, the fidelity will be lower as indicated by the black dash-dot lines. This is especially so for the edge pair, where

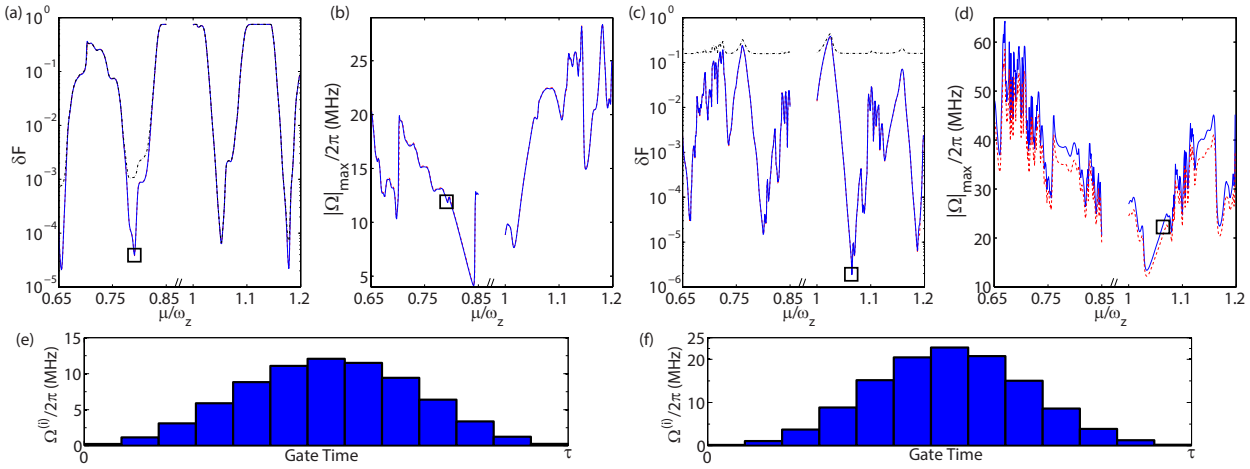

Figure 4.2.3: Gate infidelity and pulse shaping. (a), (b), and (e) are respectively the gate infidelity, the maximum Rabi frequency, and the thirteen-segment pulse pattern corresponding to the results marked by squares, for the center pair as labeled in Fig. 4.2.1. (c), (d), and (f) are the corresponding plots for the edge pair. The blue solid lines and the pulse sequences indicate the optimal results with micromotion considered. The red dashed lines are results for a genuine static harmonic trap without micromotion. Black dash-dot lines in (a) and (c) are obtained by applying the optimal solution for a static trap to the case with micromotion. All transverse modes are distributed between $0.85\omega_z$ and ω_z. We optimize the gate near either end of the spectrum. The optimal results marked by the squares are $\delta F = 4 \times 10^{-5}$ and $|\Omega|_{\max}/2\pi = 12\,\mathrm{MHz}$ ($\delta F = 4 \times 10^{-6}$ and $|\Omega|_{\max}/2\pi = 22\,\mathrm{MHz}$) for the center (edge) pair. Parameters used are: total gate time $\tau = 50 \times 2\pi/\omega_z \approx 23\,\mu\mathrm{s}$; $m = 13$ segments are used; Doppler temperature $k_B T_D/\hbar \approx 2\pi \times 10\,\mathrm{MHz}$ is assumed for all phonon modes. Other parameters are the same as in Fig. 4.2.1 and Fig. 4.2.2.

the fidelity is lower than 85% at any detuning. It is therefore critical to properly include the effect of micromotion. With corrected pulse sequences, a fidelity $F > 99.99\%$ can be attained with $|\Omega|_{\max}/2\pi \approx 12\,\mathrm{MHz}$ ($|\Omega|_{\max}/2\pi \approx 22\,\mathrm{MHz}$) for the center (edge) ions. The Rabi frequencies can be further reduced by a slower gate and/or more pulse segments.

4.2.4 Noise Estimation

Micromotion of any amplitude does not induce errors to the gates as it has been completely compensated in our gate design. We now estimate various other sources of noise for gate implementation. In considering the effect of in-plane micromotion to the transverse modes, we are accurate to the order of q^2, so an error of $q^3 \approx 10^{-4}$ is incurred. The actual error is smaller since the Coulomb potential is an order of magnitude smaller than the trapping potential along the transverse direction. The cross-talk error probability due to beam spillover is $P_c = e^{-2(d/w)^2} < 2 \times 10^{-5}$, with the ion distance $d \gtrsim 7\,\mu$m and the beam waist $w = 3\,\mu$m. At the Doppler temperature $k_B T_D/\hbar \approx 2\pi \times 10\,$MHz, thermal spread in positions may degrade the gate fidelity. Similar to micromotion, thermal motion causes the effective Rabi frequency to fluctuate. With $\omega_{x,y}/2\pi \approx 0.2\,$MHz, there is a mean phonon number $\bar{n}_0 \approx 50$ in the x-y plane. It gives rise to thermal motion with average fluctuation in positions, $\delta r \approx 0.23\,\mu$m, which can be estimated as in Ref. [248]. The resultant gate infidelity is $\delta F_1 \approx (\pi^2/4)(\delta r/w)^4 \approx 10^{-4}$. Lastly, we estimate the infidelity caused by higher-order expansion in the Lamb-Dicke parameter. The infidelity is $\delta F_2 \approx \pi^2 \eta_z^4 (\bar{n}_z^2 + \bar{n}_z + 1/8) \approx 2 \times 10^{-4}$, where $\bar{n}_z \approx 5$ is the mean phonon number in the transverse direction [239]. Other than the effects considered above, micromotion may also lead to rf heating when it is coupled to thermal motion. However, simulation has shown that at low temperature $T < 10\,$mK and small q parameters, rf heating is negligible [244, 249]. Heating effect due to rf phase shift and voltage fluctuation should also be negligible when they are well-controlled [244].

4.3 Discussion

It is worthwhile to point out that although we have demonstrated the feasibility of our gate design via a single case with $N = 127$ ions, the proposed scheme scales for larger crystals. The intuition is that through optimization of the segmented pulses, all phonon modes are nearly disentangled from the quantum qubits at the end of the gate. However, as the number of ions further increases, one would presumably need more and more precise control for all the experimental parameters ($< 1\%$ fluctuation in voltage for example). rf heating may also destabilize a much larger crystal [250], and more careful studies are necessary for larger crystals.

One may also notice that in Ref. [233], we considered gates mediated by the longitudinal phonon modes, so the effect of micromotion is a phase modulation. Here, we utilize transverse modes so the amplitude of the laser beam is modulated. There are a few advantages in using the transverse modes: first, it is experimentally easier to access the transverse phonon modes in a planar ion crystal; second, in a planar crystal, the transverse direction is tightly trapped, so micromotion along that direction can be neglected; third, the transverse phonon modes do not couple to the in-plane modes and the in-plane micromotion affects the transverse modes via the time-dependence of the equilibrium positions, the effect of which is again suppressed due to tight trapping in the transverse direction.

In summary, we have demonstrated that a planar ion crystal in a quadrupole Paul trap is a promising platform to realize scalable quantum computation when micromotion is taken into account explicitly. We show that the in-plane micromotion comes into play through three separate effects, and each of them can be resolved. This paves a new pathway for large-scale trapped-ion quantum computation.

CHAPTER V

Hamiltonian Tomography for Quantum Many-body Systems

5.1 Introduction

Characterization of qubit couplings in many-body quantum systems is essential for benchmarking quantum computation and simulation. In this chapter, we propose a tomographic measurement scheme to determine all the coupling terms in a general many-body Hamiltonian with arbitrary long-range interactions, provided the energy density of the Hamiltonian remains finite. Different from quantum process tomography, our scheme is fully scalable with the number of qubits as the required rounds of measurements increase only linearly with the number of coupling terms in the Hamiltonian. The scheme makes use of synchronized dynamical decoupling pulses to simplify the many-body dynamics so that the unknown parameters in the Hamiltonian can be retrieved one by one. We simulate the performance of the scheme under the influence of various pulse errors and show that it is robust to typical noise and experimental imperfections.

Physicists have been striving to understand and harness the power of quantumness since the

establishment of the quantum theory. With the flourishing of quantum information science in recent decades [26,27], numerous breakthroughs—both in theory and in experiment—helped to frame a clearer goal: it is the entanglement and the exponentially growing Hilbert space that distinguishes quantum many-body systems from classical systems [29,30,251]. To fully leverage the quantum supremacy, a vital step is to verify and benchmark the quantum device. The standard techniques of quantum state and process tomography [252–257], however, are plagued by the same exponential growth of dimensions [258]. A related problem is to directly identify Hamiltonians, the generators of quantum dynamics. They can often be specified by fewer number of parameters that scales polynomially with the system size.

Hamiltonian tomography for generic many-body systems is nevertheless a daunting task. The way to extract information of unknown parameters in a Hamiltonian is by measuring certain features of its generated dynamics. To make this possible, one has to solve the dynamics generated by the Hamiltonian to make a definite connection between its dynamical features and the Hamiltonian parameters. However, for general many-body Hamiltonians, their dynamics are extremely complicated and intractable by numerical simulation as the simulation time increases exponentially with the size of the system. Progress in this direction has mostly be on small systems [259–263] or special many-body systems which are either exactly solvable due to many conserved operators, of limited Hilbert space dimensions amenable to numerical simulation, or short-range interacting systems [264–270].

In this chapter, we propose a scheme to achieve Hamiltonian tomography for general many-body Hamiltonians with arbitrary long-range couplings between the qubits. The key idea is to simplify the dynamics generated by a general many-body Hamiltonian through application of a sequence of dynamical decoupling pulses on individual qubits. Dynamical decoupling (DD) is a powerful technique that uses periodic fast pulses to suppress noise and average

out unwanted couplings between the system and the environment [271–286]. We apply a sequence of synchronized DD pulses on a pair of qubits, which forms a small target system that has coupling with the rest of the qubits in the many-body Hamiltonian, the effective environment. The DD pulses keep the desired couplings within this target system intact while average out its couplings with all the environment qubits. The dynamics under the DD pulses become exactly solvable, from which we can perform a tomographic measurement to determine the coupling parameters within this small target system [259–262]. We then scan the DD pulses to different pairs of qubits to measure all the other coupling terms in the Hamiltonian. We assume the ability to address individual qubits, which is realistic for many experimental platforms, such as trapped ions [209, 287, 288], cold atoms [131, 132, 289], and solid-state qubit systems [290–293]. Several features make the scheme amenable to experimental implementation. First of all, applying the DD pulse sequence is a standard procedure in many experiments. Post-processing of data is straightforward as it only requires one or two parameter curve fitting. In addition, we demonstrate with explicit numerical simulation that the scheme is robust to various sources of errors in practical implementation, such as the remnant DD coupling error, measurement uncertainties, and different types of pulse errors.

5.2 Scheme for Hamiltonian Tomography

The system we have in mind is the most general Hamiltonian with two-body qubit interactions

$$H = \sum_{\alpha,\beta,m<n} J_{mn}^{\alpha\beta} \sigma_m^\alpha \sigma_n^\beta + \sum_{m,\alpha} b_m^\alpha \sigma_m^\alpha, \tag{5.2.1}$$

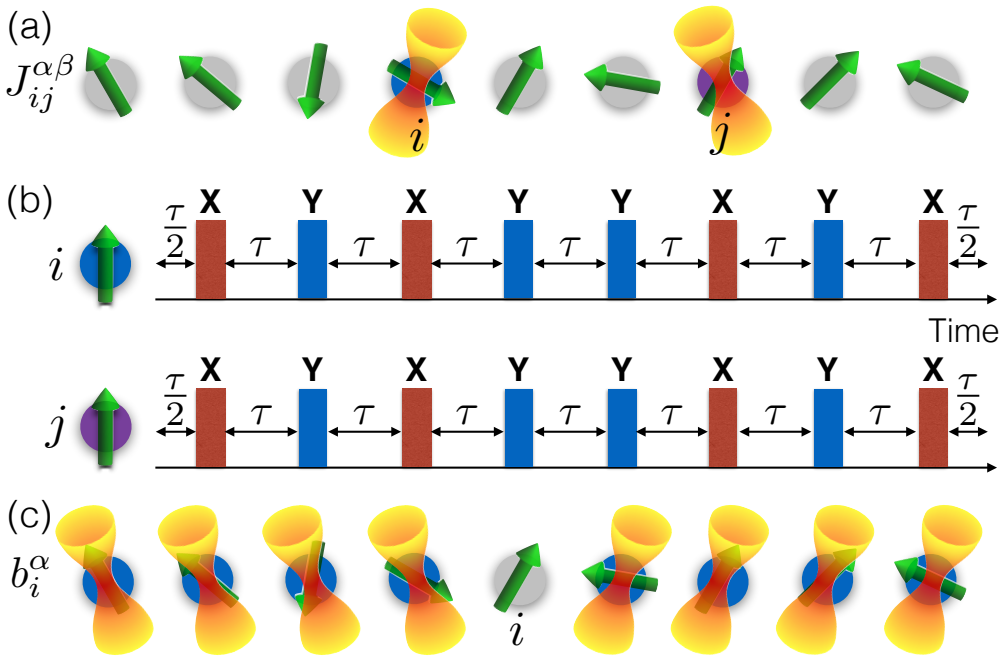

Figure 5.1.1: Schematics for the tomography procedure. (a) To map out the coupling coefficients $J_{ij}^{\alpha\beta}$, a synchronized DD sequence is applied to spins i and j. Both spins will be decoupled from the rest of the system. (b) The XY-8 DD sequence on spins i and j to probe the parameters of the Hamiltonian in Eq. (5.2.3). The initial state is for instance prepared to the $|00\rangle$ state for the two spins. (c) To retrieve information about the local fields b_i^{α}, XY-8 pulse sequences are applied to the environment spins to decouple spin i from the rest.

where $J_{mn}^{\alpha\beta}$ characterizes the coupling strength between spins m and n for the α, β components, and b_m^{α} represents the local field on spin m; $\sigma^{\alpha}\left(\sigma^{\beta}\right)$ are the Pauli matrices along the α (β) direction with $\alpha, \beta \in (x, y, z)$. To adopt consistent notations throughout the text, we use m, n to denote a general spin label and i, j to refer to the specific *target spins* that we are probing with the DD pulses, calling the rest of the spins as *environment spins*. The terms spin and qubit are used interchangeably. Let the energy unit of the Hamiltonian be J, chosen to be the largest magnitude of all coefficients, so $J_{mn}^{\alpha\beta}/J$ and b_m^{α}/J are bounded between -1 and 1. In order to map out the coupling coefficient $J_{ij}^{\alpha\beta}$ for the target spins, we propose to decouple these two spins from the environment spins by a synchronized DD

pulse sequence. A synchronized XY-4 sequence applied to both spins will average out their interactions with other spins while preserving the two-spin coherence (see Fig. 5.1.1(a-b) for the schematic and the pulse sequence). Basically, only those interactions that commute with the DD sequence will survive. More rigorously, the evolution operator in one period is

$$U_1 = U_0^{1/2}\sigma_i^x\sigma_j^x U_0 \sigma_i^y\sigma_j^y U_0 \sigma_i^x\sigma_j^x U_0 \sigma_i^y\sigma_j^y U_0^{1/2} = e^{-i4\tau(J_{ij}^{xx}\sigma_i^x\sigma_j^x + J_{ij}^{yy}\sigma_i^y\sigma_j^y + J_{ij}^{zz}\sigma_i^z\sigma_j^z + B) + O(J^2\tau^2)}, \quad (5.2.2)$$

where $U_0 = e^{-iH\tau}$, τ is the time interval between two consecutive pulses, and B, the bath, includes all terms of the Hamiltonian that only acts on environment spins. See Appendix for the detailed derivation. To bound the error term to $O(J^2\tau^2)$, we assume $\sum_n J_{in}^{\alpha\beta} = O(J)$, i.e., the interaction strength decays rapidly with spin separation distance so that the energy density of the Hamiltonian is bounded by a constant. This condition is satisfied for any finite systems as in the experiment with arbitrary interactions. In the thermodynamic limit, it is also a reasonable assumption for any physical systems whose energy is extensive. It may also be related to the generalized Lieb-Robinson bound for systems with long-range interactions [294–297]. The XY-8 pulse sequence, which is the concatenation of XY-4 sequence with its time-reversal, eliminates the error term to the third order $O(J^3\tau^3)$. Fig. 5.1.1(b) shows the XY-8 DD pulse sequence. Hence, in the Hilbert subspace of the target spins, the effective Hamiltonian is

$$H_{\text{2-spin}} = c_1\sigma_i^x\sigma_j^x + c_2\sigma_i^y\sigma_j^y + c_3\sigma_i^z\sigma_j^z, \quad (5.2.3)$$

where we use $c_1 \equiv J_{ij}^{xx}, c_2 \equiv J_{ij}^{yy}, c_3 \equiv J_{ij}^{zz}$ to simplify the notation. The effective two-spin unitary evolution after N_c cycles of XY-8 sequence is

$$U_{\text{2-spin}} = \begin{pmatrix} \frac{\cos((c_1-c_2)T)}{e^{ic_3T}} & 0 & 0 & \frac{\sin((c_1-c_2)T)}{ie^{ic_3T}} \\ 0 & \frac{\cos((c_1+c_2)T)}{e^{-ic_3T}} & \frac{\sin((c_1+c_2)T)}{ie^{-ic_3T}} & 0 \\ 0 & \frac{\sin((c_1+c_2)T)}{ie^{-ic_3T}} & \frac{\cos((c_1+c_2)T)}{e^{-ic_3T}} & 0 \\ \frac{\sin((c_1-c_2)T)}{ie^{ic_3T}} & 0 & 0 & \frac{\cos((c_1-c_2)T)}{e^{ic_3T}} \end{pmatrix},$$

where $T = 8N_c\tau$ is the total time. From the above expression, one may notice that the Hamiltonian parameters can be retrieved by preparing a particular initial state and measuring its time-evolved output probability in a given basis. In particular, we have

$$\begin{aligned} P_{|+\mathrm{I}\rangle\to|00\rangle} &= |\langle 00|U_{\text{2-spin}}|+\mathrm{I}\rangle|^2 = \tfrac{1}{4}\left[1+\sin(2(c_1-c_2)T)\right] \\ P_{|+\mathrm{I}\rangle\to|10\rangle} &= |\langle 10|U_{\text{2-spin}}|+\mathrm{I}\rangle|^2 = \tfrac{1}{4}\left[1+\sin(2(c_1+c_2)T)\right] \\ P_{|0\mathrm{I}\rangle\to|++\rangle} &= |\langle ++|U_{\text{2-spin}}|0\mathrm{I}\rangle|^2 = \tfrac{1}{4}\left[1+\sin(2(c_2-c_3)T)\right] \end{aligned}$$

where $|+\rangle = \frac{1}{\sqrt{2}}(|0\rangle + |1\rangle)$ and $|\mathrm{I}\rangle = \frac{1}{\sqrt{2}}(|0\rangle + i|1\rangle)$ are the rotated basis. The coupling strengths c_1, c_2 and c_3 can be extracted from the oscillation frequencies of these three sets of measurements at various time points. These particular sets are not the only suite to extract those parameters. They are chosen for the convenience in fitting and in state preparation. Only product states of the two target spins, disentangled from the rest, are required. We also remark that the error incurred is $O(N_cJ^3\tau^3)$, so one needs $J\tau \ll 1$ for a robust decoupling scheme. In a similar fashion, one can retrieve all other coupling coefficients. Let us denote the synchronized XY-8 DD pulse sequence as X_iX_j-Y_iY_j-8 to show explicitly the particular pulses on specific spins. Replacing the sequence with X_iY_j-Y_iZ_j-8 (Y_iX_j-Z_iY_j-8) pulses, we

will be able to extract the coefficients J_{ij}^{xy}, J_{ij}^{yz} and J_{ij}^{zx} (J_{ij}^{yx}, J_{ij}^{xz} and J_{ij}^{zy}), respectively.

By scanning the DD pulses to different target pairs, the above procedure recovers all the coupling coefficients $J_{mn}^{\alpha\beta}$. The retrieval of local field coefficients follows a similar approach. We now need to decouple the particular spin i from the rest without contaminating its own spin term $b_i^\alpha \sigma_i^\alpha$. Shining a XY-8 DD sequence on spin i removes all information about b_i^α too. Instead, one could address all the environment spins with XY-8 pulses, and decouple them from spin i (alternative schemes are discussed in the Appendix). This scheme will be very robust to pulse errors, since no laser pulses are directly applied to the target spin [Fig. 5.1.1(c)]. The effective single-spin Hamiltonian is thus $H_{\text{1-spin}} = b_i^x \sigma_i^x + b_i^y \sigma_i^y + b_i^z \sigma_i^z$ with a unitary evolution $U_{\text{1-spin}} = e^{-iH_{\text{1-spin}}T}$ executing a spin rotation on the Bloch sphere. Again, by preparing a particular state and measuring its time evolution, we get $P_{|0\rangle\to|0\rangle} = 1 + \left[(b_i^z/b)^2 - 1\right] \sin^2(bT)$ and $P_{|+\rangle\to|+\rangle} = 1 + \left[(b_i^x/b)^2 - 1\right] \sin^2(bT)$, where $b = \sqrt{(b_i^x)^2 + (b_i^y)^2 + (b_i^z)^2}$ is the magnitude of the Bloch vector. These two sets of measurements will determine b_i^x, b_i^y and b_i^z up to a sign. The correct signs from the remaining discrete set can be picked out by measuring $P_{|+\rangle\to|0\rangle}$ and $P_{|\mathrm{I}\rangle\to|0\rangle}$ at a single time point (See Appendix).

The complete scheme applies to any generic Hamiltonian with interacting qubits. In the most general case, one needs to determine $9N(N-1)/2 + 3N$ coefficients. However, in many physical systems, the particular form of the interaction is known and/or the interaction often decays fast enough that one can significantly reduce the number of measurements required. In particular, if $J_{mn}^{\alpha\beta}$ can be truncated at some spin separation distance in the case of short-range interactions, the number of measurements will be linear with the system size N. In the following, we numerically simulate the experimental procedure for the most general Hamiltonian, taking into account various sources of errors, including the remnant DD coupling error, measurement uncertainties, and different forms of pulse errors.

5.3 Numerical Simulation

We consider the general Hamiltonian given in Eq. (5.2.1) with coefficients $J_{ij}^{\alpha\beta}/J$ and b_i^α/J randomly drawn from -1 to 1. In our finite-system simulation, we ignore the decay of $J_{ij}^{\alpha\beta}$ with distance, so the system may include unphysically long-range interactions and could simulate Hamiltonians in any dimensions. To retrieve $J_{ij}^{\alpha\alpha}$, for example, we start with a product state of all spins, and perform time evolution using the entire Hamiltonian from Eq. (5.2.1), interspersed with the XY-8 DD pulses on target spins i and j. We would like to emphasize that specific state initialization for the environment spins is not required as long as they are disentangled from the target pair of qubits at the beginning. After N_c cycles of the DD sequence, the environment spins are traced out and measurements are made on spins i and j. In the simulation, we do not assume the pure unitary evolution $U_{\text{2-spin}}$ as the remnant coupling to the environment spins may entangle the two spins with the rest. However, any undesired couplings are suppressed to the order of $O(J^3\tau^3)$ and we do observe that the two-spin density matrix remains mostly pure ($\sim 99.9\%$) for our chosen parameters.

As the tomography procedure involves measuring the output probability of a certain state, each time point will be measured N_m times, which gives an estimate of the probability p_m in this state. The measurement uncertainty (standard deviation) will be $\sqrt{p_m(1-p_m)/N_m}$ following the binomial distribution. As discussed above, to map out c_1, c_2 and c_3, one needs to measure $P_{|+\mathrm{I}\rangle\to|00\rangle}, P_{|+\mathrm{I}\rangle\to|10\rangle}$ and $P_{|0\mathrm{I}\rangle\to|++\rangle}$ for the target spins at various time points and extract the corresponding oscillation frequencies. Suppose N_t different time points are measured for each set. The oscillation frequencies can be found either by Fourier transform or by curve fitting. In general, if data show numerous oscillation periods, Fourier transform will be more robust and reliable [260–262]. In our case, however, the long time observations will

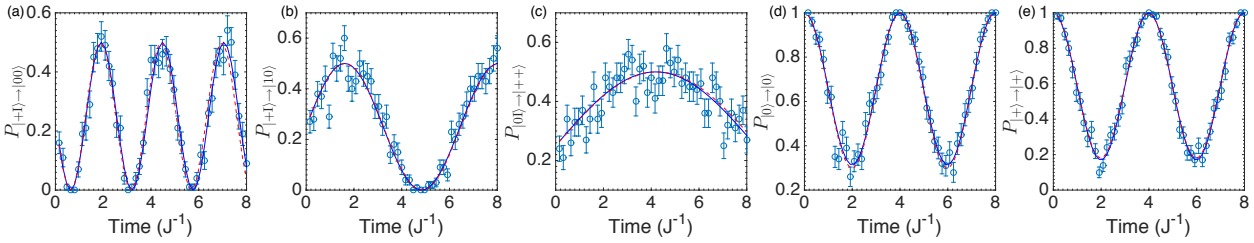

Figure 5.3.1: Numerical simulation and curving fitting results. (a)-(c) are used to retrieve J_{79}^{xx}, J_{79}^{yy} and J_{79}^{zz} between spins 7 and 9. (d) and (e) are used to extract b_6^x, b_6^y and b_6^z for spin 6. Each measurement data p_m are drawn from the binomial distribution with the true probability p as the mean and $p(1-p)/N_m$ as the variance. The measurement uncertainty of each point is thus $\sqrt{p_m(1-p_m)/N_m}$. The blue solid lines are the best-fit lines with the simulated experimental data p_m, and red dashed lines are the theoretical ones generated by the true Hamiltonian parameters. Pulse errors are not included in these plots, so any discrepancies stem from the remnant DD coupling error and measurement uncertainties. Other parameters used are $N = 12$, $\tau J = 0.01$, $N_m = 100$, $N_t = 50$.

be undermined by the remnant coupling to the environment spins and possible pulse error accumulation. Simple curving fitting with fewer oscillation periods, therefore, appears to be a better solution. In Fig. 5.3.1(a-c), we fit the data with the method of least squares with $\tau J = 0.01, N_m = 100, N_t = 50$ for spins $i = 7$ and $j = 9$ in a $N = 12$ spin system. The blue solid lines are the best-fit lines, and the red dashed lines are the theoretical lines using the true coupling coefficients. The longest time period requires 800 pulses, which is well within the current experimental technology without significant pulse error accumulation. Table 5.2 compares the true values and the estimated ones of $J_{79}^{\alpha\alpha}$. Uncertainties in the estimation stem from the curve fitting due to measurement uncertainties. Corresponding results for b_6^α of spin 6 are shown in Fig. 5.3.1(d-e) and Table 5.2. All estimated parameters are accurate within a few percent.

To simulate real experiments, one also needs to include possible pulse errors. One possible source of errors is the finite duration of each control pulse, which limits the minimum cycle

time. This is typically not the dominant source of errors and can often be well-controlled [277, 281, 298–300]. In most experiments, the major cause of errors is the deviation between the control pulses and the ideal X or Y pulses. These can either arise from the amplitude error where the rotation angle differs from the ideal π-pulse or the rotation error where the rotation axis deviates from the x or y axis. In typical experiments, individual pulse errors may be controlled within a percent level. In our simulation, we consider three different forms of pulse errors: Systematic Amplitude pulse Error (SAE), Random Amplitude pulse Error (RAE) and Random Rotation axis Error (RRE). See the caption of Table 5.2 for the specific forms of the errors. Moderate systematic errors can be self-compensated by the XY-8 DD sequence. Numerically, we found that 5% of SAE has negligible effect on the parameter estimation. In addition, we also simulated the cases where each pulse experiences a 1% RAE or RRE. Results are summarized in Table 5.2. The average deviation from the true parameters are within 5%. Here, we would like to point out a few features of our scheme that make it inherently robust to errors. First of all, the estimation of the coupling strength $J_{mn}^{\alpha\beta}$ only entails frequency estimation, which could endure large deviations of a few measurement points. In addition, the single-parameter curve fitting scheme not only makes the estimation robust but is also more convenient for experiment. Moreover, the retrieval of local fields b_m^α is remarkably tolerant to pulse errors. Since no pulse is directly applied to the target spin, any pulse errors on the environment spins will only be propagated via the remnant DD coupling error, which is suppressed to the order of $O(J^3\tau^3)$. We have numerically tested that a 10% pulse error of any kind would have negligible effects on the estimation of b_m^α. Alternative schemes to extract the local fields are detailed and discussed in the Appendix. They are less tolerant to pulse errors, but may be easier to implement in some experimental setups.

Table 5.2: Parameter estimation and noise for Hamiltonian tomography. NPE: No Pulse Error; SAE: Systematic Amplitude pulse Error; RAE: Random Amplitude pulse Error; RRE: Random Rotation axis Error; AD: Average Deviation from true values. The last digit in bracket for each number quantifies the estimation error bar due to measurement uncertainties, which is generated by the bootstrapping method. The percentage values in the brackets denote the amount of errors introduced in each pulse. The errors are in the form of: SAE, $e^{i\frac{\pi}{2}(1+\epsilon)\sigma^\nu}$; RAE, $e^{i\frac{\pi}{2}(1+\delta)\sigma^\nu}$; RRE, $e^{i\frac{\pi}{2}(\sigma^\nu+\alpha\sigma^x+\beta\sigma^y+\gamma\sigma^z)}$; where $\epsilon = 5\%$, δ is randomly chosen from $(-1\%, 1\%)$, (α, β, γ) is a vector with a random direction but fixed magnitude at 1%, and $\nu = x, y$ for the X and Y pulses respectively.

	True	Estimated Parameters			
	–	NPE	SAE(5%)	RAE(1%)	RRE(1%)
J_{79}^{xx}	-0.378	$-0.369(3)$	$-0.377(3)$	$-0.379(4)$	$-0.412(2)$
J_{79}^{yy}	0.863	0.856(3)	0.846(3)	0.867(4)	0.836(2)
J_{79}^{zz}	0.679	0.669(5)	0.649(5)	0.718(6)	0.611(4)
b_6^x	0.334	0.32(1)	0.32(1)	0.32(1)	0.32(1)
b_6^y	0.569	0.567(8)	0.567(8)	0.567(8)	0.568(8)
b_6^z	-0.431	$-0.441(8)$	$-0.443(8)$	$-0.441(8)$	$-0.441(8)$
AD	–	2%	3%	3%	5%

5.4 Discussion and Outlook

We have thus numerically demonstrated that the proposed scheme is robust to various sources of errors present in real experiments. The measurement uncertainties can be lowered by increasing N_m and the pulse errors can be reduced by limiting the maximum number of pulses needed. The optimal strategy involves a delicate balance between experimental sophistication and error control. For example, by fixing τJ and the total number of measurements for each set, $N_m \times N_t$, one could devise an optimal estimation procedure. In addition, it is also possible to eliminate the remnant DD coupling error to a higher order with more elaborate pulse sequences such as the concatenated DD sequence [276, 277] and reduce pulse errors by designing composite pulses or self-correcting sequences [280, 281, 301, 302]. The scheme can also be extended straightforwardly to qudit systems of higher spins or to bosonic or fermionic

systems.

In conclusion, we have proposed a general scheme to achieve full Hamiltonian tomography for generic interacting qubit systems with arbitrary long-range couplings. The required number of measurements scales linearly with the number of terms in the Hamiltonian, and the scheme is robust to typical experimental errors or imperfections.

CHAPTER VI

Towards Demonstrating Quantum Supremacy

In the previous two chapters, we discussed quantum computation and quantum simulation in general. The building of a universal, scalable quantum computer is one of the holy grails of modern physics. However, the conditions and resources needed for a universal quantum computer are extremely demanding. In this chapter, we focus on the possibility of using some intermediate quantum computing models to demonstrate quantum supremacy. These intermediate quantum computers, albeit non-universal, are beyond classical simulation capability and, at the same time, they are more easily implementable in experiment. An experimental demonstration of quantum supremacy will be an important milestone in the development of a full-fledged quantum computer. In this chapter, we discuss two of our studies toward this goal.

6.1 Verification of Boson Sampling with Coarse-grained Measurements

6.1.1 Introduction

A boson sampling device could efficiently sample from the output probability distribution of noninteracting bosons undergoing many-body interference. This problem is not only classically intractable, but its solution is also believed to be classically unverifiable. Hence, a major difficulty in experiment is to ensure a boson sampling device performs correctly. In this section, we present an experimental friendly scheme to extract useful and robust information from the quantum boson samplers based on coarse-grained measurements. The procedure can be applied to certify the equivalence of boson sampling devices while ruling out alternative fraudulent devices. We perform numerical simulations to demonstrate the feasibility of the method and consider the effects of realistic noise. Our approach is expected to be generally applicable to other many-body certification tasks beyond the boson sampling problem.

In the last three decades, quantum computation has stimulated considerable excitement among physicists, computer scientists, and mathematicians, with the general belief that quantum computers could solve certain tasks significantly faster than current electronic computers [26, 303]. Especially after the discovery of Shor's factoring algorithm [304], theorists and experimentalists have been teaming up to converge on the goal of demonstrating quantum supremacy [27]. Recently, an important step made by Aaronson and Arkhipov [36] is to formulate the boson sampling problem, which is intractable for classical computers but remarkably amenable to quantum experiments. A number of elegant experiments have

since implemented the problem with linear optics on a small scale [37, 38, 305–310]. Pushing the experiments beyond classical capabilities would constitute a strong demonstration of the quantum speedup and in addition lead to important implications in the foundations of computer science [36, 303].

At the core of the hardness-of-simulation property lie the exponential cost of computing a matrix permanent [311] and the exponential number of possible output events in boson sampling. These pose major difficulties in certifying the correctness of a boson sampler on a large scale [308,309,312–315]. The credibility of a certification process thus relies on gathering convincing circumstantial evidence while ruling out alternative explanations. Several efficient schemes have been proposed to validate a boson sampler against the uniform sampler [312] making use of the information in the unitary process [308, 309, 313] and against the classical sampler of distinguishable particles [37, 308, 316] exploiting the bosonic clouding behavior [309]. It is also possible to depart from the computationally hard space and design an efficient test based on predictable forbidden events with special inputs and scattering process [314, 317, 318], assuming the device would be equally operational in general. A statistical benchmark based on correlation functions is also proposed to differentiate between bosons, fermions and distinguishable particles [319]. An unsettled problem especially pertinent to experiments is whether one would be able to extract useful and robust information from a large-scale boson sampler. In other words, would any filtered information be able to verify the equivalence of two identical boson sampling devices while excluding possible fraudulent ones? In light of rapid experimental advances, this issue will be increasingly relevant when the system scales up: as the probabilities of generic output events become exponentially small, sampling noise due to limited measurement trials may conceal any distinctive information.

In this section, we introduce an experimental friendly scheme to extract useful structures from

a boson sampling device based on coarse-grained measurements. Using standard statistical tools, we simulate the experimental certification process and show that the coarse-grained information is able to provide a quantitative assessment to the degrees of matching between two alleged boson samplers. This is important when one needs to verify the equivalence of two quantum samples drawn from the same boson sampling device or from different devices with identical processes. It will also be crucial in situations wherein we can completely trust one device and need to validate another possibly fraudulent device against the reliable one. Our numerical simulation in addition demonstrates our scheme could tolerate a moderate amount of experimental noise [320, 321] while strong noise invalidates the equivalence due to mismatched interference processes. On a broader scale, our method is not specific to boson sampling, but could be applicable to other generic many-body certification problems.

6.1.2 Coarse-graining Scheme

Before proceeding to our proposed scheme, we briefly introduce the boson sampling problem and clarify why large sampling errors are involved without coarse graining. In a typical setup, there are N indistinguishable bosons prepared in M input modes and allowed to coherently interfere with one another in a (random) unitary process. We abstract away from interactions between particles, so the resultant many-body interference is purely due to the bosonic statistics. To compute the probability of an output event, one needs to calculate the permanent of the associated $N \times N$ matrix [37, 322], which requires an exponential cost for a generic complex matrix. The possible number of output events is $D = \binom{M+N-1}{N}$, which grows exponentially with N (for $M \geq N$). As the system scales up, the number of measurement runs will be unable to keep pace with the exponential growth. This gives rise to large sampling errors with limited sample size. Fig. 6.1.1 shows an example in which the

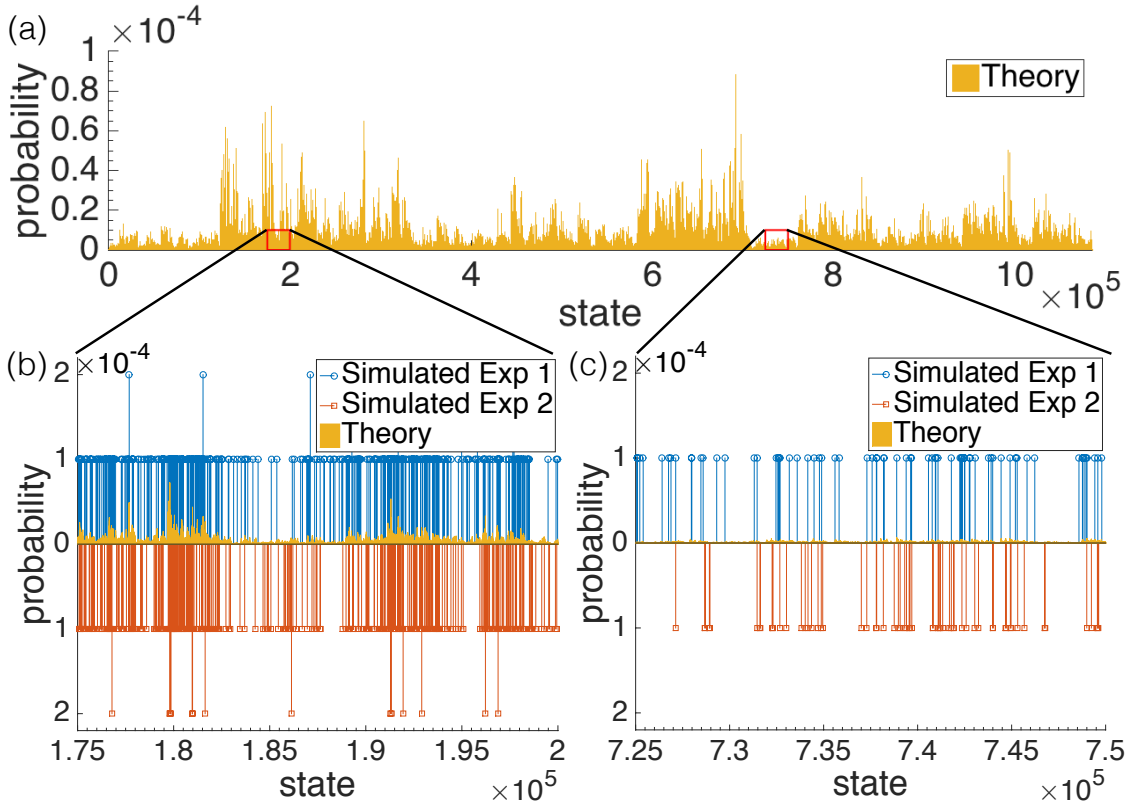

Figure 6.1.1: Original distributions from a boson sampler. (a) Theoretical distribution P^Q of a boson sampling device with $N = 5$ particles in $M = 40$ modes after a random unitary transformation. (b) and (c) shows the zoom-in distributions of two simulated experimental samples (P^Q_{S1} and P^Q_{S2}) with sample size $N_m = 10000$ drawn from P^Q. The theoretical distribution is superimposed onto the simulated samples.

sample size is less than 1% of the Hilbert space dimension. Two samples drawn from the same device could be rather dissimilar (with a low average fidelity $F \approx 0.039 \pm 0.002$, where $F = \left|\sqrt{P^Q_{S1}} \cdot \sqrt{P^Q_{S2}}\right|$). From these distributions, it is not quite possible to assess whether the samples are drawn from the same bona fide boson sampling device.

With a proper coarse-graining procedure, we show, however, that a reliable comparison between two given output samples is achievable. Coarse-graining is performed by merging a number of events into one group, which we call as a bubble. Those events enclosed into

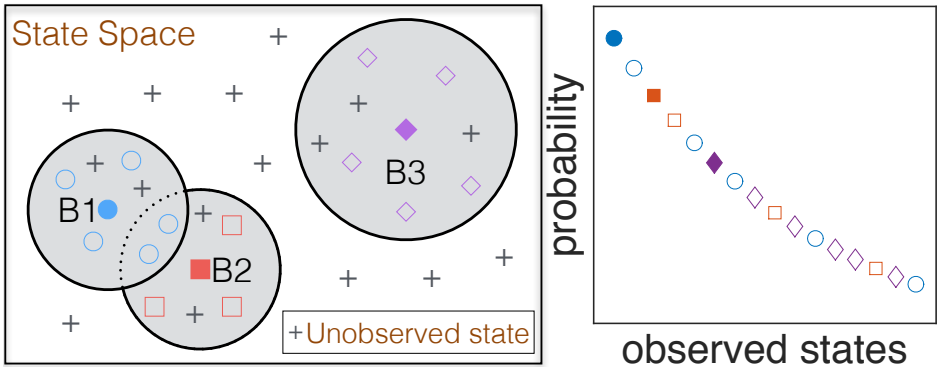

Figure 6.1.2: Schematic for the coarse-graining procedure. The filled symbols are bubble centers. The bubble structure is formed as follows: (1) Pick one set of experimental samples and sort the observed states in descending probability. (2) Consider only states that are not included in previous bubbles. Select a bubble center as the state with the highest probability (if multiple states attain the same highest probability, choose any of them as the bubble center). Form a new bubble by enclosing states with L_1 distance smaller than a cutoff radius to this bubble center (the cutoff radius may be increased for subsequent bubbles to ensure each one has comparable sample size). (3) The bubble structure is established with corresponding centers after all observed states are included. (4) Other samples and theoretical distributions are coarse grained with the same bubble structure.

the same bubble are considered as equivalent events, with their original probabilities added together. There are a few factors that a reasonable coarse-graining procedure should consider. First, it should be constructed from experimental samples. On a large scale, classical simulation is no longer feasible. Experiments may nevertheless pick out the important output states with higher probabilities. Second, the procedure should be scalable: not only the measured events but all possible events should be grouped into some bubbles, where the number of bubbles should not be subject to the exponential growth. Third, the filtered information should still carry some knowledge of the full correlations in the outputs. This is because the essence of the many-body interference lies in the many-mode correlations: previous works [314, 317, 323] have shown that few-particle observables may not capture the full bosonic features and may falsely accept some fraudulent devices. Our proposed scheme

takes the above factors into consideration, and coarse grain the states based on the L_1 distance measure. The L_1 distance between two occupation-number-basis states is defined as $L_1 = \sum_i^M |\psi_i - \phi_i|$, where ψ_i (ϕ_i) is the occupation number in the ith mode for the state $|\psi\rangle$ ($|\phi\rangle$). Details of the coarse-graining procedure are shown in Fig. 6.1.2. We note that this scheme is not the only way to perform coarse graining. We expect that other procedures meeting the above considerations may also work. Below, we show that useful and robust structures can be extracted from the samples using our method.

6.1.3 Numerical Simulation

We simulate the experimental certification process with two different systems, one with trapped ions and one with Haar-distributed random unitaries. For all simulations, we choose a fixed sample size of $N_m = 10000$, which is a reasonable detection count in experiments, but is nevertheless smaller than 1% of the Hilbert space dimension in study.

For trapped ions, the transverse local phonons are used as indistinguishable bosons with the Hamiltonian given by [239, 324, 325]

$$H_c = \sum_i^M \hbar w_{x,i} a_i^\dagger a_i + \sum_{i<j}^M \hbar t_{ij} \left(a_i^\dagger a_j + a_j^\dagger a_i \right), \tag{6.1.1}$$

where $w_{x,i} = -\sum_{j\neq i}^M t_0/|z_{i0} - z_{j0}|^3$, $t_{ij} = t_0/|z_{i0} - z_{j0}|^3$, and $t_0 = e^2/(8\pi\epsilon_0 m\omega_x)$. z_{i0} denotes the axial equilibrium position of the ith ion with mass m and charge e. w_z (w_x) is the axial (transverse) trapping frequency. In the simulation, we use experimentally relevant parameters $\omega_z = 2\pi \times 0.03\,\mathrm{MHz}$ and $\omega_x = 2\pi \times 4\,\mathrm{MHz}$ for $^{171}\mathrm{Yb}^+$ ions and consider $N = 12$ phonons on $M = 12$ ions. The total Hilbert space size is $D = 1352078$. The evolution

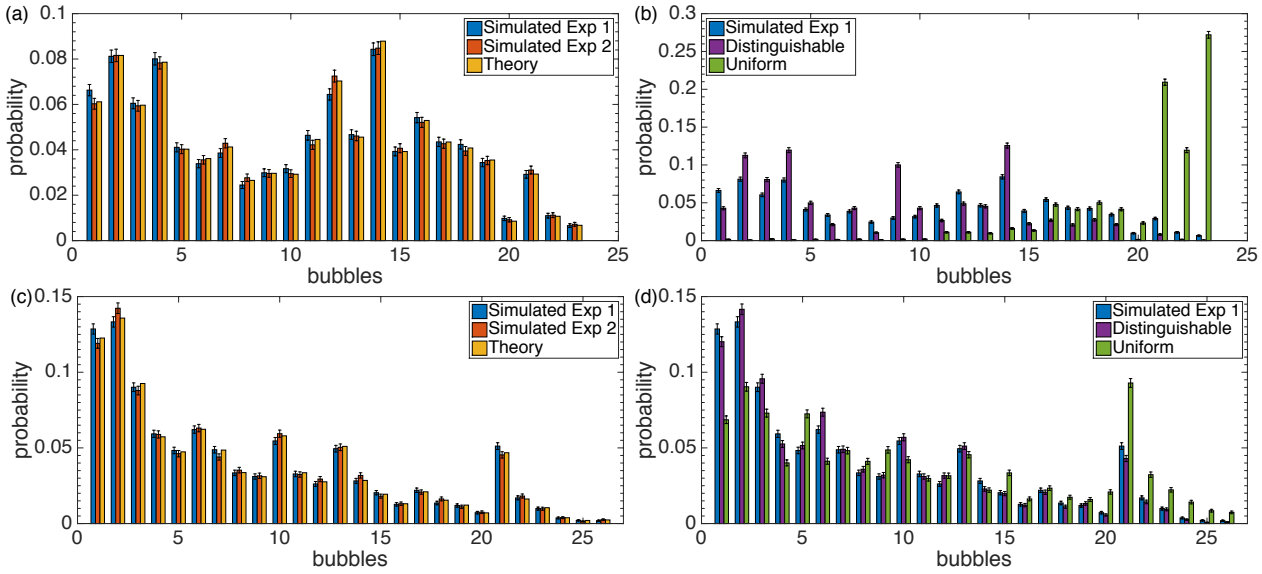

Figure 6.1.3: Coarse-grained probability distributions. All samples have a sample size $N_m = 10000$. The simulated experimental samples $\left(P_{S1}^{Q}\right.$ and $\left.P_{S2}^{Q}\right)$ are drawn from the boson sampler (P^Q); distinguishable (P_S^C) and uniform $\left(P_S^U\right)$ samples are drawn respectively from the classical (P^C) and uniform (P^U) samplers. Errors for the probabilities follow the standard deviations of the multinomial distribution. (a) and (b): probability distributions for the trapped-ion system with intermediate-time dynamics. The simulated system has $N = 12$ phonons in a $M = 12$ ion chain with one phonon on each ion as the input state. (c) and (d): probability distributions after a Haar-distributed random unitary transformation. The simulated system has $N = 5$ particles in $M = 40$ modes with $|1, 1, 1, 1, 1, 0, \cdots, 0\rangle$ as the input state.

time is chosen at some intermediate time ($\tau = 100\,\mu$s) with interesting many-body dynamics (see Appendix F.1.1 for further results in the long time limit). For the random unitary process, we simulate $N = 5$ particles in $M = 40$ modes, a setting comparable to the current experimental regime with linear optics [37, 38, 305–310] and in a limit where $M > N^2$ to suppress collision events. A Haar-distributed $M \times M$ random unitary matrix is used, with a Hilbert space dimension of $D = 1086008$.

Based on the coarse-graining procedure outlined in Fig. 6.1.2, we group the sample events into different bubbles according to one set of experimental samples. The theoretical distri-

butions are also subject to the same bubble structure. Fig. 6.1.3 shows an example of the coarse-grained distributions. This extracted information is robust and reliable with small sampling errors. By visual comparison, we can see that the boson sampling data P_{S1}^{Q} and P_{S2}^{Q} match closely with each other, but differ significantly from samples drawn from alternative distributions, such as the distinguishable (P_{S}^{C}) and uniform (P_{S}^{U}) samples. Here, it is also possible to compare the simulated data with the theoretical distribution P^{Q}, which will not be directly obtainable when experiments surpass classical simulation capabilities. By repeating the procedure, we observe that the comparisons are not sensitive to details of the coarse-graining method, such as the particular sample used to initiate the bubble structure.

To quantify the degrees of matching between coarse-grained distributions, we employ the two-sample χ^2 test. Under the null hypothesis wherein two samples are drawn from the same distribution, the χ^2 statistics follow the χ^2-distribution with degrees of freedom (df) equal to the number of bubbles (N_B) minus one. If the χ^2 statistic is large with a small associated p-value, one nominally rejects the null hypothesis. Therefore, during the certification process, one should ideally accept the null if the pair of samples come from the same boson sampling device and reject it if one is sampled from an alternative distribution. Two types of errors can be incurred, a type I error (false positive) related to falsely rejecting the true null hypothesis and a type II error (false negative) associated with the failure to reject a false null hypothesis. Prior to the test, one sets a significance level α, which will be the type I error rate if both samples are from the same distribution.

In simulation, we could generate many sets of samples and repeat the certification process to better gauge the error rates. Each time, we grouped the sample events into bubbles and compared one set of boson sampling data P_{S1}^{Q} with various other samples (P_{S2}^{Q}, P_{S}^{C}, and P_{S}^{U}). A χ^2 statistic and a p-value were computed for each χ^2 test. This process was repeated for

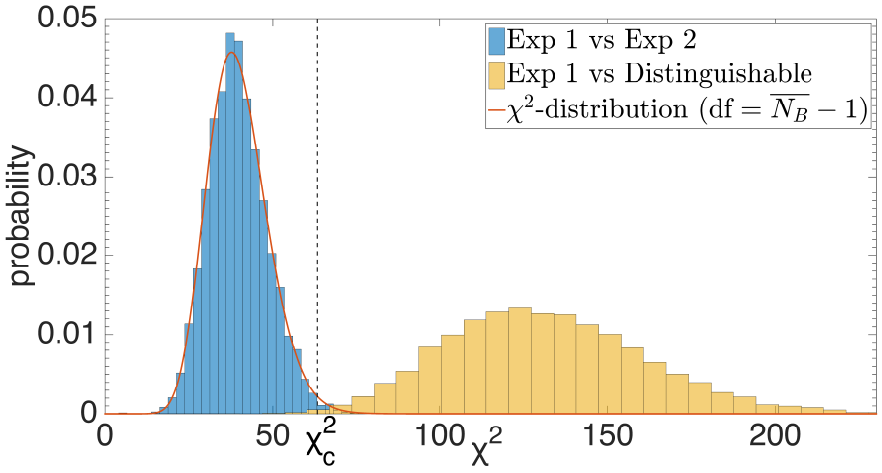

Figure 6.1.4: Distributions of the two-sample χ^2 test-statistics for the random unitary process with $\overline{N_B} \approx 40.8$. $N_s = 10000$ sets of samples are generated in the simulation and distributions of the χ^2 statistics between the corresponding pairs are plotted. The solid curve is the χ^2-distribution with df $= \overline{N_B} - 1$. The dashed line marks the cutoff χ^2 value at $\alpha = 1\%$. [326].

$N_s = 10000$ runs, with the distributions of the χ^2 statistics and p-values recorded. Fig. 6.1.4 presents the distributions of χ^2 statistics for the random unitary process with the average number of bubbles $\overline{N_B} \approx 40.8$. It can be seen clearly that the test statistics between P_{S1}^Q and P_{S2}^Q follow the χ^2 distribution with df $= \overline{N_B} - 1$, whereas those between P_{S1}^Q and P_S^C fall on the far tail of the χ^2 distribution, therefore offering a definitive answer regarding whether the samples are from the same distribution. More quantitatively, we calculate the pass rate R at a given significance level $\alpha = 1\%$. Specifically, if the p-value is greater than α, the comparison passes the test. Out of N_s tests, the pass rates in percentage are reported in Table 6.3. Between two sets of boson sampling data P_{S1}^Q and P_{S2}^Q, the pass rates $R \approx 99\%$ for all cases, with the type I error rates $1 - R$ being very close to α as expected. Between P_{S1}^Q and alternative samples (P_S^C and P_S^U), the pass rates reflect type II error. They can reach a few percent for smaller N_B but drop to $< 1\%$ as N_B increases. This also presents a tradeoff between the information obscured by the sampling noise without coarse-graining

Table 6.3: The pass rates R between simulated experimental sample 1 and various other samples. The two-sample χ^2 test is performed to assess whether they come from the same distribution. The significance level α is set at 1%. For each pair of generated samples, if the p-value is greater than α, the comparison passes the test. This is repeated for $N_s = 10000$ runs and pass rates are recorded. Noisy samples for the trapped-ion system include a 1% (3%) timing error, whereas a 1% (3%) random error is included in the random unitary matrix.

pass rate (%) compared to experimental sample 1						
	Trapped Ions			Random Unitary		
$\overline{N_B}$	24.2	40.5	69.9	25.9	40.8	70.5
Exp 2	99.1	99.2	99.1	99.1	99.2	99.1
Exp 2 (1% Noise)	98.0	98.2	98.2	98.9	98.9	99.1
Exp 2 (3% Noise)	71.1	77.1	75.9	98.3	98.4	98.6
Distinguishable	0	0	0	6.7	0.3	0.03
Uniform	0	0	0	0	0	0

and the information one discards by heavy coarse-graining. In general, to reduce sampling noise, each bubble should have a minimum number of observed events. For the χ^2 test to work reliably, this minimum number is conventionally chosen to be 10. For a detection count of $N_m = 10000$, a range of $20 \lesssim N_B \lesssim 100$ works well, with the requirement that the smallest bubble includes no less than 10 events (one could group together very small bubbles). Noticeably, this only depends on the number of detection counts, and does not scale up with the Hilbert space dimension. Our simulations demonstrate, in particular, that one could conclusively certify the boson sampling device with number of measurements less than 1% of the Hilbert space dimension.

Furthermore, we consider the effects of realistic noise in experiments. In the case of trapped ions, we included a 1% (3%) systematic error in the timing ($1\,\mu$s ($3\,\mu$s) shift in τ). This is also equivalent to a 1% (3%) error in the hopping amplitude $t_{ij} \sim \omega_z^2/\omega_x$ [325], which translates to a respective shift in the trapping frequencies in experiments. For the random unitary process, we added 1% (3%) random noise to the unitary matrix (see Appendix F.1.2

for details). As seen in Table 6.3, with small noise ($\sim 1\%$) the type I error rates are kept in check ($\lesssim 2\%$). When the noise becomes substantial, pass rates may drop sharply if the unitary process changes considerably. This also shows the sensitivity of our method to strong noise and it could serve as a stringent certification test. The dissimilar sensitivity to noise for the two systems is due to the different ways noise is included and natures of the noise (systematic versus random).

6.1.4 Conclusion

In conclusion, we have shown that useful and robust information can be extracted from the coarse-grained measurements for boson sampling. The coarse-grained distributions can be further used to certify the boson sampling device. We expect this method to be handy when experiments progress beyond classical capabilities. It should also be a useful tool for other generic many-body certification problems.

6.2 Quantum Supremacy for Simulating a Translation-Invariant Ising Spin Model

6.2.1 Introduction

In this section, we introduce an intermediate quantum computing model built from translation-invariant Ising-interacting spins. Despite being non-universal, the model cannot be classically efficiently simulated unless the polynomial hierarchy collapses. Equipped with the intrinsic single-instance-hardness property, a single fixed unitary evolution in our

model is sufficient to produce classically intractable results, compared to several other models that rely on implementation of an ensemble of different unitaries (instances). We propose a feasible experimental scheme to implement our Hamiltonian model using cold atoms trapped in a square optical lattice. We formulate a procedure to certify the correct functioning of this quantum machine. The certification requires only a polynomial number of local measurements assuming measurement imperfections are sufficiently small.

A universal quantum computer is believed to be able to solve certain tasks exponentially faster than the current computers [26, 27]. Over the past several decades, there has been tremendous progress in both theoretical and experimental developments of a quantum computer. In theory, pioneering quantum algorithms, including Shor's factorization [327] and an algorithm for linear systems of equations [328], achieve exponential speedup compared with the best-known classical algorithms. However, formidable experimental challenges still lie ahead in building a universal quantum computer large enough to demonstrate quantum supremacy. This calls for simpler tasks to demonstrate exponential quantum speedup without the need for a universal machine.

Several intermediate computing models have been developed recently for this purpose. Examples include boson sampling [36], quantum circuits with commuting gates (IQP) [329,330], sparse and "fault-tolerant" IQP [331, 332], the one-clean-qubit model [333, 334], evolution of two-qubit commuting Hamiltonians [335], quantum approximate optimization algorithm [336] and random or universal quantum circuit [39,337]. These models fall into the category of sampling problems: the task of simulating the distribution sampled from the respective quantum system is believed to be classically intractable. In particular, if a classical computer can efficiently simulate the distribution to multiplicative errors, the polynomial hierarchy, a generalization of P and NP classes, will have to collapse to the third level [338, 339], which

is believed to be unlikely in complexity theory. Several experiments (e.g. [37,38]) have been reported for realization of boson sampling in small quantum systems using photons. However, the system size is still limited, which prohibits demonstration of quantum supremacy beyond classical tractability.

In this section, we report three advancements towards demonstration of exponential quantum speedup in intermediate computing models. First, we formulate a new sampling model built from translation-invariant Ising-interacting spins, with strong connection to simulation of natural quantum many-body systems [28–30,340]. Our model only requires nearest-neighbor Ising-type interactions. The state preparation, the Hamiltonian and measurements are all constructed to be translation-invariant. Similar to Refs. [36, 330], we prove the distribution sampled from our model cannot be classically efficiently simulated based on complexity theory results under reasonable conjectures [329, 341–343]. An additional desirable feature of our model, which we call the 'single-instance-hardness' property, is that a single fixed circuit and measurement pattern are sufficient to produce a classically hard distribution once the system size is fixed. This differs from typical sampling problems, where an ensemble of instances (unitaries) with a large number of parameters is demanded for the hardness result to hold [36, 39, 329–337]. This feature offers a significant simplification for experiments since proof of quantum supremacy for this model requires implementation of only a single Hamiltonian and measurement pattern instead of a range of different realizations (typically an exponential number or even an infinite number). Ref. [36] also discussed the single-instance-hardness possibility in an abstract quantum circuit language, but no explicit circuit has been given thus far. Second, we propose a feasible experimental scheme to realize our model with cold atoms in optical lattices. The state preparation, engineering of time evolution and measurement techniques are achievable with the state-of-the-art technology.

Unlike photonic systems, cold atomic systems are much easier to scale up and reach a system size intractable to classical machines. Finally, we devise a scheme to certify our proposed quantum machine based on extension of the techniques developed in Refs. [344, 345]. Certification of functionality is critically important for a sampling quantum machine as a correct sampling is hard to be verified. Our certification scheme only requires a polynomial number of local measurements, assuming the measurement imperfections are sufficiently small.

Before introducing our model, let us make more precise the two different error requirements used here. Suppose the distribution $\{q_x\}$ is sampled from the quantum system with q_x being the probability of measuring the result x. Simulating $\{q_x\}$ to multiplicative errors translates to finding another distribution $\{p_x\}$ such that

$$\forall x, |p_x - q_x| \leq \gamma q_x \tag{6.2.1}$$

with $\gamma < 1/2$. This requirement seems too stringent for a classical sampler [36, 329]: even the quantum device may not achieve such a physically unrealistic precision. A more sensible choice is the variation distance error [36, 330, 346]

$$\sum_x |p_x - q_x| \leq \epsilon. \tag{6.2.2}$$

Other than physical motivation, another reason to use this quantification of error lies in the equivalence between search and sampling problems under the variation distance bound [347]: the separation between classical and quantum samplers under this error requirement will permit the quantum device to solve classically-intractable search problems [36]. This will have broad practical applications due to the ubiquity of search problems. For our Ising spin model, we will prove that the distribution produced by the quantum sampler can be certified

by local measurements to variation distance errors, assuming the measurement imperfections are sufficiently small.

Our model can be regarded as a special type of IQP with a constant circuit depth. A general IQP [329, 330] consists of Ising interactions between any pairs of spins and with varying strengths, while the sparse IQP [332] has $O(\sqrt{n}\log n)$ depth. Note that we are able to achieve such a low depth while maintaining classical hardness with variation distance errors (Eq. (6.2.2)) because we use a different complexity conjecture of average-case hardness. Ref. [331] proposed another type of IQP in constant circuit depth on the Raussendorf-Harrington-Goyal (RHG) lattice [348]. In their model, the classical hardness result is guaranteed with multiplicative errors under some local noise below a threshold. Their Hamiltonian is also translation-invariant but the measurements are not. Thus, this model and the general IQP do not have the single-instance-hardness property. The general interactions in IQP and the three-dimensional structure of the RHG lattice may be difficult to realize in experiments.

6.2.2 Translation-invariant Ising Model

Our main construction is based on measurement-based quantum computing models [349–351]. We first introduce a translation-invariant nonadaptive measurement-based quantum computation model with only one measurement basis required. With postselection, we show that it can simulate universal quantum computation. Next, we reinterpret the measurement-based model as a sampling model based on quantum simulation of two-dimensional (2D) spins with translation-invariant Ising interactions and local magnetic fields. It has been known that if a sampling model with postselection can simulate universal quantum computation, it will be hard to simulate classically with multiplicative error bounds unless the polynomial

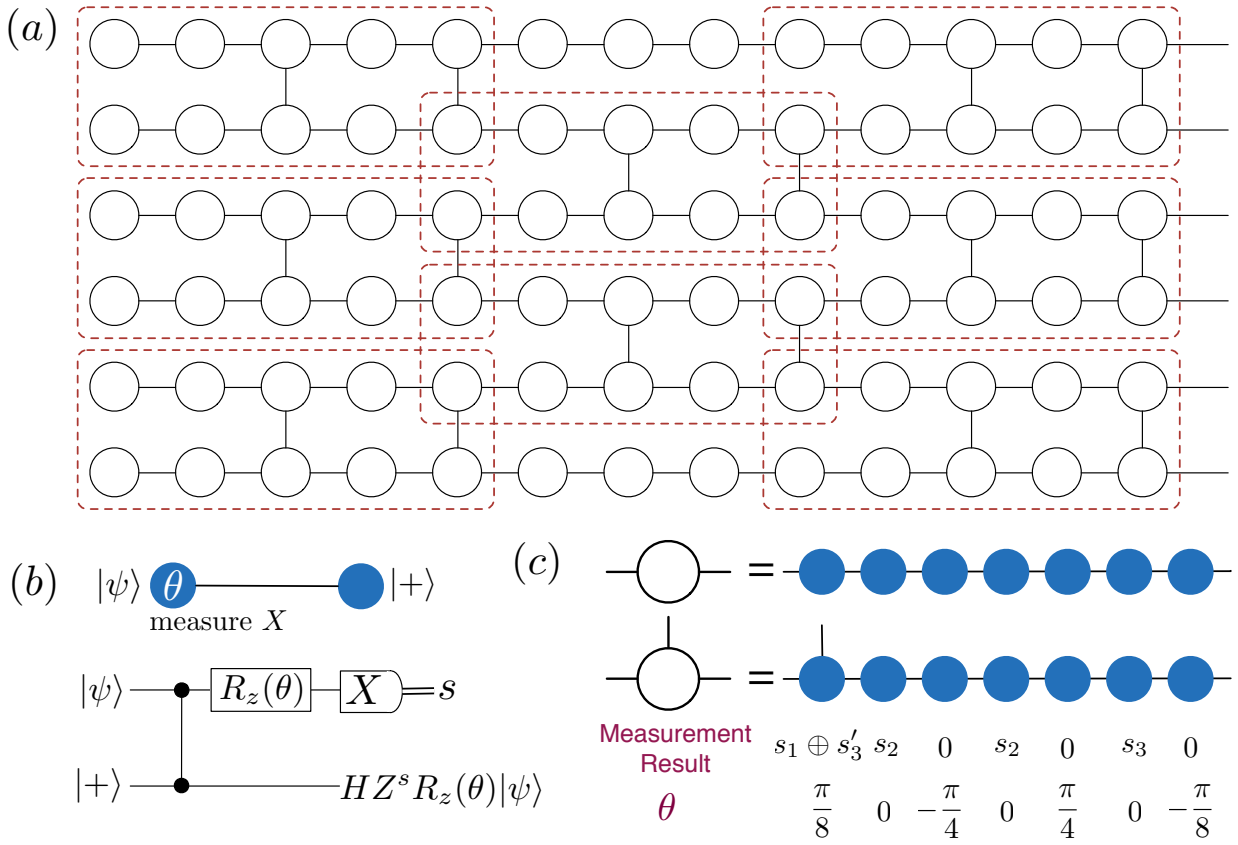

Figure 6.2.1: Schematic for the translation-invariant Ising model. (a) The brickwork state. Each circle represents a $|+\rangle$ state and each line denotes a CZ operation. (b) Propagation of the gate by measuring a qubit. (c) Each white circle with varying rotation angles is replaced by seven physical qubits with fixed rotation angles. The variation in the overall angle is encoded into different measurement outcomes.

hierarchy collapses to the third level [329,333,335]. We therefore conclude that our quantum Ising model will be classically intractable if the polynomial hierarchy does not collapse [339].

Consider the brickwork state shown in Fig. 6.2.1(a), which has been used for universal blind quantum computation [352]. Each circle represents a qubit prepared in the state $|+\rangle = (|0\rangle + |1\rangle)/\sqrt{2}$. A line connecting two neighboring circles denotes a controlled-Z operation on the qubits. As illustrated in Fig. 6.2.1(b), a measurement on one qubit in X

basis with measurement result s implements a gate $HZ^sR_z(\theta)$, where H is the Hadamard gate and $R_z(\theta) = e^{-i\theta Z/2}$ denotes a rotation on a single qubit. Ref. [352] proved that the model supports universal quantum computation given proper rotation angles θ and measurement results s (see Appendix for details). An important attribute of this model is that the graph structure and measurement patterns are independent of the computation. We further improve the model by making the angles θ translation-invariant. In terms of the sampling problem, this modification gives rise to the advantage of the single-instance-hardness property. It differs from other existing sampling problems, such as boson sampling, wherein an average over random quantum circuits is needed for the classical hardness result to hold.

To fix the angle pattern, we use seven qubits to replace one white circle (Fig. 6.2.1(c)). The primary goal is to encode rotation angle values into measurement outcomes, so that measurement postselection effectively realizes all necessary rotation angles. The basic building block is

$$HZ^sHR_z\left(-\frac{\theta}{2}\right)HZ^sHR_z\left(\frac{\theta}{2}\right) = R_z^s(\theta) \tag{6.2.3}$$

which can be realized by measuring four connecting qubits in X basis with rotation angles $\theta/2, 0, -\theta/2, 0$ and postselecting the results to be $0, s, 0, s$. This equality furnishes a mechanism to conditionally perform the rotation $R_z(\theta)$ based on the measurement result s. Because of the Solovey-Kitaev theorem [353], it is sufficient to implement $HR_z(k\pi/4), k \in \{0, \cdots, 7\}$

for universal computation [339]. Writing $k = s_1 s_2 s_3, s_i \in \{0, 1\}$ in binary form, we have

$$\begin{aligned} Z^{s_3} H R_z\left(\frac{k\pi}{4}\right) Z^{s_3'} =& Z^{s_3} H R_z^{s_1}(\pi) R_z^{s_2}\left(\frac{\pi}{2}\right) R_z^{s_3}\left(\frac{\pi}{4}\right) Z^{s_3'} \\ =& H R_z\left(-\frac{\pi}{8}\right) H Z^{s_3} H R_z\left(\frac{\pi}{4}\right) H Z^{s_2} \\ & H R_z\left(-\frac{\pi}{4}\right) H Z^{s_2} H Z^{s_1+s_3'} R_z\left(\frac{\pi}{8}\right). \end{aligned}$$

The extra term Z^{s_3} can be absorbed into the following gate and $Z^{s_3'}$ is left from the previous gate. Postselecting the measurement results as $s_1 \oplus s_3', s_2, 0, s_2, 0, s_3, 0$ with rotation angles $\pi/8, 0, -\pi/4, 0, \pi/4, 0, -\pi/8$, we can implement the gates $H R_z(k\pi/4)$ with $k = s_1 s_2 s_3$.

We now recast the nonadaptive measurement-based computation model as a sampling problem. A distribution can be sampled by measuring each spin in Fig. 6.2.1 in X basis. The above procedure is only used to prove the universality of the nonadaptive measurement-based model with a fixed circuit under postselection. We remark that neither postselection nor adaptive measurements are required for sampling the distribution. The circuit can be implemented by a unitary time evolution under a local Hamiltonian

$$\mathcal{H} = -\sum_{\langle i,j \rangle} J Z_i Z_j + \sum_i B_i Z_i \tag{6.2.4}$$

starting from the initial state $|+\rangle^{\otimes m \times n}$, with $m \times n$ being the number of spins. The second term imprints local rotation angles since $e^{-iB_i Z_i} = R_z(\theta_i)$, where $B_i = \theta_i/2$ characterizes the local Zeeman field strength on spin i. The evolution time and the reduced Planck constant $\hbar$ are set to unity. The first term performs the controlled-Z operations with $J = \pi/4$, where

$\langle i,j\rangle$ represents nearest-neighbor pairs connected by a line in Fig. 6.2.1. This can be seen as

$$\begin{aligned} CZ_{ij} &= e^{i\pi|1\rangle\langle 1|_i\otimes|1\rangle\langle 1|_j} = e^{i\pi/4(I_i-Z_i)\otimes(I_j-Z_j)} \\ &= e^{i\pi/4}e^{-i\pi/4I_i\otimes Z_j}e^{-i\pi/4Z_i\otimes I_j}e^{i\pi/4Z_i\otimes Z_j}. \end{aligned} \tag{6.2.5}$$

The two local magnetic field terms in the equation above can be absorbed into rotation angles, without changing Fig. 6.2.1(c) (see Appendix). The distribution sampled from this fixed 2D Ising model cannot be simulated by a classical computer in polynomial time to multiplicative errors unless the polynomial hierarchy collapses.

6.2.3 Implementation Proposal with Cold Atoms

The Hamiltonian in Eq. (6.2.4) exhibits a few properties that make it amenable for experimental implementation. First of all, it only consists of commuting terms, so in experiment one can choose to break up the Hamiltonian and apply simpler terms in sequence. Second, the state preparation, the Hamiltonian and measurements are all translation-invariant. This may greatly simplify the implementation for setups that can engineer the required unit cell. Another merit of our model originates from the single-instance-hardness feature. It ensures the sampling distribution after a single fixed unitary operation is already hard to simulate classically.

Here, we put forward a feasible experimental scheme based on cold atoms in optical lattices. A major difficulty arises from the special geometry required in the brickwork state. We propose to circumvent this problem by starting from the 2D cluster state (square lattice geometry) and reducing it to the brickwork state. In theory, this can be achieved by the "break" and "bridge" operations with measurement postselection as shown in Fig. 6.2.2 (see

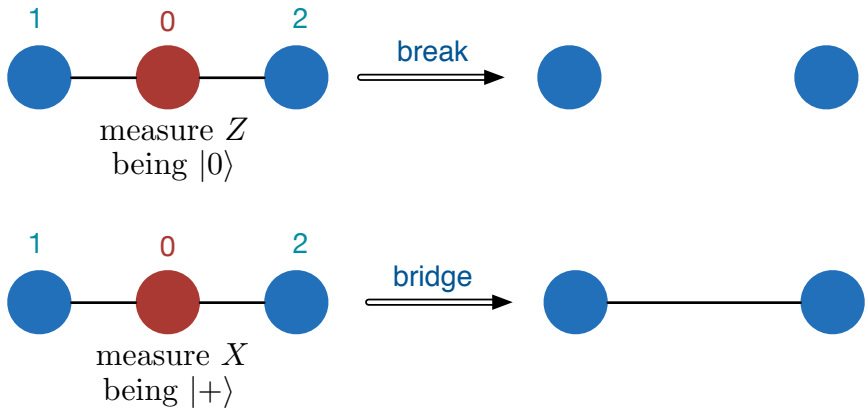

Figure 6.2.2: Break and bridge operations. Qubit 0 is first rotated by $R_z(\pi/2)$ before measured in Z and X basis respectively to perform the break and bridge operations.

Appendix for more details). In experiment, postselection is again unnecessary with regard to sampling, but one incurs an additional cost of measuring in both X and Z basis (the measurement pattern is still translation-invariant though). As a by-product, this procedure offers a concrete single-instance-hardness protocol to produce classically non-simulatable distribution from the cluster state.

A complete experimental procedure is as follows. First, create a Mott-insulator state of cold atoms in 2D optical lattices with a central core of unit filling. One atom with two relevant atomic levels (e.g., $|F = 1, m_F = -1\rangle$ and $|F = 2, m_F = -2\rangle$ hyperfine levels of ^{87}Rb atoms) can be trapped in each site forming a square lattice of qubits. A 2D cluster state can be created in a single operational step by controlled collisional interaction [354, 355]. The basic idea involves entangling neighboring atoms by spin-dependent transport together with controlled on-site collisions, which has been realized in experiment [355]. After generating the cluster state, one needs to impose the rotation angle pattern onto each qubit. This requires the ability to address individual atoms with diffraction-limited performance. Single-site addressing is currently one of the state-of-the-art quantum control techniques in cold atom

experiments [289, 356]. In particular, by using a digital micro-mirror device, it is possible to engineer holographic beam shaping with arbitrary amplitude and phase control [356]. To imprint the individual phases, one can make use of spin-dependent AC Stark shifts [289] with beam amplitude patterns given by the rotation angles. The amplitude hologram controls the strength B_i and realizes the second term in the Hamiltonian in Eq. (6.2.4). Finally, spin measurements can be performed on each site, with single-site-resolved imaging techniques [131, 132]. Because some spins have to be measured in Z basis, they should be rotated by individual addressing techniques before all atoms can be measured in X basis.

6.2.4 Simulation and Certification with Variation Distance Errors

So far, we have shown that our Ising spin model is classically intractable with multiplicative error bounds. Similar to what have been attained in boson sampling [36] and IQP [330], we can also prove classical hardness to variation distance error bounds if we assume the "worst-case" hardness result can be extended to "average-case". More specifically, let us define the partition function of

$$\mathcal{H}_x = \mathcal{H} + \frac{\pi}{2}\sum_i x_i Z_i, \text{ where } x_i \in \{0,1\} \tag{6.2.6}$$

to be $\mathcal{Z}_x = \mathrm{tr}\left(e^{-\beta\mathcal{H}_x}\right)$, setting the imaginary temperature unit as $\beta \equiv 1/k_B T = i$. In the Appendix, we prove that approximating $|\mathcal{Z}_x|^2/2^{mn}$ by $\widetilde{|\mathcal{Z}_x|^2}/2^{mn}$ to a mixture of multiplicative and additive errors such that

$$\left|\frac{\widetilde{|\mathcal{Z}_x|^2}}{2^{mn}} - \frac{|\mathcal{Z}_x|^2}{2^{mn}}\right| \leq \frac{1}{\mathrm{poly}(n)}\frac{|\mathcal{Z}_x|^2}{2^{mn}} + \frac{\epsilon}{\delta}(1+o(1)) \tag{6.2.7}$$

with $\epsilon/\delta < 1/2$ is #P-hard in the worst-case. Our classical intractability result requires lifting the #P-hardness of the estimation from the worst-case to the average-case: picking any $1-\delta$ fraction of instances x, it is still #P-hard. This conjecture is similar to the one used in Ref. [330] except that they reduced the mixture of errors to simply multiplicative errors. All the known classically intractable quantum sampling models with variation distance errors require a similar average-case complexity conjecture.

Thus, with reasonable assumptions, our Ising spin model is also classically intractable with variation distance bounds. Using techniques similar to those in Refs. [344, 345], we can in addition certify the correct functioning of a quantum device, with only a polynomial number of local measurements. Suppose $\{q'_x\}$ is the distribution sampled from our quantum device with the final state ρ' (state before measurement); the ideal ones are denoted as $\{q_x\}$ and ρ. The total variation distance between distributions $\{q_x\}$ and $\{q'_x\}$ can be bounded by [26]:

$$\sum_x |q_x - q'_x| \leq D(\rho, \rho'), \tag{6.2.8}$$

where $D(\rho, \rho') = \mathrm{tr}(|\rho - \rho'|)/2$ is the trace distance between states ρ and ρ'. Hence, if we can bound the trace distance $D(\rho, \rho') < \epsilon$, we can also bound the total variation distance. Note, however, this does not allow us to estimate q_x in experiment: statistical errors always kick in to thwart any polynomial-time efforts to estimate the distribution due to the exponential suppression of some q_x. We bypass statistical errors by assuming the correctness of quantum mechanics. To sample from $\{q'_x\}$ in experiment though, measurement imperfections may cause deviations in variation distance. However, if measurement imperfections on each spin are local and bounded by $O(\epsilon/(mn))$ [339], we can still correctly certify the quantum device. Below, we show how to bound $D(\rho, \rho')$ by a polynomial number of local measurements.

As a graph state, the brickwork state in Fig. 6.2.1(a)(c), is the unique ground state of the 4-local Hamiltonian

$$H_{\text{brickwork}} = \sum_i \frac{I - X_i \prod_{j\in\text{neighbor of } i} Z_j}{2}. \tag{6.2.9}$$

Each qubit i is connected to at most three neighboring ones, and the energy gap from the ground state is 1. The ideal state ρ is the brickwork state acted by some single qubit rotations $R_z(\theta_i)$. It is therefore the unique ground state of the Hamiltonian

$$\begin{aligned} H'_{\text{brickwork}} &= \prod_i R_z(\theta_i) H_{\text{brickwork}} \prod_j R_z^\dagger(\theta_j) \\ &= \sum_i \frac{I - R_z(\theta_i) X_i R_z^\dagger(\theta_i) \prod_{j\in\text{neighbor of } i} Z_j}{2}. \end{aligned}$$

This Hamiltonian is still 4-local, with ground state energy gap 1. Using the weak-membership quantum state certification protocol in Ref. [344], one can measure each local term of $H'_{\text{brickwork}}$ by a polynomial number of times to obtain a good estimation of $\langle H'_{\text{brickwork}}\rangle$ averaged over ρ'. The estimation will be efficient due to Hoeffding's bound and the finite norm of each local term. Since the ground state energy gap is constant, $\langle H'_{\text{brickwork}}\rangle > 0$ implies a finite component of excited states is present in ρ'. Conversely, a small $\langle H'_{\text{brickwork}}\rangle$ will be able to bound $D(\rho, \rho')$. More quantitatively, we show in the Appendix that with confidence level $1 - 2^{-O(r)}$, using $O(m^2n^2r/\epsilon^4)$ measurements on each local term is sufficient to certify $\sum_x |q_x - q'_x| \leq \epsilon$, provided the measurement imperfections on each spin are bounded by $O(\epsilon/(mn))$. Similar hardness and certification results hold if we start from the cluster state as in our experimental proposal [339]. In that case, 5-local measurements are needed.

The IQP certification protocol developed in Ref. [344] requires a much stronger quantum simulator than the IQP simulator itself since they need to generate all the history states [357].

In contrast, our certification protocol only requires preparing the state ρ' itself. This is relevant in light of demonstrating quantum supremacy [35] using practical quantum many-body systems, instead of resorting to a universal quantum simulation device.

6.2.5 Discussion

In summary, we have introduced a translation-invariant Ising spin model and shown that it is classically intractable unless the polynomial hierarchy collapses. Because our average-case conjecture bypasses the anticoncentration property used in Refs. [36, 330, 332], the classical simulability result under constant-strength local noise [332] may not apply to our model. Whether our model is robust to noise requires further analysis. There is also a natural connection between our model and sampling models of random quantum circuits such as the one in Ref. [39]: measurement on qubits in the first $n-1$ columns in our model corresponds to choosing one instance of a random circuit due to the relation between our model and measurement-based quantum computing. With the advantageous single-instance-hardness property, the amenability to experimental implementation and certification of the quantum machine, we develop a full picture of using our model to demonstrate quantum supremacy. This may shed light on the likely exponential gap in computational power between a classical and a quantum machine.

CHAPTER VII

Conclusion and Outlook

In this dissertation, we have touched on a wide range of topics related to the application of atomic systems. In particular, we focused on their applications in topological phases of matter, quantum computation and quantum simulation. In Chapter II, we introduced Hopf insulators and presented an experiment on the simulation of Hopf insulators with a nitrogen-vacancy center. In Chapter III, we included a number of theoretical studies on the simulation of topological phases with cold atomic systems. In particular, we studied chiral topological insulators in detail and presented a general method to measure topological invariants. We also found a new type of topological rings, called Weyl exceptional rings. In Chapter IV and V, we moved to the application of atomic systems in quantum computation and quantum simulation. We tackled the problem of micromotion in a two-dimensional Paul trap and show that the architecture is promising for scalable quantum computation. We also proposed a general method to perform Hamiltonian tomography, which is essential for benchmarking quantum computation and quantum simulation. In Chapter VI, we introduced an experimental friendly scheme to certify a quantum boson sampling machine and put forward a new Ising-spin model that may be used for demonstrating quantum supremacy.

There are a number of related future directions, some of them are currently under intensive

study. We will discuss a few directions below.

Strongly Correlated Regime and Nonequilibrium Quantum Dynamics

In this dissertation, we have mainly focused on weakly interacting systems for the application in topological phases of matter. Chapter II and Chapter III centered on the study and simulation of topological phases of free fermions. Strongly correlated systems exhibit much richer physics, but they are at the same time considerably more difficult to understand—that is when the use of atomic systems becomes highly relevant. Experimental realizations of some strongly correlated topological systems, such as bosonic symmetry protected topological phases [11] and those with topological order [358, 359], are highly desired. Along another path, quantum simulation with atomic systems may also shed light on some long-standing problems in condensed matter physics, such as the high-T_c superconductivity. The recent push for low entropy and the observation of antiferromagnetic spin correlations in the Fermi-Hubbard simulation have sparked great optimism in the community [360–362].

Nonequilibrium many-body quantum dynamics is another very difficult yet extremely interesting area of physics [363]. The question of how and when thermalization persists in a closed many-body system has generated strong interest recently [364], including the topic of eigenstate thermalization [365–367] and many-body localization [368, 369]. This enthusiasm is also partly fueled by the rapid experimental progress in recent years [370–376], which is bound to stimulate significant progress in both theory and experiment along these directions.

Other Approach to Scalable Quantum Computation

Scalability is undoubtedly one of the greatest challenges in realizing practical quantum computation. There are a number of other novel approaches for scalable quantum computation, some of them unique to the specific platforms. One approach common to all platforms is the modular approach [230, 377, 378]: a small number of qubits can be stored in each module, where they can be well shielded from the environment; some qubits can then be used as hubs to connect separate modules. In this way, many more qubits can be precisely and coherently controlled with slight sacrifice in direct connectivity.

Quantum Supremacy

In the introductory chapter and in Chapter VI, we discussed quantum supremacy, the scenario where quantum computation exceeds classical simulation capabilities. Last year, IBM announced the public availability of a 5-qubit programmable quantum computer based on the superconducting transmon device. A programmable 5-qubit trapped ion system has also been demonstrated soon after [379, 380]. We may very soon see a well-controlled quantum computer with, say 50 qubits, outperforming all classical computers [39]. It is fair to say that quantum computers are now ready to move out of the lab. With joint forces between the academia and the industry, we believe quantum supremacy can be experimentally demonstrated in the very near future.

APPENDICES

APPENDIX A

Experimental Observation of Hopf Insulators

A.1 Experimental Methods

A.1.1 Experimental Setup

We excite and collect fluorescence with a home-built confocal oil immersion microscopy with a 1.49NA objective (Olympus 60X) and a single mode fiber (SM600). A 532 nm diode laser (Coherent Sapphire), with an AOM (ISOMET 1250C) double pass configuration, is used to initialize and detect the electron spin. Microwave is generated by an analog signal generator (Keysight N5181B) and mixed with an AWG (Tek AWG70002A) by an IQ mixer (Marki IQ 1545LMP) for phase and amplitude control. A waveguide with impedance matching is deposited onto the cover glass for the conduction of microwave. The sample is mounted on the cover glass, which is further mounted on a closed-loop piezo (Physik Instrument P-611.3) with sub-micrometer resolution.

The sample is a type IIa single crystal diamond synthesized by chemical vapor deposition (Element Six). It is irradiated by 10 MeV electron beam with dosage $10^{14}\,\mathrm{cm}^{-3}$ and annealed

at 800°C in vacuum for two hours. Solid immersion lens with 10 μm radius is randomly fabricated on the sample by a focused ion beam. We get 250,000 counts per second with a signal-to-noise ratio 21 : 1 with 1 mW excitation power. A permanent magnetic field is applied on the sample and aligned to the NV axis. A magnetic field of strength 510 G is sufficient for nuclear polarization by excited state level anti-crossing [381].

A.1.2 Adiabatic Passage and Data Collection

The final Hamiltonian $H_{\mathbf{k}} = \hbar\Omega\,\mathbf{u}(\mathbf{k})\cdot\sigma$ at a particular parametric momentum point $\mathbf{k}$ is first normalized to $\max\{\Omega\sqrt{u_x^2+u_y^2}, \Omega u_z\} = 2\pi \times 20.83\,\text{MHz}$. For each adiabatic passage, we start from $u_x = u_y = 0$, $\Omega u_z = -2\pi \times 20.83\,\text{MHz}$ and prepare the initial state $|0\rangle$, which is the ground state of the initial Hamiltonian. We then linearly ramp Ωu_x to the maximum Rabi frequency $2\pi \times 20.83\,\text{MHz}$, linearly ramp u_z to the final value, and finally ramp u_x and u_y to the final Hamiltonian before taking measurements. Each linear ramp takes 500 ns, with the total time of the microwave being 1.5 μs. In order to get high fidelity data, the AWG works at 8 GHz sample rate.

At each momentum point $\mathbf{k}$, the initialization, adiabatic passage, and measurements are repeated 1.25×10^6 times, collecting about 9.3×10^4 photons. For each round, the fluorescence of the final state from the adiabatic passage is compared with the fluorescence under the $|0\rangle$ state, where the latter is used for normalization. Experimental density matrices are obtained by state tomography through the maximal likelihood estimation. The fidelity of each density matrix is calculated by comparing it with the ideal state, and the overall average fidelity from all the measured momentum points is 99.2% (99.7% - 98.1% with 96% confidence interval). The error bars and the confidence intervals are calculated through numerical Monte Carlo

simulation by assuming a Poisson distribution for the photon counts from the detector. A large contribution to the infidelity is actually from the statistical error associated with a finite number of photon counts. From the numerical simulation, we find that even with a perfectly prepared quantum state, the statistic error alone with the same number of photon counts as we collected in experiments will give an average fidelity of 99.4%. So the fidelity of the prepared state by the process of adiabatic passage is high due to existence of a significant energy gap for the topological phase.

A.2 Measuring the Hopf Invariant and Theoretical Scaling

In this section, we present more details on our methods to extract the Hopf index from experimental data. We also theoretically extrapolate the data to larger grid sizes. The central idea is to use tomographic methods to measure the topological invariant. This follows primarily from Ref. [42, 47]. We outline the essential procedure here for completeness.

The Hopf invariant is defined in the main text. In the experiment, we simulate the ground state of the Hopf Hamiltonian by adiabatically ramping from the $|0\rangle$ state (ground state of the Hopf Hamiltonian at $\mathbf{k} = (0, 0, 0)$) to other discrete momentum points $\mathbf{k_J}$. We can subsequently perform state tomography to map out the ground state manifold $|\psi(\mathbf{k_J})\rangle$. However, to calculate the Berry curvature from the states involves taking the derivatives $\partial_{k_{\nu,\tau}}$ (finite difference in our discrete data). This will lead to problems due to the gauge (phase) ambiguities of the wavefunction $|\psi(\mathbf{k_J})\rangle \to e^{i\varphi(\mathbf{k_J})}|\psi(\mathbf{k_J})\rangle$, where $e^{i\varphi(\mathbf{k_J})}$ is an arbitrary phase that can vary with $\mathbf{k_J}$ and is not experimentally observable. In cases where the Chern num-

ber is nonzero, gauge obstruction, in particular, forbids a well-defined global smooth Berry connection. To circumvent this difficulty, we use a discretized version of the Berry curvature defined as [47, 158]

$$\mathcal{F}_\mu(\mathbf{k_J}) \equiv \frac{i}{2\pi}\epsilon_{\mu\nu\tau} \ln U_\nu(\mathbf{k_J}) U_\tau(\mathbf{k_{J+\hat{\nu}}}), \tag{A.2.1}$$

where the $U(1)$-link is $U_\nu(\mathbf{k_J}) \equiv \langle\psi(\mathbf{k_J})|\psi(\mathbf{k_{J+\hat{\nu}}})\rangle / |\langle\psi(\mathbf{k_J})|\psi(\mathbf{k_{J+\hat{\nu}}})\rangle|$ with $\hat{\nu} = \hat{x}, \hat{y}, \hat{z}$, a unit vector in the corresponding direction. Here, the local gauge ambiguity cancels out.

This tomographic method offers a number of advantages [47]. First, it is generally applicable to any spatial dimension and to all topological invariants that can be expressed as some variant of an integral over Berry curvature (connection). Second, the topological invariants can be extracted from the states alone, without referencing to the Hamiltonian. Third, this method is highly robust to experimental imperfections and, in particular, finite discretizations.

In the experiment, we perform state tomography at various momentum points $\mathbf{k_J}$. Discrete Berry curvature is then computed using Eq. (A.2.1). Berry connection $A_\mu(\mathbf{k_J})$ can be obtained by Fourier transforming the equation $\nabla \times \mathbf{A} = \mathbf{F}$ with the Coulomb gauge $\nabla \cdot \mathbf{A} = 0$. Finally, we attain the value of the Hopf invariant χ by a discrete sum over all momentum points. As we notice from the main text, a grid size of $10 \times 10 \times 10$ is already capable of producing highly accurate estimation of the quantized topological invariant (with error $\leq 5\%$).

In Fig. A.2.1, we present theoretical scalings to larger grid sizes. We can see that the discretization error reduces when N increases. The deviation from the quantized value drops to around 10^{-2} for $N = 20$ for $h = 0$ and $h = 2$. The theoretical calculations for

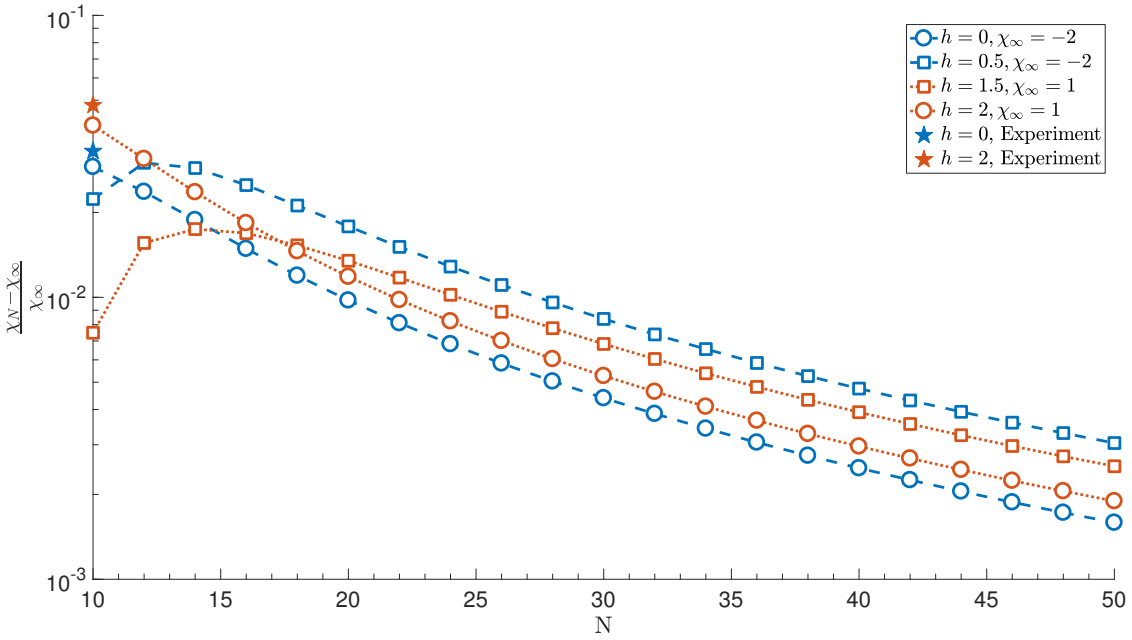

Figure A.2.1: Theoretical scaling of the deviation of the Hopf index χ_N from the ideal value χ_∞. The grid size is $N \times N \times N$. Experiments are performed at $N = 10$. The apparently smaller deviation in the case of $h = 0.5, 1.5$ for $N \leq 15$ is likely to be coincidental.

$h = 0.5$ and $h = 1.5$ are also shown. They are closer to the topological phase transition point $h = 1$, resulting in a more pronounced finite size effect. It is apparent, however, for all cases the finite-grid estimation approaches the correct quantized value as N becomes larger. The topological property is robust to perturbations and changes in parameters as long as the topological gap is maintained.

A.3 Three Dimensional Hopf Spin Texture

A two-dimentional (2D) slice of the spin texture is presented in the main text. Here, we include the full 3D spin texture from experimental data for both $h = 2$ (Fig. A.3.1) and $h = 0$ (Fig. A.3.2). Since the Hopf insulator is an intrinsic 3D topological insulator, com-

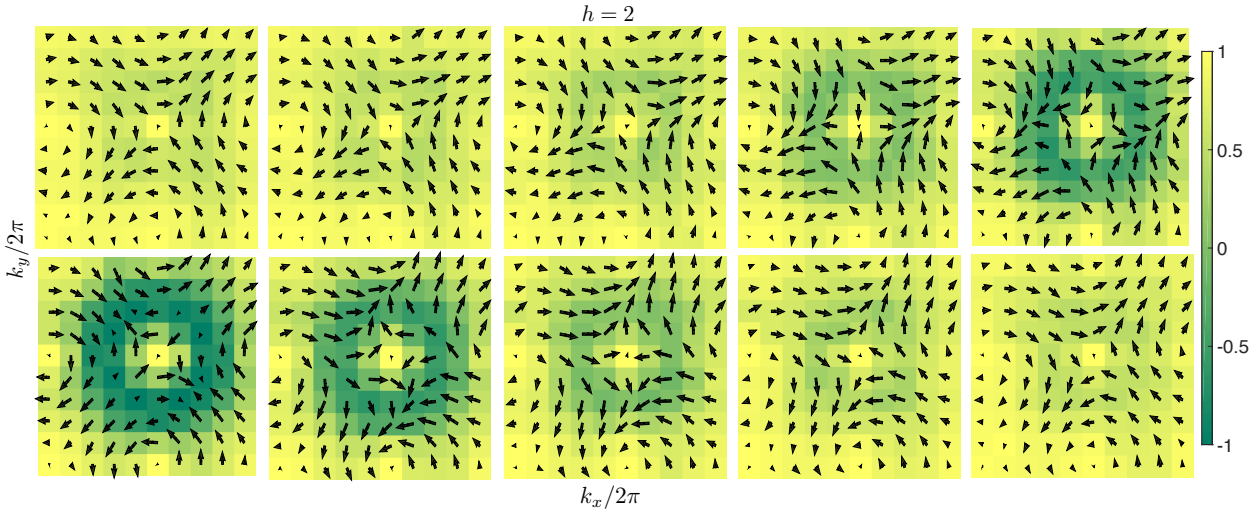

Figure A.3.1: Each layer of spin textures for $k_z = 0, 0.1, 0.2, \cdots, 0.9 \times 2\pi$ and $h = 2$. For each subfigure, $k_x/2\pi$ and $k_y/2\pi$ vary from 0 to 0.9 with an equal spacing of 0.1. At each momentum point $\mathbf{k_J}$, the state can be represented on the Bloch sphere. The arrows in the plane depict the x-y direction of the Bloch vector and the color labels the magnitude of the z component of the Bloch vector. This 3D spin texture represents a Hopfion with a Hopf invariant $\chi = 1$.

plete information can be captured only by the 3D spin texture. For $h = 0$, we have a higher (magnitude) topological index $\chi = -2$, so the spin texture is considerably more complex than that for $h = 2$. Physically, a nonzero Hopf index guarantees the spin texture can never be untwisted to be a trivial one (e.g. all point to the same direction), unless one crosses a topological phase transition. Remarkably, the Hopf spin texture is a representation of the long sought-after Hopfions, which are 3D topological solitions with widespread applications [42].

A.4 Hopf Fibration & Stereographic Coordinates

For simplicity and clarity, we did not use stereographic coordinates to represent the experimental data in the main text. The data were depicted in $\{k_x, k_y, k_z\} \in [0, 2\pi)$ without gluing

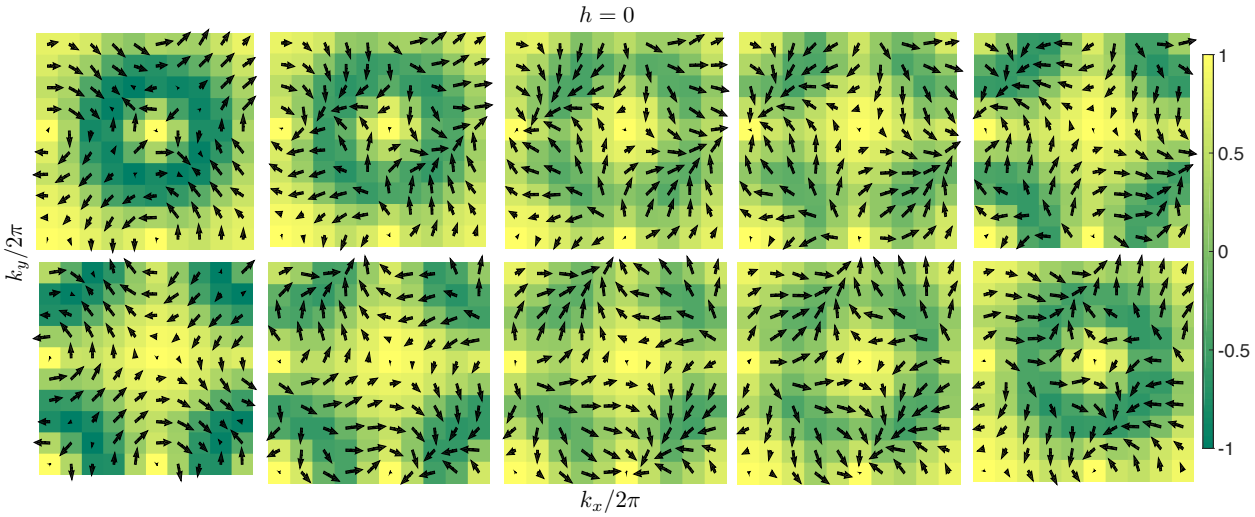

Figure A.3.2: Each layer of spin textures for $k_z = 0, 0.1, 0.2, \cdots, 0.9 \times 2\pi$ and $h = 0$. Spin representations and color scheme are the same as in Fig. A.3.1. This 3D spin texture represents a Hopfion with a Hopf invariant $\chi = 2$.

the boundaries. It did not matter for the particular spin preimage contours we measured because they form closed loops without crossing the boundaries (i.e., $k_{x,y,z} = 0$ or 2π). However, it may not be the case for other spin preimages, especially for higher Hopf index. When that happens, we have to visualize it properly on the torus $\mathbb{T}^3$; however, knots and links on the torus are difficult to see. Instead, we can map them to $\mathbb{R}^3$ for visualization. Indeed, our Hamiltonian mapping from the Brillouin zone $\mathbb{T}^3$ to the Bloch sphere $\mathbb{S}^2$ can be decomposed to two maps [42]

$$\mathbb{T}^3 \xrightarrow{g} \mathbb{S}^3 \xrightarrow{f} \mathbb{S}^2. \tag{A.4.1}$$

The map g is

$$\begin{aligned} \eta_\uparrow(\mathbf{k}) &= \sin k_x - i \sin k_y, \\ \eta_\downarrow(\mathbf{k}) &= \sin k_z - i(\cos k_x + \cos k_y + \cos k_z + h), \end{aligned} \tag{A.4.2}$$

where (k_x, k_y, k_z) lives on $\mathbb{T}^3$ and $(\eta_1, \eta_2, \eta_3, \eta_4) = (\mathrm{Re}[\eta_\uparrow], \mathrm{Im}[\eta_\uparrow], \mathrm{Re}[\eta_\downarrow], \mathrm{Im}[\eta_\downarrow])$ are points on $\mathbb{S}^3$ (up to a trivial normalization). The map f is the Hopf map

$$u_x + iu_y = 2\eta_\uparrow \bar{\eta}_\downarrow,\ u_z = (|\eta_\uparrow|^2 - |\eta_\downarrow|^2), \tag{A.4.3}$$

and the composition of the two maps produces the Hamiltonian written in the main text, $H_{\mathbf{k}}/\hbar\Omega = f \circ g(\mathbf{k}) = \mathbf{u}(\mathbf{k}) \cdot \sigma$. Therefore, the knots and links can be visualized in $\mathbb{R}^3$ from the stereographic coordinates of $\mathbb{S}^3$, for example, defined as

$$(x, y, z) = \frac{1}{1 + \eta_4}(\eta_1, \eta_2, \eta_3), \tag{A.4.4}$$

where (x, y, z) are points of $\mathbb{R}^3$. In the main text figure, the Hopf fibration is drawn under the Hopf map f. For a fixed point on the Bloch sphere $\mathbb{S}^2$, the preimage (fiber) of the point forms a closed loop in $\mathbb{S}^3$, which is then visualized in $\mathbb{R}^3$ via the stereographic coordinates. To relate the schematic to our physical system, the preimage of a fixed spin orientation measurement (on the Bloch sphere) lives in the momentum space $\mathbb{T}^3$, which can then be mapped to $\mathbb{S}^3$ via the map g and subsequently $\mathbb{R}^3$ via the stereographic coordinates.

The Hopf map from $\mathbb{S}^3 \to \mathbb{S}^2$ can be modified to the generalized Hopf map [43] where a variety of knot and link structures can be revealed from Hopf insulators [42]. We emphasize that the change of coordinates is only for the purpose of easy visualization. The nontrivial link induced by the nonzero Hopf invariant cannot be unlinked, in either $\mathbb{R}^3$, $\mathbb{S}^3$ or $\mathbb{T}^3$ since the maps between them are all continuous.

A.5 Finite Resolution & ϵ-neighborhood of Spin Orientations

To reveal the nontrivial Hopf fibration and linking structures of the spin preimage loops, in the main text, we took experimental data on the theoretically known contours. We observed that the experimentally measured spin orientations agree well with the theory (with fidelity $F \gtrsim 99\%$ and $|\mathbf{S}_{\rm exp} - \mathbf{S}_{\rm th}| \lesssim 0.08$). The nontrivial links as well as the topological phase transition were readily detected from experimental data. In situations where the theoretical contours are unknown, one has to measure the spin orientations at discrete momentum data grids and deduce the preimage loops with a prescribed tolerance threshold. In this case, we can define an ϵ-neighborhood of the desired spin orientation, $\mathbf{S}_{\rm th}$, as [42]

$$N_\epsilon(\mathbf{S}_{\rm th}) = \{\mathbf{S}_{\rm exp}(\mathbf{k}) :\ |\mathbf{S}_{\rm exp}(\mathbf{k}) - \mathbf{S}_{\rm th}| \leq \epsilon\}. \tag{A.5.1}$$

The choice of ϵ depends on the actual experimental data; it should be chosen large enough to contain sufficient data points and small enough to display a clear loop structure. This scheme is also applicable to the case when we are presented with a 3D spin texture data and aim to ascertain whether it exhibits nontrivial knot or loop structures.

To show the method works well with limited experimental data resolution and is reasonably robust to the choice of ϵ, here we use our experimental data on the $10 \times 10 \times 10$ grid to map out the nontrivial loops at $h = 2$. Fig. A.5.1 shows the results with $\epsilon = 0.3$ and $\epsilon = 0.35$ respectively. With larger tolerance, it is evident that more experimental data points are included. Being a topological property, the nontrivial loop structure is reasonably robust to the choice of ϵ. Imposing the theoretical curves as guides to the eye, the nontrivial link is

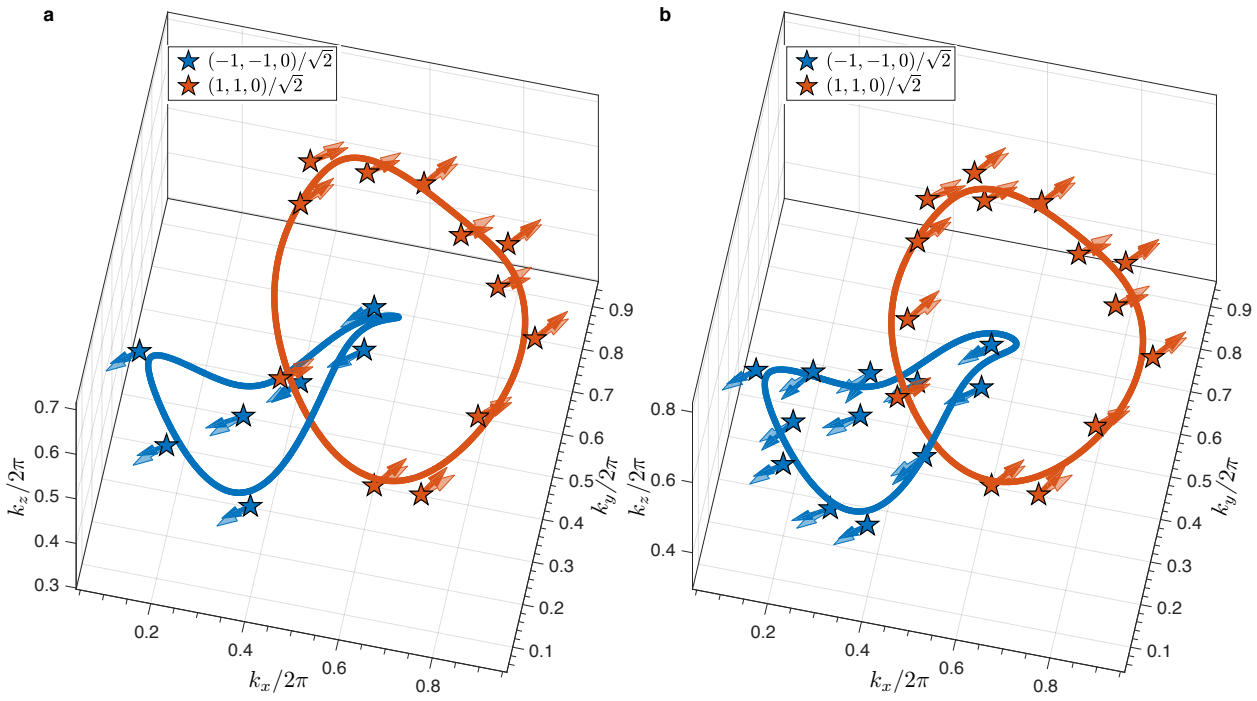

Figure A.5.1: Preimage contours using the experimental data on the $10 \times 10 \times 10$ grid for $h = 2$. Stars are experimental data on the discrete grid satisfying the condition $|\mathbf{S}_{\text{exp}} - \mathbf{S}_{\text{th}}| \leq \epsilon$, where $\mathbf{S}_{\text{th}} = (-1,-1,0)/\sqrt{2}$ or $(1,1,0)/\sqrt{2}$ for the blue and red data respectively. Solid arrows show experimentally measured spin orientations, $\mathbf{S}_{\text{exp}}$. Transparent arrows show theoretical directions, $\mathbf{S}_{\text{th}}$, imposed on the experimental grids. Solid lines are theoretical preimage curves. (**a**) $\epsilon = 0.3$. (**b**) $\epsilon = 0.35$.

discernible with experimental data. We remark that the discrepancies are predominantly due to the coarse discretization. With more experimental data on a finer grid, e.g. a $20 \times 20 \times 20$ grid, the preimage loops and the nontrivial links should be clearly visible even without the theoretical curve; they are also expected to be highly robust to small perturbations such as experimental errors, change in Hamiltonian parameters, and the choice of the tolerance threshold.

APPENDIX B

Chiral Topological Insulators: Proposal and Magneto-electric Effect

B.1 Experimental Proposal of Chiral Topological Insulator

B.1.1 Realization of the Effective Hamiltonian

In this section of the Appendix, we provide more details on the realization scheme of the chiral topological insulator Hamiltonian. Details on the parameter estimation with Wannier functions and additional density of states plots are included.

In the main text, we use Raman-assisted tunneling to realize the effective Hamiltonian of

the chiral topological insulator given by

$$
\begin{aligned}
H &= t\sum_{\mathbf{r}}\left[\left(2ihc^{\dagger}_{3,\mathbf{r}}c_{2,\mathbf{r}}+\text{H.c.}\right)+H_{\mathbf{rx}}+H_{\mathbf{ry}}+H_{\mathbf{rz}}\right],\\
H_{\mathbf{rx}} &= ic^{\dagger}_{3,\mathbf{r}-\mathbf{x}}(c_{1,\mathbf{r}}+c_{2,\mathbf{r}})-ic^{\dagger}_{3,\mathbf{r}+\mathbf{x}}(c_{1,\mathbf{r}}-c_{2,\mathbf{r}})+\text{H.c.},\\
H_{\mathbf{ry}} &= -c^{\dagger}_{3,\mathbf{r}-\mathbf{y}}(c_{1,\mathbf{r}}-ic_{2,\mathbf{r}})+c^{\dagger}_{3,\mathbf{r}+\mathbf{y}}(c_{1,\mathbf{r}}+ic_{2,\mathbf{r}})+\text{H.c.},\\
H_{\mathbf{rz}} &= 2ic^{\dagger}_{3,\mathbf{r}-\mathbf{z}}c_{2,\mathbf{r}}+\text{H.c.}
\end{aligned}
\tag{B.1.1}
$$

In the following, we provide some complementary details on the realization scheme. The major difficulty is to realize the spin-transferring hopping terms $H_{\mathbf{rx}}, H_{\mathbf{ry}}, H_{\mathbf{rz}}$ along each direction. Let us focus on a single term first, $H^{(1)}_{\mathbf{rx}} = ic^{\dagger}_{3,\mathbf{r}-\mathbf{x}}(c_{1,\mathbf{r}}+c_{2,\mathbf{r}})$. This corresponds to an atom in the spin state $|1_x\rangle = (|1\rangle+|2\rangle)/\sqrt{2}$ at site $\mathbf{r}$ hopping to site $\mathbf{r}-\mathbf{x}$ while changing the spin state to $|3\rangle$ with hopping strength $i\sqrt{2}$. Diagrammatically, it can be visualized as

$$
ic^{\dagger}_{3,\mathbf{r}-\mathbf{x}}(c_{1,\mathbf{r}}+c_{2,\mathbf{r}}) \qquad \Longleftrightarrow \qquad x\text{-direction:} \quad |3\rangle \overset{i\sqrt{2}}{\curvearrowleft} |1_x\rangle \overset{\times}{\curvearrowright}
\tag{B.1.2}
$$

where $\overset{i\sqrt{2}}{\curvearrowleft}$ means hopping along that direction with strength $i\sqrt{2}$ and $\overset{\times}{\curvearrowright}$ indicates hopping is forbidden. This hopping term can be effected by two Raman beams $\Omega_1^x = i\sqrt{2}\Omega_0 e^{ikz}$ and $\Omega_1^{\pi} = \Omega_0 e^{ikx}$ as shown in Fig. B.1.1.

The large single-photon detuning δ ensures that the population of the excited state, estimated by $|\Omega_0/\delta|^2$, is negligible. The two-photon detuning Δ_x matches the linear energy shift of the lattice per site, so that it only allows $|1_x\rangle$ to hop to the left, and the other direction is forbidden by an energy mismatch $2\Delta_x$. The addressing of spin states is done by polarization selection rule. The original spin basis $|1\rangle, |3\rangle, |2\rangle$ differ in the magnetic quantum number m by one successively. So a π-polarized beam Ω_1^{π} excites the state $|3\rangle$ and a linear $\hat{x}$-polarized

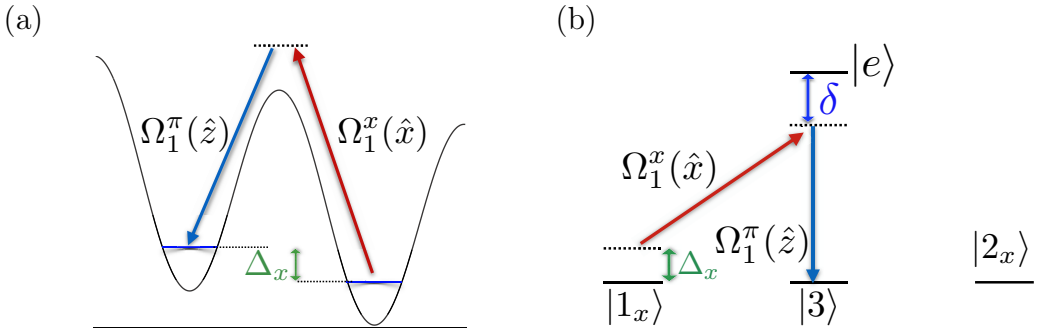

Figure B.1.1: Part of the schematic to realize chiral topological insulator. (a) A linear tilt Δ_x per site in the lattice along x-direction. (b) Two Raman beams Ω_1^x and Ω_1^π used to produce the tunneling in $H_{\mathbf{rx}}^{(1)}$. The unit vectors in brackets show the polarization direction of the corresponding beam. For the complete optical lattice setup, refer to the figure in the main text.

beam Ω_1^x excites the superposition state $|1_x\rangle = (|1\rangle + |2\rangle)/\sqrt{2}$ since $\hat{x} \sim (\sigma^+ + \sigma^-)$. So together, these two beams induce a Raman-assisted hopping between $|1_x\rangle$ and $|3\rangle$. The hopping amplitude and phase are controlled by the corresponding Raman beam amplitude and phase. In addition, the wave-vector difference of two beams $\delta\mathbf{k}$ ($(-k, 0, k)$ in this case) has to have a component along the hopping direction (x-direction) to ensure the hopping strength is non-vanishing.

All the other hopping terms in the Hamiltonian are realized in a similar manner. For example, consider the term $c^\dagger_{3,\mathbf{r}+\mathbf{y}}(c_{1,\mathbf{r}}+ic_{2,\mathbf{r}})$, which can be realized by $\Omega_2^y = \sqrt{2}\Omega_0 e^{ikz}$ and $\Omega_2^\pi = \Omega_0 e^{iky}$, polarized along $(\hat{x}+\hat{y})$-direction and $\hat{z}$-direction respectively. Since $(\hat{x}+\hat{y}) \sim (\sigma^+ + i\sigma^-)$, it couples the state $|2_y\rangle = (|1\rangle + i|2\rangle)/\sqrt{2}$ and $|3\rangle$. A wave-vector difference $\delta\mathbf{k} = (0, -k, k)$ and a two-photon energy detuning Δ_y guarantee the desired hopping along y-direction.

With a number of laser beams required to realize the full Hamiltonian, it is important to check that undesired tunneling terms are forbidden. To that end, we require a different linear energy shift per site $\Delta_{x,y,z}$ along the (x, y, z)-direction. The ratio between $\Delta_x, \Delta_y, \Delta_z$

can be adjusted by setting the direction of the gradient field to be in a specific angle with respect to the three axes of the optical lattice. In particular, we set $\Delta_x : \Delta_y : \Delta_z = 1 : 2 : 3$. The energy difference is lower bounded by Δ_x. So if we select a parameter regime such that the Raman-assisted hopping rate t satisfies $t \ll \Delta_x$, then the hopping along the z direction induced by Ω_1^x and Ω_1^π, for instance, have negligible effects because of the large detuning. Other undesired couplings between different beams are disallowed because the wave-vector difference $\delta\mathbf{k}$ may not have the component along a certain direction to induce a hopping along that direction. For example, $\Omega_1^x = i\sqrt{2}\Omega_0 e^{ikz}$ and $\Omega_2^\pi = \Omega_0 e^{iky}$ will not induce a hopping along x-direction as $\delta\mathbf{k}$ does not include a component along x-direction. Moreover, the Raman beams $\Omega_{1,2}^{x,y,z}$ and $\Omega_{1,2}^\pi$ may induce some on-site spin transferring terms, which can be compensated with some radio-frequency fields.

B.1.2 Wannier-(Stark) Function Estimation

In the second quantization representation with the Wannier function basis, the natural tunneling rate can be written as

$$t_0 = \int d^3\mathbf{r}' \bar{w}^*(\mathbf{r}' - \mathbf{r_i}) \left[-\frac{\hbar^2}{2m}\nabla^2 + V_0(\mathbf{r}') \right] \bar{w}(\mathbf{r}' - \mathbf{r_j}), \tag{B.1.3}$$

where $\bar{w}(\mathbf{r}' - \mathbf{r_j})$ is the Wannier function centered at site $\mathbf{r_j}$ and $V_0(\mathbf{r}')$ is the lattice depth at site $\mathbf{r_j}$ (We use $\bar{w}(\mathbf{r})$ to denote the Wannier function and $w(\mathbf{r})$ to denote the Wannier-Stark function to be notationally consistent with the main text). With a linear tilt in the optical lattice, translational symmetry is broken and Wannier functions are no longer the proper descriptions of the localized states. Instead, a simple modification with Wannier-Stark

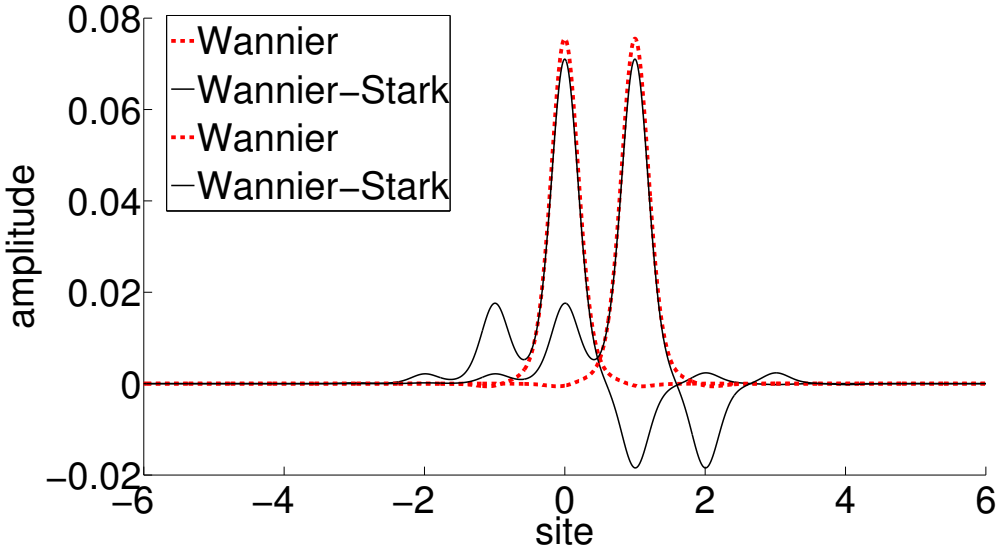

Figure B.1.2: Wannier functions and Wannier-Stark functions centered at site 0 and site 1. $V_0 \approx 2.3E_r, a = 2\pi/k = 764\,\text{nm}$, and linear tilt $\Delta_x/2\pi \approx 200\,\text{Hz}$ for ^{40}K atoms. Note that the apparent shallow potential is due to the larger separation between two sites. We take $a = \lambda$ instead of $a = \lambda/2$ in the typical case (see main text).

functions $w(\mathbf{r})$ will be sufficient [382, 383]:

$$w_i(\mathbf{r}' - \mathbf{r}_l) = \sum_m J_{m-l}\left(\frac{2t_0}{\Delta_i}\right) \bar{w}(\mathbf{r}' - \mathbf{r_m}), \tag{B.1.4}$$

where $i = x, y, z$, and $w_i(\mathbf{r})$ is the Wannier-Stark function, and Δ_i is the linear tilt per site along i direction. $J_{m-l}(x)$ are the bessel functions of the first kind. Fig. B.1.2 shows the Wannier functions and Wannier-Stark functions with $V_0 \approx 2.3E_r$. They have close overlaps on the center site, but may differ significantly on neighboring sites. Calculations with the Wannier functions or the Wannier-Stark functions produce the same natural tunneling $t_0/\hbar \approx 2\pi \times 50\,\text{Hz}$. The tunneling rate with Raman-assisted hopping can be written as an integral

of Wannier-Stark functions (as discussed in the main text):

$$t_{\mathbf{r},\mathbf{m}} = \frac{\Omega^*_{\beta\mathbf{m}}\Omega_{\alpha\mathbf{m}}}{\delta}\int d^3\mathbf{r}' w^*(\mathbf{r}'-\mathbf{r}-\mathbf{m})e^{i\delta\mathbf{k}\cdot\mathbf{r}'}w(\mathbf{r}'-\mathbf{r}). \tag{B.1.5}$$

Factorizing the Wannier-Stark functions into each direction, $w(\mathbf{r}') = w(x')w(y')w(z')$ and calculating them along each direction, we can numerically compute the overlap integral

$$\beta \equiv \int dx w^*(x+a)e^{-ikx}w(x)\int dy w^*(y)w(y)\int dz w^*(z)e^{ikz}w(z).$$

With the parameters given in Fig. B.1.2, we have $\beta \approx 0.34$. For Raman beams with $\Omega_0/2\pi \approx 15\,\mathrm{MHz}$ and the single-photon detuning $\delta/2\pi \approx 1.7\,\mathrm{THz}$, we have $\Omega_{\mathbf{R}} = |\Omega_0|^2/\delta \approx 2\pi \times 120\,\mathrm{Hz}$, and the Raman-assisted hopping rate $t/\hbar \approx 2\pi \times 40\,\mathrm{Hz}$. It is worthwhile to point out that the expression given in equation (B.1.5) is only valid in the perturbative limit when $t \lesssim t_0$. When the Rabi frequency becomes stronger, the Raman-assisted tunneling rate eventually saturates. A more accurate expression may be obtained in the nonperturbative limit with a more accurate analysis [20,383]. Nevertheless, these numerical calculations only yield rough estimations to experimental parameters, which may need to be fine-tuned in experiments to produce the best result in a topologically nontrivial phase.

B.1.3 Density of States

In the main text, we plotted the momentum distribution of atoms $\rho_{\mathrm{cry}}(\mathbf{k})$ for various h at a fixed chemical potential $\mu/2t = -2$. It is useful to include the density of states $\rho(E)$ for various values of the parameter h. In Fig. B.1.3 here, we show the density of states plots. The macroscopic zero-energy flat band is prominent in each plot. The band gap is also clearly

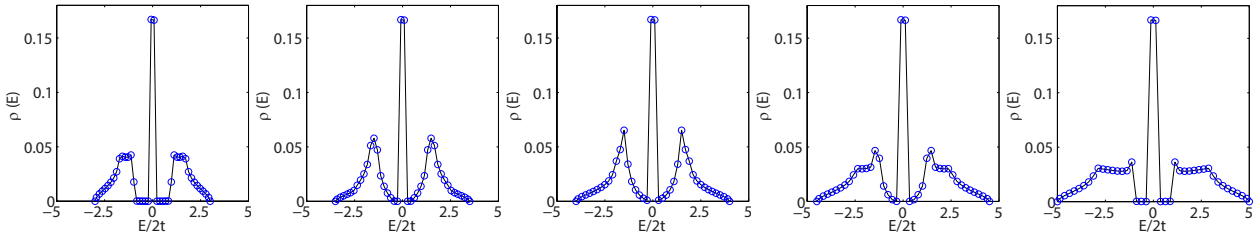

Figure B.1.3: Density of states $\rho(E)$ with respect to the energy E for various values of h ($h = 0, 0.5, 1, 1.5, 2$ from left to right). The middle flat band is clearly visible at zero energy. The bulk band gaps are $2t, t/2, 0, t/2, 2t$ respectively.

visible for $h = 0, 2$ (less visible for $h = 0.5, 1.5$). In the main text, the figures correspond to a filling up to $\mu/2t = -2$. A change of Fermi surface topology can be observed in those figures.

B.2 Physical Properties of Chiral Topological Insulators

B.2.1 Bulk-edge Correspondence

The bulk edge correspondence tells us that the bulk topological index should have a surface manifestation, typically through the number of gapless Dirac cones on the surface. This is generally verified for lower topological index, such as 1 or 2. By imposing an open boundary condition along the z direction for chiral topological insulators of different index, we find that the winding number corresponds to the total number of Dirac cones counted for all inequivalent surface states (i.e. not counting degeneracies).

Following Ref. [44] to take a quaternion power n, we can generalize the Hamiltonians in the main text from $\mathcal{H}_1(\mathbf{k})$ and $\mathcal{H}_2(\mathbf{k})$ to $\mathcal{H}_n(\mathbf{k})$. For the Hamiltonian $\mathcal{H}_1(\mathbf{k})$ (i.e. $n = 1$), when $h = 2$, the winding number $\Gamma = 1$ guarantees the existence of 1 Dirac cone [Fig. B.2.1(a)].

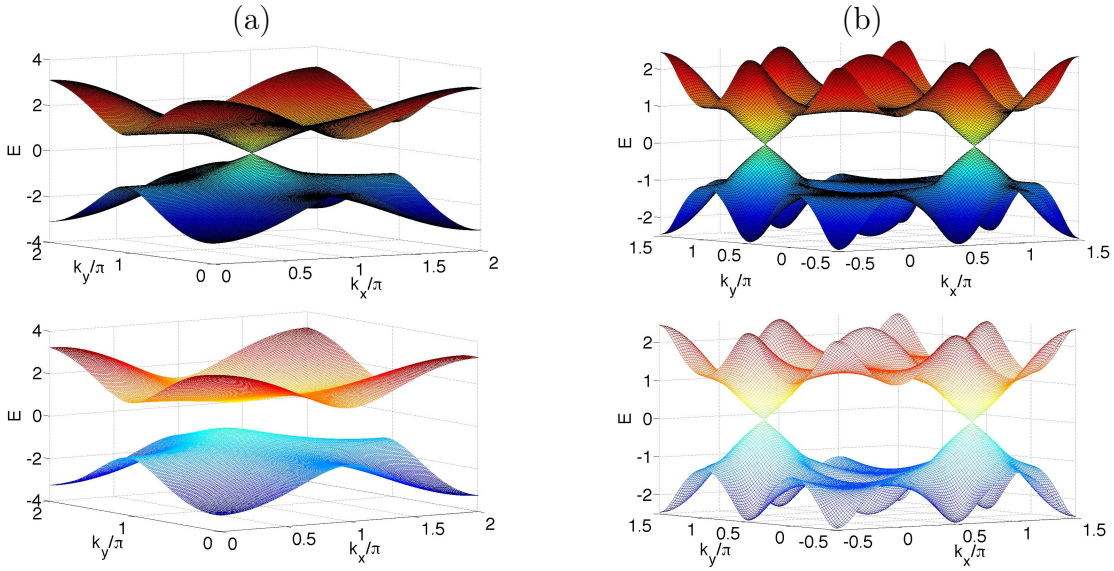

Figure B.2.1: Spectrum for the surface states showing the number of Dirac cones. The upper panels in (a) and (b) show the lowest conduction and highest valence band. The lower panels show the next two bands closest to the Fermi energy. (a) For $\mathcal{H}_1(\mathbf{k})$, $h = 2, \delta = 0.5$ with winding number $\Gamma = 1$ and 1 Dirac cone. (b) For $\mathcal{H}_2(\mathbf{k})$, $h = 0, \delta = 0$ with winding number $\Gamma = 4$ and 4 Dirac cones in total. The Γ point is displaced from the center for better display of the Dirac cones.

For the Hamiltonian $\mathcal{H}_2(\mathbf{k})$ (i.e. $n = 2$), when $h = 0$, the winding number is $\Gamma = 4$. So there are two inequivalent surface states on each surface with two Dirac cones each [Fig. B.2.1(b)]. In general, we have m inequivalent surface states with 1 Dirac cone each for $n = m, 1 < |h| < 3, \Gamma = m$, and m inequivalent surface states with 2 Dirac cones each for $n = m, -1 < h < 1, \Gamma = 2m$. These have been explicitly verified up to $n = 3$. Hence, the winding number Γ does correspond to the total number of Dirac cones for all inequivalent surface states.

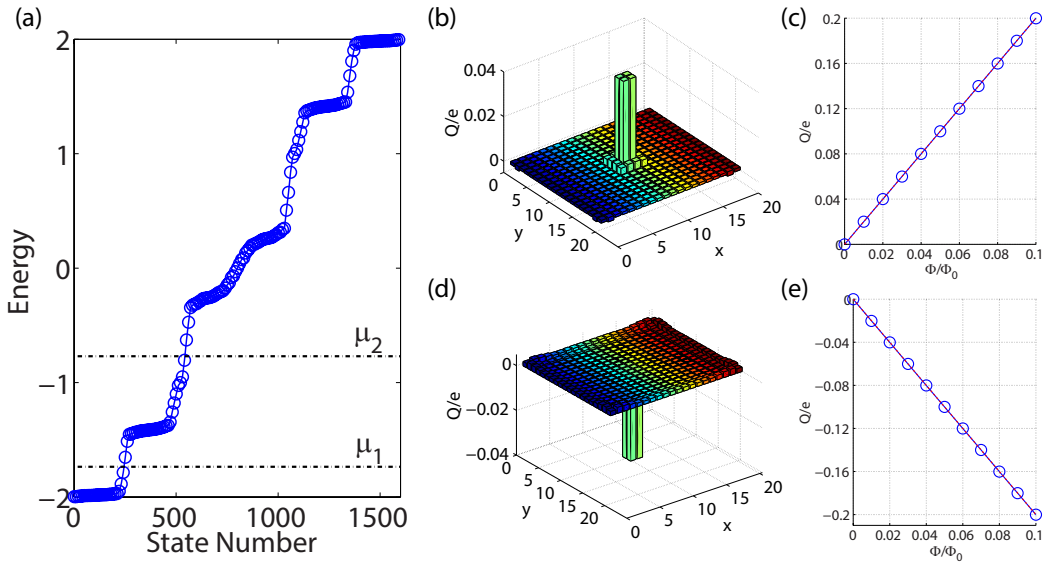

Figure B.2.2: Effect of surface orbital field. (a) Energy spectrum for the one-layer Hamiltonian $\mathcal{H}_1(\mathbf{k})$ with a strong uniform magnetic field and unit cell flux as $\frac{1}{3}\Phi_0$. An additional weak flux tube is inserted through the center lattice cell of the layer, with flux up to $\Phi/\Phi_0 = 0.1$. (b) and (c) [(d) and (e)] correspond to the charge polarization with respect to the increasing flux tube at a chemical potential μ_1 [μ_2]. Charge is accumulated around the flux tube, and by changing the chemical potential and hence the Landau level occupancy, the charge accumulation rate can be modified by an integer.

B.2.2 Surface Orbital Field and Integer Quantum Hall Layers

The 2π periodicity of the θ term is mathematically related to the gauge freedom in the low-energy effective field theory. Physically, it is associated with the freedom to coat an integer quantum Hall layer on the surface, or equivalently to change the chemical potential and hence the Landau level occupancy of the surface in an orbital magnetic field. Here, we numerically verify this physical intuition. To do that, we consider a single layer of the Hamiltonian $\mathcal{H}_1(\mathbf{k})$, so the z component drops out. A strong uniform orbital field is added to the layer via Peierls substitution with the Landau gauge $\mathbf{A} = Bx\hat{y}$. $Ba^2 = \frac{1}{3}\Phi_0$, where a is the lattice constant, and Φ_0 is the flux quantum. For the Hofstadter Hamiltonian, this

strong orbital field will produce three gapped Landau levels. Here, a similar structure is developed as shown in Fig. B.2.2(a). There are six bands with the middle two bands gapless. The extra number of bands are due to the spin and orbital degrees of freedom. On top of the strong uniform magnetic field, an additional weak flux tube is inserted through the center lattice. By Laughlin's flux insertion argument, the charge accumulated around the flux tube should be $Q/e = C\Phi/\Phi_0$, where C is the Chern number being an integer. Figures B.2.2(b) and B.2.2(c) [B.2.2(d) and B.2.2(e)] show the charge polarization at a chemical potential μ_1 [μ_2]. From the slope, we infer that the first band has a Chern number $C = 2$ and the second band has a Chern number $C = -4$. So by changing the surface chemical potential, we could modify the charge accumulation rate by an integer. Alternatively, in the absence of this strong orbital magnetic field, with a surface gapping term H_S in Eq. (3.2.9) of the main text, there is only one gap and no such integer quantum Hall layers. Therefore the $\mathbb{Z}$ character of the winding number can be observed through such integrally quantized magneto-electric polarization measurements.

APPENDIX C

Direct Measurement of Topological Invariants

This Appendix gives more details on numerical simulation of the experimental detection and extraction of the topological invariants. In section C.1, we show how to numerically calculate the atomic momentum distribution by solving the real-space Hamiltonians under open boundary condition. In section C.2, we provide details on how the random perturbation and harmonic trapping potential are incorporated into the simulation. In section C.3, we include more detailed results from the numerical simulations as well as an explicit definition of the Gell-Mann matrices used in the main text.

C.1 Numerical Simulation of the Atomic Momentum Distribution

In this section, we provide more details on how to numerically simulate the atomic momentum distribution by solving real-space Hamiltonians. Consider a generic quadratic Hamiltonian

in real space that describe free fermions:

$$H = \sum_{\mathbf{r},\mathbf{s},\alpha,\beta} a^{\dagger}_{\mathbf{r},\alpha} \mathcal{H}_{\mathbf{r}\alpha,\mathbf{s}\beta} a_{\mathbf{s},\beta}, \tag{C.1.1}$$

where $a^{\dagger}_{\mathbf{r},\alpha}(a_{\mathbf{s},\beta})$ creates (annihilates) a particle at lattice site $\mathbf{r}(\mathbf{s})$ with pseudospin $\alpha(\beta)$. One can solve the Schrödinger equation $\mathcal{H}\Phi_i = \epsilon_i \Phi_i$ to obtain the single-particle energy spectrum. In the matrix form, one can diagonalize $\mathcal{H}$ by a unitary transformation U: $\mathcal{H} = U^{\dagger}\mathcal{E}U$ to find the single-particle eigenmodes $b_{\mathbf{r},\alpha} = \sum_{\mathbf{s},\beta} U_{\mathbf{r}\alpha,\mathbf{s}\beta} a_{\mathbf{s},\beta}$. Here $\mathcal{E} = \mathrm{diag}(\epsilon_1, \epsilon_2, \cdots)$ is a diagonal matrix. For a free-fermion system described by Eq. (C.1.1), the total particle number $\mathcal{N} = \sum_{\mathbf{r},\alpha} a^{\dagger}_{\mathbf{r},\alpha} a_{\mathbf{r},\alpha}$ is a conserved quantity $[H, \mathcal{N}] = 0$. These $\mathcal{N}$ particles will occupy the first $\mathcal{N}$ eigenmodes with lowest eigenenergies. Consequently, the ground state of the system reads

$$|G\rangle = \prod_{i=1}^{\mathcal{N}} b^{\dagger}_i |0\rangle, \tag{C.1.2}$$

where we suppress $\mathbf{r}$ and α into a single index i for the occupied eigenmodes, and $|0\rangle$ is the vacuum state without any particles. The density distribution in momentum space can then be obtained as

$$n_{\alpha}(\mathbf{k}) = \langle G | a^{\dagger}_{\alpha}(\mathbf{k}) a_{\alpha}(\mathbf{k}) | G \rangle. \tag{C.1.3}$$

where $a_\alpha(\mathbf{k})$ relates to $a_{\mathbf{r},\alpha}$ by a Fourier transform,

$$\begin{aligned} n_\alpha(\mathbf{k}) &= \langle G|\frac{1}{\sqrt{\mathcal{L}}}\sum_{\mathbf{r}} e^{i\mathbf{k}\cdot\mathbf{r}} a^\dagger_{\mathbf{r},\alpha}\frac{1}{\sqrt{\mathcal{L}}}\sum_{\mathbf{r}'} e^{-i\mathbf{k}\cdot\mathbf{r}'} a_{\mathbf{r}',\alpha}|G\rangle \\ &= \frac{1}{\mathcal{L}}\sum_{\mathbf{r},\mathbf{r}'}\langle G|a^\dagger_{\mathbf{r},\alpha}a_{\mathbf{r}',\alpha}|G\rangle e^{i\mathbf{k}\cdot(\mathbf{r}-\mathbf{r}')}, \end{aligned} \tag{C.1.4}$$

where $\mathcal{L}$ denotes the number of lattice sites. As $a_{\mathbf{r},\alpha} = \sum_{\mathbf{s},\beta}(U^\dagger)_{\mathbf{r}\alpha,\mathbf{s}\beta} b_{\mathbf{s},\beta}$, the quantity $\langle G|a^\dagger_{\mathbf{r},\alpha}a_{\mathbf{r}',\alpha}|G\rangle$ can be further simplified:

$$\begin{aligned} \langle G|a^\dagger_{\mathbf{r},\alpha}a_{\mathbf{r}',\alpha}|G\rangle &= \langle G|\sum_{\mathbf{s},\beta}(U^\dagger)^*_{\mathbf{r}\alpha,\mathbf{s}\beta} b^\dagger_{\mathbf{s},\beta}\sum_{\mathbf{s}',\beta'}(U^\dagger)_{\mathbf{r}'\alpha,\mathbf{s}'\beta'} b_{\mathbf{s}',\beta'}|G\rangle \\ &= \sum_{\mathbf{s},\beta,\mathbf{s}',\beta'}\langle G|b^\dagger_{\mathbf{s},\beta}b_{\mathbf{s}',\beta'}|G\rangle (U^\dagger)^*_{\mathbf{r}\alpha,\mathbf{s}\beta}(U^\dagger)_{\mathbf{r}'\alpha,\mathbf{s}'\beta'} \\ &= \sum_{i}^{\mathcal{N}}(U^\dagger)^*_{\mathbf{r}\alpha,i}(U^\dagger)_{\mathbf{r}'\alpha,i}. \end{aligned} \tag{C.1.5}$$

In the last step of Eq. (C.1.5), we have used the following equation

$$\langle G|b^\dagger_{\mathbf{s},\beta}b_{\mathbf{s}',\beta'}|G\rangle = \begin{cases} 1 & \text{if } \mathbf{s}=\mathbf{s}', \beta=\beta' \text{ and the eigen-mode } b_{\mathbf{s},\beta} \text{ is occupied} \\ 0 & \text{otherwise.} \end{cases}$$

Combining Eq. (C.1.5) and Eq. (C.1.4), we can obtain the momentum density distribution for each pseudospin component from a generic quadratic real-space Hamiltonian with a specific filling fraction (the filling fraction is defined as the total particle number divided by the lattice site number: $f = \mathcal{N}/\mathcal{L}$). Analogously, one can rotate the pseudospin and use the same method to compute the momentum density distribution in other spin bases $n_{a|\alpha\rangle+b|\beta\rangle}(\mathbf{k})$.

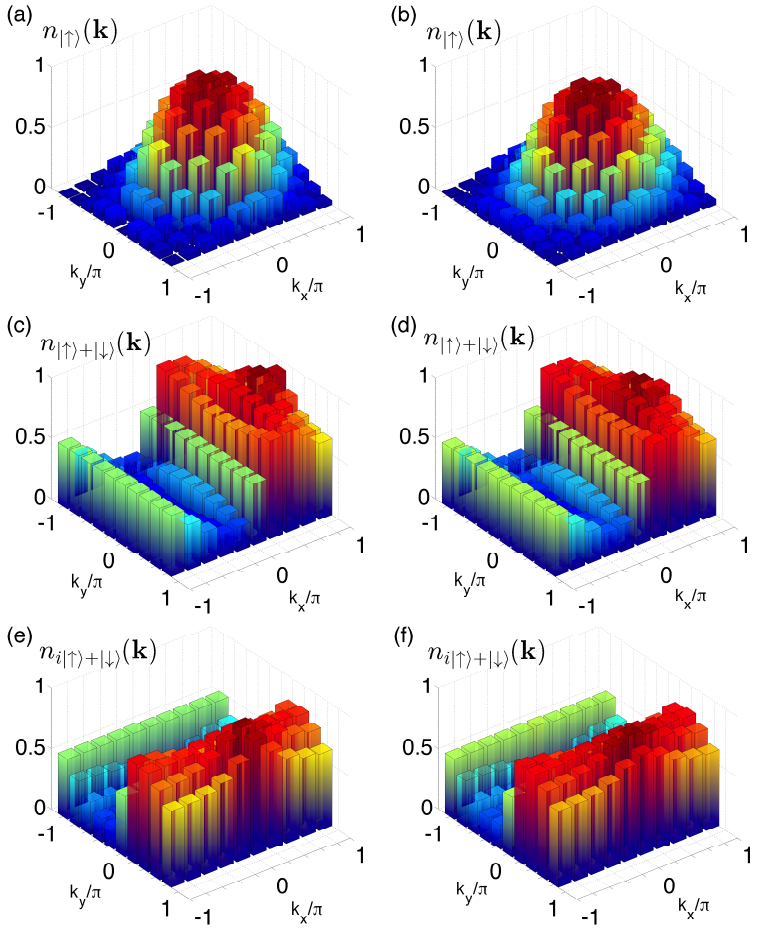

Figure C.1.1: Density distributions in momentum space for the first band with lattice size 10×10. (a), (c) and (e) correspond to the periodic boundary condition without perturbation and trapping potential; (b), (d), and (f) correspond to open boundary conditions with random perturbations and harmonic trapping (subfigures (b) and (d) are repeated from the main text for clarity and completeness). The parameters used in the calculations are chosen to be $\lambda_{\mathrm{SO}}^{(x)} = \lambda_{\mathrm{SO}}^{(y)} = t$, $h = t$, $\gamma_{\mathrm{T}} = 0.1t$, and $\gamma_{\mathrm{P}} = 0.01t$. From these distributions, we find the Chern number $C_1 = -1$ using the formula in the main text.

C.2 Random Perturbation and Harmonic Trapping Potential

As discussed in the main text, a typical optical lattice experiment includes a weak harmonic trapping potential,

$$V_{\mathrm{T}} = \frac{1}{2} m_a \omega^2 \sum_{\mathbf{r},\alpha} d_{\mathbf{r}}^2 a_{\mathbf{r},\alpha}^{\dagger} a_{\mathbf{r},\alpha}, \tag{C.2.1}$$

where $d_{\mathbf{r}}$ is the distance from the center of the trap to the lattice site $\mathbf{r}$, m_a is the atomic mass, and ω is the trap frequency. In our numerical simulation, we use $\gamma_{\mathrm{T}} = m_a \omega^2 a^2/(2t)$ to parametrize the influence of this trapping potential. Here a is the lattice constant and t is the hopping rate. For a typical experiment, $t/\hbar \sim 1$kHz, $a \sim 400$ nm, and γ_{T} ranges from 10^{-3} (^{6}Li with $\omega/2\pi = 60$ Hz) to 2×10^{-2} (^{40}K with $\omega/2\pi = 100$ Hz) [150]. To account for other possible experimental noise, we also add a random perturbation term

$$H_{\mathrm{P}} = \gamma_{\mathrm{P}} t \sum_{\mathbf{r},\mathbf{s},\alpha,\beta} a_{\mathbf{r},\alpha}^{\dagger} \mathcal{P}_{\mathbf{r}\alpha,\mathbf{s}\beta} a_{\mathbf{s},\beta}, \tag{C.2.2}$$

where $\mathcal{P}$ is a random Hermitian matrix with its largest eigenvalue normalized to unity.

In the numerical simulation, we add both V_{T} and H_{P} into the original Hamiltonians and calculate the momentum density distributions. Although only partial results are included in the main text, we have done substantial calculations with a number of different choices of parameters $(\gamma_{\mathrm{T}}, \gamma_{\mathrm{P}})$ for both the 2D quantum anomalous Hall effect (QAH) and 3D chiral topological insulators (CTIs). Our results consistently show that topological invariants extracted from the time-of-flight (TOF) measurements are very robust to the trapping potential

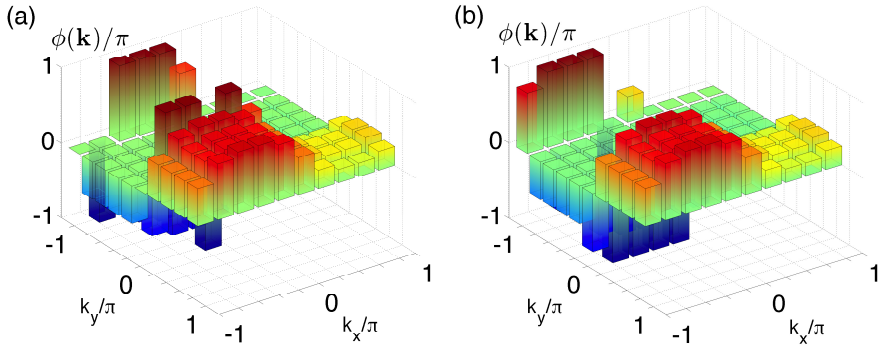

Figure C.2.1: Relative phase factors in momentum space for the first band of the Hamiltonian H_{QAH} with lattice size 10×10. (a) Periodic boundary condition without perturbations and the trapping potential. (b) Open boundary conditions with random perturbations and a harmonic trap. The parameters are chosen to be the same as in the main text.

and random perturbations.

C.3 More Results from Numerical Simulation

In this section, we provide more detailed numerical results from numerical simulation of both the 2D QAH and 3D CTI cases.

2D QAH effect—In the main text, we have plotted two momentum density distributions of the first band. Here, we present more plots of the density distributions in Fig. C.1.1, considering both periodic and open boundary conditions. As discussed in the main text, Fig. C.1.1 (b), (d) and (f) simulate the data obtained from the TOF measurements. To extract the Chern number, an intermediate step is to calculate the relative phase between the spin up and down components of the Bloch wavefunction from those density distributions.

A little algebra leads to the following equations:

$$2n_{|\uparrow\rangle+|\downarrow\rangle}(\mathbf{k}) = 1+2\sqrt{n_\uparrow(\mathbf{k})\times(1-n_\uparrow(\mathbf{k}))}\cos(\phi(\mathbf{k})) \quad \text{(C.3.1)}$$

$$2n_{i|\uparrow\rangle+|\downarrow\rangle}(\mathbf{k}) = 1+2\sqrt{n_\uparrow(\mathbf{k})\times(1-n_\uparrow(\mathbf{k}))}\sin(\phi(\mathbf{k})), \quad \text{(C.3.2)}$$

where $\phi(\mathbf{k})$ is defined as the relative phase in the lower band Bloch wavefunction between the spin up and spin down components, i.e. $|u_1(\mathbf{k})\rangle = |c_\uparrow(\mathbf{k})|\,|\uparrow\rangle + |c_\downarrow(\mathbf{k})|e^{i\phi(\mathbf{k})}\,|\downarrow\rangle$. Plugging the density distributions observed from the TOF measurements into the above equations, one obtains the relative phase. We performed the calculations for both periodic and open boundary conditions and the corresponding relative phases are shown in Fig. C.2.1. With the relative phases and the density distributions, the Bloch wavefunction for the first band is determined up to a momentum-dependent overall phase. Using the method introduced in the main text, we are able to extract the desired Chern number $C_1 = -1$.

3D Chiral TI— Let us first write down explicitly the four Gell-Mann matrices used in the Hamiltonian H_{CTI} in the main text:

$$G_4 = \begin{pmatrix} 0 & 0 & 1 \\ 0 & 0 & 0 \\ 1 & 0 & 0 \end{pmatrix}, \quad G_5 = \begin{pmatrix} 0 & 0 & -i \\ 0 & 0 & 0 \\ i & 0 & 0 \end{pmatrix}, \quad G_6 = \begin{pmatrix} 0 & 0 & 0 \\ 0 & 0 & 1 \\ 0 & 1 & 0 \end{pmatrix}, \quad G_7 = \begin{pmatrix} 0 & 0 & 0 \\ 0 & 0 & -i \\ 0 & i & 0 \end{pmatrix}.$$

A Fourier transform brings H_{CTI} to the momentum space [45, 73]:

$$H_{\mathrm{CTI}} = \sum_{\mathbf{k}} \psi^\dagger_{\mathbf{k}} \mathcal{H}_{\mathrm{CTI}}(\mathbf{k}) \psi_{\mathbf{k}},$$

where $\psi^\dagger_{\mathbf{k}} = (a^\dagger_{\mathbf{k},1}, a^\dagger_{\mathbf{k},2}, a^\dagger_{\mathbf{k},3})$ and $\mathcal{H}_{\mathrm{CTI}}(\mathbf{k}) = \sum_{j=1}^{4} G_{3+j} q_j(\mathbf{k})$ with $[q_1(\mathbf{k}), q_2(\mathbf{k}), q_3(\mathbf{k}), q_4(\mathbf{k})] =$

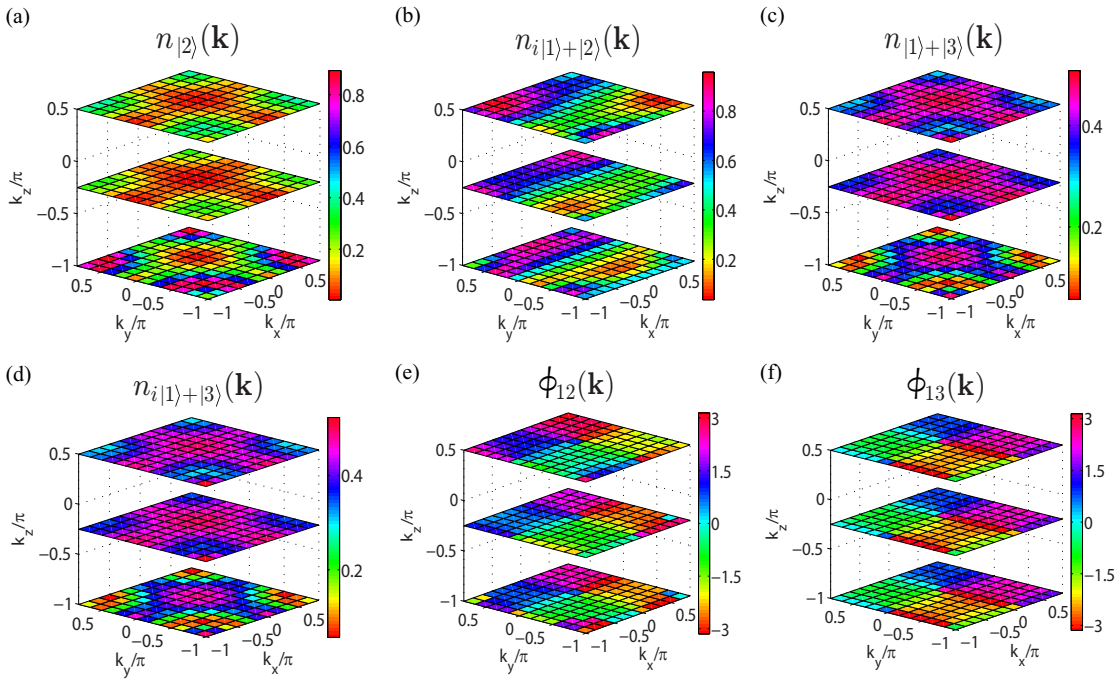

Figure C.3.1: Momentum density distributions and relative phase factors for the middle flat band with open boundary conditions for H_{CTI} including a harmonic trap and some random perturbations. The lattice size is $12 \times 12 \times 12$. Layers corresponding to $k_z = -\pi, -\pi/4, \pi/2$ are displayed. $\phi_{12}(\mathbf{k})$ ($\phi_{13}(\mathbf{k})$) is the phase factor between spin 1 and 2 (spin 1 and 3) in the Bloch wavefunction. The parameters are chosen to be the same as in the main text.

$[\sin k_x, \sin k_y, \sin k_z, m - \cos k_x - \cos k_y - \cos k_z]$. One can easily check that this Hamiltonian indeed has a chiral symmetry represented by $S\mathcal{H}_{\mathrm{CTI}}(\mathbf{k})S^{-1} = -\mathcal{H}_{\mathrm{CTI}}(\mathbf{k})$, where $S \equiv \mathrm{diag}(1, 1, -1)$ is a unitary matrix. This chiral symmetry leads to an exact zero-energy flat band as discussed in Ref. [45, 73].

In the main text, we plotted some of the momentum density distributions of the middle flat band. Here we include more results of the density distributions and the relative phases in Fig. C.3.1. Analogous to the case of QAH effect, the momentum density distributions can be directly observed from the layered TOF measurements and the relative phases can be calculated from the observed density distributions. After all density distributions are

Table C.1: The Chern-Simons terms of the first and third bands for the Hamiltonian H_{CTI}. The parameters are chosen to be the same as in the main text figure.

	Size	h/t	Periodic	Open	Trap	Pert.+Trap
CTI (CS_1/π)	10^3	2	0.246	0.228	0.231	0.231
	12^3	2	0.248	0.228	0.235	0.235
	10^3	4	5.8×10^{-5}	8.6×10^{-5}	1.5×10^{-4}	1.4×10^{-4}
CTI (CS_3/π)	10^3	2	0.246	0.226	0.227	0.227
	12^3	2	0.248	0.229	0.230	0.231
	10^3	4	5.8×10^{-5}	5.0×10^{-5}	1.7×10^{-4}	1.8×10^{-4}

observed in an actual experiment, the Chern-Simons term characterizing the topological structure of the Bloch band can be readily extracted with the method described in the main text.

Besides the Chern-Simons term for the middle flat band shown in the table of the main text, we have also calculated it for both the first (lowest) and third (highest) bands. Our results are recorded in Table I here. From this table, the extracted Chern-Simons terms converge to the expected theoretical value $CS_1/\pi = CS_3/\pi = 1/4$ as we increase the lattice size.

APPENDIX D

Quantum Computation under Micromotion in a Planar Ion Crystal

D.1 Iterative Method to Find Dynamic Ion Positions

As discussed in the main text, the equations of motion in each direction can be written in the standard form of Mathieu equations (neglecting Coulomb potential):

$$\frac{d^2 r_\nu}{d\xi^2} + \left[a_\nu - 2q_\nu \cos(2\xi)\right] r_\nu = 0, \tag{D.1.1}$$

where $\nu \in \{x, y, z\}$, $\xi = \Omega_T t/2$, and dimensionless parameters a_ν and q_ν are defined in the main text. The characteristic exponents β_ν can be computed from a_ν and q_ν iteratively [241]. A pseudopotential can then be obtained with secular frequencies $\omega_\nu = \beta_\nu \Omega_T/2$ and

$$e\left(\Phi_{\mathrm{DC}} + \Phi_{\mathrm{AC}}\right) \approx \frac{1}{2} m\omega_x^2 x^2 + \frac{1}{2} m\omega_y^2 y^2 + \frac{1}{2} m\omega_z^2 z^2. \tag{D.1.2}$$

Assuming tight trapping along the z direction, i.e. $\omega_z/\omega_{x,y} > 10$, a planar crystal is formed in the x-y plane. Adding the Coulomb potential V_C, one acquires a time-independent potential in the plane:

$$V_{\text{pseudo}}(x,\, y) = \sum_i \left(\frac{1}{2}m\omega_x^2 x_i^2 + \frac{1}{2}m\omega_y^2 y_i^2\right) + \sum_{i<j} \frac{e^2}{4\pi\epsilon_0\sqrt{(x_i - x_j)^2 + (y_i - y_j)^2}}. \quad \text{(D.1.3)}$$

$i = 1, 2, \cdots, N$, where N is the number of ions. Numerically, we start with $N = 127$ ions forming equilateral triangles in a 2D hexagonal structure [Fig. D.1.1(a)], and find the static equilibrium positions $\vec{r}^{\,(0)} = (x_1^{(0)}, y_1^{(0)}, \cdots, x_N^{(0)}, y_N^{(0)})$ under this pseudopotential approximation by solving the classical equations of motion with a frictional force $(-\eta(\dot{x} + \dot{y}))$, simulating the cooling process in experiment. This set of static equilibrium positions [marked by squares in Fig. D.1.1(b)] is the starting point to derive the oscillatory behavior of each ion under micromotion.

In a planar crystal, the ions oscillate slightly around their average positions, so it is appropriate to expand the Coulomb potential around the equilibrium positions $\vec{r}^{\,(0)}$. To the second order, the Coulomb potential can be written in a quadratic form:

$$V_C \approx \frac{1}{2}\vec{r}^{\,T} M_C \vec{r} + \vec{g}^{\,T}\vec{r} + \text{constant term}, \quad \text{(D.1.4)}$$

where $\vec{r} = (x_1, y_1, \cdots, x_N, y_N)$, M_C is a $2N \times 2N$ matrix, and $\vec{g}$ is a $2N$-vector. The trapping potential can also be written in this coordinate basis:

$$e\,(\Phi_{\text{DC}} + \Phi_{\text{AC}}) = \frac{1}{2}\vec{r}^{\,T} M_{DC} \vec{r} + \frac{V_0}{d_0^2}\cos(\Omega_T t)\vec{r}^{\,T} I_{2N}\, \vec{r}, \quad \text{(D.1.5)}$$

where I_{2N} is the $2N \times 2N$ identity matrix, and M_{DC} is a diagonal matrix with $2(1+\gamma)eU_0/d_0^2$

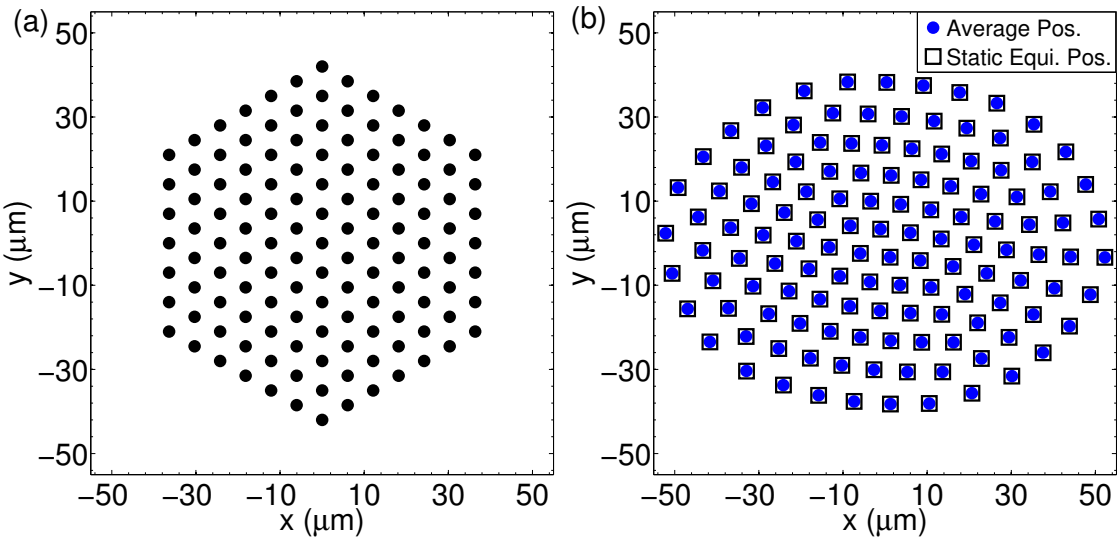

Figure D.1.1: Initial and equilibrium positions for the ion crystal. (a) Initial configuration for ion crystal. 127 ions forming equilateral triangles with ion distance 7 μm are arranged in a 2D hexagonal structure. (b) Stable ion configuration under the trap and Coulomb potential. Static equilibrium positions under the pseudopotential approximation are marked by (black) squares. Average ion positions found self-consistently by solving the Mathieu equations are marked by (blue) dots. The difference between two sets of equilibrium positions is around 0.03 μm on average, which is hardly visible in the figure.

in the odd rows (x coordinates), and $2(1-\gamma)eU_0/d_0^2$ in the even rows (y coordinates). Therefore, the total potential energy is

$$V = \frac{1}{2}\vec{r}^{\,T}(M_{DC}+M_C)\vec{r} + \frac{V_0}{d_0^2}\cos(\Omega_T t)\vec{r}^{\,T} I_{2N}\,\vec{r} + \vec{g}^{\,T}\vec{r}. \tag{D.1.6}$$

Note that the time-dependent part of the potential is isotropic in the coordinates, so it does not couple each Mathieu equations. We can find an orthogonal matrix Q that diagonalizes the first term, i.e. $Q(M_{DC}+M_C)Q^T = \Lambda$. Using the normal coordinates $\vec{s} = Q\vec{r}$, the

equations of motion form decoupled Mathieu equations:

$$\frac{d^2 s_i}{d\xi^2} + (a_i - 2q_i \cos(2\xi))s_i = f_i, \tag{D.1.7}$$

where $a_i = 4\Lambda_{ii}/m\Omega_T^2$, $q_i = q = -4eV_0/md_0^2\Omega_T^2$, and $f_i = -\frac{4}{m\Omega_T^2}(Q\vec{g})_i$. The inhomogeneous Mathieu equations can be solved by substituting a special solution in the form of $s_i = f_i \sum_{n=0}^{\infty} c_i^{(n)} \cos(2n\xi)$, and the series coefficients $c_i^{(n)}$ can be computed numerically [233]. After that, the ion coordinates can be transformed back to the Cartesian coordinates $\vec{r} = Q^T\vec{s}$, where $\vec{r}$ can be expressed successively as

$$\vec{r} = \vec{r}^{(0)} + \vec{r}^{(1)} \cos(2\xi) + \vec{r}^{(2)} \cos(4\xi) + \cdots . \tag{D.1.8}$$

$\vec{r}^{(0)}$ now becomes the new average (equilibrium) positions, and can be substituted back to the expansion in equation (D.1.4). The ion positions $\vec{r}$ can be attained self-consistently in this manner. A dynamical expansion of the Coulomb potential around $\vec{r}^{(0)} + \vec{r}^{(1)} \cos(2\xi)$ may yield a more accurate result for the normal modes in the plane [234]. For our purpose, the static expansion is sufficient as we only need accurate ion positions $\vec{r}$ to compute the normal modes along the z direction. Numerically, we found that $\vec{r}^{(1)} \approx -\frac{q}{2}\vec{r}^{(0)}$ and $\vec{r}^{(2)} \approx \frac{q^2}{32}\vec{r}^{(0)}$, which are consistent with previous results [233, 234]. Hence, micromotion only results in breathing oscillations about the average positions of each ion. The further the ion is from the center of the trap, the larger the amplitude of micromotion becomes.

Fig. D.1.2 shows the amplitude of micromotion for each ion. The largest amplitude for the edge ion is around $1.35\,\mu$m, which is well below the ion separation ($7 \sim 10\,\mu$m), necessary for the formation of a well-defined crystal and for individual addressing.

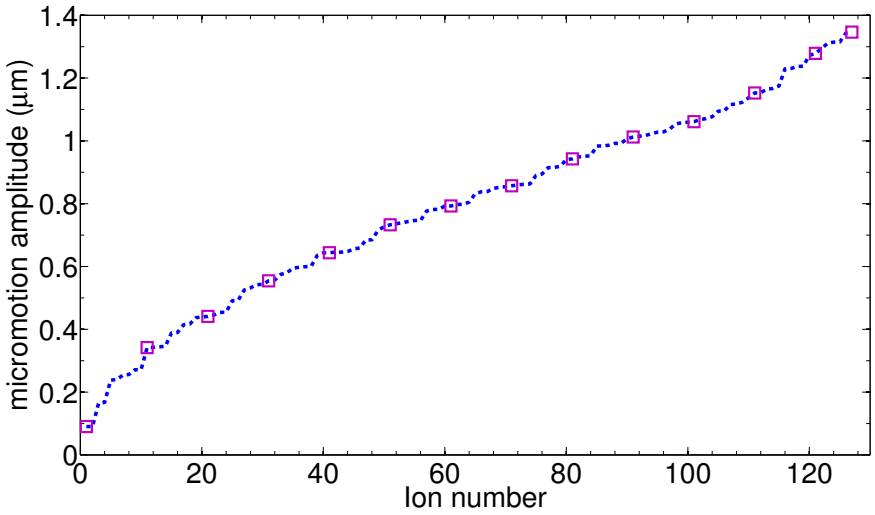

Figure D.1.2: Amplitude of micromotion for each ion (sorted in increasing order).

D.2 Normal Modes along the Transverse Direction

With the knowledge of the motion of ions in the x-y plane, we could find the normal modes and quantize the motion along the transverse (z) direction. As $z_i \approx 0$, the micromotion along the transverse direction is negligible (in the order of $O\left(q_z^3/128\right)$ [234]). A harmonic pseudopotential is thus valid for the z direction. Expanding the Coulomb potential to second order again, we have

$$V_z = \frac{1}{2} m\omega_z^2 \sum_i z_i^2 + \frac{1}{2}\frac{e^2}{4\pi\epsilon_0}\left[\sum_{i\neq j}\left(\frac{1}{r_{ij}^3}\right) z_i z_j - \sum_{i\neq j}\left(\frac{1}{r_{ij}^3}\right) z_i^2\right], \tag{D.2.1}$$

where $r_{ij} = \sqrt{(x_i - x_j)^2 + (y_i - y_j)^2}$. $x_i(t)$ and $y_i(t)$ are time-dependent though, due to the in-plane micromotion. From here, we can see explicitly that the transverse modes are decoupled from the planar modes. Expanding the term $1/r_{ij}^3(t)$ in series, one has

$$\frac{1}{r_{ij}^3} \approx \left\langle \frac{1}{r_{ij}^3} \right\rangle + M_{ij}\cos(\Omega_T t) + \cdots \tag{D.2.2}$$

The matrix element M_{ij} is in the order of $O(q)$ and can be obtained numerically from $\left\langle \cos(\Omega_T t)/r_{ij}^3 \right\rangle$. To have an intuitive understanding of the effect of micromotion on transverse modes, we take positions $\vec{r}$ in the form of Eq. (D.1.8), obtaining

$$\frac{1}{r_{ij}^3} \approx \left(\frac{1}{r_{ij}^{(0)}}\right)^3 \left(1 - \frac{q}{2}\cos(\Omega_T t) + \frac{q^2}{32}\cos(2\Omega_T t)\right)^{-3} + O(q^3), \tag{D.2.3}$$

where $r_{ij}^{(0)}$ is the zeroth order approximation using the average positions $\vec{r}^{\,(0)}$ without considering micromotion. Thus, $\left\langle 1/r_{ij}^3 \right\rangle \approx \left(1/r_{ij}^{(0)}\right)^3 (1 - 3q^2/4) + O(q^3)$, where we used the fact that $\langle \cos(\Omega_T t) \rangle = 0$ and $\langle \cos^2(\Omega_T t) \rangle = 1/2$. From the time-independent term $\left\langle 1/r_{ij}^3 \right\rangle$, we diagonalize V_z and find the normal modes as well as the eigenenergies in the transverse direction. Subsequently, we quantize the total Hamiltonian (with kinetic energy) and write $H = \sum_k \hbar\omega_k a_k^\dagger a_k$, where a_k is the annihilation operator for the quantized phonon mode, and ω_k is the corresponding eigenfrequency. In the interaction picture, $a_k \to a_k e^{-i\omega_k t}$. The time-dependent term containing $\cos(\Omega_T t)$ can then be treated as a perturbation; under the rotating wave approximation, since $\Omega_T \gg \omega_k$, the term affects the normal modes to the order of $O\left(q\omega_k^2/\Omega_T^2\right) \sim O(qq_z^2)$, which can be safely neglected. Since the first term in V_z is diagonal in z_i and the second term is reduced by a factor $(1 - 3q^2/4)$ by micromotion, the normal mode structure remains unchanged, and the mode frequencies are reduced slightly.

D.3 Two-ion Entangling Gate

The spin-dependent force on an ion is due to the AC Stark shift on each spin state. A different shift on the two internal spin states of an ion results in a Hamiltonian

$$H = \hbar \frac{|\Omega_{\text{eg}}|^2}{4\delta} \sigma^z, \tag{D.3.1}$$

where Ω_{eg} is the Rabi frequency of the laser beam and δ is the detuning from the excited state. By shining two laser beams at an angle with wave vectors $\mathbf{k}_1$, $\mathbf{k}_2$ and frequencies ω_1, ω_2, we have

$$\Omega_{\text{eg}} = \Omega_0 \left(e^{i(\mathbf{k}_1 \cdot \mathbf{r} + \omega_1 t + \phi)} + e^{i(\mathbf{k}_2 \cdot \mathbf{r} + \omega_2 t)} \right), \tag{D.3.2}$$

where ϕ is the phase difference between two beams. So we have

$$H = \hbar\Omega \left(1 + \cos(\Delta k \cdot z + \mu t + \phi)\right) \sigma^z, \tag{D.3.3}$$

where $\Omega = \Omega_0^2 / 2\delta$ is the effective two-photon Rabi frequency, $\Delta k \hat{z} = \mathbf{k}_1 - \mathbf{k}_2$ is aligned along the z direction, and $\mu = \omega_1 - \omega_2$. As we are mostly interested in the two-qubit entangling gate, which is the building block for universal quantum gates, we consider laser beams shining on two ions, and ignore the first term $\hbar\Omega\sigma^z$ in the Hamiltonian that only induces single bit operations. We therefore have

$$H = \sum_{j=1}^{2} \hbar\Omega_j \cos(\Delta k \cdot z_j + \mu t + \phi_j) \sigma_j^z, \tag{D.3.4}$$

The ion position $z_j = z_{j0} + \delta z_j$, where z_{j0} is the equilibrium position and δz_j is the small displacement. We dump the term $\Delta k \cdot z_{j0}$ to the phase ϕ_j, and expand the cosine term in

the Lamb-Dicke limit $\Delta k \cdot \delta z_j \ll 1$,

$$H = \sum_{j=1}^{2} \hbar\Omega_j \cos(\Delta k \cdot \delta z_j + \mu t + \phi_j)\sigma_j^z \tag{D.3.5}$$

$$\approx -\sum_{j=1}^{2} \hbar\Omega_j \sin(\Delta k \cdot \delta z_j) \sin(\mu t + \phi_j)\sigma_j^z \tag{D.3.6}$$

$$\approx -\sum_{j,k} \hbar\Omega_j \sin(\mu t + \phi_j)\Delta k \left[\sqrt{\frac{\hbar}{2m\omega_k}} b_j^k a_k^\dagger + \text{H.c.}\right] \sigma_j^z$$

$$= -\sum_{j=1}^{2}\sum_{k} \chi_j(t) g_j^k (a_k^\dagger + a_k)\sigma_j^z \tag{D.3.7}$$

In step (D.3.6), we drop the cosine-cosine term $\hbar\Omega_j \cos(\Delta k \cdot \delta z_j)\cos(\mu t + \phi_j)\sigma_j^z \approx \hbar\Omega_j \cos(\mu t + \phi_j)\sigma_j^z$ since $\Delta k \cdot \delta z_j \ll 1$ and it thus does not couple the phonon modes to the spin (in the first-order approximation), resulting in a single-qubit operation. Various terms are defined as

$$\delta z_j = \sum_k \sqrt{\frac{\hbar}{2m\omega_k}} b_j^k a_k^\dagger + \text{H.c.} \tag{D.3.8}$$

where b_j^k are the mode vector for mode k, $a_k^\dagger$ creates the k-th phonon mode (harmonic oscillator mode). The matrix b_n^k diagonalizes the approximate harmonic potential of the system.

$$\chi_j(t) = \hbar\Omega_j \sin(\mu t + \phi_j) \tag{D.3.9}$$

$$g_j^k = \eta_k b_j^k, \quad \text{where} \quad \eta_k = \Delta k \sqrt{\frac{\hbar}{2m\omega_k}} \tag{D.3.10}$$

η_k is the Lamb-Dicke parameter, $\eta_k \ll 1$ to be valid (for the expansion). For $\Delta k = 8\mu m^{-1}$, $m = 171u$ for Ytterbium, and take the transverse mode $\omega_k = 2\pi \times 2\text{MHz}$. We will have

$\eta_k \approx 0.03$. Going into the interaction picture and replacing $a_k \to a_k e^{-i\omega_k t}$, we have

$$H_{\mathrm{I}} = -\sum_{j=1}^{2}\sum_{k} \chi_j(t) g_j^k (a_k^\dagger e^{i\omega_k t} + a_k e^{-i\omega_k t})\sigma_j^z \tag{D.3.11}$$

The evolution operator can be obtained from the Hamiltonian as [239, 247]

$$U(\tau) = \exp\big(i\sum_j \phi_j(\tau)\sigma_j^z + i\sum_{j<n}\phi_{jn}(\tau)\sigma_j^z\sigma_n^z\big), \tag{D.3.12}$$

$$\phi_j(\tau) = -i\sum_k \alpha_j^k(\tau)a_k^\dagger - \alpha_j^{k*}(\tau)a_k \tag{D.3.13}$$

$$\alpha_j^k(\tau) = \frac{i}{\hbar}g_j^k\int_0^\tau \chi_j(t)e^{i\omega_k t}dt, \tag{D.3.14}$$

$$\phi_{jn}(\tau) = \frac{2}{\hbar^2}\sum_k g_j^k g_n^k \int_0^\tau\int_0^{t_2}\chi_j(t_2)\chi_n(t_1)\times$$
$$\sin(\omega_k(t_2-t_1))dt_1dt_2. \tag{D.3.15}$$

To obtain a two-qubit entangling gate, we need $\alpha_j^k = 0$ so that the spin and phonons are disentangled at the end of the gate, and $\phi_{jn}(\tau) = \pi/4$. This is the starting point to calculate the fidelity of the gate.

D.4 Derivation of the Fidelity for Non-ideal Gate

When $\alpha_i^k(\tau) = 0$ for all modes k and all ions and $\phi_{ij}(\tau) = \pi/4$ for only two ions i and j, the evolution operator becomes an ideal conditional phase flip (CPF) gate:

$$U_{ij}^{\text{ideal}} = \exp(i\pi\sigma_i^z\sigma_j^z/4) = \begin{pmatrix} e^{i\pi/4} & 0 & 0 & 0 \\ 0 & e^{-i\pi/4} & 0 & 0 \\ 0 & 0 & e^{-i\pi/4} & 0 \\ 0 & 0 & 0 & e^{i\pi/4} \end{pmatrix} \tag{D.4.1}$$

Here we derive the formula for the fidelity of the CPF gate in a general situation where $\alpha_i^k(\tau) \neq 0$ and $\phi_{ij}(\tau) \neq \pi/4$. Assuming the initial state is $|\Psi_0\rangle$, the ideal final state would be $U_{ij}^{\text{ideal}}|\Psi_0\rangle$, while the actual final density matrix is $\rho_r = \text{tr}_m\{U(\tau)|\Psi_0\rangle\langle\Psi_0|U(\tau)^\dagger\}$, which is the reduced density matrix of the qubits after tracing out the motional degrees of freedom. So the fidelity is defined as

$$F = \langle\Psi_0|\,(U_{ij}^{\text{ideal}})^\dagger \rho_r U_{ij}^{\text{ideal}}\,|\Psi_0\rangle \tag{D.4.2}$$

For a simplified case where only two ions are illuminated, i.e., χ_i, $\chi_j \neq 0$ and $\alpha_m^k(\tau) = 0$, if $m \neq i$, j and $\phi_{pq}(\tau) = 0$ unless $p = i(j)$, $q = j(i)$, we have a simple form of $U(\tau)$ written in the basis of $|00\rangle, |01\rangle, |10\rangle, |11\rangle$:

$$U(\tau) = \begin{pmatrix} e^{i\Phi_{00}} & 0 & 0 & 0 \\ 0 & e^{i\Phi_{01}} & 0 & 0 \\ 0 & 0 & e^{i\Phi_{10}} & 0 \\ 0 & 0 & 0 & e^{i\Phi_{11}} \end{pmatrix}, \tag{D.4.3}$$

where

$$\Phi_{00} = \phi_i + \phi_j + \phi_{ij} \qquad \Phi_{01} = \phi_i - \phi_j - \phi_{ij}$$
$$\Phi_{10} = -\phi_i + \phi_j - \phi_{ij} \quad \Phi_{11} = -\phi_i - \phi_j + \phi_{ij}. \tag{D.4.4}$$

The term $e^{i\phi_i} = \exp\left(\sum_k \alpha_j^k(\tau)a_k^\dagger - \alpha_j^{k*}(\tau)a_k\right)$ is the product of displacement operators $D(\alpha)$ for each quantum harmonic oscillator mode. Note that ϕ_{ij} is a real scalar and ϕ_i, ϕ_j are Hermitian operators. If we take the initial state $|\Psi_0\rangle = 1/2(|0\rangle + |1\rangle) \otimes (|0\rangle + |1\rangle)$, then

$$U(\tau)|\Psi_0\rangle\langle\Psi_0|U(\tau)^\dagger = \frac{1}{4}\begin{pmatrix} e^{i(\Phi_{00}-\Phi_{00}^\dagger)} & e^{i(\Phi_{00}-\Phi_{01}^\dagger)} & e^{i(\Phi_{00}-\Phi_{10}^\dagger)} & e^{i(\Phi_{00}-\Phi_{11}^\dagger)} \\ e^{i(\Phi_{01}-\Phi_{00}^\dagger)} & e^{i(\Phi_{01}-\Phi_{01}^\dagger)} & e^{i(\Phi_{01}-\Phi_{10}^\dagger)} & e^{i(\Phi_{01}-\Phi_{11}^\dagger)} \\ e^{i(\Phi_{10}-\Phi_{00}^\dagger)} & e^{i(\Phi_{10}-\Phi_{01}^\dagger)} & e^{i(\Phi_{10}-\Phi_{10}^\dagger)} & e^{i(\Phi_{10}-\Phi_{11}^\dagger)} \\ e^{i(\Phi_{11}-\Phi_{00}^\dagger)} & e^{i(\Phi_{11}-\Phi_{01}^\dagger)} & e^{i(\Phi_{11}-\Phi_{10}^\dagger)} & e^{i(\Phi_{11}-\Phi_{11}^\dagger)} \end{pmatrix}. \tag{D.4.5}$$

The trace over phonon modes reduces to

$$\begin{aligned} &\mathrm{tr}_m(e^{i(\Phi_{00}-\Phi_{01}^\dagger)}) = \mathrm{tr}_m(e^{2i(\phi_j+\phi_{ij})}) \\ =&e^{2i\phi_{ij}}\mathrm{tr}_m(e^{2\sum_k[\alpha_j^k a_k^\dagger - \alpha_j^{k*}a_k]}) \\ =&e^{2i\phi_{ij}}\prod_k \mathrm{tr}_m(D(2\alpha_j^k)) \\ =&e^{2i\phi_{ij}}e^{-1/2\sum_k\left|2\alpha_j^k\right|^2\coth(\hbar\omega_k/2k_BT)} \end{aligned} \tag{D.4.6}$$

In the above equation, we used the formula

$$\mathrm{tr}_m[D(\alpha)] = e^{-\frac{|\alpha|^2}{2}\coth(\hbar\omega/2k_BT)}. \tag{D.4.7}$$

Here, let's provide more details for this formula. The trace is over the motional modes, and we take the thermal state

$$\rho_{\text{th}} = \frac{\exp\left(-H_m/k_BT\right)}{\text{Tr}(\exp\left(-H_m/k_BT\right))}, \text{ where } H_m = \hbar\omega a^\dagger a. \tag{D.4.8}$$

In the Fock space,

$$\rho_{\text{th}} = \left(1 - e^{-\hbar\omega/k_BT}\right) \sum_{n=0}^{\infty} e^{-n\hbar\omega/k_BT} |n\rangle\langle n|. \tag{D.4.9}$$

We also have $D(\alpha) = e^{|\alpha|^2/2} e^{-\alpha^* a} e^{\alpha a^\dagger}$. Therefore,

$$\begin{aligned}
\text{tr}_m[D(\alpha)] = \text{tr}(D(\alpha)\rho_{\text{th}}) &= \left(1 - e^{-\hbar\omega/k_BT}\right) e^{|\alpha|^2/2} \sum_{n=0}^{\infty} e^{-n\hbar\omega/k_BT} \text{Tr}(e^{-\alpha^* a} e^{\alpha a^\dagger} |n\rangle\langle n|) \\
&= \left(1 - e^{-\hbar\omega/k_BT}\right) e^{|\alpha|^2/2} \sum_{n=0}^{\infty} e^{-n\hbar\omega/k_BT} \text{Tr}\left(\sum_m \frac{1}{m!}(-\alpha^* a)^m \sum_p \frac{1}{p!}(\alpha a^\dagger)^p |n\rangle\langle n|\right) \\
&= \left(1 - e^{-\hbar\omega/k_BT}\right) e^{|\alpha|^2/2} \sum_{n=0}^{\infty} e^{-n\hbar\omega/k_BT} \text{Tr}\left(\sum_m \frac{(-1)^m |\alpha|^{2m}}{(m!)^2} a^m (a^\dagger)^m |n\rangle\langle n|\right) \\
&= \left(1 - e^{-\hbar\omega/k_BT}\right) e^{|\alpha|^2/2} \sum_{n=0}^{\infty} e^{-n\hbar\omega/k_BT} \sum_{m=0}^{\infty} \frac{(-1)^m |\alpha|^{2m}}{(m!)^2} (n+1)(n+2)\cdots(n+m) \\
&= e^{-\frac{|\alpha|^2}{2}\coth(\hbar\omega/2k_BT)}.
\end{aligned} \tag{D.4.10}$$

In the second line, the trace is nonzero only when $m = p$, and the last line can be evaluated with Mathematica. This produces equation (D.4.7). Denoting $\Gamma_{i(j)} = \prod_k \text{tr}_m[D(2\alpha^k_{i(j)})]$ and

$\Gamma_\pm = \prod_k \mathrm{tr}_m[D(2(\alpha_i^k \pm \alpha_j^k))]$, we finally obtain

$$\rho_r = \mathrm{tr}_m\{U(\tau)|\Psi_0\rangle\langle\Psi_0|U(\tau)^\dagger\} = \frac{1}{4}\begin{pmatrix} 1 & \Gamma_j e^{2i\phi_{ij}} & \Gamma_i e^{2i\phi_{ij}} & \Gamma_+ \\ \Gamma_j e^{-2i\phi_{ij}} & 1 & \Gamma_- & \Gamma_i e^{-2i\phi_{ij}} \\ \Gamma_i e^{-2i\phi_{ij}} & \Gamma_- & 1 & \Gamma_j e^{-2i\phi_{ij}} \\ \Gamma_+ & \Gamma_i e^{2i\phi_{ij}} & \Gamma_j e^{2i\phi_{ij}} & 1 \end{pmatrix}. \quad \text{(D.4.11)}$$

The fidelity of the gate can thus be simplified as

$$\begin{aligned} F_g =& \langle\Psi_0| \left(U_{ij}^{\mathrm{ideal}}\right)^\dagger \rho_r U_{ij}^{\mathrm{ideal}} |\Psi_0\rangle \\ =& \frac{1}{16}\begin{pmatrix} e^{-i\pi/4} & e^{+i\pi/4} & e^{+i\pi/4} & e^{-i\pi/4} \end{pmatrix} \begin{pmatrix} 1 & \Gamma_j e^{2i\phi_{ij}} & \Gamma_i e^{2i\phi_{ij}} & \Gamma_+ \\ \Gamma_j e^{-2i\phi_{ij}} & 1 & \Gamma_- & \Gamma_i e^{-2i\phi_{ij}} \\ \Gamma_i e^{-2i\phi_{ij}} & \Gamma_- & 1 & \Gamma_j e^{-2i\phi_{ij}} \\ \Gamma_+ & \Gamma_i e^{2i\phi_{ij}} & \Gamma_j e^{2i\phi_{ij}} & 1 \end{pmatrix} \begin{pmatrix} e^{i\pi/4} \\ e^{-i\pi/4} \\ e^{-i\pi/4} \\ e^{i\pi/4} \end{pmatrix} \\ =& \frac{1}{8}\left\{2 + 2(\Gamma_i + \Gamma_j)\sin(2\phi_{ij}) + \Gamma_+ + \Gamma_-\right\}. \end{aligned} \quad \text{(D.4.12)}$$

D.5 Gate Fidelity with Segmented Pulses

When we make sure $\phi_{ij}(\tau) = \pi/4$, the gate fidelity F_g is given as

$$F_g = \frac{1}{8}\left[2 + 2(\Gamma_i + \Gamma_j) + \Gamma_+ + \Gamma_-\right] \quad \text{(D.5.1)}$$

$$\Gamma_{i(j)} = \exp(-\sum_k |\alpha_{i(j)}^k(\tau)|^2 \bar{\beta}_k), \quad \text{(D.5.2)}$$

$$\Gamma_\pm = \exp(-\sum_k |\alpha_i^k(\tau) \pm \alpha_j^k(\tau)|^2 \bar{\beta}_k) \quad \text{(D.5.3)}$$

where $\bar{\beta}_k = 2\coth(\hbar\omega_k/2k_BT)$. In the first order approximation ($|\alpha^k_{i(j)}(\tau)| \ll 1$),

$$\Gamma_{i(j)} = 1 - \sum_k |\alpha^k_{i(j)}(\tau)|^2 \bar{\beta}_k, \tag{D.5.4}$$

$$\Gamma_{\pm} = 1 - \sum_k |\alpha^k_i(\tau) \pm \alpha^k_j(\tau)|^2 \bar{\beta}_k \tag{D.5.5}$$

So the gate fidelity reduces to

$$F_g \approx 1 - \frac{1}{2}\sum_k \bar{\beta}_k(|\alpha^k_i(\tau)|^2 + |\alpha^k_j(\tau)|^2). \tag{D.5.6}$$

Now we need to find $\alpha^k_{i(j)}(\tau)$:

$$\alpha^k_j(\tau) = \frac{i}{\hbar} g^k_j \int_0^\tau \chi_j(t) e^{i\omega_k t} dt, \tag{D.5.7}$$

$$\chi_j = \hbar\Omega^{(i)}_j \Omega^{\mathrm{G}}_j(t)\sin(\mu t + \phi_j),$$
$$\text{for } (i-1)\frac{\tau}{n} < t < i\frac{\tau}{n}, \tag{D.5.8}$$

where $\Omega_j(t) = \Omega^{(i)}_j \Omega^{\mathrm{G}}_j(t)$ is divided into n equal segments with constant (real) amplitude $\Omega^{(i)}_j$ for the ith segment. The time-dependent part $\Omega^{\mathrm{G}}_j(t)$ takes a Gaussian form, taking into account of the micromotion in the x-y plane.

$$\Omega^{\mathrm{G}}_j(t) = \exp\left\{-\frac{(x_j(t) - \bar{x}_j)^2 + (y_j(t) - \bar{y}_j)^2}{w^2}\right\}, \tag{D.5.9}$$

where $(\bar{x}_j, \bar{y}_j)$ is the average position for the jth ion, and $(x_j(t), y_j(t))$ is the time-dependent position due to micromotion, w is the width for the Gaussian beam profile. With n segments,

we can write

$$\alpha_j^k(\tau) = \begin{pmatrix} \beta_{j,k}^{(1)} & \beta_{j,k}^{(2)} & \cdots & \beta_{j,k}^{(n)} \end{pmatrix} \begin{pmatrix} \Omega_j^{(1)} \\ \Omega_j^{(2)} \\ \vdots \\ \Omega_j^{(n)} \end{pmatrix} = \vec{\beta}_{j,k} \cdot \vec{\Omega}_j \tag{D.5.10}$$

where,

$$\beta_{j,k}^{(i)} = i g_j^k \int_{\frac{(i-1)\tau}{n}}^{\frac{i\tau}{n}} \Omega_j^{\mathrm{G}}(t) \sin(\mu t + \phi_j) e^{i\omega_k t} dt. \tag{D.5.11}$$

Here, there is a subtlety in the minimization. We would like to minimize $\sum_k \bar{\beta}_k |\alpha_j^k(\tau)|^2 = \sum_k \bar{\beta}_k |\vec{\beta}_{j,k} \cdot \vec{\Omega}_j|^2$. However, we intend to keep $\vec{\Omega}_j$ real, but $\vec{\beta}_{j,k}$ is complex. Minimizing the quadratic form will result in complex $\vec{\Omega}_j$ in general. The trick is to split the real and complex parts of $\vec{\beta}_{j,k}$.

$$\begin{aligned}
&\sum_k \bar{\beta}_k |\alpha_j^k(\tau)|^2 = \sum_k \bar{\beta}_k |\vec{\beta}_{j,k} \cdot \vec{\Omega}_j|^2 \\
=&\sum_k \bar{\beta}_k |\mathrm{Re}(\vec{\beta}_{j,k}) \cdot \vec{\Omega}_j + i\ \mathrm{Im}(\vec{\beta}_{j,k}) \cdot \vec{\Omega}_j|^2 \\
=&\sum_k \bar{\beta}_k \left(|\mathrm{Re}(\vec{\beta}_{j,k}) \cdot \vec{\Omega}_j|^2 + |\mathrm{Im}(\vec{\beta}_{j,k}) \cdot \vec{\Omega}_j|^2 \right) \\
=&\vec{\Omega}_j^T \sum_k \bar{\beta}_k \left(\mathrm{Re}(\vec{\beta}_{j,k}) \mathrm{Re}(\vec{\beta}_{j,k}^T) + \mathrm{Im}(\vec{\beta}_{j,k}) \mathrm{Im}(\vec{\beta}_{j,k}^T) \right) \vec{\Omega}_j \\
=&\vec{\Omega}_j^T M_j \vec{\Omega}_j
\end{aligned} \tag{D.5.12}$$

M_j is an $n \times n$ positive-definite matrix. Minimizing the term over the vector $\vec{\Omega}_j$ is equivalent to finding the minimum eigenvalue and the corresponding eigenvector for the matrix M_j. So

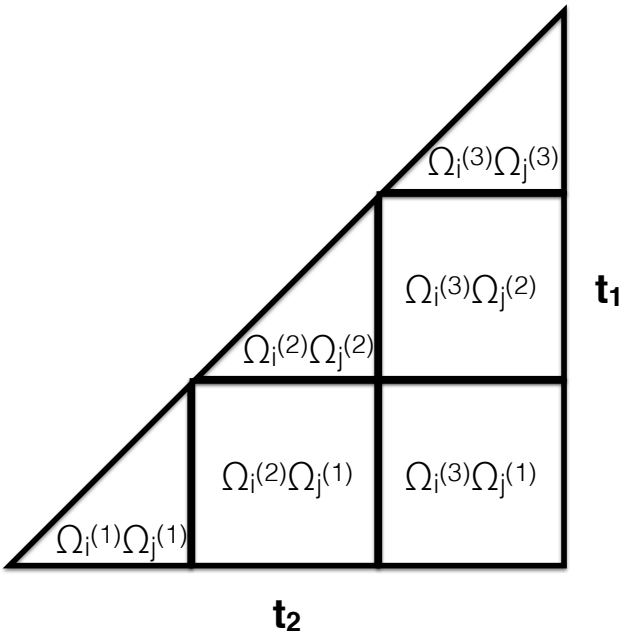

Figure D.5.1: The double time integral involved in evaluating the two-qubit phase ϕ_{ij}.

equation (D.5.6) becomes

$$F_g = 1 - \frac{1}{2}\vec{\Omega}_i^T M_i \vec{\Omega}_i - \frac{1}{2}\vec{\Omega}_j^T M_j \vec{\Omega}_j, \tag{D.5.13}$$

where $M_{i(j)}$ are the corresponding matrix defined above for the ion $i(j)$.

We now go to the two-qubit phase

$$\phi_{ij}(\tau) = \frac{2}{\hbar^2}\sum_k g_i^k g_j^k \int_0^\tau \int_0^{t_2} \chi_i(t_2)\chi_j(t_1) \times \sin(\omega_k(t_2 - t_1))dt_1 dt_2. \tag{D.5.14}$$

Dividing each beam $\Omega_{i(j)}(t)$ into n segments again, we have

$$\phi_{ij}(\tau) = \sum_{p,q=1}^{n} \Omega_i^{(p)} \gamma_{pq} \, \Omega_j^{(q)}, \tag{D.5.15}$$

$$\gamma_{pq} = \sum_k 2 g_i^k g_j^k \int_{\frac{(p-1)\tau}{n}}^{\frac{p\tau}{n}} \int_{\frac{(q-1)\tau}{n}}^{\frac{q\tau}{n}} \Omega_i^{\mathrm{G}}(t_2) \sin(\mu t_2 + \phi_i) \times$$

$$\Omega_j^{\mathrm{G}}(t_1) \sin(\mu t_1 + \phi_j) \sin(\omega_k (t_2 - t_1)) dt_1 dt_2 \text{ for } q < p, \tag{D.5.16}$$

$$\gamma_{pp} = \sum_k 2 g_i^k g_j^k \int_{\frac{(p-1)\tau}{n}}^{\frac{p\tau}{n}} \int_{\frac{(p-1)\tau}{n}}^{t_2} \Omega_i^{\mathrm{G}}(t_2) \sin(\mu t_2 + \phi_i) \times$$

$$\Omega_j^{\mathrm{G}}(t_1) \sin(\mu t_1 + \phi_j) \sin(\omega_k (t_2 - t_1)) dt_1 dt_2 \text{ for } q = p. \tag{D.5.17}$$

The double integral is only performed for $q \leq p$. This can be seen more easily in figure D.5.1, where t_1 and t_2 are divided into n segments each, and the double integral is done when $t_1 \leq t_2$. To get the entangling gate, we require $\phi_{ij} = \pi/4$. Let's take a look at the fidelity and the two-qubit phase again:

$$F_g = 1 - \frac{1}{2} \vec{\Omega}_i^T M_i \vec{\Omega}_i - \frac{1}{2} \vec{\Omega}_j^T M_j \vec{\Omega}_j \tag{D.5.18}$$

$$\phi_{ij}(\tau) = \sum_{p,q=1}^{n} \Omega_i^{(p)} \gamma_{pq} \, \Omega_j^{(q)} = \frac{\pi}{4} \tag{D.5.19}$$

Maximizing the fidelity F_g determines the direction (eigenvector) of $\vec{\Omega}_i$ and $\vec{\Omega}_j$. Setting $\phi_{ij}(\tau) = \pi/4$ will fix the magnitude of $|\vec{\Omega}_i| \times |\vec{\Omega}_j|$. Decompose the vectors into magnitude and a unit vector, $\vec{\Omega}_i = |\vec{\Omega}_i| \hat{\Omega}_i$, $\vec{\Omega}_j = |\vec{\Omega}_j| \hat{\Omega}_j$. Let the minimum eigenvalue of M_i and M_j be

c_i and c_j, and set $c_\phi = \pi/(4\hat{\Omega}_i^T \boldsymbol{\gamma} \hat{\Omega}_j)$. The problem reduces to

$$\text{minimize:} \quad c_i|\vec{\Omega}_i|^2 + c_j|\vec{\Omega}_j|^2 \tag{D.5.20}$$

$$\text{constraint:} \quad |\vec{\Omega}_i| \times |\vec{\Omega}_j| = c_\phi, \tag{D.5.21}$$

which one can solve to get the magnitude of the laser beam

$$|\vec{\Omega}_i| = \left(\frac{c_j c_\phi^2}{c_i}\right)^{1/4} \qquad |\vec{\Omega}_j| = \left(\frac{c_i c_\phi^2}{c_j}\right)^{1/4}. \tag{D.5.22}$$

Finally, the fidelity is given in this first order approximation as

$$F_g = 1 - c_\phi \sqrt{c_i c_j}. \tag{D.5.23}$$

Actual numerical calculation of the fidelity does not use the first order approximation, but use the full fidelity formula Eq. (D.4.12). When $\sum_k |\alpha^k_{i(j)}(\tau)|^2 \bar{\beta}_k \ll 1$, the first order approximation suffices. The above calculation assumes $\vec{\Omega}_i$ and $\vec{\Omega}_j$ can be individually controlled. If they share the same laser field, $\vec{\Omega}_i = \vec{\Omega}_j$, we just need to modify the computation slightly:

$$F_g = 1 - \frac{1}{2}\vec{\Omega}_i^T (M_i + M_j)\vec{\Omega}_i \tag{D.5.24}$$

$$\phi_{ij}(\tau) = \sum_{p,q=1}^{n} \Omega_i^{(p)} \gamma_{pq}\, \Omega_i^{(q)} = \frac{\pi}{4}. \tag{D.5.25}$$

So as above minimizing F_g determines the eigendirection and ϕ_{ij} determines the magnitude of $|\vec{\Omega}_i|$. There is a slight difference when we have one or two controllable Rabi frequencies. In the above, when we have two independent Rabi frequency vectors, we can always ensure $\phi_{ij}(\tau) = \pi/4$. Even when $\hat{\Omega}_i^T \boldsymbol{\gamma} \hat{\Omega}_j < 0$, one can change the direction of $\vec{\Omega}_i$ to make it positive.

However, that can't be done when there is only one Rabi vector. So in Eq. (D.5.25), if $\hat{\Omega}_i^T \boldsymbol{\gamma} \hat{\Omega}_i < 0$, we need to take $\phi_{ij}(\tau) = -3\pi/4$ to make sure $\sin(2\phi_{ij}) = 1$. The rest is the same.

APPENDIX E

Hamiltonian Tomography for Quantum Many-body Systems

E.1 Dynamical Decoupling

The most general Hamiltonian with two-body qubit interactions can be written as

$$H = \sum_{\alpha,\beta,m<n} J_{mn}^{\alpha\beta}\sigma_m^\alpha\sigma_n^\beta + \sum_{m,\alpha} b_m^\alpha\sigma_m^\alpha. \tag{E.1.1}$$

The energy unit of the Hamiltonian is taken to be J such that $J_{mn}^{\alpha\beta}/J$ and b_m^α/J are bounded between -1 and 1. The symmetric XY-4 dynamical decoupling (DD) sequence on both spins i and j produces

$$U_1 = U_0^{1/2}\left(\sigma_i^x\sigma_j^x U_0 \sigma_i^x\sigma_j^x\right)\left(\sigma_i^z\sigma_j^z U_0 \sigma_i^z\sigma_j^z\right)\left(\sigma_i^y\sigma_j^y U_0 \sigma_i^y\sigma_j^y\right)U_0^{1/2}, \tag{E.1.2}$$

where $U_0 = e^{-iH\tau}$ and τ is the time interval between consecutive pulses. We can decompose H into two parts.

$$H = H_0 + H_1, \tag{E.1.3}$$

$$H_0 = J_{ij}^{xx}\sigma_i^x\sigma_j^x + J_{ij}^{yy}\sigma_i^y\sigma_j^y + J_{ij}^{zz}\sigma_i^z\sigma_j^z, \tag{E.1.4}$$

$$\begin{aligned} H_1 = {} & J_{ij}^{xy}\sigma_i^x\sigma_j^y + J_{ij}^{xz}\sigma_i^x\sigma_j^z + J_{ij}^{yx}\sigma_i^y\sigma_j^x + J_{ij}^{yz}\sigma_i^y\sigma_j^z + J_{ij}^{zx}\sigma_i^z\sigma_j^x + J_{ij}^{zy}\sigma_i^z\sigma_j^y \\ & + \sigma_i^x B_i^x + \sigma_i^y B_i^y + \sigma_i^z B_i^z + \sigma_j^x B_j^x + \sigma_j^y B_j^y + \sigma_j^z B_j^z + B, \end{aligned} \tag{E.1.5}$$

where B_i^α includes the local field on the ith spin and interacting terms between the ith spin and all other spins other than the jth spin, i.e., $B_i^\alpha = b_i^\alpha + \sum_{\beta,n\neq i,j} J_{in}^{\alpha\beta}\sigma_n^\beta$. The bath term B includes all the environment operations, i.e., all operators that does not act on spins i and j. We define other Hamiltonian part as

$$\sigma_i^x\sigma_j^x H\sigma_i^x\sigma_j^x = H_0 + H_2, \quad \sigma_i^y\sigma_j^y H\sigma_i^y\sigma_j^y = H_0 + H_3, \quad \sigma_i^z\sigma_j^z H\sigma_i^z\sigma_j^z = H_0 + H_4, \tag{E.1.6}$$

where

$$\begin{aligned} H_2 = {} & -J_{ij}^{xy}\sigma_i^x\sigma_j^y - J_{ij}^{xz}\sigma_i^x\sigma_j^z - J_{ij}^{yx}\sigma_i^y\sigma_j^x + J_{ij}^{yz}\sigma_i^y\sigma_j^z - J_{ij}^{zx}\sigma_i^z\sigma_j^x + J_{ij}^{zy}\sigma_i^z\sigma_j^y \\ & + \sigma_i^x B_i^x - \sigma_i^y B_i^y - \sigma_i^z B_i^z + \sigma_j^x B_j^x - \sigma_j^y B_j^y - \sigma_j^z B_j^z + B, \end{aligned} \tag{E.1.7}$$

$$\begin{aligned} H_3 = {} & -J_{ij}^{xy}\sigma_i^x\sigma_j^y + J_{ij}^{xz}\sigma_i^x\sigma_j^z - J_{ij}^{yx}\sigma_i^y\sigma_j^x - J_{ij}^{yz}\sigma_i^y\sigma_j^z + J_{ij}^{zx}\sigma_i^z\sigma_j^x - J_{ij}^{zy}\sigma_i^z\sigma_j^y \\ & - \sigma_i^x B_i^x + \sigma_i^y B_i^y - \sigma_i^z B_i^z - \sigma_j^x B_j^x + \sigma_j^y B_j^y - \sigma_j^z B_j^z + B, \end{aligned} \tag{E.1.8}$$

$$\begin{aligned} H_4 = {} & +J_{ij}^{xy}\sigma_i^x\sigma_j^y - J_{ij}^{xz}\sigma_i^x\sigma_j^z + J_{ij}^{yx}\sigma_i^y\sigma_j^x - J_{ij}^{yz}\sigma_i^y\sigma_j^z - J_{ij}^{zx}\sigma_i^z\sigma_j^x - J_{ij}^{zy}\sigma_i^z\sigma_j^y \\ & - \sigma_i^x B_i^x - \sigma_i^y B_i^y + \sigma_i^z B_i^z - \sigma_j^x B_j^x - \sigma_j^y B_j^y + \sigma_j^z B_j^z + B. \end{aligned} \tag{E.1.9}$$

Basically, each term will either commute or anticommute with the operator $\sigma_i^\alpha \sigma_j^\alpha$. Those commuting with it will be left invariant, and those anticommuting will have a flipped sign. H_0 and B commute with each operator $\sigma_i^\alpha \sigma_j^\alpha$, so they are left unchanged. Now we can see explicitly that $H_1 + H_2 + H_3 + H_4 = 4B$, which is why the DD sequence effectively decouples the two spins i and j with the rest of the spins. To estimate the error, we combine the unitary evolution for a period and repeatedly make use of the formula

$$e^{\tau A} e^{\tau B} = e^{\tau A + \tau B + \frac{1}{2}\tau^2 [A,B] + O(\tau^3)}. \tag{E.1.10}$$

Ignoring τ^3 and higher-order terms, we find

$$\begin{aligned} U_1 &= e^{-i\tau/2(H_0+H_1)} e^{-i\tau(H_0+H_2)} e^{-i\tau(H_0+H_4)} e^{-i\tau(H_0+H_3)} e^{-i\tau/2(H_0+H_1)} \\ &= e^{-i4\tau(H_0+B)+C}, \end{aligned} \tag{E.1.11}$$

where the remnant coupling noise term is

$$\begin{aligned} C =& -\tfrac{1}{4}\tau^2 [H_0 + H_1, H_0 + H_2] - \tfrac{1}{2}\tau^2 \left[\tfrac{3}{2}H_0 + \tfrac{1}{2}H_1 + H_2, H_0 + H_4\right] \\ & - \tfrac{1}{2}\tau^2 \left[\tfrac{5}{2}H_0 + \tfrac{1}{2}H_1 + H_2 + H_4, H_0 + H_3\right] \\ & - \tfrac{1}{4}\tau^2 \left[\tfrac{7}{2}H_0 + \tfrac{1}{2}H_1 + H_2 + H_3 + H_4, H_0 + H_1\right] + O(\tau^3) \\ =& -\tau^2 \left\{[H_0, H_3 - H_2] + \tfrac{1}{2}[H_2 - H_3, H_4] + \tfrac{1}{2}[H_2, H_3]\right\} + O(\tau^3). \end{aligned} \tag{E.1.12}$$

In the error term C, the biggest contribution comes from terms like $[B, \sigma_m^\alpha B_m^\alpha]$. Our aim is to show that the error does not scale with the system size N, i.e., $C = O(J^2\tau^2)$. Let us

consider one such term and write it out explicitly (suppressing the α, β summation):

$$[B, \sigma_i^x B_i^x] \sim \sigma_i^x \left[\sum_{\substack{m<n \\ m,n\neq i,j}} J_{mn}^{\alpha\beta} \sigma_m^\alpha \sigma_n^\beta \, , \sum_{p\neq i,j} J_{ip}^{x\gamma} \sigma_p^\gamma \right] \sim \sigma_i^x \sum_{\substack{m<n \\ m,n\neq i,j}} J_{mn}^{\alpha\beta} J_{im}^{x\gamma} \sigma_m^\delta \sigma_n^\beta. \tag{E.1.13}$$

Since $J_{mn}^{\alpha\beta}$ and $J_{im}^{x\gamma}$ are rapidly decaying functions of the separation distance, for a fixed site i, $\sum_{m<n} J_{mn}^{\alpha\beta} J_{im}^{x\gamma} = O(J^2)$. Note that this differs from the scaling of the Hamiltonian, $H \sim \sum_{m<n} J_{mn}^{\alpha\beta} = O(NJ)$. All the other terms in C are either smaller or contribute to the same order as the above term. Therefore, we have $C = O(J^2\tau^2)$. To be able to neglect the error terms, one needs to fulfill the condition $J\tau \ll 1$.

The above discussion is pertinent to the XY-4 pulse sequence. We can cancel the second order contribution by using the XY-8 pulse sequence as $U_2 = U_1 U_1^{\mathrm{R}}$, where U_1^{R} is just the time-reversed sequence of U_1. It can be readily seen that the error terms C and C^{R} will cancel each other to the second order $O(\tau^2)$, since C^{R} contains the same terms as in C only with the role of H_2 and H_3 interchanged. Therefore, the remnant coupling error of the XY-8 pulse sequence is $O(J^3\tau^3)$ as discussed in the main text.

E.2 Local Field Retrieval

In the main text, we proposed a scheme to retrieve the local fields b_i^α by shining the XY-8 pulse sequences on all the environment spins. Here, we provide more details and outline alternative schemes that may in some experimental setups be easier to implement. By decoupling the environment spins with spin i as illustrated in the main text, we have the effective single-spin Hamiltonian $H_{\text{1-spin}} = b_i^x \sigma_i^x + b_i^y \sigma_i^y + b_i^z \sigma_i^z$. The time evolution operator

Figure E.2.1: Alternative scheme to map out the local fields b_i^α. A global pulse imposes the XY-8 pulse sequence on all spins and a focused pulse is in addition applied to spin i to cancel the DD sequence on that single spin.

is

$$U_{\text{1-spin}} = e^{-iH_{\text{1-spin}}T} = \begin{pmatrix} \cos(bT) - i\frac{b_i^z}{b}\sin(bT) & -\frac{ib_i^x + b_i^y}{b}\sin(bT) \\ \frac{b_i^y - ib_i^x}{b}\sin(bT) & \cos(bT) + i\frac{b_i^z}{b}\sin(bT) \end{pmatrix}, \tag{E.2.1}$$

where $b = \sqrt{(b_i^x)^2 + (b_i^y)^2 + (b_i^z)^2}$ is the magnitude of the Bloch vector. By measuring

$$P_{|0\rangle\to|0\rangle} = 1 + \left[(b_i^z/b)^2 - 1\right]\sin^2(bT) \tag{E.2.2}$$

$$P_{|+\rangle\to|+\rangle} = 1 + \left[(b_i^x/b)^2 - 1\right]\sin^2(bT) \tag{E.2.3}$$

at various time points, we could determine $|b_i^x|, |b_i^y|, |b_i^z|$. To pin down the correct signs, one can supplement the above two sets of measurements with another two measurement points:

$$P_{|+\rangle\to|0\rangle} = |\langle 0|U_{\text{1-spin}}|+\rangle|^2 = \frac{1}{2}\left(1 + \frac{2b_i^x b_i^z}{b^2}\sin^2 bT - \frac{b_i^y}{b}\sin 2bT\right) \tag{E.2.4}$$

$$P_{|\mathrm{I}\rangle\to|0\rangle} = |\langle 0|U_{\text{1-spin}}|\mathrm{I}\rangle|^2 = \frac{1}{2}\left(1 + \frac{2b_i^y b_i^z}{b^2}\sin^2 bT + \frac{b_i^x}{b}\sin 2bT\right). \tag{E.2.5}$$

Only one time point is needed to determine the signs. For example, one could take measurements at $bT = \pi/4$ and use $P_{|+\rangle\to|0\rangle}$ and $P_{|\mathrm{I}\rangle\to|0\rangle}$ to pick out the correct signs.

The above procedure requires applying the DD sequences to all spins other than the target

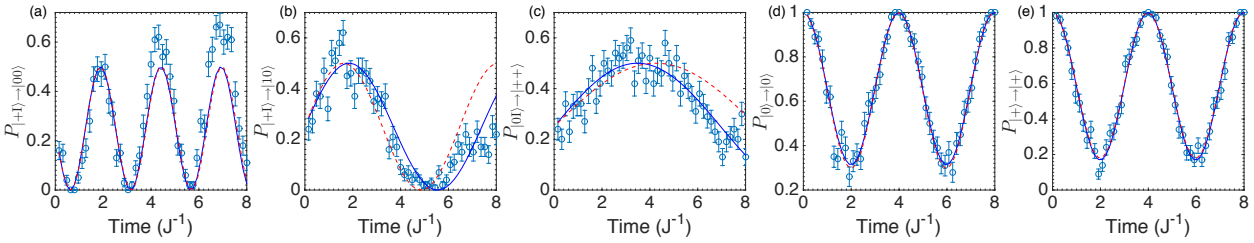

Figure E.3.1: Numerical simulation and curving fitting results with a Random Rotation axis Error (RRE) for each pulse. The RRE is of the form $e^{i\frac{\pi}{2}(\sigma^\nu+\alpha\sigma^x+\beta\sigma^y+\gamma\sigma^z)}$ where (α,β,γ) is a vector with a random direction but fixed magnitude at 1%. (a)-(c) are used to retrieve J_{79}^{xx}, J_{79}^{yy} and J_{79}^{zz} between spins 7 and 9. (d) and (e) are used to extract b_6^x, b_6^y and b_6^z for spin 6. The blue solid lines are the best-fit lines with the simulated experimental data, and red dashed lines are the theoretical ones generated by the true Hamiltonian parameters. Other parameters are the same as in the corresponding figure of the main text.

spin. In some experimental setting, it may be easier to apply a global DD sequence to all spins and add another individually addressed beam on spin i to cancel the DD sequence on that single spin. See Fig. E.2.1 for illustration. For instance, one could apply synchronized $X_{\text{All}}Y_{\text{All}}$-8 global pulses and in addition X_iY_i-8 focused pulses on spin i. In this way, spin i effectively experiences no pulses at all time. The effective Hamiltonian again reduces to the same $H_{\text{1-spin}}$ as above. However, this scheme is not very robust to pulse errors. Any deviation from the ideal pulse will be doubled on spin i and accumulate. The pulse error will affect the single-spin coherence and obscure b_i^α too. We have tested it numerically that the pulse errors have to be controlled within 0.5% for the scheme to be feasible. So it can be used in some setups where pulse errors are not an issue or the total number of pulses can be reduced. One may also use this scheme and modify the sequence by designing composite pulses or self-correcting sequences to reduce pulse errors.

E.3 Pulse Errors

In the main text, we discussed different types of pulse errors. In our numerical simulation, we considered Systematic Amplitude pulse Error (SAE), Random Amplitude pulse Error (RAE) and Random Rotation axis Error (RRE). The fitting curves in the main text do not take into account of pulse errors. Here, we include the figures (Fig. E.3.1) for the case with a 1% RRE. We can see, for example in Fig. E.3.1(a), that the frequency estimation is still very accurate while some measurement points may have a notable mismatch. We may also notice that the estimation of b_i^α is exceptionally robust to pulse errors since no pulse is applied to spin i in the scheme. Other pulse errors have similar effects on the estimation of parameters.

APPENDIX F

Towards Demonstrating Quantum Supremacy

F.1 Certification of Boson Sampling with Coarse-Grained Measurements

F.1.1 Results for the Long-time Trapped-ion System

In the main text, we included results for both the trapped-ion system with intermediate-time dynamics ($\tau = 100\,\mu$s) and for the random unitary process. In Fig. F.1.1 and Table F.1 here, we add the coarse-grained distributions and the pass rate results for the long-time trapped-ion system (at $\tau = 10\,$ms). With these coarse-grained distributions, we would like to discuss some differences between the trapped-ion system and the random unitary process. In the prototypical boson sampling problem, the hardness-of-simulation argument is based on randomly selected unitaries [36]. This is because for some structured unitary process, fast approximation algorithms may exist. For the trapped-ion system, the phonon normal modes are fixed (fixed time-independent Hamiltonian in the main text), so we may be able to

extract some distinctive structures from the output probability distributions. Nevertheless, we still expect the complex many-body dynamics in trapped ions to be classically intractable.

From the coarse-grained distributions, we can see that the boson sampling data P_S^Q for intermediate-time trapped ions are conspicuously different from alternative samples, such as the distinguishable sample P_S^C and the uniform sample P_S^U. On the other hand, the boson sampling data bear resemblance to the distinguishable samples P_S^C for random unitary processes, and the long-time trapped-ion phonon distributions are instead in closer proximity to the uniform samples P_S^U. The qualitative difference arises from the fact that the random unitary process has a Haar-distributed random unitary matrix whereas the long-time trapped-ion unitary only has random phases (eigenvalues) with a fixed crystal mode structure. We have further tested this idea by simulating the long-time trapped-ion dynamics with a unitary matrix given by the fixed mode structure and random phases. Certification results do support the notion that this system produces output probabilities in closer proximity to

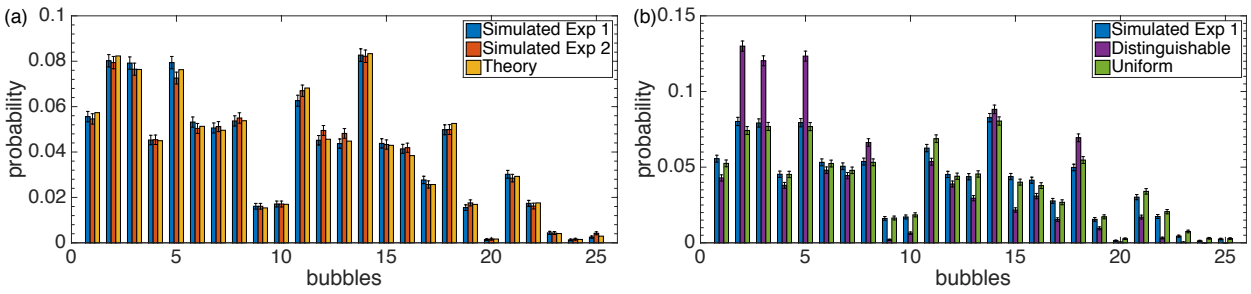

Figure F.1.1: Coarse-grained probability distributions for the trapped-ion system with long-time dynamics. All samples have a sample size $N_m = 10000$. The simulated experimental samples $\left(P_{S1}^Q \text{ and } P_{S2}^Q\right)$ are drawn from the boson sampler (P^Q); distinguishable (P_S^C) and uniform $\left(P_S^U\right)$ samples are drawn respectively from the classical (P^C) and uniform (P^U) samplers. Errors for the probabilities follow the standard deviations of the multinomial distribution. The simulated system has $N = 12$ phonons in a $M = 12$ ion chain with one phonon on each ion as the input state.

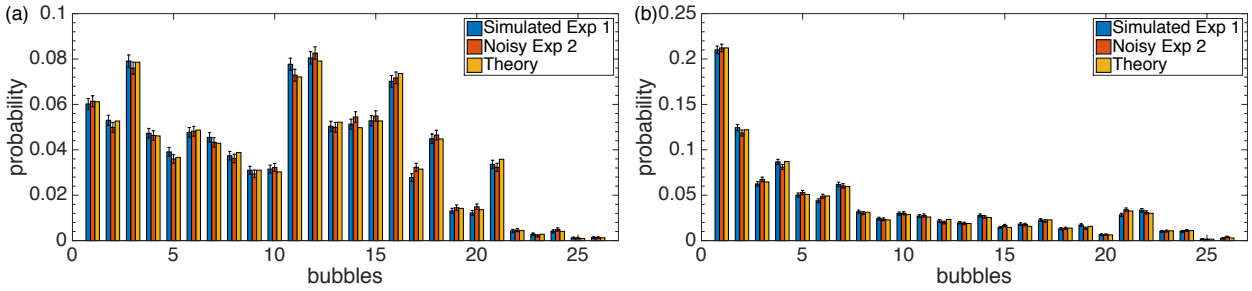

Figure F.1.2: Coarse-grained probability distributions for the noisy samples. (a) Trapped-ion system of intermediate-time dynamics with a 1% timing error included in the noisy sample. The simulated system has $N = 12$ phonons in a $M = 12$ ion chain with one phonon on each ion as the input state. (b) Distributions after a random unitary transformation. A 1% random noise is added to the unitary process in the noisy sample. The simulated system has $N = 5$ particles in $M = 40$ modes with $|1, 1, 1, 1, 1, 0, \cdots, 0\rangle$ as the input state.

the uniform samples (for example, the pass rate $R \approx 3\%$ between the simulated samples and uniform samples and $R \approx 0\%$ between the simulated samples and distinguishable samples for $\overline{N_B} \approx 39.1$). This in addition shows our method is sensitive to some structures hidden in the many-body interference process.

Table F.1: The pass rates R between simulated experimental sample 1 and various other samples for the trapped-ion system with long-time dynamics. The two-sample χ^2 test is performed to assess whether they come from the same distribution. The significance level α is set at 1%. For each pair of generated samples, if the p-value is greater than α, the comparison passes the test. This is repeated for $N_s = 10000$ runs and pass rates are recorded.

pass rate (%) compared to experimental sample 1			
	Trapped Ions (Long time)		
Average No. of bubbles	24.3	39.0	66.5
Experimental Sample 2	98.9	99.0	99.2
Distinguishable Sample	0	0	0
Uniform Sample	5.7	1.3	0.2

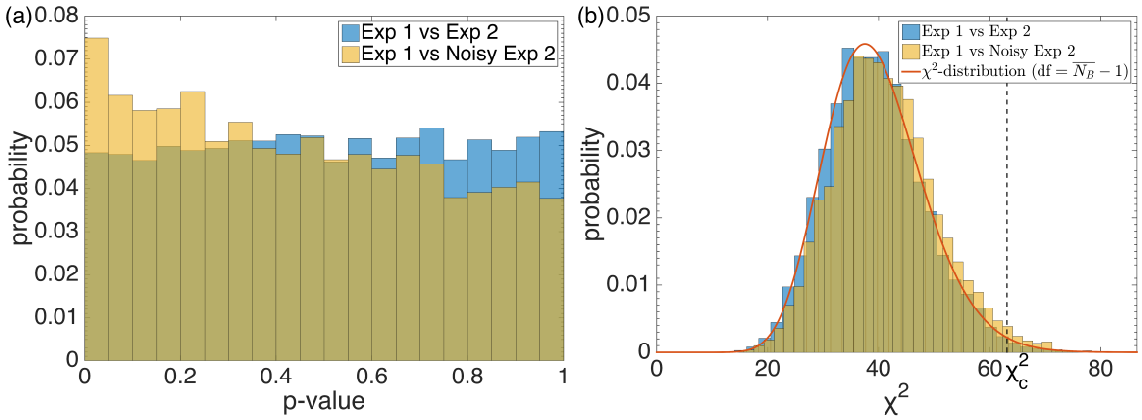

Figure F.1.3: Distributions of p-values and the two-sample χ^2 test-statistics for the trapped-ion system with intermediate-time dynamics and $\overline{N_B} \approx 40.5$. A χ^2 statistic and a p-value are calculated for each pair of samples, with a total $N_s = 10000$ runs generated in the simulation. (a) If two samples come from the same distribution, p-values should be uniformly distributed in $[0, 1]$. (b) The solid curve is the χ^2-distribution with $\overline{N_B} - 1$ degrees of freedom. The dashed line marks the cutoff χ^2 value at 1% significance level.

F.1.2 Noisy Samples

Fig. F.1.2 presents some coarse-grained distributions including the noisy samples. Visually, the 1% noise in the unitaries does not lead to substantial changes to the distributions. The noise we include for the intermediate-time trapped-ion system is a 1% systematic error in the total time (shift from $\tau = 100\,\mu$s to $\tau = 101\,\mu$s). For the random unitary process, in order to preserve the unitarity of the process, we first find the effective Hamiltonian for the Haar-distributed random unitary process, and subsequently add a 1% random noise to each entry of the hermitian Hamiltonian matrix.

F.1.3 Further Analysis on Two-sample χ^2 Test

For the two-sample χ^2 test, if the pair of samples comes from the same distribution, the χ^2 statistics should follow the χ^2-distribution with degrees of freedom being the number

Table F.2: Mean and standard deviation of p-values for the two-sample χ^2 test between one simulated experimental sample and various other samples. A p-value is calculated for each pair of generated samples and this is repeated for a total of $N_s = 10000$ sets. Mean and standard deviation (in brackets) of those p-values are tabled below. If two samples come from the same distribution, p-values should be uniformly distributed in $[0, 1]$ with mean 0.5 and standard deviation 0.289. If not, p-values should be small. Noisy samples for the trapped-ion system include a 1% timing error, whereas a 1% random error is included in the random unitary matrix. A value of 0 in the table indicates that the p-value is extremely small ($< 10^{-323}$ at the machine level).

	p-values compared to simulated experimental sample 1								
	Trapped Ions (Int. time)			Trapped Ions (Long time)			Random Unitary		
$\overline{N_B}$	24.2	40.5	69.9	24.3	39.0	66.5	25.9	40.8	70.5
Exp 2	0.50	0.51	0.51	0.50	0.50	0.51	0.50	0.50	0.50
	(0.29)	(0.29)	(0.29)	(0.29)	(0.29)	(0.29)	(0.29)	(0.29)	(0.29)
Exp 2 (1% Noise)	0.44	0.45	0.44	-	-	-	0.50	0.49	0.50
	(0.29)	(0.29)	(0.29)	-	-	-	(0.29)	(0.29)	(0.29)
Distinguishable	0	0	0	0	0	0	0.0053	2.1×10^{-4}	7.9×10^{-5}
	-	-	-	-	-	-	(0.033)	(0.0076)	(0.0071)
Uniform	0	0	0	0.0043	8.4×10^{-4}	1.1×10^{-4}	0	0	0
	-	-	-	(0.029)	(0.0098)	(0.0027)	-	-	-

of bubbles minus one. Also, if the null hypothesis is correct, p-values should be uniformly distributed in $[0, 1]$. In the main text, we plotted the distributions of the χ^2 statistics between two boson sampling data and between one boson sampling data and a distinguishable sample. One could clearly see the distinction in comparison. Here, we include in Fig. F.1.3 the plots for the noisy samples too, in the case of intermediate-time trapped-ion system with $\overline{N_B} \approx 40.5$. Without noise in experiment, it is evident that the χ^2 statistics follow the χ^2-distribution and the p-values are almost uniformly distributed. With experimental noise, χ^2 statistics shift to larger values, with p-values tilted towards smaller values. Therefore, type I error is going to increase with noise in experiments. Nevertheless, with small noise (1% in this case), one can still definitively and correctly conclude that these samples are equivalent with $\gtrsim 98\%$ confidence level (as tabled in the main text).

Other than the pass rates R tabled in the main text, here we add a table for the p-values too, which offers additional information regarding the error rates without comparing to a

specific significance level α. The mean and standard deviation of p-values are reported in Table F.2 for a set of $N_s = 10000$ runs. In the case of two boson sampling data, the mean and standard deviation are very close to the theoretical values 0.5 and 0.289 respectively. On the other hand, p-values are distinctively smaller against alternative samples. Some far-fetched distributions even have p-values smaller than the machine level ($< 10^{-323}$) with the boson sampling data, which illustrates the effectiveness of our certification method. With an appropriate significance level α and suitable number of bubbles N_B, one could minimize both type I and type II errors in the experimental certification process.

F.2 Quantum Supremacy for Simulating A Translation-Invariant Ising Spin Model

In this section of the Appendix, we provide more details on the proof that our model is classically intractable to multiplicative errors based on some complexity results. We also show that the hardness result can be extended to variation distance error bounds if the worse-case results can be strengthened to the average-case. In addition, we demonstrate how to certify the quantum sampler if measurement imperfections can be made sufficiently small.

F.2.1 Related Complexity Results

In this section, we review some definitions and results on complexity theory related to our discussions in the main text. We adopt the same definitions as in Ref. [338], which includes more detailed discussions on these complexity classes. The concept of language L (a subset

of the string $\{0,1\}^*$) is used to formalize decision problems (of which solution can only be true or false). We call an instance of the problem as x; if the solution of x is true, $x \in L$, otherwise $x \notin L$.

Before introducing those complexity classes directly used in the main text, we give a formal definition of the well known class NP. Intuitively, NP is the set of problems for which the "yes" solutions can be efficiently verified by a classical computer.

Definition 1 (NP: nondeterministic polynomial)**.** *A language L is in* NP *if there exists a polynomial p and a polynomial time classical Turing Machine M such that for every $x \in \{0,1\}^*$*

$$x \in L \Leftrightarrow \exists u \in \{0,1\}^{p(|x|)} \ s.t. \ M(x,u) = 1.$$

Polynomial hierarchy is in some sense a generalization of NP.

Definition 2 (Σ_i^p,PH: polynomial hierarchy)**.** *For $i \geq 1$, a language L is in Σ_i^p if there exists a polynomial q and a polynomial time classical Turing Machine M such that for every $x \in \{0,1\}^*$*

$$\begin{aligned} x \in L \ \Leftrightarrow \ & \exists u_1 \in \{0,1\}^{q(|x|)} \forall u_2 \in \{0,1\}^{q(|x|)} \cdots Q_i u_i \\ & \in \{0,1\}^{q(|x|)} \ s.t. \ M(x,u_1,u_2,\cdots,u_i) = 1, \end{aligned}$$

where Q_i denotes $\forall$ or $\exists$ depending on whether i is even or odd, respectively. And

$$\mathsf{PH} = \bigcup_i \Sigma_i^p.$$

Note that $\mathsf{NP} = \Sigma_1^p$ and one can generalize i to 0 such that $\mathsf{P} = \Sigma_0^p$. Clearly, $\Sigma_i^p \subseteq \Sigma_{i+1}^p \subseteq \mathsf{PH}$.

Most computer scientists believe $\mathsf{P} \neq \mathsf{NP}$. A generalization of this conjecture is that for every i, Σ_i^p is strictly contained in Σ_{i+1}^p, which means $\Sigma_i^p \neq \Sigma_{i+1}^p$. It can also be stated as "the polynomial hierarchy does not collapse". This conjecture is often used in complexity theory.

There is another way to generalize the class NP. According to the above definition, it only requires knowing whether there exists at least one witness such that the Turing machine accepts. Counting problems need to compute the number of witnesses. This class is defined as

Definition 3 ($\#\mathsf{P}$)**.** *A function f is in $\#\mathsf{P}$ if there exists a polynomial q and a polynomial time classical Turing machine M such that for every $x \in \{0,1\}^*$*

$$f(x) = \#\{y \in \{0,1\}^{q(|x|)} : M(x,y) = 1\}.$$

The following two complexity classes are directly related to sampling problems. One complexity class is $\mathsf{postBQP}$ defined in Ref. [343]. This complexity class characterizes the computational power of a universal quantum computer given the ability to do postselection. The other is a classical analog, $\mathsf{postBPP}$, defined in Ref. [342].

Definition 4 ($\mathsf{postBQP}$,$\mathsf{postBPP}$)**.** *A language L is in $\mathsf{postBQP}/\mathsf{postBPP}$ if there exists a uniform (which means can be generated by a classical polynomial Turing Machine) family of polynomial size quantum/classical circuits Q_n/C_n such that for every $x \in \{0,1\}^*$, after applying Q_n/C_n to the state*

- *the probability measuring registers $P/\widetilde{P}$ (called postselection registers) in the state $|0\cdots 0\rangle/0\cdots 0$ is nonzero;*

- *if $x \in L$, then conditioned on measuring $P/\widetilde{P}$ on state $|0\cdots0\rangle/0\cdots0$, the probability measuring the output register on state $|1\rangle/1$ is at least a (completeness error);*
- *if $x \notin L$, then conditioned on measuring $P/\widetilde{P}$ on state $|0\cdots0\rangle/0\cdots0$, the probability measuring the output register on state $|1\rangle/1$ is at most b (soundness error).*

where $a - b > 1/\mathrm{poly}(n)$.

Some relations between these classes are included in the following theorem.

Theorem 1. *The first is Toda's theorem [338], the second is proved in Ref. [343], and the third is proved in Ref. [342]:*

$$\begin{aligned} \mathsf{PH} &\subseteq \mathsf{P}^{\#\mathsf{P}} \\ \mathsf{P}^{\#\mathsf{P}} &= \mathsf{P}^{\mathsf{postBQP}} \\ \mathsf{postBPP} &\subseteq \Sigma_3^p. \end{aligned}$$

In order to simulate postBQP by postselection, we need to define an output register $O/\widetilde{O}$ which gives the result of the decision problem, and a postselection register $P/\widetilde{P}$ of which the result is postselected to be some string of $\{0,1\}$. The key point is that we can change the definition slightly without changing the classes postBQP and postBPP: replacing the result of the register $P/\widetilde{P}$ by

$$|0\cdots0\rangle/0\cdots0 \longrightarrow |s_1\cdots s_{m\times n-1}\rangle/s_1\cdots s_{m\times n-1}. \tag{F.2.1}$$

This is crucial to our result.

Suppose the result in the output register is x. Classical simulability with multiplicative error implies

$$\frac{1}{c}q_{xs_1\cdots s_{m\times n-1}} \leq p_{xs_1\cdots s_{m\times n-1}} \leq cq_{x\&s_1\cdots s_{m\times n-1}} \tag{F.2.2}$$

where the probability $\{q\}$ is sampled by our model, denoted as Ising and $\{p\}$ is sampled by a classical polynomial probabilistic Turing machine, shorted as BPP; the first digit x is in the register $O/\widetilde{O}$ and other digits $s_1\cdots s_{m\times n-1}$ are in the register $P/\widetilde{P}$; This is equivalent to the definition in the main text if we choose $\gamma = \min(1-1/c, c-1)$.

With postselection, we can define $\mathsf{postIsing}$. The output probability is

$$R(x) \equiv \frac{q_{xs_1\cdots s_{m\times n-1}}}{q_{0s_1\cdots s_{m\times n-1}} + q_{1s_1\cdots s_{m\times n-1}}}.$$

The output probability of the corresponding $\mathsf{postBPP}$ is

$$\widetilde{R}(x) \equiv \frac{p_{xs_1\cdots s_{m\times n-1}}}{p_{0\&s_1\cdots s_{m\times n-1}} + p_{1\&s_1\cdots s_{m\times n-1}}}.$$

According to the definition of multiplicative error Eq. (F.2.2), we have

$$\frac{1}{c^2}R(x) \leq \widetilde{R}(x) \leq c^2 R(x),$$

With this inequality and if $c < \sqrt{2}$ (so $\gamma < 1/2$),

$$|\widetilde{R}(0) - \widetilde{R}(1)| > 0 \,(\text{not scaling with the problem size}) \Rightarrow |R(0) - R(1)| > 0.$$

This condition means that if there is a gap between completeness and soundness error in

Ising, there will also be a gap for the BPP simulator:

$$\mathsf{postIsing} \subseteq \mathsf{postBPP}. \tag{F.2.3}$$

If we can further prove

$$\mathsf{postBQP} \subseteq \mathsf{postIsing}. \tag{F.2.4}$$

which means Ising with postselection can simulate universal quantum computer. Combined with theorem 1, we have

$$\mathsf{PH} \subseteq \mathsf{P}^{\#\mathsf{P}} = \mathsf{P}^{\mathsf{postBQP}} = \mathsf{P}^{\mathsf{postIsing}} \subseteq \mathsf{P}^{\mathsf{postBPP}} \subseteq \Sigma_3^p, \tag{F.2.5}$$

which means the polynomial hierarchy collapses to the third level. This contradicts with the generalization of the P≠NP conjecture

$$\Sigma_3^p \subsetneq \mathsf{PH}. \tag{F.2.6}$$

Here, we adopt the same idea of proof as in Ref. [329].

F.2.2 Universal Quantum Computation with the Brickwork State

Ref. [352] has given the proof of universality. For completeness, we briefly review the result. Fig. F.2.1(a) shows how to choose different angles to get any single qubit gates and the CNOT gate. They are known to be universal. Fig. F.2.1(b) shows how to combine two qubit gates together to implement universal quantum computation.

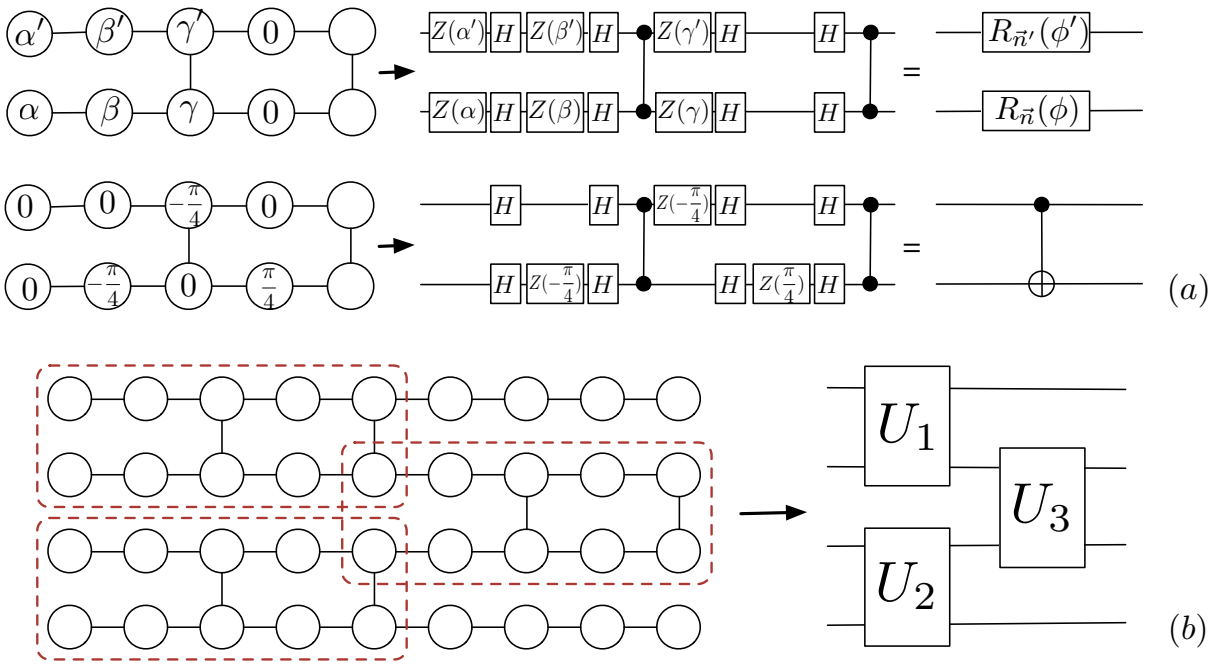

Figure F.2.1: Implementing universal quantum computation with the brickwork state. These figures are similar to the ones in Ref. [352].

F.2.3 Magnetic Field in the Ising Spin Model

In this section, we show that the extra local magnetic fields can be absorbed into the magnetic fields of the figure in the main text. We have three separate cases:

- For those spins that only couple with one other spin, there is an extra magnetic field $R_z(\pi/2)$. This spin must be on the left or the right boundary of the brickwork state. We can regard it as an ordinary unitary operation acting on the input. It can be eliminated by acting $R_z(-\pi/2)$ on the remaining quantum circuits.

- For those spins that couple with two other spins, there is an extra magnetic field $R_z(\pi)$. These spins will be acted on by an extra Z gate. It can be eliminated by flipping the

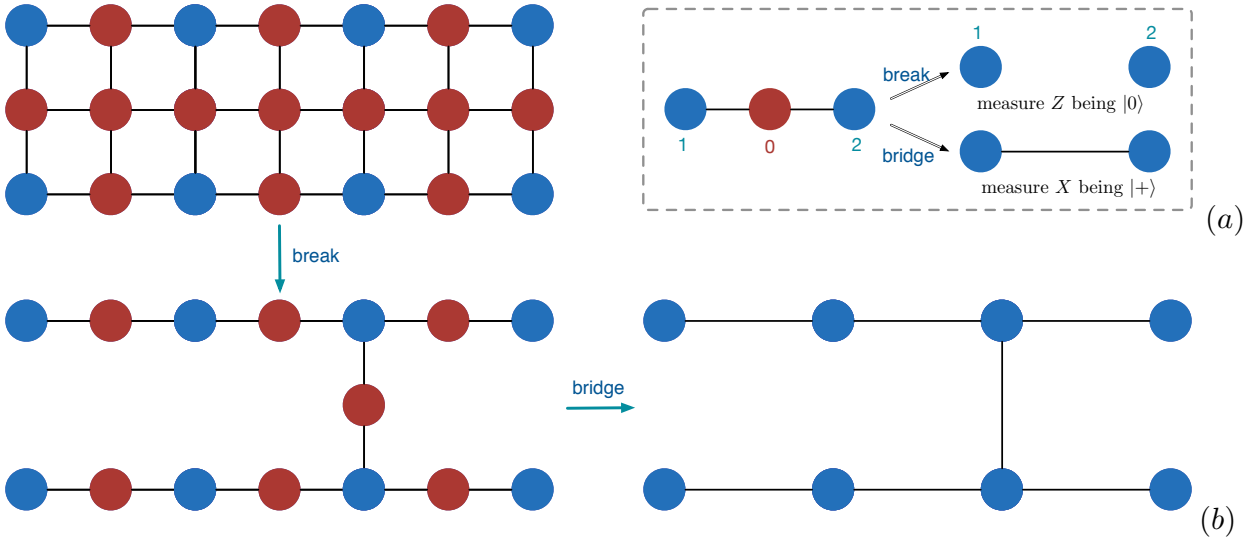

Figure F.2.2: Break and bridge operations and reducing the cluster state. (a) Break and bridge operations. Qubit 0 is first rotated by $R_z(\pi/2)$ before measured in Z and X basis respectively to perform the break and bridge operations. (b) Reduce the cluster state to the brickwork state by break and bridge operations.

measurement result.

- For those spins that couple with three other spins, there is an extra magnetic field $R_z(3\pi/2)$. These spins must have a vertical coupling; according to the figure in the main text, we can make the rotation angle θ on those spins to be $\pi/8+3\pi/2 = \pi/8-\pi/2$ mod 2π. It can be eliminated by flipping the measurement result from s_2 to $s_2 \oplus 1$ and from s_3 to $s_3 \oplus s_2$.

F.2.4 Break and Bridge Operations

In the main text, we introduced the “break" and “bridge" operations. Here, we include more details of how to reduce a cluster state to a brickwork state by those operations. For the three qubit cluster state in Fig. F.2.2(a), the red circle is rotated by $R_z(\pi/2)$. The operations

acting on qubits 1 and 2 controlled by qubit 0 can be written as

$$\frac{e^{-i\pi/4}}{\sqrt{2}}|0\rangle_0 \otimes I_1 \otimes I_2 + i|1\rangle_0 \otimes Z_1 \otimes Z_2. \tag{F.2.7}$$

with an extra global phase. Therefore, by postselecting qubit 0 being $|0\rangle$ by measuring Z, we have the operation $I_1 \otimes I_2$ on qubits 1 and 2, implementing the break operation. By postselecting qubit 0 being $|+\rangle$ by measuring X, we have

$$\frac{e^{-i\pi/4}}{\sqrt{2}}\left(I_1 \otimes I_2 + iZ_1 \otimes Z_2\right) = e^{-i\pi/4}e^{i\pi/4 Z_1 \otimes Z_2}. \tag{F.2.8}$$

This is the same as the time evolution of the Ising interaction in the Hamiltonian, implementing the bridge operation.

Fig. F.2.2(b) demonstrates how to convert the cluster state to other graph states such as the brickwork state by the break and bridge operations.

F.2.5 Simulation with variation Distance Errors

This is the most technical part of the computational complex theory in this section, so we divide it into three parts.

A #P-hard Problem in Worst-case

First of all, we introduce a problem that is #P-hard in worst-case. Later, we will find that our classically-intractable result for simulating our Ising spin model depends on a conjecture that lifts this problem from worst-case hardness to average-case hardness.

Suppose the probability of measuring result $x = x_1 \cdots x_i \cdots x_{m\times n}, x_i \in \{0,1\}$ from the quantum sampler is q_x with

$$\begin{aligned} q_x &= \left| \bigotimes_i^{m\times n} \langle +_{x_i} | e^{-i\mathcal{H}t} | + \rangle^{\otimes m\times n} \right|^2 \\ &= \frac{|\langle 0|C_x|0\rangle|^2}{2^{mn-m}} \end{aligned} \tag{F.2.9}$$

where C_x is a polynomial size quantum circuit which can be implemented by choosing proper measurement results x and $1/2^{mn-m}$ comes from equal probability for measurement in measurement-based quantum computing. We will show that approximating q_x by $\widetilde{q}_x$ to the following error

$$|\widetilde{q}_x - q_x| \leq \frac{q_x}{\text{poly}(n)} + \frac{c}{2^{mn}} \tag{F.2.10}$$

is #P-hard, where c can be any constant $0 \leq c < 1/2$.

Suppose $f(z)$ is some boolean function which can be computed efficiently by a classical computer. Define

$$\text{gap}(f) \equiv |\{z : f(z) = 0\}| - |\{z : f(z) = 1\}| = \sum_z (-1)^{f(z)} \tag{F.2.11}$$

and $\widetilde{\text{gap}(f)^2} \equiv 2^{mn}\widetilde{q}_x$. Consider the polynomial size quantum circuit C_x doing the following

operation on $|0\rangle^{\otimes m}$ $(m = 2r)$

$$\begin{aligned}
\text{Hadamard gate:} \quad |0\rangle^{\otimes r}|0\rangle^{\otimes r} &\Longrightarrow |0\rangle^{\otimes m-r}\frac{\sum_z |z\rangle}{\sqrt{2^r}} \\
\text{computing } f(z): &\Longrightarrow |0\rangle^{\otimes r-1}\frac{\sum_z |f(z)\rangle|z\rangle}{\sqrt{2^r}} \\
\text{applying } Z \text{ and uncomputing}: &\Longrightarrow |0\rangle^{\otimes r}\frac{\sum_z (-1)^{f(z)}|z\rangle}{\sqrt{2^r}} \\
\text{Hadamard gate}: &\Longrightarrow |0\rangle^{\otimes m}\frac{\sum_z (-1)^{f(z)}}{2^r} + |\text{other terms}\rangle, \qquad \text{(F.2.12)}
\end{aligned}$$

which means

$$q_x = \frac{|\langle 0|C_x|0\rangle|^2}{2^{mn-m}} = \frac{\text{gap}(f)^2}{2^{mn}}. \qquad \text{(F.2.13)}$$

Thus, Eq. (F.2.10) implies

$$|\widetilde{\text{gap}(f)}^2 - \text{gap}(f)^2| \leq \frac{\text{gap}(f)^2}{\text{poly}(n)} + c. \qquad \text{(F.2.14)}$$

This condition implies $\widetilde{\text{gap}(f)}^2$ can estimate $\text{gap}(f)^2$ to multiplicative errors since $c < 1/2$:

$$|\widetilde{\text{gap}(f)}^2 - \text{gap}(f)^2| \leq (c + o(1)) \cdot \text{gap}(f)^2. \qquad \text{(F.2.15)}$$

This is because $\text{gap}(f)^2$ is an integer: if $\text{gap}(f)^2 = 0$, then $\widetilde{\text{gap}(f)}^2 < 1/2$ such that we can infer $\text{gap}(f)^2 = 0$, which means $|\widetilde{\text{gap}(f)}^2 - \text{gap}(f)^2| = 0$; if $\text{gap}(f)^2 \geq 1$, then $c \leq c \cdot \text{gap}(f)^2$. Ref. [330] proved that approximating $\text{gap}(f)^2$ to multiplicative errors is #P-hard (actually, they proved that if f is some special boolean function, it is GapP-complete, but this implies the result we need). This proves the worst-case hardness result.

Define the partition function with imaginary temperature $\beta \equiv 1/k_B T = i$ as

$$\mathcal{Z}_x = \mathrm{tr}\, e^{-i(\mathcal{H}+\sum_i x_i \pi/2 Z_i)} = \sum_{z\in\{+1,-1\}^{mn}} e^{i(\sum_{\langle i,j\rangle} \pi/4 z_i z_j + \sum_i B_i' z_i)} \tag{F.2.16}$$

where B_i' depends on x_i. Then,

$$\begin{aligned} q_x &= \left| \bigotimes_i^{m\times n} \langle +_{x_i} | e^{-i\mathcal{H}t} | + \rangle^{\otimes m\times n} \right|^2 && \text{(F.2.17)} \\ &= \left| \langle + |^{\otimes m\times n} e^{-i(\mathcal{H}+\sum_i x_i \pi/2 Z_i)t} | + \rangle^{\otimes m\times n} \right|^2 && \text{(F.2.18)} \\ &= \frac{|\mathcal{Z}_x|^2}{2^{2mn}} && \text{(F.2.19)} \end{aligned}$$

where $|+_x\rangle = Z^x|+\rangle$ are the bases of X. Restating the above conclusion in terms of the partition function, we get

Theorem 2. *Approximating the partition function to the following error*

$$\left| \frac{\widetilde{|\mathcal{Z}_x|^2}}{2^{mn}} - \frac{|\mathcal{Z}_x|^2}{2^{mn}} \right| \leq \frac{1}{\mathrm{poly}(n)} \frac{|\mathcal{Z}_x|^2}{2^{mn}} + c \tag{F.2.20}$$

is #P*-hard in the worst-case, if* $0 \leq c < 1/2$*. (Notice that the range of* $|\mathcal{Z}_x|^2/2^{mn}$ *is from 0 to* 2^{mn} *instead of from 0 to 1.)*

Classically-intractable for Simulation With Variation Distance Error

The main ingredient is Stockmeyer's theorem [384] (see Ref. [36] or Ref. [330] for the statement here):

Theorem 3. *There exists an* $\mathsf{FBPP}^{\mathsf{NP}}$ *algorithm which can approximate*

$$P = \Pr_x[f(z) = 1] = \frac{1}{2^r} \sum_{z \in \{0,1\}^r} f(z) \tag{F.2.21}$$

by $\widetilde{P}$*, for any boolean function* $f : \{0,1\}^r \to \{0,1\}$*, to multiplicative error* $|\widetilde{P} - P| \leq P/\mathrm{poly}(n)$ *if* $f(z)$ *can be computed efficiently given* z*.*

The probability of any distribution that can be classically efficiently sampled is such kind of P: the distribution is produced by tossing the coin and regarding z as the sequence of coin-tossing results, the probability of a specific event is the union of some z such that $f(z) = 1$. Hence the above theorem states that any probability in a distribution sampled by a polynomial classical algorithm can be approximated to multiplicative errors in $\mathsf{BPP}^{\mathsf{NP}}$, which is contained in the third level of the polynomial hierarchy [36, 330, 384]. The probability in the distribution sampled by a quantum algorithm is not P since it involves sums of negative numbers. It can be proved that if $f : \{0,1\}^r \to \{-1,1\}$, it will still be $\#\mathsf{P}$-hard to approximate the sum to multiplicative errors.

Assume there is a classical sampler that can sample from the distribution $\{p_x\}$. According to Stockmeyer's theorem, $\widetilde{p}_x$ can be computed in the third level of the polynomial hierarchy such that $|\widetilde{p}_x - p_x| \leq p_x/\mathrm{poly}(n)$. If the distribution $\{p_x\}$ can approximate $\{q_x\}$ to variation distance, i.e., $\sum_x |p_x - q_x| \leq \epsilon$. Then $\mathbb{E}_x\left[|p_x - q_x|\right] \leq \epsilon/2^{mn}$. Using Markov inequality

$$\Pr_x\left[|p_x - q_x| \geq \frac{\epsilon}{2^{mn}\delta}\right] \leq \delta, \tag{F.2.22}$$

we get

$$
\begin{aligned}
|\widetilde{p}_x - q_x| &\leq |\widetilde{p}_x - p_x| + |p_x - q_x| \\
\text{Stockmeyer's theorem:} \quad &\leq \frac{p_x}{\text{poly}(n)} + |p_x - q_x| \\
&\leq \frac{q_x + |p_x - q_x|}{\text{poly}(n)} + |p_x - q_x| \\
&= \frac{q_x}{\text{poly}(n)} + \left(1 + \frac{1}{\text{poly}(n)}\right) |p_x - q_x| \\
&\quad \text{with } \geq 1 - \delta \text{ fraction of } x \\
\text{classically simulable assumption \& Markov inequality:} \quad &\leq \frac{q_x}{\text{poly}(n)} + \frac{\epsilon(1 + o(1))}{2^{mn}\delta}. \qquad \text{(F.2.23)}
\end{aligned}
$$

We have shown that approximating q_x to a mixture of multiplicative and additive errors in Eq. (F.2.23) is #P-hard in the worst-case if $\epsilon/\delta < 1/2$. Lifting this worst-case hardness result to average-case result, we will get the desired result: If for any $1 - \delta$ fraction of instances x, approximating q_x to the mixture of the multiplicative and additive errors in Eq. (F.2.23) is still #P-hard; then if we assume there is a classical sampler that can simulate the distribution of our Ising spin model to variation distance errors, there will exist a $\mathsf{BPP}^{\mathsf{NP}}$ algorithm that can solve #P-hard problems, implying the collapse of the polynomial hierarchy.

Restating the above conclusion in terms of the partition function, we get

Theorem 4. *If approximating the partition function to the following error*

$$
\left| \frac{\widetilde{|\mathcal{Z}_x|^2}}{2^{mn}} - \frac{|\mathcal{Z}_x|^2}{2^{mn}} \right| \leq \frac{1}{\text{poly}(n)} \frac{|\mathcal{Z}_x|^2}{2^{mn}} + \frac{\epsilon}{\delta} \qquad \text{(F.2.24)}
$$

is also #P-hard for any $1-\delta$ fraction of instances x, then simulating the distribution sampled by our Ising spin model to the variation distance ϵ is classically intractable, otherwise the

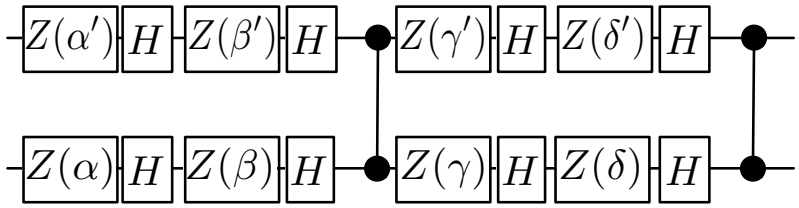

Figure F.2.3: Random 2-qubit gate in C_x. $\alpha, \beta, \gamma, \delta, \alpha', \beta', \gamma', \delta'$ are chosen from $\{0, \pi/4, \pi/2, 3\pi/4, \pi, 5\pi/4, 3\pi/2, 7\pi/4\}$ randomly and independently.

polynomial hierarchy will collapse.

Intuition of Our Average-case Hardness Conjecture

Substitute q_x in Eq. (F.2.23) by Eq. (F.2.9)

$$\left| |\langle 0|\widetilde{C_x}|0\rangle|^2 - |\langle 0|C_x|0\rangle|^2 \right| \leq \frac{|\langle 0|C_x|0\rangle|^2}{\text{poly}(n)} + \frac{\epsilon(1+o(1))}{2^m \delta} \tag{F.2.25}$$

where $|\langle 0|\widetilde{C_x}|0\rangle|^2$ is an estimation of $|\langle 0|C_x|0\rangle|^2$ and m is the width of the circuit C_x. The circuit C_x is formed by random 2-qubit gates layer by layer (n layers) similar to Fig. F.2.1(b). Except some single qubit gates on the boundary, each 2-qubit gate has the form shown in Fig. F.2.3, where the angles $\alpha, \beta, \gamma, \delta, \alpha', \beta', \gamma', \delta'$ are chosen from $\{0, \pi/4, \pi/2, 3\pi/4, \pi, 5\pi/4, 3\pi/2, 7\pi/4\}$ randomly and independently. This can be verified directly by choosing random measurement results on blue circles in the main text figure. If either δ or δ' is different from 0 or π, this 2-qubit gate will produce entanglement on some product states. In our opinion, with high probability, this kind of circuits will likely produce highly entangled states. Therefore, we conjecture that calculating the amplitudes of the circuit to the error in Eq. (F.2.25) is #P-hard in the average-case.

There is a natural connection between our model and sampling models of random quantum circuits like the one in Ref. [39]. In Ref. [39], the quantum circuit is basically $\sqrt{n}$ layers of single qubit gates (chosen from $\{X^{1/2}, Y^{1/2}, R_z(\pi/4)\}$ randomly) and control-Z gates applied to $\sqrt{n}\times\sqrt{n}$ input qubits on square lattice. The intuition of classical hardness of this sampling problem is from the relation between quantum chaos and random quantum circuits. The distribution produced by their sampling model is expected to satisfy the Porter-Thomas distribution [385] with a sufficient circuit depth. This is supported by numerical simulations in Ref. [39]. Then there is a large fraction of $|\langle 0|U|z\rangle|^2 \geq 1/2^m$ where U is a random circuit, which implies that approximating output probabilities to multiplicative errors is #P-hard in average-case and the noncollapse of the polynomial hierarchy is sufficient to prove the classical hardness result. Although the ensembles used in our model and the one in Ref. [39] are different, we think there is no fundamental difference since they both try to produce sufficiently random quantum circuits. Besides, it is expected that the distribution of our model approaches the Porter-Thomas distribution if $n \sim m$ because the "input" in our model is on a linear array (the depth is expected to grow as $n^{1/D}$ for a D dimensional qubit lattice. See corresponding discussions in Ref. [39]). Therefore, we should be able to convert Eq. (F.2.24) and Eq. (F.2.25) with multiplicative errors in our conjecture to be similar to the one in Ref. [330].

F.2.6 Certification to Variation Distance Errors

With the reasonable assumption that the errors of X measurements are local and small (scales as $O(1/mn)$), we can certify whether the distribution sampled by a quantum sampler in the laboratory satisfies the variation distance bound. First, we give the condition that the measurement errors should satisfy; then we reduce the certification to bounding the trace

distance between the ideal final state and the actual one prepared in the laboratory (before measurement).

Suppose $\{q'_x\}$ is the distribution sampled by the quantum sampler and the density matrix just before measurements is ρ'; $\{q_x\}$ is the ideal one with the corresponding density matrix ρ. Denote the trace distance by $D(\rho, \rho') = \mathrm{tr}(|\rho - \rho'|)/2$. It is known that [26]

$$\sum_x |q_x - q'_x| \leq D(\rho, \rho'). \tag{F.2.26}$$

So if the measurements are perfect, bounding the trace distance will imply that variation distance is bounded.

Let us consider measurement imperfections. Denote the ideal measurement as a quantum operator $\mathcal{E}$ and the imperfect one as $\mathcal{E}'$. If the measurement errors are small and local, $\mathcal{E}'$ can be approximated as

$$\mathcal{E}' \approx \mathcal{E} \circ \left(\mathcal{I} + \varepsilon \sum_i \omega_i \right) \tag{F.2.27}$$

where $\mathcal{I}$ is the identity quantum operation, ω_i is some local operation around spin i, and ε is some small number. Bounding the variation distance can be reduced by

$$\sum_x |q_x - q'_x| = D(\mathcal{E}(\rho), \mathcal{E}'(\rho')) \leq D(\mathcal{E}(\rho), \mathcal{E}(\rho')) + D(\mathcal{E}(\rho'), \mathcal{E}'(\rho')) \leq D(\rho, \rho') + D(\mathcal{E}(\rho'), \mathcal{E}'(\rho')). \tag{F.2.28}$$

The term $D(\rho, \rho')$ characterizes the error produced in the process of preparing the final state (time evolution and initial state preparation errors). The term $D(\mathcal{E}(\rho'), \mathcal{E}'(\rho'))$ characterizes the error due to imperfect measurements.

We divide the certification of the variation distance error into two parts:

$$\begin{aligned} D(\rho, \rho') &\leq \epsilon_d \\ D(\mathcal{E}(\rho'), \mathcal{E}'(\rho')) &\leq \epsilon_m \\ \epsilon_d + \epsilon_m &\leq \epsilon. \end{aligned} \tag{F.2.29}$$

The error due to imperfect measurements is

$$\|\mathcal{E}'(\sigma) - \mathcal{E}(\sigma)\| \approx \left\| \varepsilon \mathcal{E} \circ \left(\sum_i \omega_i \right) (\sigma) \right\| \leq mn\varepsilon \tag{F.2.30}$$

where σ is some arbitrary density matrix. So as long as the measurement error on every spin can be made smaller than $\varepsilon = \epsilon_m/(mn)$, it can be guaranteed that the total measurement error is bounded by ϵ_m.

The remaining is to certify whether $D(\rho, \rho') \leq \epsilon_d$. We reduce the problem to certifying whether the state produced in the laboratory is close to the ideal state, which is made to be the ground state of a given local gapped Hamiltonian. The method in Ref. [344] can achieve this task. Recall a lemma in Ref. [344]:

Lemma 1. *Suppose ρ is the ground state of $H = \sum_\lambda h_\lambda$ where h_λ is a local Hermitian operator, the ground state is unique and the ground state energy is 0. To estimate $\mathrm{tr}(h_\lambda \rho')$ where ρ' is the state produced in the laboratory, M measurements on ρ' in the basis of h_λ are needed. By summing over all the estimations of h_λ, we can get an estimation of $\mathrm{tr}(H\rho')$. By this estimation, we can estimate $F(\rho, \rho') = \mathrm{tr}(\rho\rho')$ by F^* where*

$$\Pr[|F^* - F| \leq \epsilon'] \geq 1 - \alpha. \tag{F.2.31}$$

If we choose M as

$$M \geq \frac{Jm^2n^2}{2\Delta^2\epsilon'^2} \ln\left[-\frac{mn+1}{\ln(1-\alpha)}\right] \approx \frac{Jm^2n^2}{2\Delta^2\epsilon'^2}\left(\ln mn + \ln\frac{1}{\alpha}\right) \text{ for } m,n \text{ large and } \alpha \text{ small} \tag{F.2.32}$$

where Δ is the energy gap and $J = \max_\lambda \|h_\lambda\|$.

Because $D(\rho,\rho') \leq \sqrt{1-F^2(\rho,\rho')}$, $F(\rho,\rho') \geq \sqrt{1-\epsilon_d^2}$ implies $D(\rho,\rho') \leq \epsilon_d$. So we require

$$F^* \geq \sqrt{1-\epsilon_d^2} + \epsilon'. \tag{F.2.33}$$

In our problem, the Hamiltonian is

$$H'_{\text{brickwork}} = \frac{1}{2}\sum_i \left(I - R_z(\theta_i)X_iR_z^\dagger(\theta_i)\prod_{j\in\text{neighbor of }i} Z_j\right) \tag{F.2.34}$$

on the brickwork lattice as shown in the main text figure, and $J=1$, $\Delta=1$.

If we choose $\epsilon_d = O(\epsilon)$, $\epsilon_m = O(\epsilon)$ and $\epsilon' = O(\epsilon^2)$, then we need to measure each local term in the Hamiltonian $M = O(m^2n^2r/\epsilon^4)$ times to get a confidence level of $1-2^{-O(r)}$. The certification protocol is therefore efficient.

F.2.7 Hardness of Classically Simulating the Square Lattice Model to Variation Distance Errors

When doing break and bridge operations, we need to measure Z being $|0\rangle$ and X being $|+\rangle$ on the red circles in Fig. F.2.2, but the results $|1\rangle$ and $|-\rangle$ are also present as we sample. According to Eq. (F.2.7), we can conclude

- Measuring Z on qubit 0, the probabilities of getting $|0\rangle$ and $|1\rangle$ are both 1/2. When the result is $|1\rangle$, the operation is $iZ_1 \otimes Z_2$, so the effect is just flipping the measurement result on the blue circles in Fig. F.2.2.

- Measuring X on qubit 0, the probability of getting $|+\rangle$ and $|-\rangle$ are also 1/2 each. When the result is $|-\rangle$, the operation is

$$\frac{e^{-i\pi/4}}{\sqrt{2}}\left(I_1 \otimes I_2 - iZ_1 \otimes Z_2\right) = e^{-i\pi/4} e^{-i\pi/4 Z_1 \otimes Z_2}. \tag{F.2.35}$$

  Since

$$e^{-i\pi/4 Z_1 \otimes Z_2} = -ie^{i\pi/4 Z_1 \otimes Z_2} Z_1 \otimes Z_2, \tag{F.2.36}$$

  the effect is also flipping the measurement result on the blue circles.

Denote the measurement result on blue circles as x' and result on red circles as y (for the bridge operation, denote $|+\rangle$ as 0) and q_x is the probability of measuring x on the brickwork model. Because the effect of y may be just flipping some bit of x, given y, we can infer x and x' from each other. Besides, $q_y \equiv \sum_{x'} q_{x',y} = 1/2^r$ where r is the number of red circles (actually, $r = 3mn - 2m - 2n + 1$) and $q_{x'|y} = q_x$, so

$$\sum_y q_{x',y} = \sum_y q_{x'|y} q_y = \sum_y \frac{1}{2^r} q_x = q_x. \tag{F.2.37}$$

Suppose there exists a quantum sampler that can generate a distribution $\{p_{x',y}\}$ to approximate the distribution of square lattice model to variation distance errors:

$$\sum_{x',y} |p_{x',y} - q_{x',y}| \leq \epsilon. \tag{F.2.38}$$

We can then define a new classical sampler to simulate the distribution of the brickwork model: suppose the outcome is x', y and define the result to be x (x', y can determine a unique x), so the probability of getting x is $p_x = \sum_y p_{x',y}$, implying

$$\begin{aligned}\sum_{x',y} |p_{x',y} - q_{x',y}| &= \sum_{x,y} |p_{x',y} - q_{x',y}| \\ &\geq \sum_{x} |\sum_{y} p_{x',y} - \sum_{y} q_{x',y}| \\ &= \sum_{x} |p_x - q_x|. \end{aligned} \tag{F.2.39}$$

The first equality is because given y, x and x' can determine each other. The last equality is due to the definition of p_x and Eq. (F.2.37). This implies that there exists a classical sampler to simulate the brickwork model. So the hardness result of the square lattice model is based on the same conjectures (polynomial hierarchy does not collapse and Theorem 4).

BIBLIOGRAPHY

Bibliography

[1] L. D. Landau, E. Lifshitz, and L. Pitaevskii, "Statistical physics, part i," 1980.

[2] K. v. Klitzing, G. Dorda, and M. Pepper, "New method for high-accuracy determination of the fine-structure constant based on quantized hall resistance," *Phys. Rev. Lett.*, vol. 45, pp. 494–497, Aug 1980.

[3] D. C. Tsui, H. L. Stormer, and A. C. Gossard, "Two-dimensional magnetotransport in the extreme quantum limit," *Phys. Rev. Lett.*, vol. 48, pp. 1559–1562, May 1982.

[4] M. Z. Hasan and C. L. Kane, "*Colloquium*: Topological insulators," *Rev. Mod. Phys.*, vol. 82, pp. 3045–3067, Nov 2010.

[5] X.-L. Qi and S.-C. Zhang, "Topological insulators and superconductors," *Rev. Mod. Phys.*, vol. 83, pp. 1057–1110, Oct 2011.

[6] J. E. Moore, "The birth of topological insulators," *Nature*, vol. 464, no. 7286, pp. 194–198, 2010.

[7] C. L. Kane and E. J. Mele, "Z_ {2} topological order and the quantum spin hall effect," *Phys. Rev. Lett.*, vol. 95, no. 14, p. 146802, 2005.

[8] L. Fu, C. L. Kane, and E. J. Mele, "Topological insulators in three dimensions," *Phys. Rev. Lett.*, vol. 98, p. 106803, Mar 2007.

[9] A. Kitaev, "Periodic table for topological insulators and superconductors," *AIP Conf. Proc.*, vol. 1134, no. 1, pp. 22–30, 2009.

[10] A. P. Schnyder, S. Ryu, A. Furusaki, and A. W. W. Ludwig, "Classification of topological insulators and superconductors in three spatial dimensions," *Phys. Rev. B*, vol. 78, p. 195125, Nov 2008.

[11] X. Chen, Z.-C. Gu, Z.-X. Liu, and X.-G. Wen, "Symmetry-protected topological orders in interacting bosonic systems," *Science*, vol. 338, no. 6114, pp. 1604–1606, 2012.

[12] M. König, S. Wiedmann, C. Brüne, A. Roth, H. Buhmann, L. W. Molenkamp, X.-L. Qi, and S.-C. Zhang, "Quantum spin hall insulator state in hgte quantum wells," *Science*, vol. 318, no. 5851, pp. 766–770, 2007.

[13] D. Hsieh, D. Qian, L. Wray, Y. Xia, Y. S. Hor, R. J. Cava, and M. Z. Hasan, "A topological dirac insulator in a quantum spin hall phase," *Nature*, vol. 452, pp. 970–974, 04 2008.

[14] Y. L. Chen, J. G. Analytis, J.-H. Chu, Z. K. Liu, S.-K. Mo, X. L. Qi, H. J. Zhang, D. H. Lu, X. Dai, Z. Fang, S. C. Zhang, I. R. Fisher, Z. Hussain, and Z.-X. Shen, "Experimental realization of a three-dimensional topological insulator, Bi_2Te_3," *Science*, vol. 325, no. 5937, pp. 178–181, 2009.

[15] M. Lewenstein, A. Sanpera, V. Ahufinger, B. Damski, A. Sen(De), and U. Sen, "Ultracold atomic gases in optical lattices: mimicking condensed matter physics and beyond," *Advances in Physics*, vol. 56, no. 2, pp. 243–379, 2007.

[16] I. Bloch, J. Dalibard, and W. Zwerger, "Many-body physics with ultracold gases," *Rev. Mod. Phys.*, vol. 80, pp. 885–964, Jul 2008.

[17] N. Goldman, G. Juzeliūnas, P. Öhberg, and I. B. Spielman, "Light-induced gauge fields for ultracold atoms," *Rep. Prog. Phys.*, vol. 77, no. 12, p. 126401, 2014.

[18] Y.-J. Lin, K. Jimenez-Garcia, and I. Spielman, "Spin-orbit-coupled bose-einstein condensates," *Nature*, vol. 471, no. 7336, pp. 83–86, 2011.

[19] Z. Wu, L. Zhang, W. Sun, X.-T. Xu, B.-Z. Wang, S.-C. Ji, Y. Deng, S. Chen, X.-J. Liu, and J.-W. Pan, "Realization of two-dimensional spin-orbit coupling for bose-einstein condensates," *Science*, vol. 354, no. 6308, pp. 83–88, 2016.

[20] H. Miyake, G. A. Siviloglou, C. J. Kennedy, W. C. Burton, and W. Ketterle, "Realizing the harper hamiltonian with laser-assisted tunneling in optical lattices," *Phys. Rev. Lett.*, vol. 111, p. 185302, Oct 2013.

[21] M. Aidelsburger, M. Atala, M. Lohse, J. T. Barreiro, B. Paredes, and I. Bloch, "Realization of the hofstadter hamiltonian with ultracold atoms in optical lattices," *Phys. Rev. Lett.*, vol. 111, p. 185301, Oct 2013.

[22] G. Jotzu, M. Messer, R. Desbuquois, M. Lebrat, T. Uehlinger, D. Greif, and T. Esslinger, "Experimental realization of the topological haldane model with ultracold fermions," *Nature*, vol. 515, pp. 237–240, 11 2014.

[23] M. Aidelsburger, M. Lohse, C. Schweizer, M. Atala, J. T. Barreiro, S. Nascimbene, N. R. Cooper, I. Bloch, and N. Goldman, "Measuring the chern number of hofstadter bands with ultracold bosonic atoms," *Nat Phys*, vol. 11, pp. 162–166, 02 2015.

[24] N. Fläschner, B. S. Rem, M. Tarnowski, D. Vogel, D.-S. Lühmann, K. Sengstock, and C. Weitenberg, "Experimental reconstruction of the berry curvature in a floquet bloch band," *Science*, vol. 352, no. 6289, pp. 1091–1094, 2016.

[25] T. Li, L. Duca, M. Reitter, F. Grusdt, E. Demler, M. Endres, M. Schleier-Smith, I. Bloch, and U. Schneider, "Bloch state tomography using wilson lines," *Science*, vol. 352, no. 6289, pp. 1094–1097, 2016.

[26] M. A. Nielsen and I. L. Chuang, *Quantum computation and quantum information*. Cambridge university press, 2010.

[27] T. D. Ladd, F. Jelezko, R. Laflamme, Y. Nakamura, C. Monroe, and J. L. O'Brien, "Quantum computers," *Nature*, vol. 464, pp. 45–53, 03 2010.

[28] S. Lloyd, "Universal quantum simulators," *Science*, vol. 273, p. 1073, Aug 23 1996.

[29] J. I. Cirac and P. Zoller, "Goals and opportunities in quantum simulation," *Nat. Phys.*, vol. 8, pp. 264–266, 04 2012.

[30] R. P. Feynman, "Simulating physics with computers," *Int. J. Theoret. Phys.*, vol. 21, pp. 467–468, 1982.

[31] I. M. Georgescu, S. Ashhab, and F. Nori, "Quantum simulation," *Rev. Mod. Phys.*, vol. 86, pp. 153–185, Mar 2014.

[32] K. Kim, M. S. Chang, S. Korenblit, R. Islam, E. E. Edwards, J. K. Freericks, G. D. Lin, L. M. Duan, and C. Monroe, "Quantum simulation of frustrated ising spins with trapped ions," *Nature*, vol. 465, pp. 590–593, 06 2010.

[33] J. Simon, W. S. Bakr, R. Ma, M. E. Tai, P. M. Preiss, and M. Greiner, "Quantum simulation of antiferromagnetic spin chains in an optical lattice," *Nature*, vol. 472, pp. 307–312, 04 2011.

[34] P. Roushan, C. Neill, Y. Chen, M. Kolodrubetz, C. Quintana, N. Leung, M. Fang, R. Barends, B. Campbell, Z. Chen, B. Chiaro, A. Dunsworth, E. Jeffrey, J. Kelly, A. Megrant, J. Mutus, P. J. J. O'Malley, D. Sank, A. Vainsencher, J. Wenner, T. White, A. Polkovnikov, A. N. Cleland, and J. M. Martinis, "Observation of topological transitions in interacting quantum circuits," *Nature*, vol. 515, pp. 241–244, 11 2014.

[35] J. Preskill, "Quantum computing and the entanglement frontier," *ArXiv e-prints*, Mar. 2012.

[36] S. Aaronson and A. Arkhipov, "The computational complexity of linear optics," in *Proceedings of the Forty-third Annual ACM Symposium on Theory of Computing*, STOC '11, (New York, NY, USA), pp. 333–342, ACM, 2011.

[37] M. A. Broome, A. Fedrizzi, S. Rahimi-Keshari, J. Dove, S. Aaronson, T. C. Ralph, and A. G. White, "Photonic boson sampling in a tunable circuit," *Science*, vol. 339, no. 6121, pp. 794–798, 2013.

[38] J. B. Spring, B. J. Metcalf, P. C. Humphreys, W. S. Kolthammer, X.-M. Jin, M. Barbieri, A. Datta, N. Thomas-Peter, N. K. Langford, D. Kundys, J. C. Gates, B. J. Smith, P. G. R. Smith, and I. A. Walmsley, "Boson sampling on a photonic chip," *Science*, vol. 339, no. 6121, pp. 798–801, 2013.

[39] S. Boixo, S. V. Isakov, V. N. Smelyanskiy, R. Babbush, N. Ding, Z. Jiang, J. M. Martinis, and H. Neven, "Characterizing quantum supremacy in near-term devices," *ArXiv e-prints*, Aug. 2016.

[40] A. P. Lund, M. J. Bremner, and T. C. Ralph, "Quantum Sampling Problems, Boson-Sampling and Quantum Supremacy," *ArXiv e-prints*, Feb. 2017.

[41] J. E. Moore, Y. Ran, and X.-G. Wen, "Topological surface states in three-dimensional magnetic insulators," *Phys. Rev. Lett.*, vol. 101, p. 186805, Oct 2008.

[42] D.-L. Deng, S.-T. Wang, K. Sun, and L.-M. Duan, "Probe knots and Hopf insulators with ultracold atoms," *ArXiv e-prints*, Dec. 2016.

[43] D.-L. Deng, S.-T. Wang, C. Shen, and L.-M. Duan, "Hopf insulators and their topologically protected surface states," *Phys. Rev. B*, vol. 88, p. 201105(R), Nov 2013.

[44] D.-L. Deng, S.-T. Wang, and L.-M. Duan, "Systematic construction of tight-binding Hamiltonians for topological insulators and superconductors," *Phys. Rev. B*, vol. 89, p. 075126, Feb 2014.

[45] S.-T. Wang, D.-L. Deng, and L.-M. Duan, "Probe of three-dimensional chiral topological insulators in an optical lattice," *Phys. Rev. Lett.*, vol. 113, p. 033002, Jul 2014.

[46] S.-T. Wang, D.-L. Deng, J. E. Moore, K. Sun, and L.-M. Duan, "Quantized electromagnetic response of three-dimensional chiral topological insulators," *Phys. Rev. B*, vol. 91, p. 035108, Jan 2015.

[47] D.-L. Deng, S.-T. Wang, and L.-M. Duan, "Direct probe of topological order for cold atoms," *Phys. Rev. A*, vol. 90, p. 041601(R), Oct 2014.

[48] Y. Xu, S.-T. Wang, and L.-M. Duan, "Weyl exceptional rings in a three-dimensional dissipative cold atomic gas," *Phys. Rev. Lett.*, vol. 118, p. 045701, Jan 2017.

[49] C. Monroe, D. M. Meekhof, B. E. King, W. M. Itano, and D. J. Wineland, "Demonstration of a fundamental quantum logic gate," *Phys. Rev. Lett.*, vol. 75, pp. 4714–4717, 1995.

[50] S.-T. Wang, C. Shen, and L.-M. Duan, "Quantum computation under micromotion in a planar ion crystal," *Sci. Rep.*, vol. 5, p. 8555, 02 2015.

[51] S.-T. Wang, D.-L. Deng, and L.-M. Duan, "Hamiltonian tomography for quantum many-body systems with arbitrary couplings," *New J. Phys.*, vol. 17, no. 9, p. 093017, 2015.

[52] S.-T. Wang and L.-M. Duan, "Certification of Boson Sampling Devices with Coarse-Grained Measurements," *ArXiv e-prints*, Jan. 2016.

[53] X. Gao, S.-T. Wang, and L.-M. Duan, "Quantum supremacy for simulating a translation-invariant ising spin model," *Phys. Rev. Lett.*, vol. 118, p. 040502, Jan 2017.

[54] D.-L. Deng, S.-T. Wang, K. Sun, and L.-M. Duan, "Proposal for observing non-abelian statistics of majorana-shockley fermions in an optical lattice," *Phys. Rev. B*, vol. 91, p. 094513, Mar 2015.

[55] J. Jiang, L. Zhao, S.-T. Wang, Z. Chen, T. Tang, L.-M. Duan, and Y. Liu, "First-order superfluid-to-Mott-insulator phase transitions in spinor condensates," *Phys. Rev. A*, vol. 93, p. 063607, Jun 2016.

[56] C. Nayak, S. H. Simon, A. Stern, M. Freedman, and S. Das Sarma, "Non-abelian anyons and topological quantum computation," *Rev. Mod. Phys.*, vol. 80, pp. 1083–1159, Sep 2008.

[57] R. B. Laughlin, "Anomalous quantum hall effect: An incompressible quantum fluid with fractionally charged excitations," *Phys. Rev. Lett.*, vol. 50, pp. 1395–1398, May 1983.

[58] V. Kalmeyer and R. B. Laughlin, "Equivalence of the resonating-valence-bond and fractional quantum hall states," *Phys. Rev. Lett.*, vol. 59, pp. 2095–2098, Nov 1987.

[59] N. Read and S. Sachdev, "Large-n expansion for frustrated quantum antiferromagnets," *Phys. Rev. Lett.*, vol. 66, pp. 1773–1776, Apr 1991.

[60] R. Moessner and S. L. Sondhi, "Resonating valence bond phase in the triangular lattice quantum dimer model," *Phys. Rev. Lett.*, vol. 86, pp. 1881–1884, Feb 2001.

[61] X. G. Wen, F. Wilczek, and A. Zee, "Chiral spin states and superconductivity," *Phys. Rev. B*, vol. 39, pp. 11413–11423, Jun 1989.

[62] X. G. Wen, "Mean-field theory of spin-liquid states with finite energy gap and topological orders," *Phys. Rev. B*, vol. 44, pp. 2664–2672, Aug 1991.

[63] J. E. Moore and L. Balents, "Topological invariants of time-reversal-invariant band structures," *Phys. Rev. B*, vol. 75, p. 121306, Mar 2007.

[64] R. Roy, "Topological phases and the quantum spin hall effect in three dimensions," *Phys. Rev. B*, vol. 79, p. 195322, May 2009.

[65] F. Haldane, "Continuum dynamics of the 1-d heisenberg antiferromagnet: Identification with the o(3) nonlinear sigma model," *Physics Letters A*, vol. 93, no. 9, pp. 464 – 468, 1983.

[66] I. Affleck, T. Kennedy, E. H. Lieb, and H. Tasaki, "Valence bond ground states in isotropic quantum antiferromagnets," *Communications in Mathematical Physics*, vol. 115, no. 3, pp. 477–528, 1988.

[67] M. Nakahara, *Geometry, topology and physics*. CRC Press, 2003.

[68] S. Ryu, A. P. Schnyder, A. Furusaki, and A. W. W. Ludwig, "Topological insulators and superconductors: tenfold way and dimensional hierarchy," *New J. Phys.*, vol. 12, p. 065010, June 2010.

[69] J. C. Budich, "Charge conservation protected topological phases," *Phys. Rev. B*, vol. 87, p. 161103, Apr 2013.

[70] R. H. Fox, "Homotopy groups and torus homotopy groups," *Annals of Mathematics*, vol. 49, no. 2, pp. 471–510, 1948.

[71] J. H. C. Whitehead, "An expression of hopf's invariant as an integral," *Proceedings of the National Academy of Sciences of the United States of America*, vol. 33, pp. 117–123, 05 1947.

[72] F. Wilczek and A. Zee, "Linking numbers, spin, and statistics of solitons," *Phys. Rev. Lett.*, vol. 51, pp. 2250–2252, Dec 1983.

[73] T. Neupert, L. Santos, S. Ryu, C. Chamon, and C. Mudry, "Noncommutative geometry for three-dimensional topological insulators," *Phys. Rev. B*, vol. 86, p. 035125, Jul 2012.

[74] J. Dalibard, F. Gerbier, G. Juzeliūnas, and P. Öhberg, "Colloquium: Artificial gauge potentials for neutral atoms," *Rev. Mod. Phys.*, vol. 83, pp. 1523–1543, Nov. 2011.

[75] Y.-J. Lin, R. L. Compton, K. Jimenez-Garcia, W. D. Phillips, J. V. Porto, and I. B. Spielman, "A synthetic electric force acting on neutral atoms," *Nat Phys*, vol. 7, pp. 531–534, 07 2011.

[76] I. Bloch, J. Dalibard, and S. Nascimbene, "Quantum simulations with ultracold quantum gases," *Nat Phys*, vol. 8, pp. 267–276, 04 2012.

[77] A. Micheli, G. K. Brennen, and P. Zoller, "A toolbox for lattice-spin models with polar molecules," *Nat Phys*, vol. 2, pp. 341–347, 05 2006.

[78] A. Chotia, B. Neyenhuis, S. A. Moses, B. Yan, J. P. Covey, M. Foss-Feig, A. M. Rey, D. S. Jin, and J. Ye, "Long-lived dipolar molecules and feshbach molecules in a 3d optical lattice," *Phys. Rev. Lett.*, vol. 108, p. 080405, Feb 2012.

[79] N. Y. Yao, A. V. Gorshkov, C. R. Laumann, A. M. Läuchli, J. Ye, and M. D. Lukin, "Realizing fractional chern insulators in dipolar spin systems," *Phys. Rev. Lett.*, vol. 110, p. 185302, Apr 2013.

[80] M. Karski, L. Förster, J.-M. Choi, A. Steffen, W. Alt, D. Meschede, and A. Widera, "Quantum walk in position space with single optically trapped atoms," *Science*, vol. 325, no. 5937, pp. 174–177, 2009.

[81] M. A. Broome, A. Fedrizzi, B. P. Lanyon, I. Kassal, A. Aspuru-Guzik, and A. G. White, "Discrete single-photon quantum walks with tunable decoherence," *Phys. Rev. Lett.*, vol. 104, p. 153602, Apr 2010.

[82] T. Kitagawa, "Topological phenomena in quantum walks: elementary introduction to the physics of topological phases," *Quantum Information Processing*, vol. 11, no. 5, pp. 1107–1148, 2012.

[83] T. Kitagawa, M. A. Broome, A. Fedrizzi, M. S. Rudner, E. Berg, I. Kassal, A. Aspuru-Guzik, E. Demler, and A. G. White, "Observation of topologically protected bound states in photonic quantum walks," *Nature Communications*, vol. 3, pp. 882 EP –, 06 2012.

[84] M. D. Schroer, M. H. Kolodrubetz, W. F. Kindel, M. Sandberg, J. Gao, M. R. Vissers, D. P. Pappas, A. Polkovnikov, and K. W. Lehnert, "Measuring a topological transition in an artificial spin-1/2 system," *Phys. Rev. Lett.*, vol. 113, p. 050402, Jul 2014.

[85] F. Kong, C. Ju, Y. Liu, C. Lei, M. Wang, X. Kong, P. Wang, P. Huang, Z. Li, F. Shi, L. Jiang, and J. Du, "Direct measurement of topological numbers with spins in diamond," *Phys. Rev. Lett.*, vol. 117, p. 060503, Aug 2016.

[86] A. Gruber, A. Dräbenstedt, C. Tietz, L. Fleury, J. Wrachtrup, and C. v. Borczyskowski, "Scanning confocal optical microscopy and magnetic resonance on single defect centers," *Science*, vol. 276, no. 5321, pp. 2012–2014, 1997.

[87] M. W. Doherty, N. B. Manson, P. Delaney, F. Jelezko, J. Wrachtrup, and L. C. Hollenberg, "The nitrogen-vacancy colour centre in diamond," *Phys. Rep.*, vol. 528, no. 1, pp. 1 – 45, 2013.

[88] J. Cai, A. Retzker, F. Jelezko, and M. B. Plenio, "A large-scale quantum simulator on a diamond surface at room temperature," *Nat Phys*, vol. 9, pp. 168–173, 03 2013.

[89] L. Childress and R. Hanson, "Diamond nv centers for quantum computing and quantum networks," *MRS Bulletin*, vol. 38, pp. 134–138, 002 2013.

[90] L. Childress, R. Walsworth, and M. Lukin, "Atom-like crystal defects: From quantum computers to biological sensors," *Phys. Today*, vol. 67, no. 10, pp. 38–43, 2014.

[91] L. Faddeev and A. J. Niemi, "Stable knot-like structures in classical field theory," *Nature*, vol. 387, pp. 58–61, 05 1997.

[92] X. Z. Yu, Y. Onose, N. Kanazawa, J. H. Park, J. H. Han, Y. Matsui, N. Nagaosa, and Y. Tokura, "Real-space observation of a two-dimensional skyrmion crystal," *Nature*, vol. 465, pp. 901–904, 06 2010.

[93] M. Atala, M. Aidelsburger, J. T. Barreiro, D. Abanin, T. Kitagawa, E. Demler, and I. Bloch, "Direct measurement of the zak phase in topological bloch bands," *Nat Phys*, vol. 9, pp. 795–800, 12 2013.

[94] S. Mittal, S. Ganeshan, J. Fan, A. Vaezi, and M. Hafezi, "Measurement of topological invariants in a 2d photonic system," *Nat Photon*, vol. 10, pp. 180–183, 03 2016.

[95] N. Goldman, J. C. Budich, and P. Zoller, "Topological quantum matter with ultracold gases in optical lattices," *Nat Phys*, vol. 12, pp. 639–645, 07 2016.

[96] M. Greiner, O. Mandel, T. Esslinger, T. W. Hansch, and I. Bloch, "Quantum phase transition from a superfluid to a mott insulator in a gas of ultracold atoms," *Nature*, vol. 415, pp. 39–44, 01 2002.

[97] R. Jordens, N. Strohmaier, K. Gunter, H. Moritz, and T. Esslinger, "A mott insulator of fermionic atoms in an optical lattice," *Nature*, vol. 455, pp. 204–207, 09 2008.

[98] U. Schneider, L. Hackermüller, S. Will, T. Best, I. Bloch, T. A. Costi, R. W. Helmes, D. Rasch, and A. Rosch, "Metallic and insulating phases of repulsively interacting fermions in a 3d optical lattice," *Science*, vol. 322, no. 5907, pp. 1520–1525, 2008.

[99] X.-L. Qi, T. L. Hughes, S. Raghu, and S.-C. Zhang, "Time-reversal-invariant topological superconductors and superfluids in two and three dimensions," *Phys. Rev. Lett.*, vol. 102, no. 18, p. 187001, 2009.

[100] A. P. Schnyder, S. Ryu, and A. W. W. Ludwig, "Lattice Model of a Three-Dimensional Topological Singlet Superconductor with Time-Reversal Symmetry," *Phys. Rev. Lett.*, vol. 102, p. 196804, May 2009.

[101] P. Hosur, S. Ryu, and A. Vishwanath, "Chiral topological insulators, superconductors, and other competing orders in three dimensions," *Phys. Rev. B*, vol. 81, p. 045120, Jan. 2010.

[102] A. M. Essin and V. Gurarie, "Antiferromagnetic topological insulators in cold atomic gases," *Phys. Rev. B*, vol. 85, no. 19, p. 195116, 2012.

[103] D. Jaksch and P. Zoller, "Creation of effective magnetic fields in optical lattices: the hofstadter butterfly for cold neutral atoms," *New J. Phys.*, vol. 5, no. 1, p. 56, 2003.

[104] C. Chin, R. Grimm, P. Julienne, and E. Tiesinga, "Feshbach resonances in ultracold gases," *Rev. Mod. Phys.*, vol. 82, no. 2, p. 1225, 2010.

[105] G.-B. Jo, J. Guzman, C. K. Thomas, P. Hosur, A. Vishwanath, and D. M. Stamper-Kurn, "Ultracold atoms in a tunable optical kagome lattice," *Phys. Rev. Lett.*, vol. 108, no. 4, p. 045305, 2012.

[106] E. Tang, J.-W. Mei, and X.-G. Wen, "High-temperature fractional quantum hall states," *Phys. Rev. Lett.*, vol. 106, no. 23, p. 236802, 2011.

[107] T. Neupert, L. Santos, C. Chamon, and C. Mudry, "Fractional quantum hall states at zero magnetic field," *Phys. Rev. Lett.*, vol. 106, no. 23, p. 236804, 2011.

[108] K. Sun, Z. Gu, H. Katsura, and S. DasSarma, "Nearly flatbands with nontrivial topology," *Phys. Rev. Lett.*, vol. 106, no. 23, p. 236803, 2011.

[109] I. B. Spielman, W. D. Phillips, and J. V. Porto, "Mott-insulator transition in a two-dimensional atomic bose gas," *Phys. Rev. Lett.*, vol. 98, p. 080404, Feb 2007.

[110] V. A. Kashurnikov, N. V. Prokof'ev, and B. V. Svistunov, "Revealing the superfluid–mott-insulator transition in an optical lattice," *Phys. Rev. A*, vol. 66, p. 031601, Sep 2002.

[111] M. Köhl, H. Moritz, T. Stöferle, K. Günter, and T. Esslinger, "Fermionic atoms in a three dimensional optical lattice: Observing fermi surfaces, dynamics, and interactions," *Phys. Rev. Lett.*, vol. 94, no. 8, p. 080403, 2005.

[112] D. M. Stamper-Kurn, A. P. Chikkatur, A. Görlitz, S. Inouye, S. Gupta, D. E. Pritchard, and W. Ketterle, "Excitation of phonons in a bose-einstein condensate by light scattering," *Phys. Rev. Lett.*, vol. 83, no. 15, p. 2876, 1999.

[113] S.-L. Zhu, B. Wang, and L.-M. Duan, "Simulation and detection of dirac fermions with cold atoms in an optical lattice," *Phys. Rev. Lett.*, vol. 98, no. 26, p. 260402, 2007.

[114] See Supplemental Material for more details on the realization scheme of the effective Hamiltonian, the estimation with Wannier functions and some additional plots of the density of states.

[115] Due to the linear tilt, the correct description is to use Wannier-Stark functions, instead of Wannier functions [20,114]. We will call them Wannier functions here for simplicity.

[116] X.-J. Liu, K. T. Law, and T. K. Ng, "Realization of 2d spin-orbit interaction and exotic topological orders in cold atoms," *Phys. Rev. Lett.*, vol. 112, p. 086401, Feb 2014.

[117] P. Wang, Z.-Q. Yu, Z. Fu, J. Miao, L. Huang, S. Chai, H. Zhai, and J. Zhang, "Spin-orbit coupled degenerate fermi gases," *Phys. Rev. Lett.*, vol. 109, p. 095301, Aug 2012.

[118] A. E. Leanhardt, T. A. Pasquini, M. Saba, A. Schirotzek, Y. Shin, D. Kielpinski, D. E. Pritchard, and W. Ketterle, "Cooling bose-einstein condensates below 500 picokelvin," *Science*, vol. 301, no. 5639, pp. 1513–1515, 2003.

[119] P. Medley, D. M. Weld, H. Miyake, D. E. Pritchard, and W. Ketterle, "Spin gradient demagnetization cooling of ultracold atoms," *Phys. Rev. Lett.*, vol. 106, p. 195301, May 2011.

[120] I. Bloch, "Ultracold quantum gases in optical lattices," *Nat. Phys.*, vol. 1, no. 1, pp. 23–30, 2005.

[121] B. A. Bernevig, T. L. Hughes, and S.-C. Zhang, "Quantum spin hall effect and topological phase transition in hgte quantum wells," *Science*, vol. 314, no. 5806, pp. 1757–1761, 2006.

[122] D. J. Thouless, M. Kohmoto, M. P. Nightingale, and M. Den Nijs, "Quantized hall conductance in a two-dimensional periodic potential," *Phys. Rev. Lett.*, vol. 49, pp. 405–408, 1982.

[123] X.-L. Qi, T. L. Hughes, and S.-C. Zhang, "Topological field theory of time-reversal invariant insulators," *Phys. Rev. B*, vol. 78, p. 195424, Nov. 2008.

[124] A. M. Essin, J. E. Moore, and D. Vanderbilt, "Magnetoelectric polarizability and axion electrodynamics in crystalline insulators," *Phys. Rev. Lett.*, vol. 102, p. 146805, Apr 2009.

[125] K. Shiozaki and S. Fujimoto, "Electromagnetic and thermal responses of z topological insulators and superconductors in odd spatial dimensions," *Phys. Rev. Lett.*, vol. 110, no. 7, p. 076804, 2013.

[126] R. B. Laughlin, "Quantized hall conductivity in two dimensions," *Phys. Rev. B*, vol. 23, pp. 5632–5633, May 1981.

[127] G. Rosenberg, H.-M. Guo, and M. Franz, "Wormhole effect in a strong topological insulator," *Phys. Rev. B*, vol. 82, no. 4, p. 041104, 2010.

[128] C.-Z. Chang, J. Zhang, X. Feng, J. Shen, Z. Zhang, M. Guo, K. Li, Y. Ou, P. Wei, L.-L. Wang, Z.-Q. Ji, Y. Feng, S. Ji, X. Chen, J. Jia, X. Dai, Z. Fang, S.-C. Zhang, K. He, Y. Wang, L. Lu, X.-C. Ma, and Q.-K. Xue, "Experimental observation of the quantum anomalous hall effect in a magnetic topological insulator," *Science*, vol. 340, no. 6129, pp. 167–170, 2013.

[129] A. M. Essin, A. M. Turner, J. E. Moore, and D. Vanderbilt, "Orbital magnetoelectric coupling in band insulators," *Phys. Rev. B*, vol. 81, p. 205104, May 2010.

[130] K. D. Nelson, X. Li, and D. S. Weiss, "Imaging single atoms in a three-dimensional array," *Nat. Phys.*, vol. 3, no. 8, pp. 556–560, 2007.

[131] W. S. Bakr, A. Peng, M. E. Tai, R. Ma, J. Simon, J. I. Gillen, S. Fölling, L. Pollet, and M. Greiner, "Probing the superfluid–to–mott insulator transition at the single-atom level," *Science*, vol. 329, no. 5991, pp. 547–550, 2010.

[132] J. F. Sherson, C. Weitenberg, M. Endres, M. Cheneau, I. Bloch, and S. Kuhr, "Single-atom-resolved fluorescence imaging of an atomic mott insulator," *Nature*, vol. 467, pp. 68–72, 09 2010.

[133] K. von Klitzing, "The quantized hall effect," *Rev. Mod. Phys.*, vol. 58, pp. 519–531, Jul 1986.

[134] S. D. Sarma and A. Pinczuk, *Perspectives in quantum hall effects: Novel quantum liquids in low-dimensional semiconductor structures*. John Wiley & Sons, 2008.

[135] Y. J. Lin, R. L. Compton, K. Jimenez-Garcia, J. V. Porto, and I. B. Spielman, "Synthetic magnetic fields for ultracold neutral atoms," *Nature*, vol. 462, pp. 628–632, 12 2009.

[136] X.-J. Liu, M. F. Borunda, X. Liu, and J. Sinova, "Effect of induced spin-orbit coupling for atoms via laser fields," *Phys. Rev. Lett.*, vol. 102, p. 046402, Jan 2009.

[137] L. W. Cheuk, A. T. Sommer, Z. Hadzibabic, T. Yefsah, W. S. Bakr, and M. W. Zwierlein, "Spin-injection spectroscopy of a spin-orbit coupled fermi gas," *Phys. Rev. Lett.*, vol. 109, p. 095302, Aug 2012.

[138] V. Galitski and I. B. Spielman, "Spin-orbit coupling in quantum gases," *Nature*, vol. 494, pp. 49–54, 02 2013.

[139] S.-L. Zhu, H. Fu, C.-J. Wu, S.-C. Zhang, and L.-M. Duan, "Spin hall effects for cold atoms in a light-induced gauge potential," *Phys. Rev. Lett.*, vol. 97, p. 240401, Dec 2006.

[140] S.-L. Zhu, L.-B. Shao, Z. D. Wang, and L.-M. Duan, "Probing non-abelian statistics of majorana fermions in ultracold atomic superfluid," *Phys. Rev. Lett.*, vol. 106, p. 100404, Mar 2011.

[141] B. Béri and N. R. Cooper, "F_2 topological insulators in ultracold atomic gases," *Phys. Rev. Lett.*, vol. 107, p. 145301, Sep 2011.

[142] L. B. Shao, S.-L. Zhu, L. Sheng, D. Y. Xing, and Z. D. Wang, "Realizing and detecting the quantum hall effect without landau levels by using ultracold atoms," *Phys. Rev. Lett.*, vol. 101, p. 246810, Dec 2008.

[143] A. Dauphin and N. Goldman, "Extracting the chern number from the dynamics of a fermi gas: Implementing a quantum hall bar for cold atoms," *Phys. Rev. Lett.*, vol. 111, p. 135302, Sep 2013.

[144] P. Hauke, M. Lewenstein, and A. Eckardt, "Tomography of band insulators from quench dynamics," *Phys. Rev. Lett.*, vol. 113, p. 045303, Jul 2014.

[145] L. Wang, A. A. Soluyanov, and M. Troyer, "Proposal for direct measurement of topological invariants in optical lattices," *Phys. Rev. Lett.*, vol. 110, p. 166802, Apr 2013.

[146] X.-J. Liu, X. Liu, C. Wu, and J. Sinova, "Quantum anomalous hall effect with cold atoms trapped in a square lattice," *Phys. Rev. A*, vol. 81, p. 033622, Mar 2010.

[147] N. Goldman, J. Beugnon, and F. Gerbier, "Detecting chiral edge states in the hofstadter optical lattice," *Phys. Rev. Lett.*, vol. 108, p. 255303, Jun 2012.

[148] N. Goldman, J. Dalibard, A. Dauphin, F. Gerbier, M. Lewenstein, P. Zoller, and I. B. Spielman, "Direct imaging of topological edge states in cold-atom systems," *Proc. Natl. Acad. Sci. USA*, vol. 110, no. 17, pp. 6736–6741, 2013.

[149] E. Zhao, N. Bray-Ali, C. J. Williams, I. B. Spielman, and I. I. Satija, "Chern numbers hiding in time-of-flight images," *Phys. Rev. A*, vol. 84, p. 063629, Dec 2011.

[150] E. Alba, X. Fernandez-Gonzalvo, J. Mur-Petit, J. K. Pachos, and J. J. Garcia-Ripoll, "Seeing topological order in time-of-flight measurements," *Phys. Rev. Lett.*, vol. 107, p. 235301, Nov 2011.

[151] H. M. Price and N. R. Cooper, "Mapping the berry curvature from semiclassical dynamics in optical lattices," *Phys. Rev. A*, vol. 85, p. 033620, Mar 2012.

[152] X.-J. Liu, K. T. Law, T. K. Ng, and P. A. Lee, "Detecting topological phases in cold atoms," *Phys. Rev. Lett.*, vol. 111, p. 120402, Sep 2013.

[153] D. A. Abanin, T. Kitagawa, I. Bloch, and E. Demler, "Interferometric approach to measuring band topology in 2d optical lattices," *Phys. Rev. Lett.*, vol. 110, p. 165304, Apr 2013.

[154] N. Goldman, E. Anisimovas, F. Gerbier, P. Öhberg, I. B. Spielman, and G. Juzeliūnas, "Measuring topology in a laser-coupled honeycomb lattice: from chern insulators to topological semi-metals," *New J. Phys.*, vol. 15, no. 1, p. 013025, 2013.

[155] J. K. Pachos, E. Alba, V. Lahtinen, and J. J. Garcia-Ripoll, "Seeing majorana fermions in time-of-flight images of staggered spinless fermions coupled by s-wave pairing," *Phys. Rev. A*, vol. 88, p. 013622, Jul 2013.

[156] W. Ketterle and M. W. Zwierlein, "Making, probing and understanding ultracold Fermi gases," *Nuovo Cimento Rivista Serie*, vol. 31, pp. 247–422, May 2008.

[157] L.-M. Duan, "Detecting correlation functions of ultracold atoms through fourier sampling of time-of-flight images," *Phys. Rev. Lett.*, vol. 96, p. 103201, Mar 2006.

[158] T. Fukui, Y. Hatsugai, and H. Suzuki, "Chern numbers in discretized brillouin zone: Efficient method of computing (spin) hall conductances," *J. Phys. Soc. Jpn.*, vol. 74, no. 6, pp. 1674–1677, 2005.

[159] F. D. M. Haldane, "Model for a quantum hall effect without landau levels: Condensed-matter realization of the "parity anomaly"," *Phys. Rev. Lett.*, vol. 61, pp. 2015–2018, Oct 1988.

[160] X.-J. Liu, K. T. Law, and T. K. Ng, "Realization of 2d spin-orbit interaction and exotic topological orders in cold atoms," *Phys. Rev. Lett.*, vol. 112, p. 086401, Feb 2014.

[161] A. A. Burkov, "Topological semimetals," *Nat Mater*, vol. 15, pp. 1145–1148, 11 2016.

[162] S. Jia, S.-Y. Xu, and M. Z. Hasan, "Weyl semimetals, fermi arcs and chiral anomalies," *Nat Mater*, vol. 15, pp. 1140–1144, 11 2016.

[163] A. A. Burkov, M. D. Hook, and L. Balents, "Topological nodal semimetals," *Phys. Rev. B*, vol. 84, p. 235126, Dec 2011.

[164] Y. Xu, F. Zhang, and C. Zhang, "Structured weyl points in spin-orbit coupled fermionic superfluids," *Phys. Rev. Lett.*, vol. 115, p. 265304, Dec 2015.

[165] A. A. Soluyanov, D. Gresch, Z. Wang, Q. Wu, M. Troyer, X. Dai, and B. A. Bernevig, "Type-ii weyl semimetals," *Nature*, vol. 527, pp. 495–498, 11 2015.

[166] B. Bradlyn, J. Cano, Z. Wang, M. G. Vergniory, C. Felser, R. J. Cava, and B. A. Bernevig, "Beyond dirac and weyl fermions: Unconventional quasiparticles in conventional crystals," *Science*, vol. 353, no. 6299, 2016.

[167] X. Wan, A. M. Turner, A. Vishwanath, and S. Y. Savrasov, "Topological semimetal and fermi-arc surface states in the electronic structure of pyrochlore iridates," *Phys. Rev. B*, vol. 83, p. 205101, May 2011.

[168] K.-Y. Yang, Y.-M. Lu, and Y. Ran, "Quantum hall effects in a weyl semimetal: Possible application in pyrochlore iridates," *Phys. Rev. B*, vol. 84, p. 075129, Aug 2011.

[169] A. A. Burkov and L. Balents, "Weyl semimetal in a topological insulator multilayer," *Phys. Rev. Lett.*, vol. 107, p. 127205, Sep 2011.

[170] G. Xu, H. Weng, Z. Wang, X. Dai, and Z. Fang, "Chern semimetal and the quantized anomalous hall effect in $hgcr_2se_4$," *Phys. Rev. Lett.*, vol. 107, p. 186806, Oct 2011.

[171] L. Lu, L. Fu, J. D. Joannopoulos, and M. Soljacic, "Weyl points and line nodes in gyroid photonic crystals," *Nat Photon*, vol. 7, pp. 294–299, 04 2013.

[172] M. Gong, S. Tewari, and C. Zhang, "Bcs-bec crossover and topological phase transition in 3d spin-orbit coupled degenerate fermi gases," *Phys. Rev. Lett.*, vol. 107, p. 195303, Nov 2011.

[173] B. M. Anderson, G. Juzeliūnas, V. M. Galitski, and I. B. Spielman, "Synthetic 3d spin-orbit coupling," *Phys. Rev. Lett.*, vol. 108, p. 235301, Jun 2012.

[174] Y. Xu, R.-L. Chu, and C. Zhang, "Anisotropic weyl fermions from the quasiparticle excitation spectrum of a 3d fulde-ferrell superfluid," *Phys. Rev. Lett.*, vol. 112, p. 136402, Mar 2014.

[175] S. A. Yang, H. Pan, and F. Zhang, "Dirac and weyl superconductors in three dimensions," *Phys. Rev. Lett.*, vol. 113, p. 046401, Jul 2014.

[176] T. Dubček, C. J. Kennedy, L. Lu, W. Ketterle, M. Soljačić, and H. Buljan, "Weyl points in three-dimensional optical lattices: Synthetic magnetic monopoles in momentum space," *Phys. Rev. Lett.*, vol. 114, p. 225301, Jun 2015.

[177] B. Liu, X. Li, L. Yin, and W. V. Liu, "Weyl superfluidity in a three-dimensional dipolar fermi gas," *Phys. Rev. Lett.*, vol. 114, p. 045302, Jan 2015.

[178] L. Lu, Z. Wang, D. Ye, L. Ran, L. Fu, J. D. Joannopoulos, and M. Soljačić, "Experimental observation of weyl points," *Science*, vol. 349, no. 6248, pp. 622–624, 2015.

[179] S.-Y. Xu, I. Belopolski, N. Alidoust, M. Neupane, G. Bian, C. Zhang, R. Sankar, G. Chang, Z. Yuan, C.-C. Lee, S.-M. Huang, H. Zheng, J. Ma, D. S. Sanchez, B. Wang, A. Bansil, F. Chou, P. P. Shibayev, H. Lin, S. Jia, and M. Z. Hasan, "Discovery of a weyl fermion semimetal and topological fermi arcs," *Science*, vol. 349, no. 6248, pp. 613–617, 2015.

[180] B. Q. Lv, H. M. Weng, B. B. Fu, X. P. Wang, H. Miao, J. Ma, P. Richard, X. C. Huang, L. X. Zhao, G. F. Chen, Z. Fang, X. Dai, T. Qian, and H. Ding, "Experimental discovery of weyl semimetal taas," *Phys. Rev. X*, vol. 5, p. 031013, Jul 2015.

[181] G. E. Volovik, *The universe in a helium droplet*, vol. 117. Oxford University Press on Demand, 2003.

[182] G. Bian, T.-R. Chang, R. Sankar, S.-Y. Xu, H. Zheng, T. Neupert, C.-K. Chiu, S.-M. Huang, G. Chang, I. Belopolski, D. S. Sanchez, M. Neupane, N. Alidoust, C. Liu, B. Wang, C.-C. Lee, H.-T. Jeng, C. Zhang, Z. Yuan, S. Jia, A. Bansil, F. Chou, H. Lin, and M. Z. Hasan, "Topological nodal-line fermions in spin-orbit metal pbtase2," *Nature Communications*, vol. 7, pp. 10556 EP –, 02 2016.

[183] Y. Xu and C. Zhang, "Dirac and weyl rings in three-dimensional cold-atom optical lattices," *Phys. Rev. A*, vol. 93, p. 063606, Jun 2016.

[184] D.-W. Zhang, Y. X. Zhao, R.-B. Liu, Z.-Y. Xue, S.-L. Zhu, and Z. D. Wang, "Quantum simulation of exotic $\mathcal{PT}$-invariant topological nodal loop bands with ultracold atoms in an optical lattice," *Phys. Rev. A*, vol. 93, p. 043617, Apr 2016.

[185] N. Moiseyev, *Non-Hermitian quantum mechanics*. Cambridge University Press, 2011.

[186] M. Berry, "Physics of nonhermitian degeneracies," *Czechoslovak Journal of Physics*, vol. 54, no. 10, pp. 1039–1047, 2004.

[187] I. Rotter, "A non-hermitian hamilton operator and the physics of open quantum systems," *J. Phys. A*, vol. 42, no. 15, p. 153001, 2009.

[188] W. D. Heiss, "The physics of exceptional points," *J. Phys. A*, vol. 45, no. 44, p. 444016, 2012.

[189] A. Guo, G. J. Salamo, D. Duchesne, R. Morandotti, M. Volatier-Ravat, V. Aimez, G. A. Siviloglou, and D. N. Christodoulides, "Observation of $\mathcal{PT}$-symmetry breaking in complex optical potentials," *Phys. Rev. Lett.*, vol. 103, p. 093902, Aug 2009.

[190] C. E. Ruter, K. G. Makris, R. El-Ganainy, D. N. Christodoulides, M. Segev, and D. Kip, "Observation of parity-time symmetry in optics," *Nat Phys*, vol. 6, pp. 192–195, 03 2010.

[191] Y. D. Chong, L. Ge, and A. D. Stone, "$\mathcal{PT}$-symmetry breaking and laser-absorber modes in optical scattering systems," *Phys. Rev. Lett.*, vol. 106, p. 093902, Mar 2011.

[192] B. Zhen, C. W. Hsu, Y. Igarashi, L. Lu, I. Kaminer, A. Pick, S.-L. Chua, J. D. Joannopoulos, and M. Soljacic, "Spawning rings of exceptional points out of dirac cones," *Nature*, vol. 525, pp. 354–358, 09 2015.

[193] M. Müller, S. Diehl, G. Pupillo, P. Zoller, *et al.*, "Engineered open systems and quantum simulations with atoms and ions," *Advances in Atomic Molecular and Optical Physics*, vol. 61, p. 1, 2012.

[194] J. Li, A. K. Harter, J. Liu, L. de Melo, Y. N. Joglekar, and L. Luo, "Observation of parity-time symmetry breaking transitions in a dissipative Floquet system of ultracold atoms," *ArXiv e-prints*, Aug. 2016.

[195] M. Liertzer, L. Ge, A. Cerjan, A. D. Stone, H. E. Türeci, and S. Rotter, "Pump-induced exceptional points in lasers," *Phys. Rev. Lett.*, vol. 108, p. 173901, Apr 2012.

[196] L. Feng, Z. J. Wong, R.-M. Ma, Y. Wang, and X. Zhang, "Single-mode laser by parity-time symmetry breaking," *Science*, vol. 346, no. 6212, pp. 972–975, 2014.

[197] H. Hodaei, M.-A. Miri, M. Heinrich, D. N. Christodoulides, and M. Khajavikhan, "Parity-time–symmetric microring lasers," *Science*, vol. 346, no. 6212, pp. 975–978, 2014.

[198] T. Gao, E. Estrecho, K. Y. Bliokh, T. C. H. Liew, M. D. Fraser, S. Brodbeck, M. Kamp, C. Schneider, S. Hofling, Y. Yamamoto, F. Nori, Y. S. Kivshar, A. G. Truscott, R. G. Dall, and E. A. Ostrovskaya, "Observation of non-hermitian degeneracies in a chaotic exciton-polariton billiard," *Nature*, vol. 526, pp. 554–558, 10 2015.

[199] C. M. Bender and S. Boettcher, "Real spectra in non-hermitian hamiltonians having $\mathcal{PT}$ symmetry," *Phys. Rev. Lett.*, vol. 80, pp. 5243–5246, Jun 1998.

[200] M. Kleman and O. D. Laverntovich, *Soft matter physics: an introduction*. Springer Science & Business Media, 2007.

[201] D. Xiao, M.-C. Chang, and Q. Niu, "Berry phase effects on electronic properties," *Rev. Mod. Phys.*, vol. 82, pp. 1959–2007, Jul 2010.

[202] G. Sundaram and Q. Niu, "Wave-packet dynamics in slowly perturbed crystals: Gradient corrections and berry-phase effects," *Phys. Rev. B*, vol. 59, pp. 14915–14925, Jun 1999.

[203] Y. Xu and L.-M. Duan, "Type-ii weyl points in three-dimensional cold-atom optical lattices," *Phys. Rev. A*, vol. 94, p. 053619, Nov 2016.

[204] T. E. Lee, "Anomalous edge state in a non-hermitian lattice," *Phys. Rev. Lett.*, vol. 116, p. 133903, Apr 2016.

[205] D. Leykam, K. Y. Bliokh, C. Huang, Y. D. Chong, and F. Nori, "Edge modes, degeneracies, and topological numbers in non-hermitian systems," *Phys. Rev. Lett.*, vol. 118, p. 040401, Jan 2017.

[206] R. Blatt and D. Wineland, "Entangled states of trapped atomic ions," *Nature*, vol. 453, pp. 1008–1015, 06 2008.

[207] H. Haffner, C. F. Roos, and R. Blatt, "Quantum computing with trapped ions," *Phys. Rep.*, vol. 469, pp. 155–203, 2008.

[208] J. I. Cirac and P. Zoller, "Quantum computations with cold trapped ions," *Phys. Rev. Lett.*, vol. 74, pp. 4091–4094, 1995.

[209] F. Schmidt-Kaler, H. Haffner, M. Riebe, S. Gulde, G. P. T. Lancaster, T. Deuschle, C. Becher, C. F. Roos, J. Eschner, and R. Blatt, "Realization of the cirac-zoller controlled-not quantum gate," *Nature*, vol. 422, pp. 408–411, 03 2003.

[210] Q. A. Turchette, C. S. Wood, B. E. King, C. J. Myatt, D. Leibfried, W. M. Itano, C. Monroe, and D. J. Wineland, "Deterministic entanglement of two trapped ions," *Phys. Rev. Lett.*, vol. 81, pp. 3631–3634, Oct 1998.

[211] C. A. Sackett, D. Kielpinski, B. E. King, C. Langer, V. Meyer, C. J. Myatt, M. Rowe, Q. A. Turchette, W. M. Itano, D. J. Wineland, and C. Monroe, "Experimental entanglement of four particles," *Nature*, vol. 404, pp. 256–259, 03 2000.

[212] C. F. Roos, M. Riebe, H. Häffner, W. Hänsel, J. Benhelm, G. P. T. Lancaster, C. Becher, F. Schmidt-Kaler, and R. Blatt, "Control and measurement of three-qubit entangled states," *Science*, vol. 304, no. 5676, pp. 1478–1480, 2004.

[213] M. G. Raizen, J. M. Gilligan, J. C. Bergquist, W. M. Itano, and D. J. Wineland, "Ionic crystals in a linear paul trap," *Phys. Rev. A*, vol. 45, pp. 6493–6501, May 1992.

[214] J. P. Schiffer, "Phase transitions in anisotropically confined ionic crystals," *Phys. Rev. Lett.*, vol. 70, pp. 818–821, Feb 1993.

[215] D. Gottesman, "Fault-tolerant quantum computation with local gates," *J. Mod. Opt.*, vol. 47, no. 2-3, pp. 333–345, 2000.

[216] K. M. Svore, B. M. Terhal, and D. P. DiVincenzo, "Local fault-tolerant quantum computation," *Phys. Rev. A*, vol. 72, p. 022317, Aug 2005.

[217] T. Szkopek, P. Boykin, H. Fan, V. Roychowdhury, E. Yablonovitch, G. Simms, M. Gyure, and B. Fong, "Threshold error penalty for fault-tolerant quantum computation with nearest neighbor communication," *IEEE Trans. Nanotechnol.*, vol. 5, pp. 42–49, Jan 2006.

[218] W. M. Itano, J. J. Bollinger, J. N. Tan, B. Jelenković, X.-P. Huang, and D. J. Wineland, "Bragg diffraction from crystallized ion plasmas," *Science*, vol. 279, no. 5351, pp. 686–689, 1998.

[219] M. Drewsen, C. Brodersen, L. Hornekær, J. Hangst, and J. Schifffer, "Large ion crystals in a linear paul trap," *Phys. Rev. Lett.*, vol. 81, pp. 2878–2881, Oct 1998.

[220] A. Mortensen, E. Nielsen, T. Matthey, and M. Drewsen, "Observation of three-dimensional long-range order in small ion coulomb crystals in an rf trap," *Phys. Rev. Lett.*, vol. 96, p. 103001, Mar 2006.

[221] R. Raussendorf and J. Harrington, "Fault-tolerant quantum computation with high threshold in two dimensions," *Phys. Rev. Lett.*, vol. 98, p. 190504, May 2007.

[222] R. Raussendorf, J. Harrington, and K. Goyal, "Topological fault-tolerance in cluster state quantum computation," *New J. Phys.*, vol. 9, no. 6, p. 199, 2007.

[223] A. G. Fowler, A. M. Stephens, and P. Groszkowski, "High-threshold universal quantum computation on the surface code," *Phys. Rev. A*, vol. 80, p. 052312, Nov 2009.

[224] D. P. DiVincenzo, "Fault-tolerant architectures for superconducting qubits," *Physica Scripta*, vol. 2009, no. T137, p. 014020, 2009.

[225] J. I. Cirac and P. Zoller, "A scalable quantum computer with ions in an array of microtraps," *Nature*, vol. 404, pp. 579–581, 04 2000.

[226] D. Porras and J. I. Cirac, "Quantum manipulation of trapped ions in two dimensional coulomb crystals," *Phys. Rev. Lett.*, vol. 96, p. 250501, 2006.

[227] P. Zou, J. Xu, W. Song, and S.-L. Zhu, "Implementation of local and high-fidelity quantum conditional phase gates in a scalable two-dimensional ion trap.," *Phys. Lett. A*, vol. 374, no. 13-14, pp. 1425–1430, 2010.

[228] T. B. Mitchell, J. J. Bollinger, D. H. E. Dubin, X.-P. Huang, W. M. Itano, and R. H. Baughman, "Direct observations of structural phase transitions in planar crystallized ion plasmas," *Science*, vol. 282, no. 5392, pp. 1290–1293, 1998.

[229] D. Kielpinski, C. Monroe, and D. J. Wineland, "Architecture for a large-scale ion-trap quantum computer," *Nature*, vol. 417, pp. 709–711, 2002.

[230] C. Monroe and J. Kim, "Scaling the ion trap quantum processor," *Science*, vol. 339, no. 6124, pp. 1164–1169, 2013.

[231] D. Berkeland, J. Miller, J. Bergquist, W. Itano, and D. Wineland, "Minimization of ion micromotion in a paul trap," *J. Appl. Phys.*, vol. 83, no. 10, pp. 5025–5033, 1998.

[232] D. Leibfried, R. Blatt, C. Monroe, and D. Wineland, "Quantum dynamics of single trapped ions," *Rev. Mod. Phys.*, vol. 75, pp. 281–324, Mar 2003.

[233] C. Shen and L.-M. Duan, "High-fidelity quantum gates for trapped ions under micromotion," *Phys. Rev. A*, vol. 90, p. 022332, Aug 2014.

[234] H. Landa, M. Drewsen, B. Reznik, and A. Retzker, "Modes of oscillation in radiofrequency paul traps," *New J. Phys.*, vol. 14, no. 9, p. 093023, 2012.

[235] H. Kaufmann, S. Ulm, G. Jacob, U. Poschinger, H. Landa, A. Retzker, M. B. Plenio, and F. Schmidt-Kaler, "Precise experimental investigation of eigenmodes in a planar ion crystal," *Phys. Rev. Lett.*, vol. 109, p. 263003, Dec 2012.

[236] H. Landa, A. Retzker, T. Schaetz, and B. Reznik, "Entanglement generation using discrete solitons in coulomb crystals," *Phys. Rev. Lett.*, vol. 113, p. 053001, Jul 2014.

[237] B. Yoshimura, M. Stork, D. Dadic, W. C. Campbell, and J. K. Freericks, "Creation of two-dimensional coulomb crystals of ions in oblate Paul traps for quantum simulations," *ArXiv e-prints*, June 2014.

[238] S.-L. Zhu, C. Monroe, and L.-M. Duan, "Arbitrary-speed quantum gates within large ion crystals through minimum control of laser beams," *Europhys. Lett.*, vol. 73, no. 4, p. 485, 2006.

[239] S.-L. Zhu, C. Monroe, and L.-M. Duan, "Trapped ion quantum computation with transverse phonon modes," *Phys. Rev. Lett.*, vol. 97, p. 050505, Aug 2006.

[240] T. Choi, S. Debnath, T. A. Manning, C. Figgatt, Z.-X. Gong, L.-M. Duan, and C. Monroe, "Optimal quantum control of multimode couplings between trapped ion qubits for scalable entanglement," *Phys. Rev. Lett.*, vol. 112, p. 190502, May 2014.

[241] N. W. McLachlan, *Theory and application of Mathieu functions*. Clarendon Press, 1951.

[242] B. E. King, *Quantum state engineering and information processing with trapped ions*. PhD thesis, University of Colorado, 1999.

[243] D. James, "Quantum dynamics of cold trapped ions with application to quantum computation," *Appl. Phys. B*, vol. 66, no. 2, pp. 181–190, 1998.

[244] C. B. Zhang, D. Offenberg, B. Roth, M. A. Wilson, and S. Schiller, "Molecular-dynamics simulations of cold single-species and multispecies ion ensembles in a linear paul trap," *Phys. Rev. A*, vol. 76, p. 012719, Jul 2007.

[245] J. P. Schiffer, M. Drewsen, J. S. Hangst, and L. Hornekær, "Temperature, ordering, and equilibrium with time-dependent confining forces," *Proc. Natl. Acad. Sci.*, vol. 97, no. 20, pp. 10697–10700, 2000.

[246] D. Leibfried, B. DeMarco, V. Meyer, D. Lucas, M. Barrett, J. Britton, W. M. Itano, B. Jelenkovic, C. Langer, T. Rosenband, and D. J. Wineland, "Experimental demonstration of a robust, high-fidelity geometric two ion-qubit phase gate," *Nature*, vol. 422, pp. 412–415, 03 2003.

[247] K. Kim, M.-S. Chang, R. Islam, S. Korenblit, L.-M. Duan, and C. Monroe, "Entanglement and tunable spin-spin couplings between trapped ions using multiple transverse modes," *Phys. Rev. Lett.*, vol. 103, p. 120502, Sep 2009.

[248] G.-D. Lin, S.-L. Zhu, R. Islam, K. Kim, M.-S. Chang, S. Korenblit, C. Monroe, and L.-M. Duan, "Large-scale quantum computation in an anharmonic linear ion trap," *Europhys. Lett.*, vol. 86, no. 6, p. 60004, 2009.

[249] V. L. Ryjkov, X. Zhao, and H. A. Schuessler, "Simulations of the rf heating rates in a linear quadrupole ion trap," *Phys. Rev. A*, vol. 71, p. 033414, Mar 2005.

[250] I. Buluta, M. Kitaoka, S. Georgescu, and S. Hasegawa, "Investigation of planar coulomb crystals for quantum simulation and computation," *Phys. Rev. A*, vol. 77, p. 062320, Jun 2008.

[251] R. Horodecki, P. Horodecki, M. Horodecki, and K. Horodecki, "Quantum entanglement," *Rev. Mod. Phys.*, vol. 81, pp. 865–942, Jun 2009.

[252] K. Vogel and H. Risken, "Determination of quasiprobability distributions in terms of probability distributions for the rotated quadrature phase," *Phys. Rev. A*, vol. 40, pp. 2847–2849, Sep 1989.

[253] D. T. Smithey, M. Beck, M. G. Raymer, and A. Faridani, "Measurement of the wigner distribution and the density matrix of a light mode using optical homodyne tomography: Application to squeezed states and the vacuum," *Phys. Rev. Lett.*, vol. 70, pp. 1244–1247, Mar 1993.

[254] I. L. Chuang and M. A. Nielsen, "Prescription for experimental determination of the dynamics of a quantum black box," *J. Mod. Opt.*, vol. 44, no. 11-12, pp. 2455–2467, 1997.

[255] D. F. V. James, P. G. Kwiat, W. J. Munro, and A. G. White, "Measurement of qubits," *Phys. Rev. A*, vol. 64, p. 052312, Oct 2001.

[256] H. Haffner, W. Hansel, C. F. Roos, J. Benhelm, D. Chek-al kar, M. Chwalla, T. Korber, U. D. Rapol, M. Riebe, P. O. Schmidt, C. Becher, O. Guhne, W. Dur, and R. Blatt, "Scalable multiparticle entanglement of trapped ions," *Nature*, vol. 438, pp. 643–646, 12 2005.

[257] A. I. Lvovsky and M. G. Raymer, "Continuous-variable optical quantum-state tomography," *Rev. Mod. Phys.*, vol. 81, pp. 299–332, Mar 2009.

[258] M. Paris and J. Rehacek (eds), *Quantum state estimation*, vol. 649 in Lecture Notes in Physics. Springer Science & Business Media, 2004.

[259] S. G. Schirmer, A. Kolli, and D. K. L. Oi, "Experimental hamiltonian identification for controlled two-level systems," *Phys. Rev. A*, vol. 69, p. 050306, May 2004.

[260] J. H. Cole, S. G. Schirmer, A. D. Greentree, C. J. Wellard, D. K. L. Oi, and L. C. L. Hollenberg, "Identifying an experimental two-state hamiltonian to arbitrary accuracy," *Phys. Rev. A*, vol. 71, p. 062312, Jun 2005.

[261] J. H. Cole, S. J. Devitt, and L. C. L. Hollenberg, "Precision characterization of two-qubit hamiltonians via entanglement mapping," *J. Phys. A: Math. Gen.*, vol. 39, no. 47, p. 14649, 2006.

[262] S. J. Devitt, J. H. Cole, and L. C. L. Hollenberg, "Scheme for direct measurement of a general two-qubit hamiltonian," *Phys. Rev. A*, vol. 73, p. 052317, May 2006.

[263] C. Senko, J. Smith, P. Richerme, A. Lee, W. C. Campbell, and C. Monroe, "Coherent imaging spectroscopy of a quantum many-body spin system," *Science*, vol. 345, no. 6195, pp. 430–433, 2014.

[264] D. Burgarth and K. Maruyama, "Indirect hamiltonian identification through a small gateway," *New J. Phys.*, vol. 11, no. 10, p. 103019, 2009.

[265] D. Burgarth, K. Maruyama, and F. Nori, "Coupling strength estimation for spin chains despite restricted access," *Phys. Rev. A*, vol. 79, p. 020305, Feb 2009.

[266] D. Burgarth, K. Maruyama, and F. Nori, "Indirect quantum tomography of quadratic hamiltonians," *New J. Phys.*, vol. 13, no. 1, p. 013019, 2011.

[267] C. Di Franco, M. Paternostro, and M. S. Kim, "Hamiltonian tomography in an access-limited setting without state initialization," *Phys. Rev. Lett.*, vol. 102, p. 187203, May 2009.

[268] J. Zhang and M. Sarovar, "Quantum hamiltonian identification from measurement time traces," *Phys. Rev. Lett.*, vol. 113, p. 080401, Aug 2014.

[269] M. P. da Silva, O. Landon-Cardinal, and D. Poulin, "Practical characterization of quantum devices without tomography," *Phys. Rev. Lett.*, vol. 107, p. 210404, Nov 2011.

[270] N. Wiebe, C. Granade, C. Ferrie, and D. G. Cory, "Hamiltonian learning and certification using quantum resources," *Phys. Rev. Lett.*, vol. 112, p. 190501, May 2014.

[271] T. Gullion, D. B. Baker, and M. S. Conradi, "New, compensated carr-purcell sequences," *Journal of Magnetic Resonance (1969)*, vol. 89, no. 3, pp. 479 – 484, 1990.

[272] L. Viola and S. Lloyd, "Dynamical suppression of decoherence in two-state quantum systems," *Phys. Rev. A*, vol. 58, pp. 2733–2744, Oct 1998.

[273] L. Viola, E. Knill, and S. Lloyd, "Dynamical decoupling of open quantum systems," *Phys. Rev. Lett.*, vol. 82, pp. 2417–2421, Mar 1999.

[274] L.-M. Duan and G.-C. Guo, "Suppressing environmental noise in quantum computation through pulse control," *Phys. Lett. A*, vol. 261, no. 3–4, pp. 139 – 144, 1999.

[275] P. Zanardi, "Symmetrizing evolutions," *Phys. Lett. A*, vol. 258, no. 2–3, pp. 77 – 82, 1999.

[276] K. Khodjasteh and D. A. Lidar, "Fault-tolerant quantum dynamical decoupling," *Phys. Rev. Lett.*, vol. 95, p. 180501, Oct 2005.

[277] K. Khodjasteh and D. A. Lidar, "Performance of deterministic dynamical decoupling schemes: Concatenated and periodic pulse sequences," *Phys. Rev. A*, vol. 75, p. 062310, Jun 2007.

[278] G. S. Uhrig, "Keeping a quantum bit alive by optimized π-pulse sequences," *Phys. Rev. Lett.*, vol. 98, p. 100504, Mar 2007.

[279] W. Yang, Z.-Y. Wang, and R.-B. Liu, "Preserving qubit coherence by dynamical decoupling," *Front. Phys. China*, vol. 6, no. 1, pp. 2–14, 2011.

[280] A. M. Souza, G. A. Álvarez, and D. Suter, "Robust dynamical decoupling for quantum computing and quantum memory," *Phys. Rev. Lett.*, vol. 106, p. 240501, Jun 2011.

[281] A. M. Souza, G. A. Álvarez, and D. Suter, "Robust dynamical decoupling," *Phil. Trans. R. Soc. A*, vol. 370, no. 1976, pp. 4748–4769, 2012.

[282] G. A. Álvarez, M. Mishkovsky, E. P. Danieli, P. R. Levstein, H. M. Pastawski, and L. Frydman, "Perfect state transfers by selective quantum interferences within complex spin networks," *Phys. Rev. A*, vol. 81, p. 060302, Jun 2010.

[283] J. J. L. Morton, A. M. Tyryshkin, A. Ardavan, S. C. Benjamin, K. Porfyrakis, S. A. Lyon, and G. A. D. Briggs, "Bang-bang control of fullerene qubits using ultrafast phase gates," *Nat. Phys.*, vol. 2, pp. 40–43, 01 2006.

[284] M. J. Biercuk, H. Uys, A. P. VanDevender, N. Shiga, W. M. Itano, and J. J. Bollinger, "Optimized dynamical decoupling in a model quantum memory," *Nature*, vol. 458, pp. 996–1000, 04 2009.

[285] J. Du, X. Rong, N. Zhao, Y. Wang, J. Yang, and R. B. Liu, "Preserving electron spin coherence in solids by optimal dynamical decoupling," *Nature*, vol. 461, pp. 1265–1268, 10 2009.

[286] J. R. West, D. A. Lidar, B. H. Fong, and M. F. Gyure, "High fidelity quantum gates via dynamical decoupling," *Phys. Rev. Lett.*, vol. 105, p. 230503, Dec 2010.

[287] M. Johanning, A. Braun, N. Timoney, V. Elman, W. Neuhauser, and C. Wunderlich, "Individual addressing of trapped ions and coupling of motional and spin states using rf radiation," *Phys. Rev. Lett.*, vol. 102, p. 073004, Feb 2009.

[288] S. Crain, E. Mount, S. Baek, and J. Kim, "Individual addressing of trapped 171Yb$^+$ ion qubits using a microelectromechanical systems-based beam steering system," *Appl. Phys. Lett.*, vol. 105, no. 18, pp. –, 2014.

[289] C. Weitenberg, M. Endres, J. F. Sherson, M. Cheneau, P. Schausz, T. Fukuhara, I. Bloch, and S. Kuhr, "Single-spin addressing in an atomic mott insulator," *Nature*, vol. 471, pp. 319–324, 03 2011.

[290] M. H. Devoret and R. J. Schoelkopf, "Superconducting circuits for quantum information: An outlook," *Science*, vol. 339, no. 6124, pp. 1169–1174, 2013.

[291] R. Barends, J. Kelly, A. Megrant, A. Veitia, D. Sank, E. Jeffrey, T. C. White, J. Mutus, A. G. Fowler, B. Campbell, Y. Chen, Z. Chen, B. Chiaro, A. Dunsworth, C. Neill, P. O'Malley, P. Roushan, A. Vainsencher, J. Wenner, A. N. Korotkov, A. N. Cleland, and J. M. Martinis, "Superconducting quantum circuits at the surface code threshold for fault tolerance," *Nature*, vol. 508, pp. 500–503, 04 2014.

[292] R. Barends, L. Lamata, J. Kelly, L. Garcia-Alvarez, A. G. Fowler, A. Megrant, E. Jeffrey, T. C. White, D. Sank, J. Y. Mutus, B. Campbell, Y. Chen, Z. Chen, B. Chiaro, A. Dunsworth, I. C. Hoi, C. Neill, P. J. J. O/'Malley, C. Quintana, P. Roushan, A. Vainsencher, J. Wenner, E. Solano, and J. M. Martinis, "Digital quantum simulation of fermionic models with a superconducting circuit," *Nat Commun*, vol. 6, 07 2015.

[293] Y. Salathé, M. Mondal, M. Oppliger, J. Heinsoo, P. Kurpiers, A. Potočnik, A. Mezzacapo, U. Las Heras, L. Lamata, E. Solano, S. Filipp, and A. Wallraff, "Digital quantum simulation of spin models with circuit quantum electrodynamics," *Phys. Rev. X*, vol. 5, p. 021027, Jun 2015.

[294] M. B. Hastings and T. Koma, "Spectral gap and exponential decay of correlations," *Commun. Math. Phys.*, vol. 265, no. 3, pp. 781–804, 2006.

[295] B. Nachtergaele and R. Sims, "Lieb-robinson bounds and the exponential clustering theorem," *Commun. Math. Phys.*, vol. 265, no. 1, pp. 119–130, 2006.

[296] Z.-X. Gong, M. Foss-Feig, S. Michalakis, and A. V. Gorshkov, "Persistence of locality in systems with power-law interactions," *Phys. Rev. Lett.*, vol. 113, p. 030602, Jul 2014.

[297] M. Foss-Feig, Z.-X. Gong, C. W. Clark, and A. V. Gorshkov, "Nearly linear light cones in long-range interacting quantum systems," *Phys. Rev. Lett.*, vol. 114, p. 157201, Apr 2015.

[298] L. Viola and E. Knill, "Robust dynamical decoupling of quantum systems with bounded controls," *Phys. Rev. Lett.*, vol. 90, p. 037901, Jan 2003.

[299] T. E. Hodgson, L. Viola, and I. D'Amico, "Towards optimized suppression of dephasing in systems subject to pulse timing constraints," *Phys. Rev. A*, vol. 81, p. 062321, Jun 2010.

[300] G. S. Uhrig and S. Pasini, "Efficient coherent control by sequences of pulses of finite duration," *New J. Phys.*, vol. 12, no. 4, p. 045001, 2010.

[301] M. H. Levitt, "Composite pulses," *Prog. Nucl. Magn. Reson. Spectrosc.*, vol. 18, no. 2, pp. 61 – 122, 1986.

[302] C. A. Ryan, J. S. Hodges, and D. G. Cory, "Robust decoupling techniques to extend quantum coherence in diamond," *Phys. Rev. Lett.*, vol. 105, p. 200402, Nov 2010.

[303] S. Aaronson, *Quantum computing since Democritus*. Cambridge University Press, 2013.

[304] P. W. Shor, "Polynomial-time algorithms for prime factorization and discrete logarithms on a quantum computer," *SIAM J. Comput.*, vol. 26, pp. 1484–1509, Oct. 1997.

[305] M. Tillmann, B. Dakic, R. Heilmann, S. Nolte, A. Szameit, and P. Walther, "Experimental boson sampling," *Nat Photon*, vol. 7, pp. 540–544, 07 2013.

[306] A. Crespi, R. Osellame, R. Ramponi, D. J. Brod, E. F. Galvao, N. Spagnolo, C. Vitelli, E. Maiorino, P. Mataloni, and F. Sciarrino, "Integrated multimode interferometers with arbitrary designs for photonic boson sampling," *Nat Photon*, vol. 7, pp. 545–549, 07 2013.

[307] N. Spagnolo, C. Vitelli, L. Sansoni, E. Maiorino, P. Mataloni, F. Sciarrino, D. J. Brod, E. F. Galvão, A. Crespi, R. Ramponi, and R. Osellame, "General rules for bosonic bunching in multimode interferometers," *Phys. Rev. Lett.*, vol. 111, p. 130503, Sep 2013.

[308] N. Spagnolo, C. Vitelli, M. Bentivegna, D. J. Brod, A. Crespi, F. Flamini, S. Giacomini, G. Milani, R. Ramponi, P. Mataloni, R. Osellame, E. F. Galvao, and F. Sciarrino, "Experimental validation of photonic boson sampling," *Nat Photon*, vol. 8, pp. 615–620, 08 2014.

[309] J. Carolan, M. D. A., P. J. Shadbolt, N. J. Russell, N. Ismail, K. Wörhoff, T. Rudolph, M. G. Thompson, J. L. O'Brien, M. C. F., and A. Laing, "On the experimental verification of quantum complexity in linear optics," *Nat Photon*, vol. 8, pp. 621–626, 08 2014.

[310] M. Bentivegna, N. Spagnolo, C. Vitelli, F. Flamini, N. Viggianiello, L. Latmiral, P. Mataloni, D. J. Brod, E. F. Galvão, A. Crespi, R. Ramponi, R. Osellame, and F. Sciarrino, "Experimental scattershot boson sampling," *Science Advances*, vol. 1, no. 3, p. e1400255, 2015.

[311] L. Valiant, "The complexity of computing the permanent," *Theoretical Computer Science*, vol. 8, no. 2, pp. 189 – 201, 1979.

[312] C. Gogolin, M. Kliesch, L. Aolita, and J. Eisert, "Boson-Sampling in the light of sample complexity," *ArXiv e-prints*, June 2013.

[313] S. Aaronson and A. Arkhipov, "Bosonsampling is far from uniform," *Quantum Info. Comput.*, vol. 14, pp. 1383–1423, Nov. 2014.

[314] M. C. Tichy, K. Mayer, A. Buchleitner, and K. Mølmer, "Stringent and efficient assessment of boson-sampling devices," *Phys. Rev. Lett.*, vol. 113, p. 020502, Jul 2014.

[315] L. Aolita, C. Gogolin, M. Kliesch, and J. Eisert, "Reliable quantum certification of photonic state preparations," *Nat Commun*, vol. 6, p. 8498, 11 2015.

[316] M. Tillmann, S.-H. Tan, S. E. Stoeckl, B. C. Sanders, H. de Guise, R. Heilmann, S. Nolte, A. Szameit, and P. Walther, "Generalized multiphoton quantum interference," *Phys. Rev. X*, vol. 5, p. 041015, Oct 2015.

[317] M. C. Tichy, "Interference of identical particles from entanglement to boson-sampling," *Journal of Physics B: Atomic, Molecular and Optical Physics*, vol. 47, no. 10, p. 103001, 2014.

[318] V. S. Shchesnovich, "Partial indistinguishability theory for multiphoton experiments in multiport devices," *Phys. Rev. A*, vol. 91, p. 013844, Jan 2015.

[319] M. Walschaers, J. Kuipers, J.-D. Urbina, K. Mayer, M. C. Tichy, K. Richter, and A. Buchleitner, "Statistical benchmark for bosonsampling," *New J. Phys.*, vol. 18, no. 3, p. 032001, 2016.

[320] P. P. Rohde and T. C. Ralph, "Error tolerance of the boson-sampling model for linear optics quantum computing," *Phys. Rev. A*, vol. 85, p. 022332, Feb 2012.

[321] V. S. Shchesnovich, "Sufficient condition for the mode mismatch of single photons for scalability of the boson-sampling computer," *Phys. Rev. A*, vol. 89, p. 022333, Feb 2014.

[322] S. Scheel, "Permanents in linear optical networks," *eprint arXiv:quant-ph/0406127*, June 2004.

[323] K. Mayer, M. C. Tichy, F. Mintert, T. Konrad, and A. Buchleitner, "Counting statistics of many-particle quantum walks," *Phys. Rev. A*, vol. 83, p. 062307, Jun 2011.

[324] D. Porras and J. I. Cirac, "Bose-einstein condensation and strong-correlation behavior of phonons in ion traps," *Phys. Rev. Lett.*, vol. 93, p. 263602, Dec 2004.

[325] C. Shen, Z. Zhang, and L.-M. Duan, "Scalable implementation of boson sampling with trapped ions," *Phys. Rev. Lett.*, vol. 112, p. 050504, Feb 2014.

[326] Rigorously speaking, each set of generated samples may have different N_B since we do not strictly control it. Hence each χ^2 statistic may have different df. However, N_B does not vary much in each run, and we can see that the χ^2 statistics for a pair of experimental samples roughly follow the χ^2-distribution with $\mathrm{df} = \overline{N_B} - 1$. The pass rates in table 6.3 are calculated properly as p-values are computed for each pair of samples with the actual df.

[327] P. W. Shor, "Algorithms for quantum computation: discrete logarithms and factoring," in *Foundations of Computer Science, 1994 Proceedings., 35th Annual Symposium on*, pp. 124–134, Nov 1994.

[328] A. W. Harrow, A. Hassidim, and S. Lloyd, "Quantum algorithm for linear systems of equations," *Phys. Rev. Lett.*, vol. 103, p. 150502, Oct 2009.

[329] M. J. Bremner, R. Jozsa, and D. J. Shepherd, "Classical simulation of commuting quantum computations implies collapse of the polynomial hierarchy," *Proc. R. Soc. A*, vol. 467, no. 2126, pp. 459–472, 2010.

[330] M. J. Bremner, A. Montanaro, and D. J. Shepherd, "Average-case complexity versus approximate simulation of commuting quantum computations," *Phys. Rev. Lett.*, vol. 117, p. 080501, Aug 2016.

[331] K. Fujii and S. Tamate, "Computational quantum-classical boundary of noisy commuting quantum circuits," *Sci. Rep.*, vol. 6, p. 25598, 2016.

[332] M. J. Bremner, A. Montanaro, and D. J. Shepherd, "Achieving quantum supremacy with sparse and noisy commuting quantum computations," *ArXiv e-prints*, Oct. 2016.

[333] T. Morimae, K. Fujii, and J. F. Fitzsimons, "Hardness of classically simulating the one-clean-qubit model," *Phys. Rev. Lett.*, vol. 112, p. 130502, Apr 2014.

[334] K. Fujii, H. Kobayashi, T. Morimae, H. Nishimura, S. Tamate, and S. Tani, "Impossibility of Classically Simulating One-Clean-Qubit Computation," *ArXiv e-prints*, Sept. 2014.

[335] A. Bouland, L. Mančinska, and X. Zhang, "Complexity classification of two-qubit commuting hamiltonians," *ArXiv e-prints*, Feb. 2016.

[336] E. Farhi and A. W. Harrow, "Quantum Supremacy through the Quantum Approximate Optimization Algorithm," *ArXiv e-prints*, Feb. 2016.

[337] K. Fujii, "Noise Threshold of Quantum Supremacy," *ArXiv e-prints*, Oct. 2016.

[338] S. Arora and B. Barak, *Computational complexity: a modern approach*. Cambridge University Press, 2009.

[339] See Supplemental Material for more details on the proof of the hardness result and the simulation and certification with variation distance errors.

[340] I. Buluta and F. Nori, "Quantum simulators," *Science*, vol. 326, no. 5949, pp. 108–111, 2009.

[341] S. Toda, "Pp is as hard as the polynomial-time hierarchy," *SIAM J. Comput.*, vol. 20, no. 5, pp. 865–877, 1991.

[342] Y. Han, L. A. Hemaspaandra, and T. Thierauf, "Threshold computation and cryptographic security," *SIAM J. Comput.*, vol. 26, no. 1, pp. 59–78, 1997.

[343] S. Aaronson, "Quantum computing, postselection, and probabilistic polynomial-time," *Proc. R. Soc. A*, vol. 461, no. 2063, pp. 3473–3482, 2005.

[344] D. Hangleiter, M. Kliesch, M. Schwarz, and J. Eisert, "Direct certification of a class of quantum simulations," *ArXiv e-prints*, Apr. 2016.

[345] M. Cramer, M. B. Plenio, S. T. Flammia, R. Somma, D. Gross, S. D. Bartlett, O. Landon-Cardinal, D. Poulin, and Y.-K. Liu, "Efficient quantum state tomography," *Nat. Commun.*, vol. 1, p. 149, Dec. 2010.

[346] B. Fefferman and C. Umans, "The Power of Quantum Fourier Sampling," *ArXiv e-prints*, July 2015.

[347] S. Aaronson, "The equivalence of sampling and searching," *Theor. Comp. Sys.*, vol. 55, no. 2, pp. 281–298, 2014.

[348] R. Raussendorf, J. Harrington, and K. Goyal, "A fault-tolerant one-way quantum computer," *Ann. Phys.*, vol. 321, no. 9, pp. 2242 – 2270, 2006.

[349] H. J. Briegel, D. E. Browne, W. Dür, R. Raussendorf, and M. Van den Nest, "Measurement-based quantum computation," *Nat. Phys.*, vol. 5, no. 1, pp. 19–26, 2009.

[350] R. Raussendorf and H. J. Briegel, "A one-way quantum computer," *Phys. Rev. Lett.*, vol. 86, pp. 5188–5191, May 2001.

[351] R. Raussendorf, D. E. Browne, and H. J. Briegel, "Measurement-based quantum computation on cluster states," *Phys. Rev. A*, vol. 68, p. 022312, Aug 2003.

[352] A. Broadbent, J. Fitzsimons, and E. Kashefi, "Universal blind quantum computation," in *Foundations of Computer Science, 2009. FOCS '09. 50th Annual IEEE Symposium on*, pp. 517–526, Oct 2009.

[353] A. Y. Kitaev, "Quantum computations: algorithms and error correction," *Russ. Math. Surv.*, vol. 52, no. 6, p. 1191, 1997.

[354] D. Jaksch, H.-J. Briegel, J. I. Cirac, C. W. Gardiner, and P. Zoller, "Entanglement of atoms via cold controlled collisions," *Phys. Rev. Lett.*, vol. 82, pp. 1975–1978, Mar 1999.

[355] O. Mandel, M. Greiner, A. Widera, T. Rom, T. W. Hansch, and I. Bloch, "Controlled collisions for multi-particle entanglement of optically trapped atoms," *Nature*, vol. 425, pp. 937–940, 10 2003.

[356] P. Zupancic, P. M. Preiss, R. Ma, A. Lukin, M. E. Tai, M. Rispoli, R. Islam, and M. Greiner, "Ultra-precise holographic beam shaping for microscopic quantum control," *ArXiv e-prints*, Apr. 2016.

[357] A. Y. Kitaev, A. Shen, and M. N. Vyalyi, *Classical and quantum computation*, vol. 47. American Mathematical Society Providence, 2002.

[358] X. G. WEN, "Topological orders in rigid states," *International Journal of Modern Physics B*, vol. 04, no. 02, pp. 239–271, 1990.

[359] A. Kitaev and J. Preskill, "Topological entanglement entropy," *Phys. Rev. Lett.*, vol. 96, p. 110404, Mar 2006.

[360] R. A. Hart, P. M. Duarte, T.-L. Yang, X. Liu, T. Paiva, E. Khatami, R. T. Scalettar, N. Trivedi, D. A. Huse, and R. G. Hulet, "Observation of antiferromagnetic correlations in the hubbard model with ultracold atoms," *Nature*, vol. 519, pp. 211–214, 03 2015.

[361] M. Boll, T. A. Hilker, G. Salomon, A. Omran, J. Nespolo, L. Pollet, I. Bloch, and C. Gross, "Spin- and density-resolved microscopy of antiferromagnetic correlations in fermi-hubbard chains," *Science*, vol. 353, no. 6305, pp. 1257–1260, 2016.

[362] A. Mazurenko, C. S. Chiu, G. Ji, M. F. Parsons, M. Kanász-Nagy, R. Schmidt, F. Grusdt, E. Demler, D. Greif, and M. Greiner, "Experimental realization of a long-range antiferromagnet in the Hubbard model with ultracold atoms," *ArXiv e-prints*, Dec. 2016.

[363] A. Polkovnikov, K. Sengupta, A. Silva, and M. Vengalattore, "Colloquium: Nonequilibrium dynamics of closed interacting quantum systems," *Rev. Mod. Phys.*, vol. 83, pp. 863–883, Aug 2011.

[364] J. Eisert, M. Friesdorf, and C. Gogolin, "Quantum many-body systems out of equilibrium," *Nat Phys*, vol. 11, pp. 124–130, 02 2015.

[365] J. M. Deutsch, "Quantum statistical mechanics in a closed system," *Phys. Rev. A*, vol. 43, pp. 2046–2049, Feb 1991.

[366] M. Srednicki, "Chaos and quantum thermalization," *Phys. Rev. E*, vol. 50, pp. 888–901, Aug 1994.

[367] M. Rigol, V. Dunjko, and M. Olshanii, "Thermalization and its mechanism for generic isolated quantum systems," *Nature*, vol. 452, pp. 854–858, 04 2008.

[368] A. Pal and D. A. Huse, "Many-body localization phase transition," *Phys. Rev. B*, vol. 82, p. 174411, Nov 2010.

[369] R. Nandkishore and D. A. Huse, "Many-body localization and thermalization in quantum statistical mechanics," *Annual Review of Condensed Matter Physics*, vol. 6, no. 1, pp. 15–38, 2015.

[370] T. Kinoshita, T. Wenger, and D. S. Weiss, "A quantum newton's cradle," *Nature*, vol. 440, pp. 900–903, 04 2006.

[371] P. Richerme, Z.-X. Gong, A. Lee, C. Senko, J. Smith, M. Foss-Feig, S. Michalakis, A. V. Gorshkov, and C. Monroe, "Non-local propagation of correlations in quantum systems with long-range interactions," *Nature*, vol. 511, pp. 198–201, 07 2014.

[372] P. Jurcevic, B. P. Lanyon, P. Hauke, C. Hempel, P. Zoller, R. Blatt, and C. F. Roos, "Quasiparticle engineering and entanglement propagation in a quantum many-body system," *Nature*, vol. 511, pp. 202–205, 07 2014.

[373] A. M. Kaufman, M. E. Tai, A. Lukin, M. Rispoli, R. Schittko, P. M. Preiss, and M. Greiner, "Quantum thermalization through entanglement in an isolated many-body system," *Science*, vol. 353, no. 6301, pp. 794–800, 2016.

[374] M. Schreiber, S. S. Hodgman, P. Bordia, H. P. Lüschen, M. H. Fischer, R. Vosk, E. Altman, U. Schneider, and I. Bloch, "Observation of many-body localization of interacting fermions in a quasirandom optical lattice," *Science*, vol. 349, no. 6250, pp. 842–845, 2015.

[375] J.-y. Choi, S. Hild, J. Zeiher, P. Schauß, A. Rubio-Abadal, T. Yefsah, V. Khemani, D. A. Huse, I. Bloch, and C. Gross, "Exploring the many-body localization transition in two dimensions," *Science*, vol. 352, no. 6293, pp. 1547–1552, 2016.

[376] J. Smith, A. Lee, P. Richerme, B. Neyenhuis, P. W. Hess, P. Hauke, M. Heyl, D. A. Huse, and C. Monroe, "Many-body localization in a quantum simulator with programmable random disorder," *Nat Phys*, vol. 12, pp. 907–911, 10 2016.

[377] C. R. Monroe, R. J. Schoelkopf, and M. D. Lukin, "Quantum connections," *Scientific American*, vol. 314, no. 5, pp. 50–57, 2016.

[378] L.-M. Duan and C. Monroe, "Colloquium: Quantum networks with trapped ions," *Rev. Mod. Phys.*, vol. 82, pp. 1209–1224, Apr 2010.

[379] S. Debnath, N. M. Linke, C. Figgatt, K. A. Landsman, K. Wright, and C. Monroe, "Demonstration of a small programmable quantum computer with atomic qubits," *Nature*, vol. 536, pp. 63–66, 08 2016.

[380] N. M. Linke, D. Maslov, M. Roetteler, S. Debnath, C. Figgatt, K. A. Landsman, K. Wright, and C. Monroe, "Experimental Comparison of Two Quantum Computing Architectures," *ArXiv e-prints*, Feb. 2017.

[381] V. Jacques, P. Neumann, J. Beck, M. Markham, D. Twitchen, J. Meijer, F. Kaiser, G. Balasubramanian, F. Jelezko, and J. Wrachtrup, "Dynamic polarization of single nuclear spins by optical pumping of nitrogen-vacancy color centers in diamond at room temperature," *Phys. Rev. Lett.*, vol. 102, p. 057403, Feb 2009.

[382] M. Glück, A. R Kolovsky, and H. J. Korsch, "Wannier–stark resonances in optical and semiconductor superlattices," *Physics Reports*, vol. 366, no. 3, pp. 103–182, 2002.

[383] H. Miyake, *Probing and Preparing Novel States of Quantum Degenerate Rubidium Atoms in Optical Lattices*. PhD thesis, Massachusetts Institute of Technology, 2013.

[384] L. Stockmeyer, "On approximation algorithms for #p," *SIAM J. Comput.*, vol. 14, no. 4, pp. 849–861, 1985.

[385] C. E. Porter and R. G. Thomas, "Fluctuations of nuclear reaction widths," *Phys. Rev.*, vol. 104, pp. 483–491, Oct 1956.